

# SCIENTIFIC & TECHNICAL REPORT 2021

## IMPRINT

---

**Full report title** CSEM Scientific and Technical Report 2021

**Editor and publisher** CSEM SA  
[info@csem.ch](mailto:info@csem.ch)  
T +41 32 720 5111

**Publication** Frequency yearly  
Media printed and electronic Website  
[www.csem.ch/str2021](http://www.csem.ch/str2021)

**Cover page design** Contreforme  
[www.contreforme.ch](http://www.contreforme.ch)

**Printing** Imprimerie Baillod SA, Bevaix (Switzerland)

# PREFACE

Dear Reader,

CSEM is an incredible innovation factory and value creation engine, working with and for our industrial partners. Daily we establish contacts with new companies, launch exciting projects, and deliver impactful prototypes, products, and services—most of which find their way to market.

Nothing is permanent but change. We must all work on our ability to remain at the forefront of technological advancement in the digital era. One of CSEM's great strengths lies in developing Deep Tech. But these technologies have a relatively long maturation period, so the seeds we sow today will only bear fruit in several years' time. It's never an easy task deciding which ideas we should pursue now to secure our future, but we are on track for success.

Making the right change now is also a challenge facing many so-called "traditional" companies. In our increasingly connected world, the time has come for the business models of old to be transformed, and for companies to be bold and take a chance on the digital realm. They say you can't teach an old dog new tricks, but I beg to differ. Even though these "traditional" companies were not conceived in the digital age, engaging with the digital transformation will help them remain competitive, driving growth through the development of new products and digital services, and reducing cost through optimized internal processes.

Digital technologies are now everywhere. Look at the revamp taking place in the energy landscape, where thanks to digitalization we are now seeing continuous energy efficiency gains. In manufacturing, digital technologies are improving production safety, productivity, reliability, and maintenance. The positives of going digital outweigh the negatives. This is why CSEM is so important, we not only connect companies to the digital realm, we help them discover technologies of the future.

Research, innovation, and technology transfer are at the core of CSEM's DNA. We will continue to build on this genetic legacy, combining the strengths of the physical and digital worlds to face the challenges of our time.

Alexandre Pauchard  
CEO, CSEM SA



# CONTENTS

## PREFACE

## MULTIDISCIPLINARY INTEGRATED PROJECTS—MIPS

UC-MORE—Ultra-compact Multispectral Snapshot Camera Based on Optical Nanostructures

INFENITT—Interfacial Engineering of Electrodes for Improved Battery Performance

CHAMELEON—Additively Manufactured Compliant Mechanism with Printed Strain Gauge for Motion Measurement and Control

LINIO-PIC—Lithium Niobate on Insulator (LNOI) PIC Platform

SIOSCAPE—A Novel Constant Force Escapement

## DIGITAL TECHNOLOGIES

$\mu$ 111MP—Implementing Kernel-to-Kernel Communication on 64-bit Dual-Core RISC-V Processor

Long-Range IoT Communication on ULP  $\mu$ 111 RTOS

Secure Boot and Firmware Update for  $\mu$ 111 RTOS

End-to-end Security and Key Provisioning for Wireless Sensor Networks

Ultra-low-power Multi-standard Communication Miniature IoT Node

Authenticated Encryption with Flexible Authenticator Length for Energy-Efficient IoT

A Robust Data Collection Infrastructure for Localization and Sensing in Large Structures

MANTIS, an Indoor Localization and Navigation Framework with Machine Learning Support

AMPWISE, an Energy Autonomous and Wireless Electrical Current Sensor

Guardian, a Lightweight AIoT Modular Platform

Metallic Additive Manufacturing Technologies for 3D-shaped Millimeter-Wave Components Production

Powerline Communications across Battery Cells

Compostable Chipless Sensor Tag for Green Smart Packaging

Harnessing the Power of 3D Data through Deep Learning and Computer Vision

How Little is Too Little? Image Generation Performance in a Small Industrial Data Setting

It's a Match—Your Profile in the Cloud

Gemstones, Place of Origin and Heat Treatments: Automatic Recognition and Classification using Deep Learning

Linear Adaptive Model Identification with Gaussian Processes

Uncertainty-Aware Prognosis via Deep Gaussian Processes

Cuffless 24-Hour Ambulatory Blood Pressure Monitoring

1	VO2Max and Fitness Level Estimated with Speed and Heart Rate	37
9	Measurement Location Influences Reflectance Pulse Oximetry During Sleep	38
10	Sleep Staging with Convolutional Recurrent Neural Networks	39
11	Miniature ECG Cooperative Sensors for Daily Monitoring	40
12	ULTEEM—Ultra-long-term EEG Monitoring	41
13	Secure Ultra-long-term Ambulatory Monitoring of Subscalp EEG for Epilepsy Management	42
14	Collaborative Privacy-Preserving Training of Decision Trees	43
15	Improving Cockpit Safety through Real-Time Monitoring of Pilots with a Smart Vision System	44
17	Live Analysis of Grains Morphology and Flowing Speed	45
18	Data Augmentation for Machine Learning Based Multi-illumination Defect Detection	46
19	Optical Neural Network for an Ultra-secure Vision System	47
20	Distributed Encryption for Robust Data Confidentiality and Integrity for IoT	48
21	Hierarchical Machine Learning for Low-power IoT: Let's Exit Early!	49
22	Ultra-low-power Networks for Neuromorphic Devices	50
23	SWISSMODICS—Toward Combined Visible, Infrared and X-Ray Imaging	51
24	PreciSense, a High-Performance, Low-Cost, Absolute Position Sensor	52
25	Towards Battery-Less Machine Learning Inference at the Edge	53
26	An Ultra-energy-efficient AI Chip for Next-Generation ICT Applications	54
27	An Ultra-low-power Short-Range 60-GHz FMCW Radar in 22-nm FDSOI CMOS: Performance Characterization	55
28	An Ultra-low-power $\Delta\Sigma$ Analog to Digital Converter for High-Resolution Applications	56
29	Miniature Quantum Sensor Prototypes: Development Status	57
30	Two-Photon Atomic Clock Targeting Miniature Dimensions and High Performances	58
31	Ultra-short Pulse Non-Classical Light Emitters Utilizing Multiple Wide Quantum Wells	59
32	<b>PRECISION MANUFACTURING</b>	61
33	Advances in the Development of Highly Piezoelectric $\text{Al}_{0.7}\text{Sc}_{0.3}\text{N}$ Layers	63
34	Silicon Carbide Pressure Sensor Characterization	64
35	Optoelectronic Packaging for Mid-IR OEM Laser Sources	65
36	Thermal Management Simulations Based on Advanced Materials and Assembly Configurations	66
	Active Cooling-based Packages for Power Electronics	67
	Reliability Assessment and Development of Qualification Standard for Miniaturized RF Electromechanical Relay for Space Applications	68

Highly Efficient AM-based Cooling System for High-Power Electronics	69	Design for Manufacturing Tools: Freeform Micro-optics Surface Topology and Functionality of Freeform Micro-optical Arrays	100
Promising Metallic Additive Manufacturing Technologies for 3D-shaped Millimeter-Wave Components Production	70	Wearable Temperature Sensor based on Photonic Technologies for Blood Composition Measurement	101
Development of Additively Manufactured Functionally Graded Components	71	Novel Microvibration Test Facility	102
Development of High-Specific Stiffness Composites by LPBF	72	COOLER, a Louvered, Passive Radiator for CubeSats	103
Validation of the Metal Additive Manufacturing Pilot Line Manuela	73	ISOL—Development of a High-Performance Microvibration Isolation System	104
Towards Metal-Organic Framework based Field Effect Chemical Sensors for Pesticides Detection	74	LOSORA—Novel Actuator Concept for Unidirectional Displacement	105
Molecular Imprinted Polymer Sensor for Nicotine Detection	75	Blue-Chirped Emission in Fabry-Perot Cavity Quantum Cascade Laser at Room Temperature	106
Barrier Treatment on Cellulose to Control Release of Elements in Blood Testing Device	76	Agile High-Power Femtosecond Laser with Programmable Burst Generation	107
Selective Electroless Metal Deposition on Micropatterns Produced by Aerosol Jet Printing	77	Versatile Flash LiDAR Integrated in Drones	108
Colored Surfaces Based on Micro and Nanoparticle Self-assembly	78	<b>SUSTAINABLE ENERGY</b>	<b>111</b>
Self-cleaning Surfaces for Optical Sensors in Harsh Environment	79	PeroCUBE—Development of Ubiquitous Perovskite-based Energy Harvesters and Light Emitters	114
Anti-corrosion Coating by Liquid Deposition on Watch Components	80	Progress Towards High-Efficiency Silicon/Perovskite Tandems	115
Inkjet Printable and Slot-Die Coatable Formulations for Pre-encapsulation of Solar Cells and Flexible OLEDs	81	Building Blocks for PERx Solar Cells Upgrade	116
Self-assembled Monolayers for Streamlined Process Flows in High-Efficiency Tandem Solar Cells	82	Technology Platform for High-Efficiency HJT Solar Cells	117
SMART LIDS—Standardized Cell and Tissue Culture in Multi-well Plates	83	From R&D at CSEM to Meyer Burger New PV Product Launch	118
Microtissues and Organoids High-Throughput Histology	84	CSEM Coloring Technologies for Building Integration of Photovoltaics (BIPV)	119
denovoCast—Automated Skin Tissue Formation Machine	85	Copper Metallization for Silicon Heterojunction Solar Cells	120
Deep-Learning Powered Organoid Handling and Sorting Platform for Liver Tissue Engineering	86	Reliable Photovoltaic Solution for Stratospheric Applications	121
Cell Culture Monitoring	87	Energym, an Open-Source Library for Data-driven Building Control	122
PEPS—Printed Electrochemical Protein Sensor	88	Field Demonstration of Data-driven Control for the Provision of Flexibility from Distributed Resources	123
DigiLab—Automated Calibration Platform for Liquid Handling Systems	89	Real-Time Forecasting of PV Production for Individual Plants at Country Scales	124
Coatings for SWCNT-based Glucose Biosensors Applied in Cell Culture Monitoring	90	A Control Software for Air Handling Units in Commercial Buildings	125
Enhancing the Performances of Lateral Flow Assays	91	Battery Energy Storage for Optimal Renewable Power Trading	126
Cartridge for Digital Urine Analysis with Electrochemical Sensors	92	Battery Accelerated Testing for Second-Life Li-ion Cells	127
Modular Electronic Readout Platform for Electrochemical Sensing	93	Impact of Vehicle-to-Grid Service Provision on Batteries	128
LEDLight—Multiwavelength Imaging System for Security Feature Inspection	94		
Nanoimprinted Diffractive Waveguides with Refractive Index above 1.9 for Augmented Reality	95		
Narrowband Spectral Filters Based on Nanostructured Arrays	96		
Femtochip—Electro-Optic Frequency Combs and Integrated Photonic Circuits	97		
Microlenses: Capability Overview	98		
Fabrication of Arrays of Quasi-micro-beads for Parallel Nanojet Super-resolution Imaging	99		

## **ANNEXES**

**129**

Publications	129
Proceedings	131
Conferences and Workshops	133
Research Projects	135
Innosuisse – Swiss Innovation Agency	138
European Commission Projects	142
Space Projects	144
Industrial Property	145
Collaboration with Research Institutes and Universities	145
Teaching	151
Theses	152
Commissions and Committees	154
Prizes and Awards	157



# CSEM SA

CSEM is a Swiss research and innovation center that actively works in the fields of digital technologies, precision microfabrication, and renewable energy. CSEM builds ties between industry and academia, supporting companies as an ingenuity hub, a center of Deep Tech excellence and innovation, and an accelerator of digital transformation.

The Center's research strategy builds on three main axes, which are crucial for our future environmental, economic, and social sustainability:

**Digital Technologies**—CSEM provides state-of-the-art technological solutions for Data and Artificial Intelligence, the Internet of Things, Vision Systems, Industry 4.0, Digital Health, and Quantum Technologies, covering a wide range of potential applications and industries undergoing digital transformation.

#visionsensors #machinelearning #AI #edgecomputing #IoT  
#SystemOnChip #wireless #neuralnetworks #datascience  
#medicaldevices #wearable #quantumtechnology #Industry4.0

**Precision Manufacturing**—CSEM's precision manufacturing domain brings research to life, finding ways to fabricate at a scale that can minimize cost and waste, increase quality (while maintaining reliability and functionality), and push engineering expertise to new heights. CSEM provides businesses and manufacturers with flexible, affordable, customized precision manufacturing solutions in MEMS Design and Integration, Functional Surfaces, Additive Manufacturing, Photonics, Tools for Life Sciences, and Scientific Instrumentation.

#additivemanufacturing #AM #mems #3Dprinting #packaging  
#lifesciences #photonics #time&frequency #laser  
#functionalization #biosensing #biosurface #lifesciences

**Sustainable Energy**—From PV and Energy Harvesting solutions to Digital Energy and Energy Storage, CSEM's connected and integrated energy solutions help to preserve the natural environment, to drive economic development, and to advance innovation across the whole energy sector, paving the way toward an optimized, renewable future.

#smartgrid #storage #energydata #bipv #solarenergy #thinfilm  
#photovoltaics #bipv #batteryresearch



# MULTIDISCIPLINARY INTEGRATED PROJECTS—MIPS

Harry Heinzelmann

Multidisciplinary integrated projects (MIPs) form an interdisciplinary program that builds on the combination of technologies developed in the three Research Priorities **Precision Manufacturing**, **Digital Technologies**, and **Sustainable Energy**. The goal of the MIP program is to better exploit synergies and to create innovative solutions.

Every year CSEM dedicates an important part of its resources to the program, targeting demonstrators with a high level of maturity (i.e., a high technology readiness level (TRL)) for novel applications with high market potential in relatively short development times. Classical MIPs typically last 1–2 years, while Technology MIPs address longer term co-developments of novel technology bricks.

The MIP program is re-evaluated annually and consists of new proposals and ongoing projects. In this way, CSEM's MIPs complement its Research Priorities in an ideal way. The program enables CSEM to offer its industrial clients an even richer portfolio of solutions, beyond the scope of its thematic research programs alone.

An overview of 2021 MIPs is given below; the projects are presented in more detail in the following pages. Due to the sanitary situation in 2021 and the consequent delays in development work, these projects include MIPs that were already started in 2020.

## Classical MIPs

### UC-MORE—Ultra-compact Multispectral Snapshot Camera based on Optical Nanostructures

Multispectral cameras allow images to be taken at multiple wavelength ranges, which provides valuable information in application areas such as environmental surveillance, industrial monitoring, and agriculture. The bulkiness and rather high cost of currently available multispectral camera systems prevent their wider application in consumer markets such as wellness, cosmetics, or photography. The miniaturization of multispectral cameras down to a scale that allows their integration into smartphones is therefore of particular interest.

The project UC-MORE targets a multispectral camera with a small form factor. The design is based on the use of novel nanostructured optical filters and a microlens array, which allow the thickness of the device to be limited to below 3 mm. A neural network is used to support the reconstruction of the spectrally separated images.

### INFENITT—Interfacial Engineering of Electrodes for Improved Battery Performance

Rechargeable batteries are a key technology for clean energy and a sustainable future. Current lithium-based batteries feature complex multilayer interfaces that are critical for their performance characteristics in charging and discharging cycles as well as for their long-term stability.

The surface properties of battery electrodes play a crucial role in battery performance. INFENITT aims at optimizing such surfaces through functionalization with specifically designed nano-coatings. Self-assembled monolayer (SAM) film coatings have proven to be well suited for this application due to their chemical

versatility and the simple and controlled way of depositing thin conformal films.

## Technology MIPs

### CHAMELEON—Additively Manufactured Compliant Mechanism with Printed Strain Gauge for Motion Measurement and Control

The development of additive manufacturing (AM) has led to the introduction of new design concepts and production processes, in particular by enabling tool-less and small-series production. The integration of functional elements, such as sensors and actuators, will further contribute to the potential of AM technologies in flexible and resource-efficient manufacturing.

The project CHAMELEON addresses the design and fabrication of metal-based 3D-printed parts with embedded functionalities. The resulting components feature integrated sensors, compliant mechanisms, feedthroughs, and actuators. These developments rely on a wide range of 3D-printing technologies including laser powder bed fusion (L-PBF) and aerosol jet printing (AJP). Space and aeronautics applications in particular show considerable interest in advanced components with increased functionalities.

### LINIO-PIC—Lithium Niobate on Insulator (LNOI) PIC Platform

Photonic integrated circuits (PICs) are devices that integrate several optical functions. They are conceptually similar to electronic integrated circuits in the electronics domain. PICs are currently mostly applied in optical communication and are mostly based on indium phosphide (InP).

Lithium niobate (LiNb) has interesting electro-optical properties that make it a promising candidate for use in PICs. The recent availability of LiNb on insulators (LNOIs) has made it easier to machine. The objective of the LINIO-PIC project is to develop the technologies necessary to process LiNb with sufficient quality and precision for the resulting structures and components to be used in PICs.

### SIOSCAPE—A novel Constant-Force Escapement

The processes developed for the precise structuration of silicon and related materials have allowed the fabrication of microelectromechanical systems (MEMS) with feature sizes down to the micrometer range. More recently, techniques such as deep reactive ion etching (DRIE) have been optimized for the fabrication of macroscopic silicon structures that surpass their metallic equivalents in many mechanical properties. Flexure-based watch parts in particular benefit from the excellent elastic behavior of silicon as well as from its nonmagnetic and corrosion-free nature.

The SIOSCAPE project is concerned with exploiting the potential of silicon-based flexure mechanisms in mechanical watches. The developed silicon-based oscillators and escapements are optimized for performance characteristics such as precision or low power consumption, and their manufacturability and ease of handling. By our providing the design, production, and characterization of such prototypes, development risks can be lowered prior to proposing the technology to our partners from the Swiss watch industry.

# UC-MORE—Ultra-compact Multispectral Snapshot Camera Based on Optical Nanostructures

C. Gimkiewicz, S. A. Bigdeli, M. Fretz, C. Schneider, L. A. Dunbar, R. Ferrini, B. Gallinet

A multispectral camera with a form factor of less than 3 mm thickness is reported. Its ultra-compact architecture is ideal for integration in IoT, wearable or smartphone devices. We show accurate spectral reconstruction of colorful objects. Further applications include color, skin, plants or food analysis.

Multispectral cameras can capture an image of a scene with a high number of spectral channels, which makes them highly attractive for accurate color rendering in photography, the analysis of skin, plants or food. However, current multispectral cameras are limited by their physical size and the cost of components. Here, we present a design of a multispectral snapshot camera with a small form factor and a thickness of <3 mm, which is ideal for integration in IoT, wearable or smartphone devices. Our design uses standard imaging optics and image sensor, with nanostructured filters and a microlens array inserted in the optical path creating no additional thickness in the optics. As the multispectral optics is fabricated and integrated independently of the image sensor, it is compatible with miniaturization of the pixel size. The chosen filtering approach is not suffering from mosaicking effects and the pixel resolution is not limited by spectral requirements.

Figure 1 shows a schematic of the multispectral camera, with a twin optics architecture [1]. The light-field emanating from an object point is imaged onto a microlens array. A filter whose transmission spectrum depends on the incidence angle is placed between the imaging optics and the microlens array. After transmission through the filter, the light angular distribution is imaged under each microlens. The signal in the image sensor under all microlenses of the array is reconstructed with a neural network to form a multispectral image. The other half of the image sensor is used to acquire a high-resolution RGB signal from the sensor, which is processed in fusion with the light-field multispectral signal.

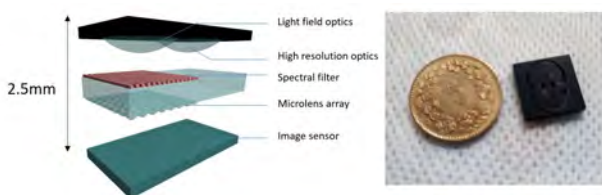


Figure 1: Multispectral imaging optics based on imaging optics, nanostructured filters with angle-dependent transmission, microlens array and an RGB image sensor.

The nanostructured filter is based on a hybrid dielectric-metallic periodic nanostructure [2]. The microlens array is originated by photolithography and reflow and replicated by UV imprint lithography on a substrate with absorbing microapertures. The nanostructured filter and microlens array are placed on the optical path at a controlled distance from the image sensor to maximize the spectral resolution.

For the neural network training, a ground truth signal is acquired with an 8-channel filter wheel placed in front of the high-resolution optics, each filter having a 20 nm bandwidth. A

reference device, (called twin-RGB device for simplicity) has both sides of the RGB sensor with high resolution (i.e. non light-field) optics. A U-NET-like convolutional neural network that benefitted from down- and up-sampling layers to enhance the region of support has been used. The model currently runs at 2p fps for the resolution of  $712 \times 712$  spectral reconstruction. A neural network with the same architecture is trained for spectral reconstruction on the reference twin-RGB device. The aim is to separate contributions from software to the hardware and to directly compare the two filtering approaches. Their performance in spectral reconstruction is compared in Figure 2. In addition to the spectral distribution of the different signals, a deviation summed over the entire spectrum has been calculated for the two approaches. Overall, the spectral reconstruction is significantly improved by the light-field architecture compared to the twin-RGB device, especially on colorful objects. Histograms of RGB values extracted from standard image acquisition with an RGB sensor shows significantly less information.

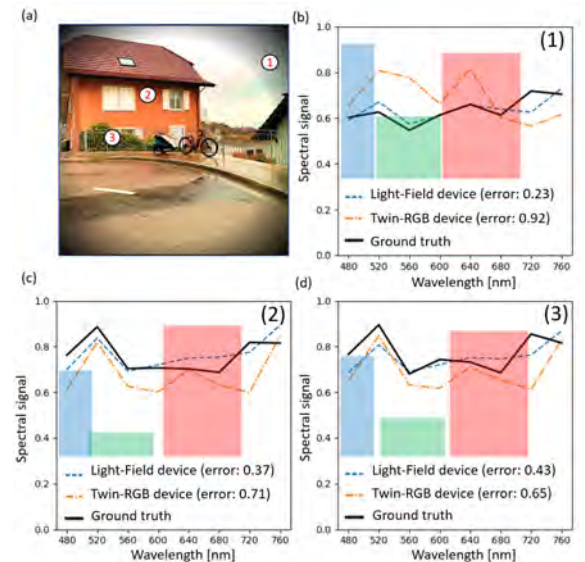


Figure 2: Spectral analysis of a street scene. Three areas (1-2-3) in the image are selected. a) Reference RGB image; b-c-d) The reconstructed spectral signals with the light field multispectral device, a twin-RGB device compared with the ground truth. A neural network is trained for spectral reconstruction on both light field and twin-RGB reference devices. In brackets: deviation from ground truth summed over the entire spectrum. Red-green-blue histograms report raw RGB values of a single camera.

In summary, we have reported on an ultra-compact multispectral camera for smartphone cameras. We have shown that it can provide more accurate spectral reconstruction of colorful objects. Further steps include an extension of its spectral range and neural network training for applications beside color analysis.

[1] Patent pending

[2] B. Gallinet, G. Quaranta, C. Schneider, "Narrowband transmission filters based on resonant waveguide gratings and conformal

# INFENITT—Interfacial Engineering of Electrodes for Improved Battery Performance

G. Andreatta, J. Gay, X. Lefèvre, J. J. Diaz Leon, L. Pires Da Veiga

Lithium-ion batteries (LiBs) and lithium-metal batteries (LMBs) are amongst the most prevailing technologies for rechargeable batteries. Interfacial engineering is recognized as critical in the improvement of performance, stability and even safety of such multi-layered systems. It is also arguably one of the least understood aspect of such systems. In the INFENITT project, the implementation of interfacial layers on key battery interfaces such as electrodes/electrolyte is investigated to improve performance, safety, and sustainability of these systems

Rechargeable batteries with a very high round-trip efficiency are a key technology enabling energy storage for a vast number of applications. Batteries can accelerate the shift towards sustainable and smart mobility; help supply clean, affordable, and secure energy and mobilize industry for a cleaner, circular economy. Unsurprisingly, battery demand is rising dramatically with a predicted market volume of 125 billion USD in 2030 (up from 25 billion USD in 2019). Europe alone will need an annual cell production capacity of > 200 GWh in the next five years [1].

Controlling and designing the function of interfaces and interphases is key for the development of ultra-performing, smart, and sustainable batteries. CSEM strong know-how and technological offer in the field of nano-coatings and functionalization of surfaces is employed to design novel interfaces at the interfaces of electrodes and electrolytes.

CSEM has been investigating novel approaches for surface modification using self-assembled monolayers (SAMs) [2] to alter the surface properties of a wide range of materials including silicon oxide, indium tin oxide and other metal oxides. SAMs can be formed on solid surfaces via simple processes, are intrinsically thin, conformal, and uniform. They are particularly suited for the surface modification of electrode materials, maintaining a uniform conduction of lithium ions without sacrificing in energy density [3].

SAMs chemistry is versatile; we thus selected molecules with functional groups compatible with the electrolyte chemistry used in LiB (hydrophilic SAM). We also compared with a chemistry which would lower the wettability of the electrolyte at the electrode surface and is expected to have an adverse effect on the electrode-electrolyte interface (hydrophobic SAM).

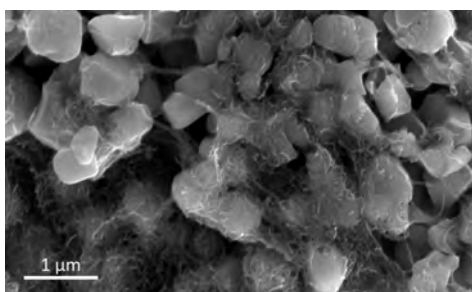


Figure 1: Scanning electron micrograph of a pristine lithium manganese oxide commercial cathode. The filaments correspond to the polymeric binder.

[1] K. Edström, S. Perraud, "BATTERY 2030+: a long-term roadmap for forward-looking battery research in Europe" 2018.

[2] G. Andreatta, N. Blondiaux, J. Gay, S. Unterhofer, A. Lachowicz, A. Faes, "Spray coating vs. immersion for self-assembly of gemini perfluorinated phosphonic acids on indium tin oxide", *Thin Solid Films*, 732 (2021) 138783.  
G. Andreatta, A. Lachowicz, N. Blondiaux, C. Allebé, A. Faes

Prior to the surface modification, commercially available LMO cathodes (Figure 1) are activated by a rapid plasma, then dipped into the appropriate solution for SAM formation. The effect of the SAM on the water contact angle is shown in Figure 2.

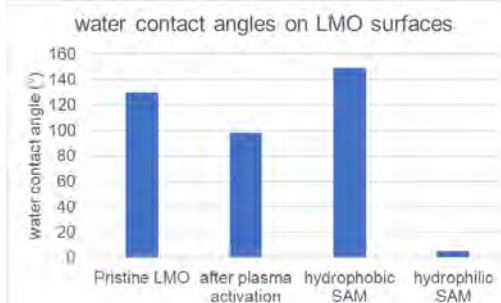


Figure 2: Effect of surface modifications on the static water contact angle.

After integration of the cathodes in coin cells, the effect of the SAM presence on the charging and discharging cycles is measured (Figure 3). Hydrophilic SAMs, meant to enhance the wettability of the electrolyte on the electrode surface and to decrease the contact resistance, are shown to have a positive effect at high discharging rates while hydrophobic SAMs are, as expected, having a negative effect at similar discharges.

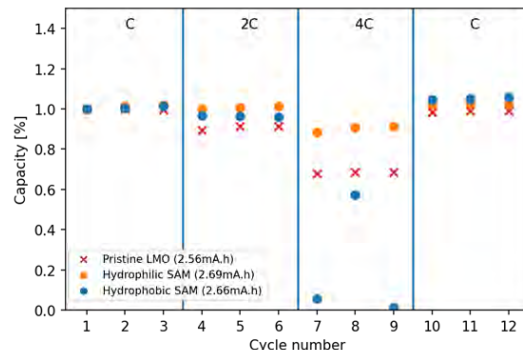


Figure 3: Effect of surface modifications during charge and discharge at different C-rates (at 1C, it takes 1h to discharge the battery, and at 4C it takes 15min).

Characterization of the SAM effect by electro-impedance spectroscopy is currently in progress to confirm above-mentioned hypothesis on the electrode-electrolyte interaction. Further work will investigate other types of SAM chemistries and their impacts on the lifespan of the batteries.

"Patterning solar cell metal grids on transparent conductive oxides using self-assembled phosphonic acid monolayers", *Thin Solid Films*, 691 (2019) 137624.

[3] W. Gu, Q. Dong, L. Zheng, Y. Liu, Y. Mao, Y. Zhao, W. Duan, H. Lin, Y. Shen, L. Chen, "Ambient Air Stable Ni-Rich Layered Oxides Enabled by Hydrophobic Self-Assembled Monolayer", *ACS Appl. Mater. Interfaces*, 12 (2020) 1937.

# CHAMELEON—Additively Manufactured Compliant Mechanism with Printed Strain Gauge for Motion Measurement and Control

S. Lani, N. Hendricks, F. Boudoire, L. Kiener, H. Saudan, D. Novo, V. Schaffter, F. Cosandier

Structural health monitoring for preventive maintenance, control feed-back of moveable mechanisms, integrated actuation and adaptive objects necessitate a heterogeneous integration of numerous technologies. To bring additive manufacturing (AM) beyond state-of-the-art technologies of topology optimization, it is important to develop concepts and technologies allowing such functionalities while keeping the versatility and flexibility advantages of AM. Hence, CHAMELEON aims at developing technologies to manufacture metal-based 3D parts with embedded functionalities such as compliant mechanisms, electrical/pneumatic feedthroughs, sensors, and actuators by combining advanced design, aerosol jet printing (AJP), polymer casting, laser powder bed fusion (L-PBF), and surface post treatment. The main applications will focus on markets already using AM in production (space, aeronautic, and medical) that are requesting additional functionalities.

AM is taking more and more importance for producing high-end components in applications like space, aeronautics, and medical fields. Such industries have critical needs for which AM has appealing features. Among them, they benefit from a manufacturing technology able to produce components with complex geometries that are suitable for moderate production volume as well as weight reduction thanks to topology optimization. However, most of today's applications, for which AM is used, is for manufacturing "passive" elements with no functionality except providing a mechanical structure. To grow the market attractiveness of AM, it is important to develop technologies to bring new functionalities while keeping the advantages of flexibility and versatility of AM. Hence, CSEM is investigating the opportunity to combine 3D printing with 2D printing to obtain 3D compliant mechanisms with embedded sensors in order to elaborate complex AM-based Mechatronics devices.

To demonstrate the capability to add embedded electrical wiring to nearly any 3D printed metal components, a compliant rotation to translation mechanism (CRTM) was designed and electrical wires were integrated within the topology optimized structural part (Figure 1 with the structure in transparency and the electrical wires with different colors), to power the motor and the strain gauge sensor which is directly printed by AJP on one of the flexure elements (the sensor allows closed-loop position control). The fabrication result is presented in Figure 2.

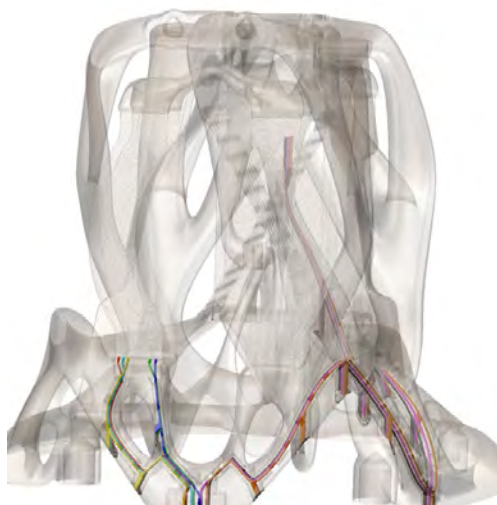


Figure 1: CAD of the CRTM part with embedded wiring highlighted.

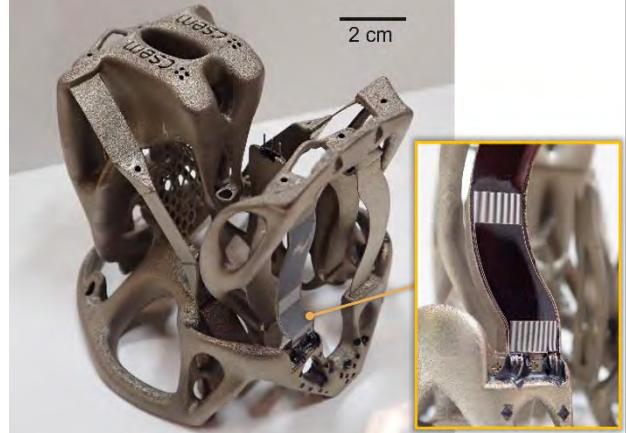


Figure 2: Produced CRTM after thermal treatment and supports removal, with aerosol jet printed strain gauge sensor on the left flexure

The performances of the strain gauge sensor have been improved by adding a second sensor for temperature compensation. Strain gauge characterization on representative samples have revealed a Gauge factor larger than 2 (equivalent or better than commercial strain gauges), with a minimum measurable strain down to  $10\mu\epsilon$ . Repeatability and linearity is comparable to commercial metal-based strain gauge as depicted in Figure 3 with error bars between cycles not distinguishable from the measurement point (light blue dot). The characterization of the sensor on the CRTM as well as the design of a dedicated readout electronics are currently on-going.

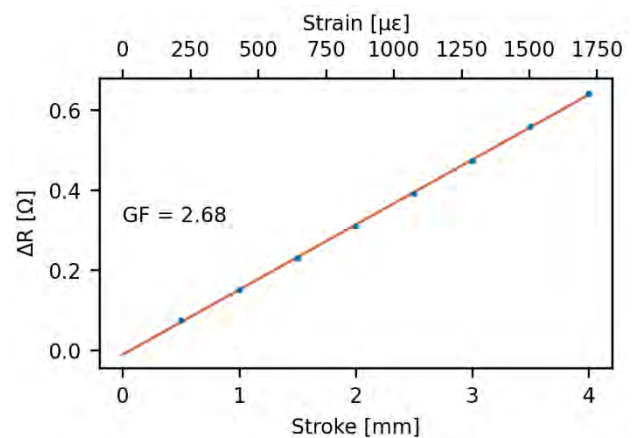


Figure 3: Thermally compensated response to strain of an aerosol jet printed strain gauge.

This work is supported by the state of Neuchâtel.

# LINIO-PIC—Lithium Niobate on Insulator (LNOI) PIC Platform

A. H. Ghadimi, H. Sattari, E. Obrzud, D. Grassani, G. Spinola Durante, G. Choong, Y. Petremand, V. Brasch, O. Dubochet, S. Lecomte, S. Mohrdiek, M. Despont

*Lithium niobate on insulator (LNOI) is one of the most promising emerging platforms for photonic integrated circuits (PICs) that comprises a unique set of interesting optical properties: a high electro-optic (EO) coefficient, high intrinsic 2nd and 3rd order nonlinearities, and a large transparency window (350 to 5500 nm). The aim of this project is to develop the expertise and know-how within CSEM, on different steps of the value chain such as fabrication processes, PIC design and simulations, photonics packaging and finally testing and experimental demonstrators. The goal is to support our customers with complete PIC solutions from the idea to the system implementation and packaging. The results of this multi-year project will pave the way for the creation of the first open European PIC foundry for LNOI that will be available to all stakeholders in coming years.*

Lithium niobate (LiNb) has attracted a lot of attention since its invention in 1970s as an electro-optics material, however, most of its industrial success in photonics domain has been limited so far to devices made from bulk crystals in the form of free-space or fiber-coupled components. Recent advancements in bonding of single crystal thin films of LiNb onto silicon substrates (LNOI), opened a new avenue to explore the advantages of LiNb in the context of PICs and benefit from the cost reduction, manufacturability and integration aspects offered by integrated circuits. Here waveguides are fabricated using reactive ion etching (RIE) etching in a LiNb thin film which allows for significantly higher refractive index contrast ( $\Delta n \sim 0.7$ ) between the core and cladding compared to standard ion implantation technology ( $\Delta n \sim 0.02$ ) and thus more than  $\sim 100x$  reduction of mode volume. Such a tight confinement results in more efficient and faster modulators as well as significantly smaller bending radius and PIC footprint. This ultimately allows designing complex PICs with tens of components in millimeters-sized chip.

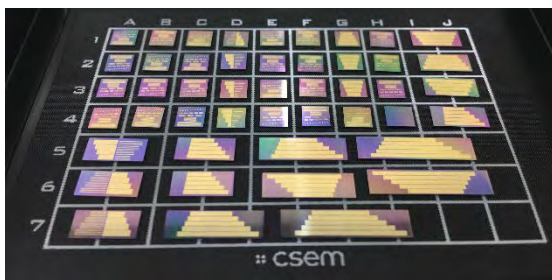


Figure 1: Active LNOI chips fabricated at CSEM in different die sizes.

Due to its unique material properties a LNOI PIC platform can serve vast range of applications including telecom, 5G, LiDAR, sensing as well as optical signal processing, metrology, quantum computing and other quantum technologies. LNOI is a platform that not only outperforms other PIC platforms in areas such as ultra-fast low-loss and efficient modulators [1], but also enables new functionalities that are currently beyond the capability of other PIC platforms such as sum or difference frequency generation, second harmonic generation (SHG), creation of entangled photon sources (SPDC) and acousto-optic modulators (AOMs) that are needed for advancing novel quantum and sensing technologies.

However, so far, LNOI technology has been limited to few academic groups around the world. This is mainly because currently there are no PIC foundry that offers LNOI technology as standard platform to the industry. Establishing a reliable, high yield fabrication process for LNOI PICs is the key to ensure wide spread of this novel technology. CSEM is set to establish an open LNOI foundry based on a reliable process design kit (PDK) library.

In the first year of the project, a LNOI etching recipe based on Ar+ milling has been optimized at CSEM for 150 mm wafers to achieve smooth sidewalls that are highlighted in Figure 2. Smooth optical sidewalls are the key to achieve low optical losses, which is extremely important for many applications. At CSEM, we have fabricated high quality components such as ring resonators and measured optical quality factors  $> 10^6$  at 1550 nm, corresponding to linear losses  $< 0.2$  dB/cm in uncladded waveguides. We have also demonstrated MZI modulators with  $V\pi \sim 1$  V and modulation efficiency  $< 2$  V.cm.

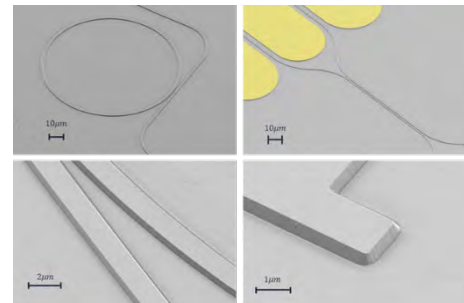


Figure 2: SEM images of LNOI devices fabricated at CSEM.

CSEM's LNOI platform is manufactured on commercially available LNOI wafers (purchased from NanoLN Co.) in which the standard thin film layer stack consists of a 600 nm x-cut monocrystalline LNOI thin film on a 4.7  $\mu$ m thick buried oxide (BOX) layer. The waveguides are formed by etching 400 nm into the LiNb layer. The 500 nm thick gold plates are patterned a few microns from the waveguides to provide efficient EO control of the light within the waveguides. Finally, the LNOI waveguides are protected by a 4  $\mu$ m of SiO<sub>2</sub> cladding.

Over the past year, the nonlinear LNOI waveguides designed and fabricated at CSEM have been used in a demonstrator to stabilize a frequency comb. In this experiment an octave spanning supercontinuum and the 2nd harmonic of the pump laser are both generated in a 5 mm long LNOI waveguide and their beat note detected using a silicon photodetector in a very compact setup (Figure 3a). The results have been recently published in APL photonics [2]. Next year the device will be packaged in a compact butterfly housing that will provide fiber to chip coupling as well as an electrical interface.

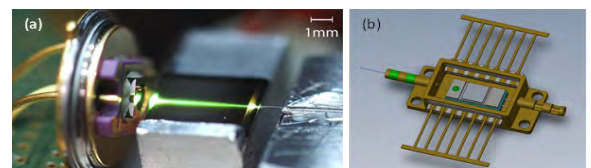


Figure 3: (a) The setup for f-2f self-stabilization of frequency comb using 5 mm LNOI waveguides. (b) 3D rendering of device in butterfly housing.

[1] M. Zhang et. al., Nature 2019, doi:10.1038/s41586-019-1008-7

[2] E. Obrzud, et. al., APL Photonics, 2021, doi: 10.1063/5.0070103

# SIOSCAPE—A Novel Constant Force Escapement

F. Barrot, G. Musy, O. Laesser<sup>\*</sup>, R. Winiger<sup>\*</sup>, F. Cosandier, L. Giriens, E. Dominé, Y. Petremand, M. Amine, S. Ischer, F. Rigoletti

With its combined expertise in micro-manufacturing techniques and precision mechanisms, CSEM has been a pioneer in the design and production of centimeter scale silicon parts featuring fine mechanical functions comprising flexures (FlexMEMS), opening up new opportunities for the design and production of novel and innovative watch mechanisms. In the frame of SIOSCAPE MIPS, CSEM is focusing on the design and production of novel high-performance watch oscillators and escapements. This year CSEM presents a novel constant force escapement based on the FlexMEMS design approach.

Mechanical watch parts are known to be tiny, delicate and very precisely machined; this is particularly true for the constitutive parts at the very heart of any watch mechanism, namely the escapement and the oscillator. Towards the end of the 20th century, CSEM has been a world precursor in the use of silicon microfabrication techniques<sup>[1]</sup> for the design and production of very precise and thermally compensated Silicon watch hairsprings (the most critical part of the oscillator); doing so, CSEM paved the way to a new trend in the watch industry: the use of silicon as a base material for the design and production of mechanical watch parts. Since then, CSEM has kept on carrying its pioneering role by pushing further the frontiers of the micromechanical structuration of silicon<sup>[2]</sup> and by improving its expertise in the design and production of novel watch mechanisms based on this approach<sup>[3]</sup>. Building upon its extensive background and experience in the design of precision mechanisms guided by flexure blades in lieu of classical bearings, CSEM has proposed a novel approach combining the advantages provided by the precise micro-structuration of silicon to those of flexure bearings for the design and production of novel high-end oscillators and escapements. The so-called "FlexMEMS approach" is particularly useful when lubrication is prohibited due to the environment (eg: vacuum, space) or due to contamination restrictions (fine optics).

For the past 15 years CSEM has proposed several original designs of mechanical watch oscillators<sup>[4]</sup> and, in a close partnership with Vaucher Manufacture Fleurier, integrated at the watch level, the very first FlexMEMS Genequand escapement<sup>[5]</sup>, the first flexure-based watch regulator (escapement + oscillator) ever designed and implemented at the watch scale. Since then, CSEM has proposed the Siloscape escapement<sup>[6]</sup> a novel FlexMEMS escapement: featuring a power reserve three times better than a conventional system and a classical precision performance, it is auto-starting by nature, which means that a large accidental shock cannot stop it.

The so-called Double Hammer escapement is the latest FlexMEMS based escapement designed and produced by CSEM (Figures 1 and 2). This innovative escapement is a constant force escapement which is targeting a very precise time keeping (typically +/- 2 s/d) with a regular power reserve. Two silicon parts pivoted on flexure blades and called "hammers", are successively (at each alternance) armed by the escapement wheel which rotates them at a prescribed angle. It is storing a prescribed amount of energy in their flexure pivot, before releasing them so that the potential energy stored in their flexures

is provided to maintain the oscillations of a Wittrick type FlexMEMS oscillator. Since, in the operating range, the potential energy stored in the hammers is constant and independent from the torque available at the escapement wheel, the oscillator will receive the same impulse energy at each alternance, keeping its amplitude as constant as possible during operation and therefore improving the time keeping precision of the watch.

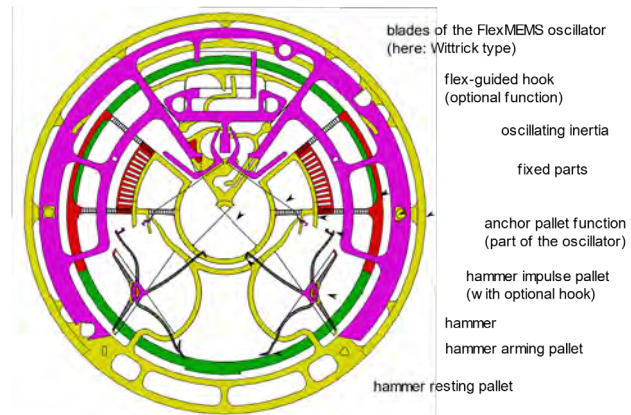


Figure 1: Main constituent parts of the "Double Hammer".

The equivalents of the classical anchor impulse pallets are directly integrated on the oscillator which is produced as a monolithic silicon part assembled wafer-level. A second monolithic silicon part, comprising the two hammers and optional flex-guided hooks, is manually assembled to the oscillator. The flex-guided hooks are used to keep the hammer from touching the oscillator during the resting phase, minimizing the perturbations. With the "Double Hammer" and the Siloscape escapements, CSEM addresses two complementary market segments: high power reserve and chronometric performances.



Figure 2: The "Double Hammer" escapement integrated in a watch.

<sup>\*</sup> External key contributors: "Olivier Laesser" and "Winiger Horloger"

<sup>[1]</sup> A. Perret, "Le silicium comme matériau dans la fabrication de pièces mécaniques", SSC, 2001.

<sup>[2]</sup> O. Dubochet, *et al.*, "L'hybridation du silicium", SSC, 2015.

<sup>[3]</sup> M. Despont, *et al.*, "Tic-Tac" made in Silicon", SSC, 2019.

<sup>[4]</sup> F. Barrot, *et al.*, "Flexure based oscillators for mechanical watches CSEM Scientific and Technical Report (2018) 19.

<sup>[5]</sup> F. Barrot, *et al.*, "Un nouveau régulateur mécanique pour une réserve de marche exceptionnelle", SSC, 2014.

<sup>[6]</sup> F. Barrot, *et al.*, "A Novel Silicon-based Flextech Watch Escapement", CSEM Scientific and Technical Report (2019) 20.

# DIGITAL TECHNOLOGIES

Alain-Serge Porret

The world is undergoing a digital transformation that is reshaping every aspect of our lives: how we manufacture things, how we conduct business, how we travel, how we stay healthy, and—of course—how we entertain ourselves. As valid data becomes the main source of wealth, entirely new business models, new jobs, and new ways to collaborate have been emerging. The process of digitalization fuels this revolution by providing the underlying tools used to collect, distribute, and analyze the information required to improve, accelerate, simplify, automate, and increase the flexibility of potentially every trade.

It is obvious that Switzerland must be at the forefront of this profound transformation for our economy to stay relevant and continue to thrive.

Anticipating the trend, CSEM grew from its historical beginnings as a leader in microtechnology focused on hardware devices and sensors, to being able today to provide complete verticalized solutions for “smart data” (in contrast to the “big data” approach, in which indiscriminate data are accumulated, we often focus on measurements qualified by pre-processing near the point of collection), from sensing to decision-making.

## Digitalization @ CSEM

The broad impact of digitalization affects almost all CSEM activities to an extent, making it hard to provide a concise and complete overview. Our actions are structured along two orthogonal axes—applicative and technological—each divided into three Focus Areas. On the application side, the areas are:

- **IoT and Vision**—Covering markets such as consumer devices and smartwatches, but also a wide range of applications where distributed sensors can be used, from agriculture to infrastructure monitoring. The aspirational goal is to provide the tools to sense and process locally anything (images, sound, vibrations, vital signs, environmental data), anywhere, and in unobtrusive ways.
- **Industry 4.0**—In relation with the impact of digitalization on manufacturing in a wide variety of industries, such as machines, transportation, robots, pharmaceuticals, chemicals, and food. It includes condition monitoring, predictive maintenance, self-diagnosis, and smart robotics.
- **Digital Health**—Already a hot topic before the pandemic because of our aging population, it covers medical, wellness and sport applications, and encompasses a variety of devices from wearables to implantables and the handling and exploitation of the data they generate.

Our aim is to be able to provide support for any part of a complete vertical solution, from sensing to cloud analytics, and is grounded in our decades of experience building specialized hardware and software. Energy monitoring and planning is another important application, and is covered in the Research Priority Sustainable Energy. Together, these application areas cover most of the digitalization needs of the Swiss industries dealing with physical goods.

Three transversal “enabling technologies,” with roots in CSEM’s rich past, complement our applicative effort:

- **Data & AI** deals with the information processing bottlenecks common to many applications: (1) Security and privacy: how to guarantee that data are kept safe from unauthorized access, from the sensor to the cloud to the end user. (2) Efficient and assisted data annotation: how to reduce the effort of labelling data, one of the main elements that deter people from engaging in AI implementations. And (3) distributed and hierarchical computing: how to partition the processing of information from the end node to the cloud to minimize data traffic, promote privacy, and preserve edge resources.
- **ASICs for the Edge** provides hardware integrated circuit solutions (ASICs) to acquire, preprocess, and send information wirelessly from an end node. The effort focuses on ultra-efficient accelerators for embedded inference, analog sensing interfaces, imagers, and radios, all of which constitute the core building blocks of System-on-Chips (SoCs) for autonomous smart sensors.
- **Quantum Technology** represents the next revolution in terms of exploiting the laws of physics for computation, communication, and sensing. In this module, we are developing miniaturized devices to accurately measure time, magnetic fields, angular accelerations, and gas concentrations.

## Long-term objectives

The research priority Digital Technologies aims at providing solutions for sensing, communicating, and analyzing data in the three target domains of application (digital health, Industry 4.0, and the IoT) and focuses on solving identified technology gaps, in terms of systems, components, hardware, and software, from the end node to cloud processing.

Regarding the interface to the physical world, CSEM can leverage decades of hands-on experience in the development of state-of-the-art sensors, with an emphasis on four specific domains: wireless sensing nodes, vital-sign monitoring devices, special imagers, and miniaturized atomic clocks (MACs).

**IoT and Vision, ASICs for the Edge:** There is a huge potential for tiny autonomous sensors able to acquire, process, and transmit wirelessly information extracted from complex data (such as images, sounds, or vibrations) with minimum power, so that they could ultimately operate from harvested energy. To make this vision a reality, we are developing extremely efficient integrated circuits that are able, for instance, to analyze the occupancy of a room, using multiple sensors and AI, with a mW-range of power—much less than existing solutions. We are also exploring ways to optimally balance the processing load between the end nodes, the base stations, and the cloud, to improve the autonomy of this kind of sensors. New directions include distributed network security and sustainable (eco-friendly) motes.

**Industry 4.0:** We provide solutions that can be easily implemented in a practical industrial environment and in SMEs. Quality monitoring and process control continue to be pillars of this activity, together with the prediction of the status and health of machines with data limited in amount and quality and by

reusing as much as possible existing sensors. Another topic looks at the fusion of AI techniques and robotics to increase manufacturing flexibility, for instance with cognitive robotics, which endows robots with intelligent behaviors based on autonomous learning and reasoning about their complex environment.

**Digital Health:** CSEM also has a long-standing track record in noninvasive human vital sign monitoring through electrical (ExG) and optical (PPG) means, work carried out in compliance with the ISO 13485 standard. If anything, the current pandemic has confirmed the need for innovative digital health tools for the study, prevention, and monitoring of diseases. We plan to compound the impact of our multi-parameter cooperative sensor technology by combining it with other domains of experience at CSEM, such as ASIC design, the IoT, AI, and edge computing. We contribute to the fight against hypertension, a scourge of wealthy nations, with our proprietary oBPM® technology (optical blood-pressure monitoring), which recently received EC medical approval and is continuously being improved with extended capabilities.

**Data & AI:** The intrinsic inability of AI to learn from a limited amount of training data creates a high barrier of entry for SMEs. This holds true across many applications, from monitoring rare medical conditions to predicting the breakdown of heavy machinery, to monitoring defects with quality control applications or detecting the fall of an elderly person at home. We are developing both generic tools and application-dedicated algorithms to mitigate this issue, based on techniques such as assisted labelling and data augmentation. Recently, the automatic generation of convincingly accurate synthetic reference data has been showcased and tested in a variety of use cases (from consumer to Industry 4.0 and medical data).

**ASICs for the Edge, Data & AI, IoT, Industry 4.0:** Cameras based on multi- and hyperspectral imaging, able to extract information across a wide range of wavelengths, beyond the classic RGB model, are expected to revolutionize many fields, from quality control to health and building management. We are leveraging our expertise in conventional visible-spectrum imagers to build such new devices, and extend their capabilities to X-rays, THz, or the near infrared. We also co-develop the AI algorithms necessary to optimally exploit these and other innovative off-the-shelf devices, such as those based on light-field operations.

**Quantum Technology:** Our expertise in building several key MAC (miniaturized atomic clock) building blocks, including a proprietary atomic vapor MEMS cells, is at the heart of several projects pushing for better accuracy, lower cost, and miniaturization. Targeted applications include both the next generation of compact high-performing atomic clocks for spatial applications and new derivative quantum sensors such as magnetometers and gas detectors in the European Quantum Flagship project macQSimal.

## Highlights

In many applications, the progress of machine learning is hampered by a lack of high-quality training sets. Acquiring and manually labelling such sets is often challenging and labor-intensive, to the point where it becomes impractical for many industrial applications, especially in SMEs. The paper "How Little is Too Little? Image Generation Performance in a Small Industrial Data Setting" discusses recent developments in generative

adversarial networks (GANs) that have provided unprecedented performance in data synthesis tasks, therefore eliminating the bottleneck of painstakingly assembling large enough data sets. In our experiment, we found that, for some of the most common problems found in industry, models trained with 50 or more images can already produce high-quality results.

On the device side, "Towards Battery-Less Machine Learning Inference at the Edge" discusses how the power consumption of distributed sensors such as cameras can be drastically reduced by locally processing the raw information and therefore massively reducing the quantity of data sent to the cloud. This paradigm will enable many new applications where battery life needs to be maximized and provide further advantages in terms of latency and privacy. The dedicated ASIC designed for this application is described in "An Ultra-energy-efficient AI Chip for Next-Generation ICT Applications" and a possible alternative technique to reduce the power consumption of the required local computation can be found in the article "Ultra-low-power Networks for Neuromorphic Devices."

One growing concern regarding the Internet of Things is related to guaranteeing a sufficient level of security, even in resource-limited platforms such as end nodes. "End-to-end Security and Key Provisioning for Wireless Sensor Networks" proposes a framework adapted to the specific constraints of the problem that is modular, reusable, and easy to adapt to different communication protocols and messaging paradigms.

The availability of such new technologies is proving useful in many verticals, including wearables and medical devices. An example of wearables is presented in "ULTEEM: Ultra-long-term EEG Monitoring," where electroencephalography (EEG) technology monitoring devices are clipped to ordinary eyeglasses to noninvasively record the brain activity of the temporal lobes, providing valuable information for long-term generalized epilepsy monitoring or for vigilance monitoring based on an electrooculogram (EOG). On a related topic, the article "Secure Ultra-long-term Ambulatory Monitoring of Subscalp EEG for Epilepsy Management" presents a medical device designed to monitor seizure occurrences by collecting and processing signals from implanted electrodes.

The formal diagnosis of high blood pressure (BP), or hypertension, often requires 24-hour ambulatory blood pressure monitoring with cumbersome, cuff-based measurements. "Cuffless 24-hour Ambulatory Blood Pressure Monitoring" explores the revolutionary possibility of using a cuffless, watch-like photoplethysmographic (PPG) sensor instead, with very encouraging results.

Sustainability is becoming a more pressing concern with regard to the billions of sensors manufactured every year. "Compostable Chipless Sensor Tag for Green Smart Packaging" explores some potential ways of limiting the impact of electronic waste.

Finally, "Miniature Quantum Sensor Prototypes: Development Status" describes the effort, through an H2020 project CSEM coordinates, to exploit advances in atomic quantum metrology to create extremely sensitive and accurate devices such as miniature atomic clocks (MACs) and optically pumped magnetometers (OPMs). The first OPM prototypes are being assembled and tested at CSEM, while the extraordinary sensitivity of this prototype is expected to lie in the fT range.

# $\mu$ 111MP—Implementing Kernel-to-Kernel Communication on 64-bit Dual-Core RISC-V Processor

F. Baldo, M. I. Ben Salah, J.-M. Koller, E. Franzi

Multicore architectures are widely used in embedded processors for their exceptional flexibility and performance. CSEM evolved the single-core version of the  $\mu$ 111 RTOS to a multi-kernel version based on a shared memory communication between the kernels. A new inter-kernel communication protocol extends the RTOS primitives for taking advantage of multicore capabilities while improving the maintainability of the RTOS.

The CSEM  $\mu$ 111MP RTOS can now fully exploit the capabilities of the numerous multicore CPUs, such as dual-core Cortex-A7, dual-core RISC-V or big.LITTLE architectures, by implementing an inter-kernel communication mechanism based on messages exchanged in a memory shared between the cores of the processor. The first implementation runs on a Kendryte K210 RISC-V 64-bit dual-core SoC.

The mechanism used for sending messages between the different kernels of the system requires the following hardware features:

- Both cores can send software interruptions to each other
- A shared memory region is accessible for reading and writing by both the cores

Each core has a dedicated instance of the kernel running, including a new dedicated daemon program, responsible for serving and supervising the exchange of kernel-to-kernel messages.

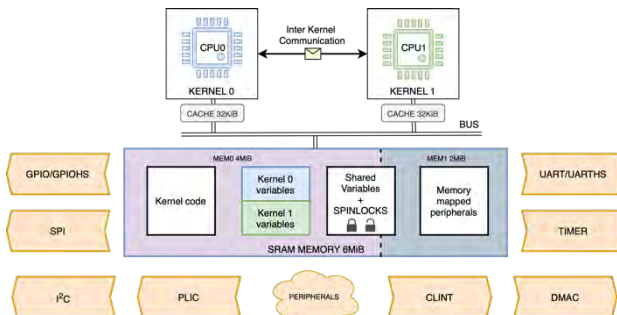


Figure 1:  $\mu$ 111 kernels deployed on the K210 multicore SoC.

## The kernel-to-kernel communication protocol

The mechanism at the core of the inter-kernel communication protocol (IKC) can be summarized with the following list of operations:

- The sending kernel writes the message (Type of message, message size, message data, etc.) in a shared memory region, which is accessible by all the kernels in the system.
- The sending kernel triggers an interprocessor interrupt to the core executing the kernel which is the destination of the message.
- When the inter-processor interrupt is received in the destination kernel, the assigned ISR awakes the daemon process which handles the reception and processing of the inter-kernel messages.
- The daemon reads from the shared memory region used for storing the message, the information regarding the type of message and forwards the incoming message to the destination kernel.

To experiment and validate the IKC protocol, the single-core kernel implementation has undergone the following changes for running two kernels on the dual-core RISC-V:

- Duplication of kernel structures and modification of the boot sequence.
- Duplication of the timers needed for the scheduling as we have two independent kernels running.
- Adding SoC specific spinlocks on shared variables for managing concurrent accesses.
- Implementing a shared memory circular buffer for message management.
- Reconfiguration of the interrupt management HW to allow inter-processor interrupts.
- Adding IKC API for message creation, read/write and callbacks to support multiple use cases (data sharing, Remote Procedure Call, measurement request, etc.)

A first use case of the inter-kernel communication is peripheral sharing such as UART channels, where one of the kernels i.e., CPU1 doesn't have access to UART. In this case data is sent through the communication protocol to CPU0 to be transmitted afterwards on the UART channel whenever it's possible.

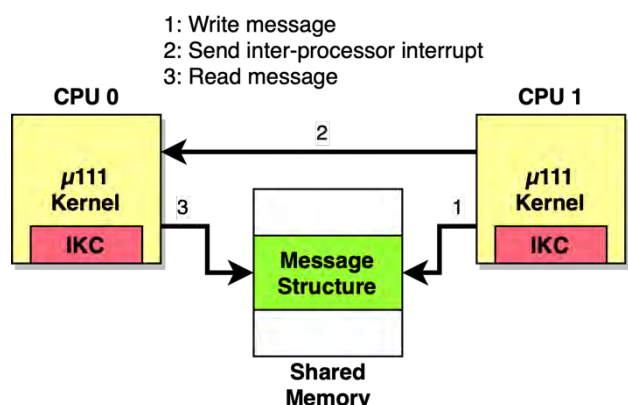


Figure 2:  $\mu$ 111 kernels communicating through inter-kernel communication protocol.

The current version of  $\mu$ 111MP is a proof-of-concept of a multi-kernel architecture, which lays the foundation by being based on a minimal set of primitives to ensure easy portability to other architectures/SoC, including

further improvements, such as high-level implementation and optimised message handling and reception algorithm of inter-kernel messages, faster DMA-based data transfer between the cores and inter-kernel load balancing through the introduction of "transferable" kernel primitives through the communication layer.

# Long-Range IoT Communication on ULP μ111 RTOS

M. Sénéclauze, P. Dallemagne

The CSEM μ111 ULP RTOS now integrates a LoRa communication stack on an asymmetric dual core SoC from STMicroelectronics. The main processor runs the μ111 RTOS and the application, whereas the second core acts as a communication co-processor running the LoRaWAN stack. This complete modularity between OS and Radio stack will allow reconfiguration of the device based on its environment and simplify the protocol certification process.

Low Power Wide Area Networks (LPWAN) have been around for several years, allowing for the deployment of IoT applications requiring long range, low-power and low-data rate communication. LoRa operates in a license-free band allowing its standardized Medium Access Control, LoRaWAN®, to be deployed by anyone.

The present work uses a STMicroelectronics STM32WL55, which integrates a CPU with two different STM32 cores (one L4 and one M0) and a multi-protocol radio ([G]FSK, [G]MSK, PBSK and LoRa) compatible with many existing protocols (LoRaWAN, SigFox, W-MBUS, mioty, Wisemac, etc.).

An IoT implementation can exploit dual-core platforms using two different OS architectures:

- Allow the OS to run application on the two asymmetric cores<sup>[1]</sup> and implement the protocol stack as part of the OS.
- Assign the application to one core and the communication stack to the other, as illustrated in Figure 1.

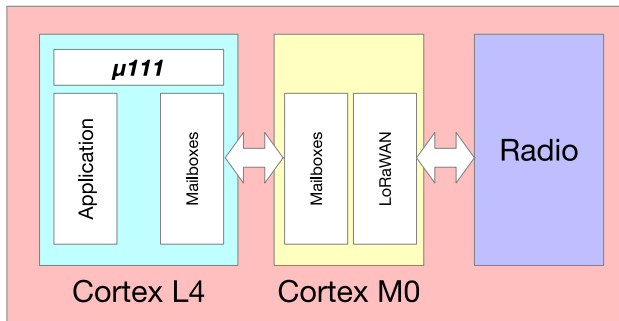


Figure 1: Message exchange between STM32WL55JC components.

The first architecture has the advantages of allowing multiple protocols to co-exist in the same implementation, since the RTOS can integrate and schedule several protocol stacks. The operating system capabilities would allow the user to switch, update the application or the communication stack as any other module of the OS. Moreover, it can offer a much more consistent and efficient behavior of the system, by completely relying on the RTOS for the management of power and time. However, it is more complex, takes more resources, require adaptations of existing communication stacks.

The second option requires each core to handle power and time, at the cost of double design, testing and ad-hoc synchronization across the two cores. Compared to the first architecture, in which the protocol stack would have been directly implemented in the operating system, this later solution brings a very important

advantage since the solution designer only has to worry about the certification of the protocol stack. Once it is certified by the relevant authority, it remains compliant regardless of the modifications made to the application simplifying the life cycle of the application and of the device itself.

This second architecture forms the ground of the current implementation. μ111 was ported to the STM32L4 core. This porting necessitated the adaptation of the OS to cope with the absence of a floating-point unit and to run at the full speed of the processor. The STMicroelectronics flavor of the LoRaWAN protocol stack was then linked to run the M0 core and it was initially tested by establishing a point-to-point communication link with another LoRaWAN capable device (e.g., a gateway). Finally, a mailbox mechanism is implemented on the Cortex L4 to be compatible with the API defined on the Cortex M0 to allow μ111 to interact with and control the LoRa communication stack and exchange messages.

Figure 2 shows a typical miniature LoRa IoT node designed by CSEM.

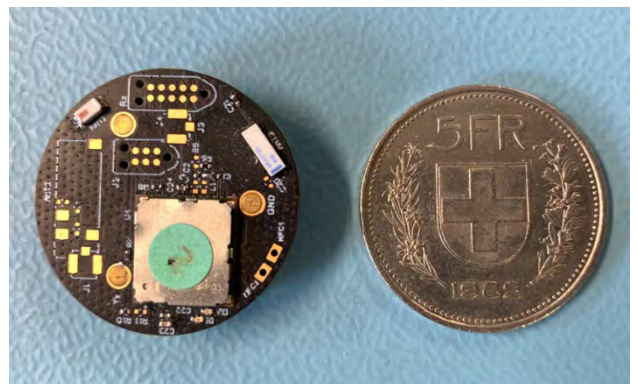


Figure 2: Miniature LoRa node.

This platform fulfills the requirements of a very large number of applications ranging from infrastructure monitoring to long range asset tracking for which we are now capable of prototyping an IoT device very quickly. The fact that we are using a very limited number of components is a real advantage in terms of power consumption, cost and size and for reducing the time to market.

The mechanisms experimented here could lead to the development of platforms embedding several communication stacks and radios for addressing the multi-protocol needs of modern IoT applications.

<sup>[1]</sup> F. Baldo, M. I. Ben Salah, J.-M. Koller, E. Franzi, "μ111MP—Implementing kernel-to-kernel communication on 64-bit dual-core RISC-V processor", CSEM Scientific and Technical Report (2021), 17.

# Secure Boot and Firmware Update for μ111 RTOS

D. Vizár, M. I. Ben Salah, A. Ferragni

Ensuring that only authentic firmware will ever boot on a device is among the baseline security requirements of virtually any application with remote embedded devices, notably in IoT, Industry 4.0 and eHealth markets. CSEM has introduced a secure boot and firmware update for the ultra-low-power μ111 RTOS, based on the recognized MCUBoot library, and verified the security of the framework in a new formal security model for embedded secure boot.

The remote (a.k.a. over-the-air) firmware update is among the most crucial tools for all applications seeing embedded devices deployed with no or restricted physical access by the application owner, allowing to fix bugs, patch security vulnerabilities, or add new features. This capability also opens a critical attack vector allowing an attacker to insert permanent modifications into the firmware, resulting in the implantation of advanced persistent threats into a device. This risk is further elevated if the device in question may be physically manipulated by a potential attacker interested in modifying the behavior of the device without authorization (including the user of the device in interactive applications, e.g., in the consumer electronics segment), or if the device connects to Internet (or other Internet-connected devices). A notorious application paradigm combining all these attack vectors is that of Internet of Things, threatening to turn everyday objects into infected bots on a mass scale.

A secure boot and secure firmware update have been developed for CSEM's ultra-low-power RTOS μ111, illustrated in Figure 1. The secure bootloader is based on the MCUBoot [1]. Open-source project, which has been integrated with the OS and augmented with tools allowing the reception of an updated firmware image and the verification of the correctness and basic security properties of a porting of the secured bootloader to a new HW platform. Compatible with the philosophy of μ111, the solution is easily portable, thanks to clean abstraction layers. The integration and tests of the bootloader and updates have been verified on the ARM Cortex M architecture, using the STM Nucleo-H753ZI. A full industrialization requires a routine optimization and further testing is required.

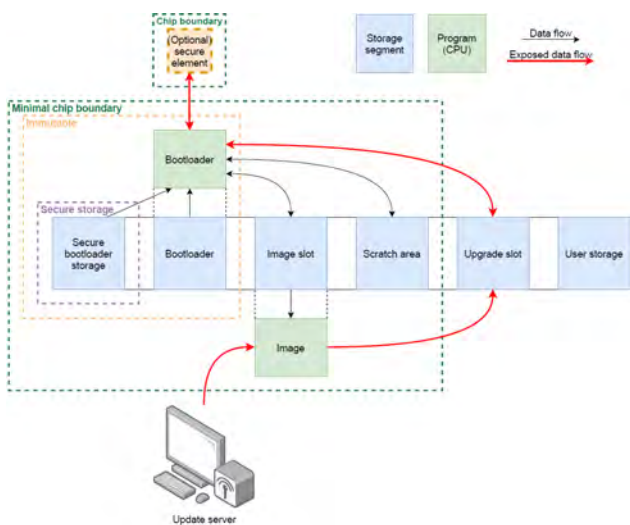


Figure 1: Diagram of the MCUBoot-based solution.

Secure boot and firmware update are effective mitigations against this type of threat. In brief, secure boot ensures that only authentic, non-modified firmware image will execute on a device. A secure remote update mechanism extends this with a framework for the creation of new authenticated firmware images, their delivery to the target device(s) and the replacement of old images by new ones, while ensuring the integrity and confidentiality of the firmware, and preventing from the bricking of the device with a robust update process. Designed correctly, these features give a high confidence in the firmware executed on the device throughout its lifetime.

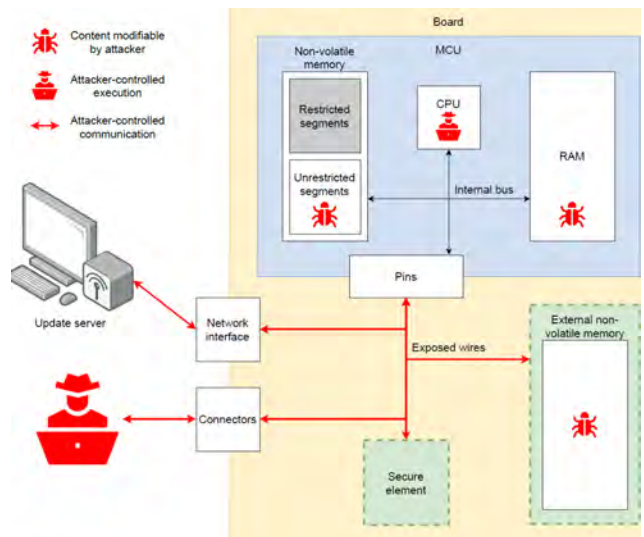


Figure 2: Threat model, illustrating the adversarial powers within scope.

Achieving the aforementioned security objectives requires certain HW security features on the device. However, the exact nature and strength of the HW security features required depends on the threat model of the application, notably whether an attacker is likely to have access to the device and its internals. Similarly, a secure boot solution that is effective against a remote-only attacker may fail against a physical attacker. At the same time, trying to defend against all attacks, including the most sophisticated ones (such as using focused ion beam) would require defensive features that are prohibitively costly for most IoT applications. A correct modelling of the relevant attacks is therefore of importance for selection of appropriate HW and evaluation of a solution's security. Improving upon the existing models in terms of formalism and attack coverage (appropriate for IoT), a new formal model has been developed (see Figure 2).

Augmented with secure boot capabilities, μ111 is now well-suited for industrial applications requiring (ultra) low-power consumption and an industry-grade assurance of the firmware's confidentiality, authenticity, and integrity.

[1] Linaro Limited, "Secure boot for 32-bit microcontrollers", <https://www.mcuboot.com/> (accessed 19.08.2021).

# End-to-end Security and Key Provisioning for Wireless Sensor Networks

D. Vizár, C. Kassapoglou Faist

A framework for end-to-end communication security and key management in wireless sensor is proposed, specifically designed for resource-constrained devices. The framework is modular, with a generic and an implementation-specific part, making the framework highly reusable and easy to adapt to different communication protocols and messaging paradigms in virtually any data collection set-up involving low-resource devices.

Wireless sensor networks are perhaps the most notorious example of the security-constraints tension; on one hand sensor nodes (SN) are constrained in cost, computational resources and tend to be powered by a battery. On the other hand, the nodes are often deployed in untrusted environments, where an attacker can effortlessly tamper with the wireless communication and possibly with the nodes themselves. For a targeted evaluation and an optimal solution to this problem, CSEM methodology is based on a semi-quantitative threat analysis (allowing for an informed identification and prioritization of security controls tailored to the application)<sup>[1]</sup>, yielding a specification of end-to-end communication security and key management.

The framework is applied to sensor networks in two projects: AMPWISE (AMP; continuous aircraft monitoring) and OffshoreMuster (OSM; personnel localization and condition monitoring for offshore safety). The considered networks involve ultra-low-power (ULP) SNs that communicate with fixed-position devices (data collectors in AMP or gateways in OSM) capable of long-range communication used to relay the SN data to a remote collection point (a server). The sensor nodes can be static (e.g., grouped in a star topology around a data collector) or mobile (capable to use any gateway). Envisioning end-to-end security, our approach is independent of the medium access protocol (TDMA in AMP, WiseMAC-HA in OSM) or the messaging scheme (unicast, Publish/Subscribe).

Threat analysis was based on a realistic model of attacker that may eavesdrop on and modify all communication (wireless or wired) and get a device's cryptographic material, e.g., by the means of physical access<sup>[1]</sup>. An identification of assets (SN data messages, gateway reports, downlink commands, etc.) and an analysis of high-level threat events (damage to a SN, to a gateway, etc.) broken down to fine-grained attack vectors using attack trees, allowed for a systematic likelihood and impact quantification for the threats (e.g., risk due to the damage at the gateway is "high", due to, i.e., a possible injection of false data).

Based on the threat analysis, secret key authenticated encryption (AE) is applied to all unicast messages as well as to broadcasts within a fixed group, while all broadcast commands from the server are treated with a public key digital signature (without being encrypted), as per Figure 1. The key management ensures a use of independent sets of secret keys per SN and gateway to mitigate the impact of key leakage due to corruption of an individual device. Additional HW and SW measures against physical (side-channel) attacks are considered as per the exposure, value and cost of protection of each application. A security layer, added on top of a protocol send and receive functions, encrypts and/or authenticates the frames. A 4-byte security header is inserted in the frames, containing the security-specific parameters needed by both communication

partners (encryption and key counters or signature counter) and indicating whether authenticated, encryption or digital signature is used. With the former, the payload is encrypted while the frame header elements (addresses, sequence numbers etc.) that must remain in clear are authenticated in associated data or the nonce. With the latter, all relevant fields are signed. The selection of concrete cryptographic algorithms is per-implementation, adapted to, e.g., available hardware accelerators.

The proposed key management solution is tractable and provides computational independence of the device symmetric keys. All AE keys are derived from a single system master key stored in the server using diversifying information such as unique device identifiers, key ID, key refresh counter, or communication direction using AES-128 ECB as a key derivation function. Each device must also store the server public key.

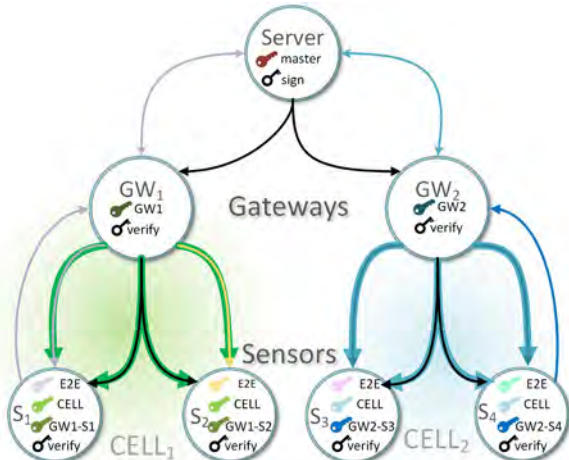


Figure 1: Example deployment of wireless sensor network security. The color of the transmission indicates the used key, double line encapsulated encryption/signature.

Each key management scheme requires an initial bootstrapping, where devices must be securely provisioned with the initial key material. The most practical but also risky option sees the keys generated by the server and the transmitted wirelessly (in clear) to the devices upon first activation in a trusted environment. A second variant uses a one-time bootstrapping key pre-installed in all devices to protect the transfer of the device keys. This key is unique to each installation and destroyed after key provisioning. The safest but least scalable variant is to pre-load each device's keys manually.

The proposed framework yields an effective wireless network security with low overhead by combining, cryptography with appropriate key management in a resource conscious manner.

<sup>[1]</sup> D. Vizár, A. Olteanu, C. Kassapoglou Faist, "IoT SPAT: Security and privacy analysis toolbox for IoT applications", CSEM Scientific and Technical Report (2020), 111.

# Ultra-low-power Multi-standard Communication Miniature IoT Node

D. Piguet

*Internet of Things (IoT) systems collect data in a wide variety of places, from the human body to machines and out in the wild. Such systems need to be compact, robust, secure, and be able to operate using low and unreliable energy sources. They also need to support various wireless communication standards, from short-range personal area networks low-power wide area networks with a range at distance of 10s of km. CSEM's WiseNode platform supports all of these requirements and more, on a tiny 2 by 2 cm electronic board.*

The Internet of Things is all about data collection and system actuation. IoT devices may be located almost anywhere and support virtually any kind of application from the human body to machines, transportation, utility networks, buildings and large infrastructure to agriculture and the environment (e.g., cliffs, forests and rivers).

Wireless coverage widely differs from one application to another. A person may have a smartphone nearby to relay data collected by wearable sensors. Public Low-power Wide Area Networks (LPWAN) are available in inhabited areas to collect data from sensors installed on structures, buildings, and utility networks. In areas without wireless coverage such as inside aircrafts, satellites, on offshore platforms, or for applications with special requirements, tailor made solutions can be necessary. The latter may require features such as accurate synchronization and multi-hop communication, where the wireless nodes autonomously organize to relay data, or protocols that can switch from a low to a high data rate mode, while retaining their low-power properties. Versatile solutions are needed. The result of more than 15 years of experience, the latest version of CSEM's WiseNode platform provides the required versatility. Moreover, it is also optimized to deliver state-of-the-art performance in terms of robustness, security and energy conservation.

The WiseNode block diagram is shown in Figure 1. It is a 25 by 25 mm PCB. The central element is a Nordic Semiconductor nRF52840 communications and MCU SoC. The nRF52840 provides 2.4 GHz low-power communication, supporting the Bluetooth Low Energy standard, IEEE802.15.4, as well as, proprietary modes. The MCU is a powerful, yet low-power consumption, 64 MHz Arm Cortex M4 with 8 ADC channels and a rich set of the digital interfaces (SPI, I2C, UART). Program memory (1 MB) and RAM (256 KB) are large enough to support complex communications protocols, as well as, most sensing and actuation applications. CSEM's real-time OS  $\mu$ 111 was ported to the new WiseNodes platform. The MCU is powerful enough to implement simple signal processing, either for edge applications, or to reduce the amount of transmitted data. The WiseNode also has a LoRa SX1261 868 MHz transceiver to support longer range and LPWAN connectivity.

An external real-time clock provides the system alarm clock and metronome. The ability to program a wake-up interrupt enables the nRF52840 to be completely shutdown and awaken the next time it is needed. The low deviation of the real-time clock, compared to a quartz clock, allows ultra-optimized implementation of time-division multiple access protocols (TDMA), with minimal guard times to compensate deviations, even with large intervals between communication events.

On the power supply side, the WiseNode can be operated via a primary battery, but it also includes a power management circuit, which accepts irregular, low voltage, and unreliable input from an energy harvester to charge a secondary, rechargeable battery or a supercapacitor. The power management circuit can be

configured to implement a hysteresis: 1) the system is powered on when the energy storage has a sufficient reserve of energy for a clean start-up and sufficient operation time, 2) when the energy storage discharges, and the available energy is no longer sufficient, the power management circuit is configured to gracefully shut-down the WiseNode, placing it into deep sleep. When in deep sleep, the WiseNode consumes only 3  $\mu$ A.

Finally, the WiseNode also includes a secure element that supports a full range of security, including confidentiality, data integrity, and authentication with hardware-based cryptographic key storage and cryptographic countermeasures, which eliminate potential backdoors linked to software weaknesses.

The WiseNode can be stacked with other CSEM boards, in particular, with tailor-made sensor / data acquisition systems (including vision sensors), embedded data processing and machine learning platforms. In the same manner, it can be interfaced to other communication systems to make gateways.

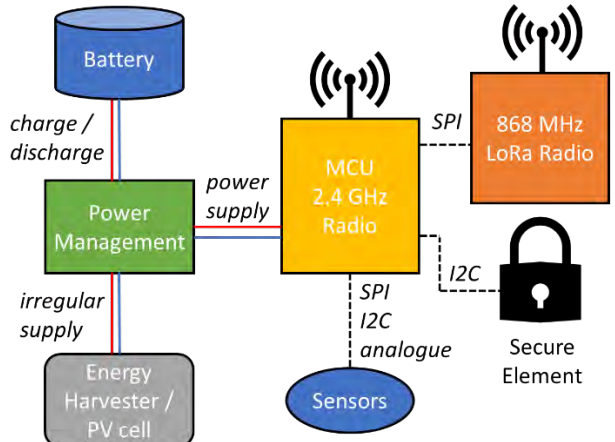


Figure 1: block diagram of CSEM WiseNode multi-interface and multi-standard ULP sensor, data processing and communication node.

On the software side, and thanks to its 2.4 GHz and 868 MHz transceivers, the WiseNode provides multi-interface communications, as it is capable of combining: standard and proprietary protocols, including multi-hop; high and low data rate protocols; short and long-range connectivity. Any combination of protocols can be achieved using CSEM implementations on  $\mu$ 111 OS. Demonstrators and prototypes can be developed in record time thanks to the flexibility of both hardware and software.

The WiseNode has been successfully demonstrated in different applications including aeronautics, wearables, and civil engineering.

# Authenticated Encryption with Flexible Authenticator Length for Energy-Efficient IoT

D. Vizár, E. Gjiriti, R. Reyhanitabar\*

*Lightweight cryptography algorithms seek to deliver cost, performance and/or security trade-offs aimed at specific applications, such as those that comprise constrained, low-power devices. A secret-key authenticated encryption scheme allowing for the authentication-related ciphertext overhead to be adjusted flexibly has been developed. This enables a precise allocation of resources (as per application risk assessment) in constrained applications, notably saving energy related to wireless communication. The latter has been confirmed experimentally using CSEM's ULP HW and OS.*

The field of lightweight cryptography (LWC) provides algorithms catering to (highly) specific targets in the design trade-off space that are not well covered by the existing "conventional" cryptography standards, such as AES-GCM. Often, these targets are related to constrained devices, such as low-power sensor nodes (e.g., aggressive minimization of energy consumption or cost-minimization of side-channel mitigations), optimization for particularities of applications such as sensor networks (e.g., predominantly short messages) or extreme performance requirements, such as in industrial control (e.g., an extremely low latency in HW). The relevance of this direction is underlined by NIST's ongoing lightweight cryptography standardization effort, which stipulates the importance of performance and cost optimization for short messages, among other things. Complementing the features required by NIST's LWC call for submissions is the so-called "variable stretch" [1], allowing a sliding-scale tradeoff between the overhead (in ciphertext length) and integrity, while not compromising any other security aspects of an authenticated encryption scheme. This feature can thus bring measurable benefits to constrained applications, notably those with wireless communication and a limited energy budget.

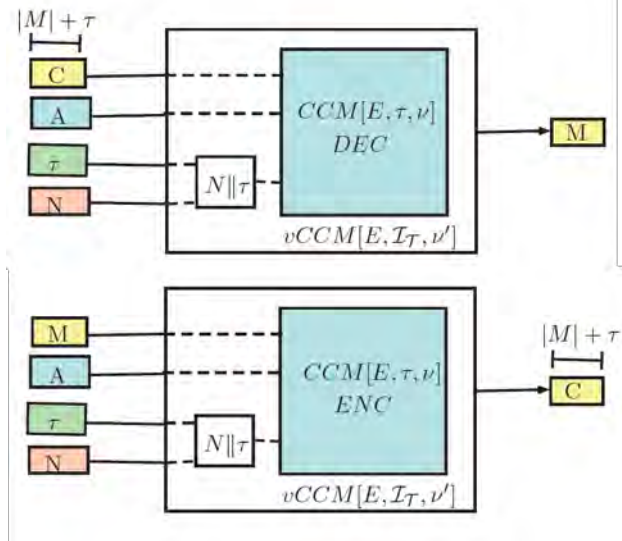


Figure 1: Illustration of the black box transform of CCM to vCCM.

Having identified a gap among the existing AE schemes, the scheme vCCM (*Variable tag CCM*)<sup>[2]</sup>, a provably secure nonce-based authenticated encryption scheme with variable-stretch (*nvae*)<sup>[1]</sup> has been developed. Unlike conventional nonce-based authenticated encryption (*nae*) schemes, which

\* Siemens Energy, Erlangen, Germany

<sup>[1]</sup> R. Reyhanitabar, S. Vaudenay, D. Vizár, "Authenticated encryption with variable stretch", ASIACRYPT (2016), LNCS 10031(1), 396.

process a secret key, a nonce, an authenticated-only associated data and a plaintext, *nvae* schemes expose an additional input, a tag length (to be chosen from a set of supported tag lengths) and remain secure (in the intuitive sense) as long as the nonces are unique in encryptions with the same tag length but not necessarily between them. The design of vCCM is based on the standard *nae* scheme CCM [3], which is most frequently used in embedded applications and protocols, such as BLE or ZigBee, using a black box transform (see Figure 1). I.e., CCM remains unchanged, retaining all existing analysis and all existing implementations (SW or HW) can be reused to implement vCCM.

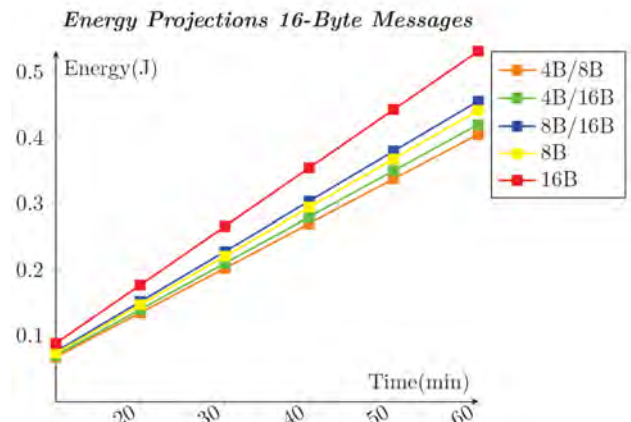


Figure 2: Projected energy consumption of a sensor node transmitting over a LoRa radio data with shorter auth. tags every 10 s and control packets with longer tags every 60 s, vs the same with constant size tags. The energy reported accounts for the full operation, including OS, encryption by vCCM and sleep.

The direct benefit of using vCCM is the reduction of auth.-related overhead for most exchanged messages, while not compromising on security of the critical ones, which is most beneficial in low-power wireless devices. An experimental verification with a CSEM ultra-low-power HW platform Wisenode and RTOS μ111 showed that, in a simple sensor-node application, the correct use of vCCM can reduce the *overall* energy consumption by up to 20% (see Figure 2).

As the experiments indicate, vCCM can bring tangible efficiency improvements to all applications with low-power requirements, with its simple API and negligible overhead (compared to CCM) make smooth. The provable security and a black-box use of CCM, on the other hand, provide ample guarantees of security.

<sup>[2]</sup> E. Gjiriti, R. Reyhanitabar, D. Vizár, "Power yoga: variable-stretch security of CCM for energy-efficient lightweight IoT", IACR Transactions on Symmetric Cryptology (2021) (2), 446.

<sup>[3]</sup> D. Whiting, R. Housley, N. Ferguson, "Counter with CBC-MAC (CCM)", IETF RFC 3610 (Informational), September 2003.

# A Robust Data Collection Infrastructure for Localization and Sensing in Large Structures

C. Kassapoglou Faist, A. Restrepo Zea, R. Berguerand, M. Sénéclauze, P. Dallemande

A reliable, scalable and robust infrastructure for data collection and wireless device network management has been developed to support localization and person condition monitoring in an Oil&Gas operations environment. It provides a powerful tool, streaming the data across processing, storage, application logic or visualization units and, thanks to its modularity, it can be customized to support a variety of IoT applications.

ULP wireless systems are enablers of numerous novel applications in everyday life, industrial processes, person condition monitoring, safety, etc. Although progress is spectacular, deploying large scale networks (e.g., a few hundred nodes and the required infrastructure) still remains challenging, due to either installation, networking issues or to poor scalability of the backend components governing data collection, processing or storage. An optimal design over all stages of the workflow is necessary for critical applications, such as decision support in emergency situations, to meet their strong requirements in terms of robustness, reliability, and low latency.

CSEM proposed a radical departure from the traditional client-server communication model by adopting the Publish-Subscribe scheme and a robust messaging framework in the EU OffshoreMuster (OSM) project [1]. The latter extends the Lynceus safe evacuation system to the Gas&Oil industry, benefitting from a good maturity in the wireless devices and decision support tools, which had been tested at large scale [2]. OSM raises the system TRL, enhancing, among others, data collection, the localization processes and system security.

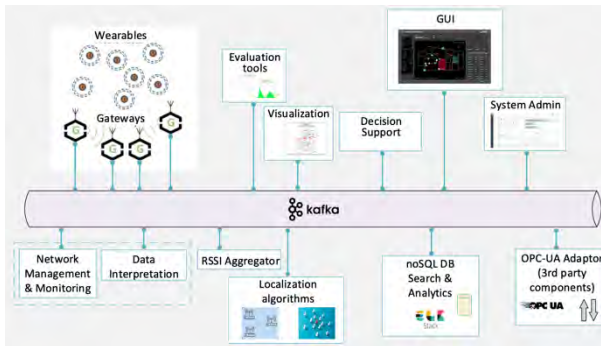


Figure 1: Event streaming in OSM, using Apache Kafka.

The new architecture builds upon a powerful, open-source message exchange framework, Apache Kafka (see Figure 1). Kafka is a robust, performant and scalable event-streaming platform, with replication and workload distribution capabilities. One or more Kafka servers stream events from data producers (e.g., devices, middleware components for processing or network management, storage units, applications) to data consumers, in real time or retrospectively, independently of component technology. Light-weight Kafka clients establish secure connections with the Kafka server. The data are organized in topics and are accessible using the Publish/Subscribe scheme, at any stage of the workflow. In our implementation, all middleware components are isolated in docker containers. This infrastructure can be generalized to most IoT applications.

In OSM, localization is based on Received Signal Strength (RSSI), using very low-power RF signals at 868 MHz, transmitted

by the wearables. Fixed infrastructure devices (gateways) connected to a backbone (TCP/IP) network act as anchors in the process, receiving periodic beacons from nearby mobile devices and publishing the information on Kafka. The gateways have a modular architecture, making them easy to adapt to other wireless technologies. Their networking is achieved using embedded Linux platforms (Raspberry Pis in our testbed, Octavo SiP in the OSM demonstration deployment).

The data from the wireless device network are encoded in binary and are validated and translated to JSON by the Data Interpretation module, which splits the gateway reports into application layer topics such as RSSI reports, accelerator data, alert-button notification etc., depending on the encapsulated information in the binary messages. Following the localization workflow, the RSSI aggregator sorts the RSSI reports by wearable and time, preparing the input to the (centralized) localization algorithm. The latter computes and publishes the wearable locations, making them available for display to the user interface. In parallel, the data can be viewed at any stage of the flow for system/component operation or performance validation, or it can be retrieved and collected for later use (e.g., further algorithm improvements using machine learning).

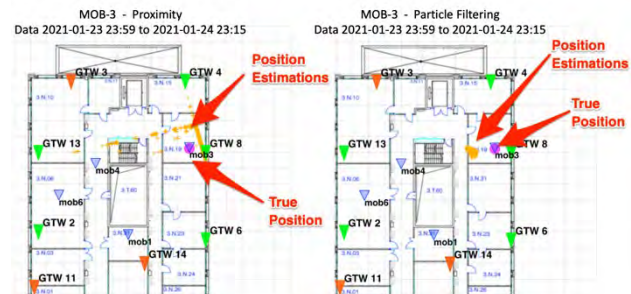


Figure 2: Localization algorithm results (accuracy comparison between simple proximity and particle filtering).

The adopted architecture allowed us to run in parallel and compare two localization algorithms: a simple proximity-based one (used in Lynceus) and particle filtering. Preparing the upcoming OSM project deployment in an Oil&Gas operations barge, we deployed a testbed of 14 gateways and 11 target devices at our premises. We could thus test and validate our system, collect RSSI measurements, tune algorithm parameters etc. in real conditions. A sample of results is shown in Figure 2. The accuracy obtained for particle filtering during this run is below 4.77 m 95% of the time (over all target nodes).

CSEM and its partners have developed a reliable, scalable and robust infrastructure for the collection, processing and visualization of large data sets. We are currently using it to push our localization techniques further. Easily customizable, this technology can suit to many IoT applications.

[1] <https://offshoremuster.com/>, EU H2020 FTI, Grant Agreement No. 878950

[2] C. Kassapoglou Faist, P. Dallemande, "Large scale demonstration of RF-based localization of persons in cruise ships", CSEM Scientific and Technical Report (2019), 105.

# MANTIS, an Indoor Localization and Navigation Framework with Machine Learning Support

L. Bergamini, A. Restrepo Zea, M. Sénéclauze, S. A. Bigdely, S. Narduzzi

*Indoor localization is becoming a key feature of digital devices in numerous applications, requiring more and more precise and robust estimations. CSEM recently explored the combination of Bayesian filtering and machine learning approaches, including their training, to improve the accuracy and the speed of localization algorithms, with the objective of optimizing the resulting solutions for the IoT applications.*

CSEM developed in the past years a framework to support indoor and outdoor localization using different wireless technologies, starting with Received Signal Strength Indication (RSSI) and extending it to support various forms of signal (Time of Flight, Angle of Arrival, etc.). Although RSSI is not as reliable as the others, it allows for estimations that are accurate enough for many use cases, as shown in numerous deployments using our localization engine. However, this approach suffers from some difficulties that can be mitigated thanks to machine learning algorithms (MLA). One of the experienced problems with the current framework is that sometimes it indicates someone/something as being in a certain room, while the user/object is in a different room; this could have serious consequences on the application, e.g., in case of evacuations or emergency situations or for a digital inventory in case of objects.

The study has shown that formulating the localization as a classification problem allows for benefiting the most from the ML integration. For example, MLA can successfully identify the class to which a given set of RSSI values belong, after having divided the area of interest in many classes corresponding to specific areas of the building (typically a room), providing a correct classification in about 97% of the cases. CSEM's MANTIS now integrates the MLA classification output and implements the architecture depicted in Figure 1.

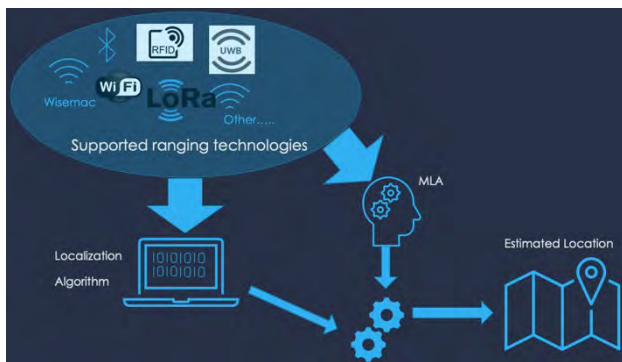


Figure 1: Indoor localization with ML support.

Starting from data coming from the supported ranging technologies, MLA and localization algorithms will work in parallel to estimate the location. The MLA will produce an array of probable rooms, while the algorithm will produce an (x,y) location. These information will then be combined to produce an estimated location (x,y) but placed in the most probable room.

This approach involves a training phase of the MLA, which requires a big amount of data (thousands of RSSI values for thousands of different positions), whose collection from a real installation is not realistic. CSEM chose to circumvent this obstacle by performing computer simulations to produce large training datasets (a few gigabytes for the moment). The study shows that the simulated data are suitable to produce effective training datasets, as demonstrated by reproducing a real in-house deployment on the simulator (Castalia OmNET++

framework) and by running simulations using two different sets of parameters: we first used default parameters, and then we tuned the parameters using values collected from the real installation. We then executed our localization algorithms on both the simulated datasets and on the real installation, resulting in the cumulative error distribution function illustrated in Figure 1. On the x-axis we find the error in meters, on the y-axis the percentage of estimations below a given error (e.g., in 50% of the produced estimations the error with respect to the real position is less than 3.94 meters).

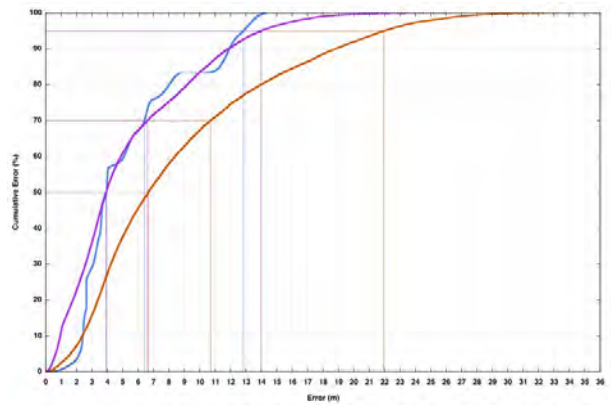


Figure 2: CDF when using real data (blue), default simulations (orange) and tuned simulations (purple).

When the simulator is properly tuned, the average localization error using simulated data is similar to the one we obtain with real data; this is enough for using the datasets for training the MLA. An analysis of the generated dataset confirms that considering a uniform sampling of positions, the classification of datasets allows a training thanks to a realistic balance of sample occurrences.

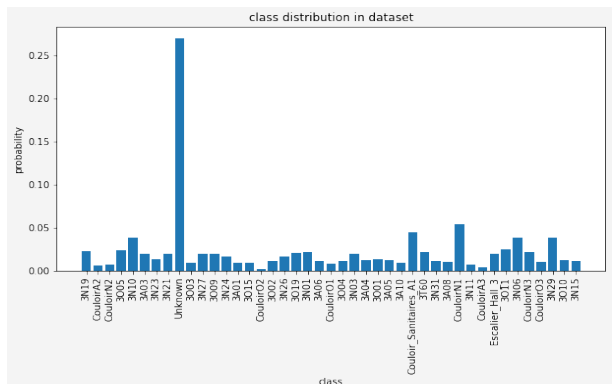


Figure 3: Classification of the dataset for MLA training.

This will allow for a proper training of the MLA. The development of the algorithms is currently ongoing, and in the end, we will realize a complete localization system based uniquely on RSSI values that will be permanently installed at CSEM. As a future work, we also plan to include data from additional sensors (e.g., accelerometer) to improve even further accuracy and speed of MANTIS.

# AMPWISE, an Energy Autonomous and Wireless Electrical Current Sensor

D. Piguet

Together with partners SENIS AG (CH), Serma Ingénierie (F) and Imperial College (GB), CSEM has developed a wireless sensor to measure the electrical current that flows in structural elements such as aircraft frames. The system is light-weight, non-invasive, and consumes so little energy that it can be supplied by harvesting energy from the magnetic fields created by the current it measures. The wireless sensor is usable on any vehicle or structure with a sensitivity below 0.3 A. The ultra-low-power and secure communication system created by CSEM supports potentially hundreds of nodes.

Land, air, and sea transportation systems face new integration challenges. These include increasing electrification combined with the use of lighter non-conductive structural materials. This is the case in commercial aircrafts where the return current must flow through existing conductive elements which were not necessarily designed for this purpose. For instance, narrow interconnection points may suffer from corrosion. This results in a need for non-invasive, easy to install and lightweight electrical sensors to monitor and detect for potentially adverse phenomenon caused by the electrical current flow.

However, added complexity and weight must be kept to a minimum. A solution that avoids heavy and complex cables is therefore desirable, and the presence of current provides an opportunity to harvest the energy that the sensor needs to acquire and transmit measurements.

Within the H2020 Cleansky Joint Understanding of the European Union, a call for proposals was initiated by Safran Electrical & Power to develop a wireless sensor technology for the monitoring of the return current in aircraft structures. The AMPWISE project, coordinated by CSEM, was selected.

The project, which finished in July 2021, delivered a prototype (Figure 1) that meets stringent specifications and has outstanding performance:

- AC (360, 500, and 800 Hz) and DC measurements
- 1% precision
- Range 0 to 20 A
- Ultra-low-power communication system with less than 25  $\mu$ A average current consumption with one AC/DC measurement every 5 minutes on each node
- Electro-magnetic energy harvester that delivers 0.4 mW in presence of 25 A 360 Hz alternative current (RMS)
- Cold start demonstrated

CSEM has adapted its WiseNode communication and sensing platform to interface with the current sensor made by Swiss project partner SENIS. The sensor is based on the Hall effect and requires data post-processing which is done directly on board the WiseNode.

The measured AC and DC values are sent to a concentrator using AirTDMA, an adaptive and reliable communication protocol developed by CSEM. To ease installation, each wireless sensor associates automatically with the nearest concentrator.

The sensor network is secured against tampering and eavesdropping end-to-end, on both the wireless links (wireless sensor to concentrator) and the wired links (concentrators to avionics). Several methods have been proposed to realize the initial key exchange out of band in a production environment and with minimal logistics constraints.

The wireless sensor includes an energy management circuit that stores and distributes the energy provided by the electro-magnetic energy harvester developed by Imperial College London. The circuit charges a supercapacitor with any amount of current provided by the harvester. When a sufficient reserve of energy has been stored, the power management circuit starts to supply the wireless sensor, which connects to its concentrator and enters a low-power mode with a 2-second wake-up delay from the concentrator. When an electrical current measurement is requested, the concentrator sets all wireless sensors to the active mode and collects the data. The concentrator monitors the incoming data to minimize the time spent in active mode and forwards it to the avionics. The power management circuit is also able to detect when the supercapacitor is close to being depleted and then shuts down the wireless sensor gracefully.

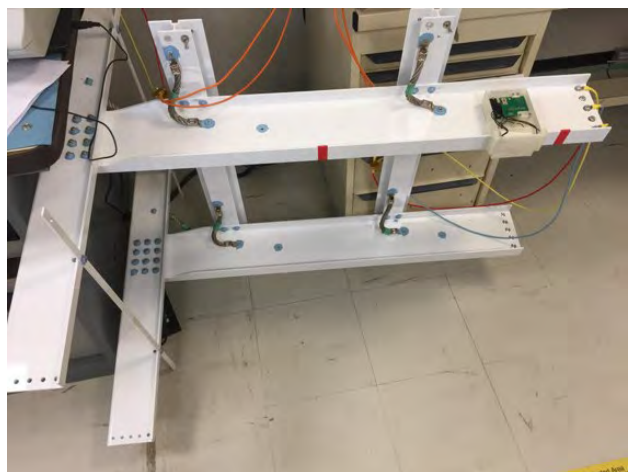


Figure 1: AMPWISE wireless electrical current sensor installed on a mock-up aircraft structure (top-right). The sensor Hall elements, the electronic and the antenna are installed on the wide area of the rail. The energy harvester is on the narrow part of the rail where the electromagnetic field concentration is maximal.

The AMPWISE wireless sensor and communication system can be adapted to any environment where non-invasive electrical current measurement is required: transport, energy systems, industry and many more. The communication range can be adapted, from personal to wide area networks as the sensor has both a short-range 2.4 GHz radio and a longer range LoRa 868 MHz transceiver.

This work was partly funded by the European Union H2020 Clean Sky Program under grant agreement 785495. CSEM thanks them for their support.

# Guardian, a Lightweight IoT Modular Platform

L. André, L. von Allmen, D. Piguet, L. Bergamini, M. Sénéclauze, P. Nussbaum

*Guardian is a multi-purpose platform combining multiple CSEM building blocks for providing multi-modal sensing, AI-powered processing, and connectivity into a compact and energy efficient package. Its modular architecture supports multiple vision and audio sensors, allowing analysis of the environment or subjects. The platform can be easily adapted to meet the requirements of many IoT applications, enabling quick appraisal of CSEM technologies directly in the field.*

Guardian is a smart wireless remote sensing system dedicated to visual and acoustic analysis. It embeds the sensing and wireless communication components, and edge processing capabilities, optimized for neural-network computations and multi-modal analysis. This allows for finding an optimal balance between local data interpretation and communication throughput. Eventually, Guardian forms a convenient platform for fast exploration and prototyping of use-cases in the field of smart IoT applications.

The system aggregates several key technological features developed at CSEM:

- Image sensing in visible and IR with application-dependent fusion schemes
- Acoustic sensing and localization using a microphone array for fusion with visual information or separated use
- Rich connectivity resources combining WiFi, LoRa, BLE and NFC with proprietary communication protocols for energy efficient sensing networks deployment

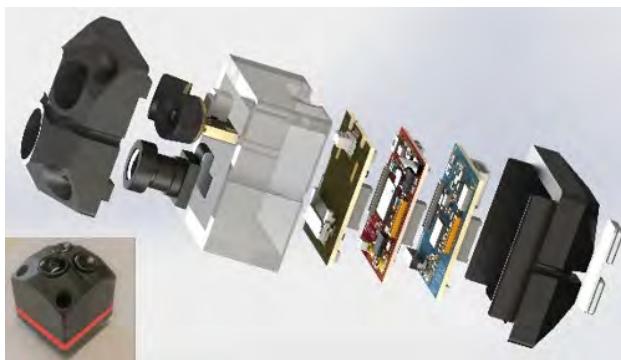


Figure 1: *Guardian, exploded and assembled views.*

The system is composed of 3 stacked boards, as illustrated in Figure 1 from top-left to bottom-right:

- Sensing and processing board
- Communication board
- Internet connection board including battery management

The processing power needed for sensing interpretation is provided by a dual RISC-V processor (Kendryte K210) bringing HW acceleration for neural network (NN) based image processing and for audio processing. This product has been selected for a first version of the system because being the only one on the market capable to internally host small-footprint standard NN models like MobileNet or YoLo. Applications run on top of the CSEM μ111 real-time operating system, which has been ported to this processor, along the necessary drivers and libraries for the sensors and processing.

The communication board provides power optimized solution with short (13 MHz), medium (2.4 GHz) and long (868 MHz) range communication links which can be managed using

standardized protocols (NFC, BLE, LoRa) or proprietary solutions like WiseMAC. The latter allows the best possible profiles of power consumption to establish network operations.

Guardian is targeting use-cases of surveillance, security, and inspection in a broad range of applications:

- Care unit patients monitoring, with activity, gait, and behaviour monitoring (cough, cry, abnormal breathing, ...)
- Precision agriculture with livestock monitoring (Figure 2), food delivery, early sickness detection and treatment, ...
- Infrastructure surveillance, with early fire detection, abnormal conditions detection in machinery (heat, noise, motion, ...), safety range compliance detection, ...
- Smart cities, with parking management, littering detection, frequentation monitoring, ...

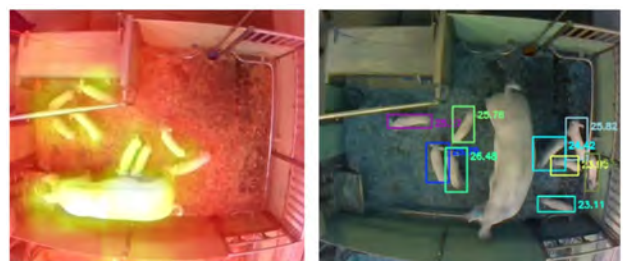


Figure 2: *Example of optical + IR sensing and resulting piglets counting and health assessment.*

The exploitation scheme consists in using groups of Guardian platforms to harvest the data to be analyzed in the field, proceed to off-site analysis and NN training and then embed the resulting algorithm in Guardian. The trained configuration can be deployed and tested for evaluating the in-situ performances in terms of detection reliability, power consumption profiles, communication.

Deriving a low-cost solution from the design reference of Guardian will be the preferred way to converge to an industrial prototype that would both fit application specification, user expectations and market requirements, including costs. Depending on market size, further scale-up in volume and cost reduction will be proposed with the design of an ASIC leveraging on CSEM IPs like VISAGE (CNN/BDT hardware accelerator), icyflex-V (ULP RISC-V) and icyTRX (ULP BLE transceiver) or the general purpose, ultra-low-power, multi-protocol and multi-transceiver WiseNode.

# Metallic Additive Manufacturing Technologies for 3D-shaped Millimeter-Wave Components Production

A. Vorobyov, S. Unterhofer, M. Dadras, O. Sereda

Development of additive manufacturing (AM) and, laser powder bed fusion (LPBF), opens new horizons allowing the fabrication of parts, that are, for example, limited in quantity or cannot be produced in a conventional way. AM offers the advantage of enabling the production of radio frequency (RF) components with a high freedom of design, while making the production of waveguide-based mm-wave or sub-THz antennas and components in one piece possible, as compared to machining, which requires at least one assembly step.

Nowadays, the manufacturing of waveguide-based mm-wave or sub-THz antennas (20 GHz to 500 GHz) and components relies on conventional machining techniques. The trend shifts towards higher frequencies, where conventional manufacturing techniques, may not be suitable due to the required precision and challenging tolerances. Additive manufacturing (AM) can facilitate the development of devices that meet the requirements of the future. As such, it can play a very important role, opening a vast field of opportunities in the world of RF and antennas.

Many design advantages have already been demonstrated with additive manufacturing, such as, weight reduction, assembly simplification and the ability to embed cooling channels. The integration of electrical functionalities like connectors, wires, and sensors after the printing process by assembly or 2D printing have been demonstrated at CSEM in 2018 withing the "AMAR" project.

Integration of the electrical wires by additive manufacturing can potentially be used within the waveguide structure for MEMS cantilevers actuation. The concept of the 3D printed waveguide section with integrated reconfigurable phase shifters is illustrated by Figure 2.

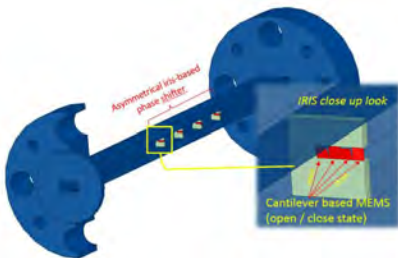


Figure 2: Concept of the 3D printed waveguide section with integrated reconfigurable phase shifters.

CSEM, and its partners (TTi and UPM), received a grant for the Clean Sky project (3DGUIDE) [1]. Within this project an efficient and affordable production method for high-precision mm-wave waveguide antennas and RF components will be developed.

Our focus is on establishing a full chain process for 3D printing technology: Pre-processing (i.e., powder morphology, powder granularity, flowability, chemical composition); 3D printing (establish printing parameters); Post processing (heat treatment, surface finishing).

A large variety of AM technologies exist, such as binder jetting, electron beam melting, but the chosen technology, L-PBF metal printing, has been found to be the best compromise in terms of:

material properties (mechanical and thermal stability, surface roughness, density), smallest feature size (<0.1 mm), throughput, high yield (~100%) and accuracy (<1%, low deformation).



Figure 3: 3D-printed waveguide sections in comparison with micromachined (left).

Waveguide structures have been prototyped at CSEM to evaluate L-PBF metal printing and limitations and improve AM manufacturing process (Figure 3 and 4). Measurements of the 3D printed waveguide samples, without surface posttreatment losses, show performances ( $S_{12} \leq -0.3$  dB @50 mm long WR-10 waveguide) already close to the regular machined parts.

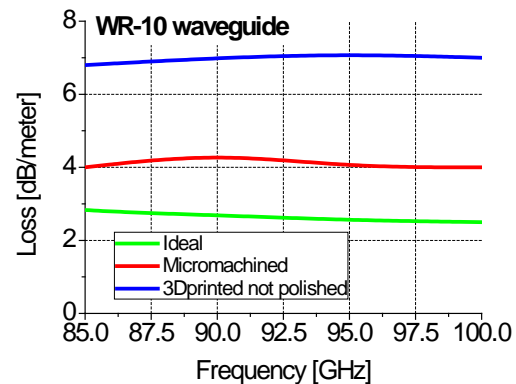


Figure 4: WR-10 (2.54 mm x 1.27 mm) loss.

The initial measurement results of the 3D-printed waveguide sections (Figure 3) have demonstrated promising RF performance. The measured  $S_{12}$  parameter of a 50 mm long WR-10 waveguide section, without internal surface treatment, is about -0.8 dB @94 GHz. Further, surface post processing could potentially reduce structural losses and provide as good (or even better) results than traditional techniques at such high frequencies. As in the case of any other emerging technology, further study and analysis are required to implement and validate improvement strategies.

[1] Feasibility demonstration of 3D printing for a new efficient production method of mm-wave waveGUIDE antenna (886696).

# Powerline Communications across Battery Cells

D. Piguet, A. Vorobiov, E. Le Roux

CSEM develops an interconnection technology, based on Powerline Communication (PLC), that allows for the monitoring and management of battery cells. Large modern batteries are made of dozens of interconnected cells grouped in packs. An appropriate management at cell level is essential to maximize the battery life, based on its state of charge and state of health. As cells are controlled individually, each of them must be able to communicate with the pack management computer or with other cells.

The electrification of vehicles and the increase of irregular energy sources such as wind turbines and solar panels boosts the demand for high capacity and high-power batteries. These are made of packs that contain dozens, potentially hundreds of cells.

A drawback of batteries is the high environmental impact due to their weight and to their production: raw materials, rare earth, hazardous substances. It is therefore highly desirable that batteries are as light as possible and that their life duration is maximal before recycling.

Maximizing the life of a battery pack is the task of its Battery Management System (BMS). The BMS is a distributed system with sensors, actuators, and minimal processing on each cell, all connected to a pack management unit. One can also imagine a completely decentralized system without central unit. In all cases, cells must be able to transmit their measurements and receive actuation commands through a data communication channel.

The first approach involves wired solutions, including serial buses and standards such as Controller Area Network (CAN), which is already widely present in vehicles. However, adding extra cables for communication has a cost in weight and complexity. Any new cable is a new failure risk.

Powerline Communication is a technology that transmits data over power supply cables, which avoids using additional wires dedicated to communication: cells are connected together in series and possibly also in parallel by the main power supply cable, which are also used for communication. The ROBIN project designed and prototyped such a solution, which validates the approach. In particular, one important project objective is to change the communication system of CSEM "BATMAN" BMS demonstrator from serial to PLC.

Originally, the PLC technology was introduced as a replacement for Ethernet cables in homes and also for broadband access over medium voltage supply lines to compete with coaxial cable and DSL. Both applications focus on large bandwidth, whilst a battery management system usually needs only low to medium data rate but has stringent latency and reliability requirements.

Fortunately, the emerging BMS market has attracted the interest of some communication circuit manufacturers. In ROBIN, CSEM has decided to evaluate and integrate the communication module DCB1M from Israeli manufacturer Yamar. The DCB1M is a low data rate, robust PLC transceiver with bit rates between 225 Kb/s and 1.4 Mb/s, selectable carrier frequency between 5 and 30 MHz and support for Carrier-Sense Multiple Access with Collision Avoidance (CSMA/CA) and priority arbitration.

The choice of the DCB1M is based on a traffic analysis which started from the messages produced by the earlier version of CSEM BMS prototype, with packs of up to 100 cells currently and many more in the future. The analysis was done by calculations and confirmed by simulations on the OMNeT++ network simulator. It shows that CSMA/CA and the circuit performance

can sustain the expected traffic while respecting the time constraints of the highest priority messages (100 ms).

The type of messages transmitted by cells are periodic measurements, responses to commands with detailed reporting information (hundreds of bytes), and alarms when a malfunction is detected. On the downlink, cells receive commands to start some detailed analysis algorithms, to return some particular data and actuation commands such as switch on or switch off. This allows the BMS to bypass some cells for some time in order to increase its life duration.

Following the theoretical analysis, a demonstrator based on development kits was implemented and tested. On-PCB Rogowski coils were specifically designed to inject the communication signal on the powerline. They can be seen on Figure 1. Communication tests were performed on a battery pack mock-up with 10 cells. The results show a residual packet success rate of 100% when the carrier frequency of the DCB1M is set to match the resonance frequency of the coils.

An integrated demonstrator is built on a  $18 \times 7$  cm PCB which is compliant with typical cells and battery packs made by the industry, where tens of cells are stacked in series and several packs can be connected in parallel. The cells are interconnected using the PLC technology. A CAN interface was added to link one of the cells to the BMS central entity.

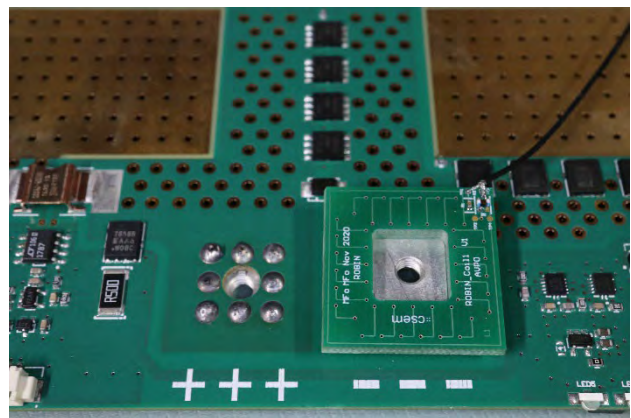


Figure 1: ROBIN BMS demonstrator. The Rogowski coils transmit and receive the communication signal by electromagnetic coupling with the main power connectors.

The laboratory validation of the complete demonstrator including the BMS, and PLC is underway for demonstrating the feasibility and benefits of using the PLC technology for interconnecting large battery packs. Once completed, it will be made available for tests in representative environments such as electrical vehicles platforms.

# Compostable Chipless Sensor Tag for Green Smart Packaging

O. Vorobyov, D. Schmid, C. Beyer, R. Limacher, J. Bourely<sup>\*</sup>, D. Briand<sup>\*</sup>, G. Nystroem<sup>\*\*</sup>

Compostable and biodegradable materials are the pillars of solutions for fighting against the electronic waste. Within the SNF-BRIDGE project GREENSPACK<sup>[1]</sup>. CSEM, together with EMPA and EPFL, proposes ultra-low cost, simple and eco-friendly chipless sensors and identification tags that are seamlessly used by the existing infrastructure and processes in authentication and logistics.

The GREENSPACK project aims at a simple eco-friendly chipless, printed and fully biodegradable sensing tag. It is based on cellulose-based substrate, containing no other harmful materials, and being ready for safe direct biodegradation, disposal or recycling, without requiring any return chain logistics or waste separation. This property meets the requirements of applications such as smart tagging of parcels for tracking them and monitoring their storage conditions, as illustrated in Figure 1. This is particularly relevant for perishable goods, such as pharmaceuticals that must be kept below 25°C and below 60% relative humidity.



Figure 1: GREENSPACK aims at developing green chipless sensor and identification tags for perishable goods monitoring.

The identification and sensor reading principles proposed by CSEM rely on spectral signature-based principles for identification and authentication with an 8-bit ID, temperature as well as humidity sensing for sensitive goods and sends the information on demand wirelessly to a fixed UWB reader.

CSEM is responsible for the chipless readout and system integration (integration & system characterization) and collaborates with EMPA for the development of materials for the substrate and the electrical tracks and sensors (biodegradable materials & inks), while EPFL develops new sensing materials and the printing processes for fabrication (additive manufacturing, devices & components).

The current prototype demonstrates the use of paper-based material for the substrate, and of the combinations of biodegradable organic and inorganic materials for inks, as shown in Figure 2.

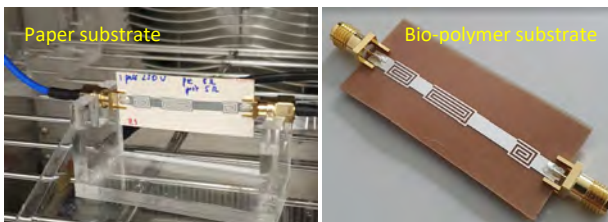


Figure 2: Climatic chamber biodegradable ink and substrate RF performance testing.

\* EPFL Lausanne, Switzerland  
\*\* EMPA, Switzerland

These inks are used for printing the electronics and the sensing components with compatible chemistry (orthogonal) and thermal budget for their sintering when required.

The short-range tag (up to 10 cm) will use magnetic coupling between the reader antenna and the LC resonant tag and operate at a frequency between 1 GHz and 10 GHz (Figure 3a).

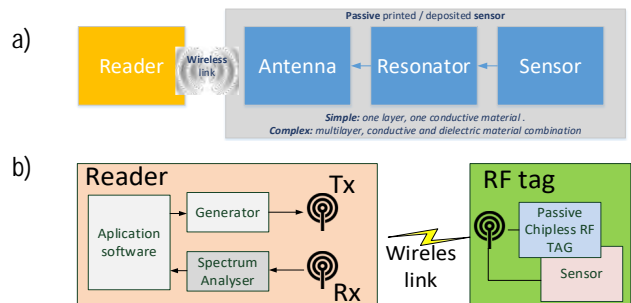


Figure 3: Innovation roadmap, highlighting demonstrator evolution.

The long range (above 1 m) tag will be based on retransmission of the interrogation signal with the encoded unique spectral ID. Encoded data are integrated into the spectrum using resonant structures. Each data bit corresponds to the presence or absence of a resonant peak at a predetermined frequency in the spectrum (see Figure 3b).

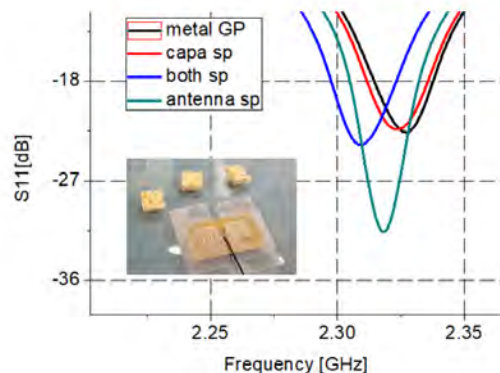


Figure 4: Short range tag with passive humidity sensor (absorber).

Figure 4 depicts some preliminary results of the short-range passive humidity sensor. The material placed on the top of the tag elements changes the tag FR performance when humidity increases. Future fields of use are food packaging, medicines transport monitoring, environmental sensors, agriculture, buildings, or point-of-care.

"GREENSPACK – Green Smart Packaging" receives funding from the BRIDGE–DISCOVERY program under grant agreement No. 187223. CSEM thanks them for their support.

[1] <https://p3.snf.ch/project-187223>

Harnessing the Power of 3D Data through Deep Learning and Computer Vision

B. Platerrier, F. Auf der Maur, M. Höchemer, T. Parkel, P. A. E. Schmid

The growing availability of low-cost 3D sensors over the past few years is fueling demand for 3D data processing and deep learning algorithms that can process the measurements. 3D technology enables robots to get a better understanding of their environment, improves the augmented reality experience, and allows for quality inspection of big and complex 3D objects (e.g., airplanes, trains, space). CSEM is bringing its expertise in 2D data processing into the third dimension, by evaluating available hardware and software solutions and developing its own set of tools for complex 3D data analysis.

3D sensors are becoming a low-cost commodity, being integrated into mass-market mobile devices such as smartphones and game console systems. Whether it is a LiDAR (e.g., Intel RealSense LiDAR) or a depth sensing camera (e.g., Microsoft Azure Kinect), these devices deliver depth information as well as 2D texture pictures that can be used for computer vision and machine learning. As prices fall, industrial demand rises rapidly. 3D data is becoming more and more important for many industrial solutions. Expected market growth can only be served by easy-to-use flexible software solutions.

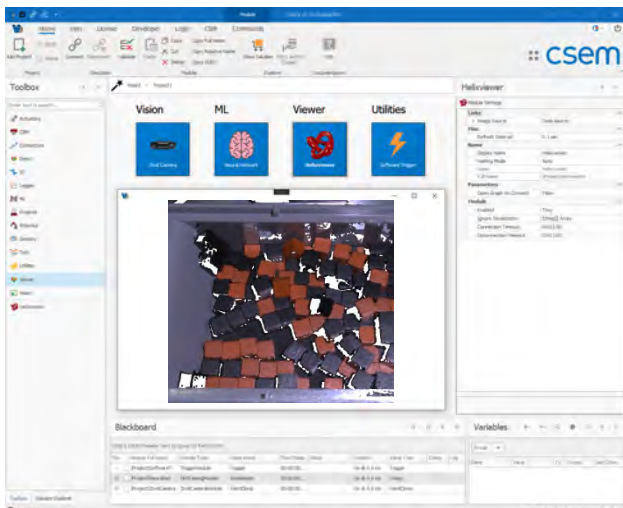


*Figure 1: Integration of a 3D depth sensing camera and a 3D point cloud visualizer into ViSARD (Vision Automation Robotics Designer).*

Computer Vision for 2D image processing is well established in many markets. However, to use the information provided by 3D sensors to its full extent and ensure best performance in industrial applications, highly customized solutions are necessary. CSEM is building know-how and toolsets for 3D data processing with a focus on low-cost mobile devices.

In the first phase the evaluation of available hardware solutions was performed. A selection of these devices was integrated into the CSEM ViSARD (Vision Automation Robotics Designer, [www.visard.ch](http://www.visard.ch)) framework. This allows for easy-to-use acquisition, visualization, and processing of the 3D data in any industrial application (Figure 1). Processing of the raw data is then performed with classical vision filters through available OpenCV and Open3D libraries as well as more advanced machine learning (ML) frameworks. CSEM's strong expertise in deep learning applications allowed to develop algorithms specifically designed for individual industrial applications.

With these new software tools, CSEM aims to facilitate the entry to the field of 3D and the integration into connected industrial systems. Such a technology can enable robots to make sense of their surrounding (e.g., objects, humans, obstacles). One goal is to solve bin-picking tasks for small parts. Despite two decades of robot development this is still one of the biggest challenges in industrial part handling and logistics (Figure 2).

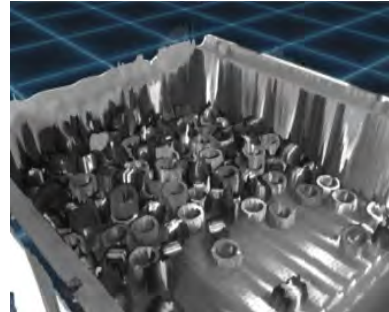


*Figure 2: Visualization of 3D measurements obtained from a Raytrix 3D light field camera for a bin-picking application.*

Beyond grasping parts and quality inspection, 3D data obtained from a scanning process can be used to automate or assist humans in the design of complex 3D objects.

CSEM is currently working on the automatic design of seat cushions for disabled people. Paraplegic people do not feel whether they are sitting comfortably and evenly. A perfect matching cushion is thus essential to prevent injuries resulting from prolonged pressure on the skin. Nowadays, the design process is rather tedious and requires the patient to sit on a vacuum or pressure cushion. The cushion is 3D scanned and post-processed manually, before finally being used in the workshop to design and build a customized seat cushion.

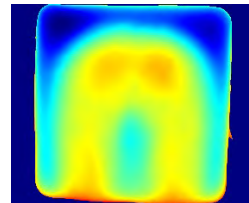


Figure 3: 3D scan of a vacuum seat cushion. The colors correspond the depth (or distance) from the camera viewpoint.

CSEM's solution is based on a scan of the patient body. The 3D data is then processed with a machine learning algorithm that is trained to estimate the shape of the cushion (Figure 4). This approach makes the acquisition process four times faster, error-proof, and more comfortable for the patient.

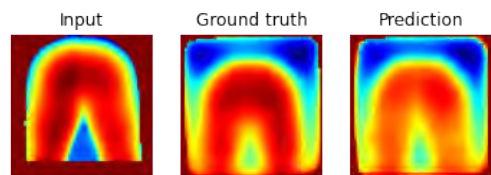


Figure 4: Comparison of ground truth (center) with predicted cushion (right) shapes from a (cropped) body scan (left).

This work is supported by the Cantons of Central Switzerland.

# How Little is Too Little? Image Generation Performance in a Small Industrial Data Setting

E. Ntavelis, I. Kastanis, P. A. E. Schmid

Recent developments in Generative Adversarial Networks (GAN) have provided unprecedented performance in data synthesis tasks. The need for image generation in the industrial domain is urgent for data hungry requirements of deep learning approaches, yet the collection of sufficient industrial data remains a practicably unsolvable task in many cases. It is of utmost importance to examine the extend and limitations of modern GAN approaches in the industrial setting to enable future data practitioners to integrate data generation aspects into their machine learning pipelines. It is the aim of this study to present a methodology for exploring industrial image generation in the limited-data regime.

In this study, a methodology for the analysis of the suitability of GANs to a particular dataset is examined. We aim to both understand the quality of generated data, get insights on the limitations of the dataset, and design an appropriate dataset that will meet the requirements of their application.

We run our experiments on a homogeneous dataset of injection molded pump parts, that vary in the surface structure due to the manufacturing process and the effects of transportation; an atypically small dataset for GAN development<sup>[1]</sup>. To find the lower limit for realistic industrial image synthesis we further subsample the dataset to obtain 4 sub-datasets of 5, 50, 100, 300.

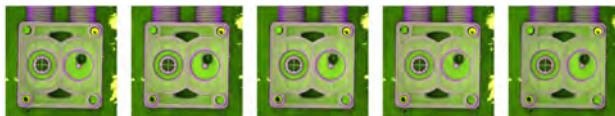


Figure 1: Real and Synthesized samples. The first column has a real image. Then each next column has a sample from the GAN models trained on the 5, 50, 100, 300 images respectively.

As our generative model, we use the work of "Towards Faster and Stabilized GAN Training for High-Fidelity Few-Shot Image Synthesis" proposed by Liu, et al.<sup>[2]</sup>. Additionally, we augment the discriminator's input with a probability of 25%.

As many evaluation metrics in the literature were designed for natural images, we propose an exploratory analysis based on the histogram of Mean Squared Error (MSE) computed in a pairwise fashion between two sets: (a) generated images set vs the ground-truth dataset and (b) the generated images set vs itself.

Our industrial dataset exhibits only small variation. This can be observed in the real intra-dataset curve in Figure 2. Additionally, proposed image-pair MSE loss histogram shows the effect of the dataset size. All experiments with different dataset sizes, albeit the smallest one (e.g., with 5-images), exhibit similar behavior. When we compute the intra-dataset variation histogram, we see that almost all cases produce similar curves to the one produced by measuring the intra-dataset variability of our full ground truth dataset. However, the smallest dataset produces an abundance of problematic cases as can be seen in the various peaks in Figure 2. The same conclusion can be drawn by exploring the Real vs Fake dataset variation, where we compare all the fake images produced at each setting against the real ones. This is indicating that there is a lower limit on how little data is little to produce realistic samples, which in this setting, we found to be less than 50 images in line with our visual inspection study.

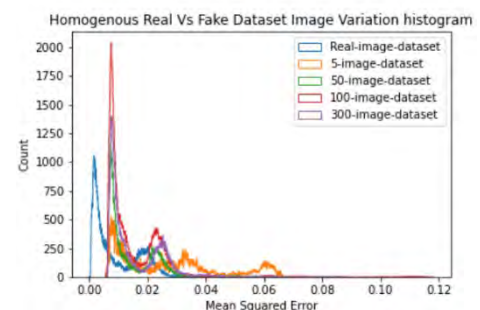
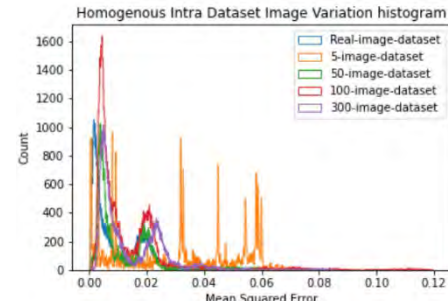


Figure 2: Our proposed qualitative approach for assessing performance in an industrial setting.

In this work we are conducting a study on the performance of the state-of-the-art GAN networks in a limited data industrial setting. We propose a qualitative methodology designed for industrial images that compares the variation curves of generated images. Moreover, we show that recent GAN methods can sufficiently perform with only a handful of training image samples. In our experiments we found that models trained with 50 or more images produce high quality results.

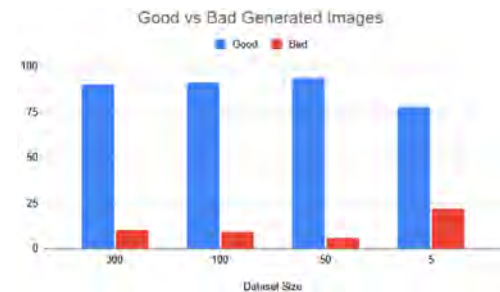


Figure 3: Visual inspection shows the percentage of failure cases in different settings. We found that only on the smallest dataset we observe an increase in spurious samples.

This work is supported by the Cantons of Central Switzerland.

[1] T. Karras, S. Laine, M. Aittala, J. Hellsten, J. Lehtinen, T. Aila, "Analyzing and Improving the Image Quality of StyleGAN", 2020 IEEE/CVF Conference on Computer Vision and Pattern Recognition (CVPR), 8107-8116.

[2] B. Liu, Y. Zhu, K. Song, A. Elgammal, (2021), "Towards Faster and Stabilized GAN Training for High-fidelity Few-shot Image Synthesis". ArXiv, abs/2101.04775.

# It's a Match—Your Profile in the Cloud

M. Russi, B. Platerrier, M. Höchemer, P. A. E. Schmid

Aluminum profiles are everywhere: furniture, cars, planes, windows, etc. At the production facilities, thousands of profiles are in stock. Since they are getting coated in the manufacturing process, an order sheet is placed inside or around the profile describing its properties and required process. However, this paper can easily get lost or mixed up. Since some profiles look extremely similar, high risk is that the wrong profile ends up at the wrong client with the wrong color. To overcome these challenges, E. Luterbach AG partnered together with CSEM in a novel AI approach. The solution consists of a Web App, deep learning algorithms, a large database in the cloud, and an easy way of adding new profiles without retraining the algorithms.

Profiles can be found nearly everywhere. One essential step in the production line is powder coating, where the profile gets its colored surface finishing. At production, the stocks often include several thousands of different profile types. Often in storage are multiple profiles of each type, resulting in a huge inventory.



Figure 1: Thousands of profiles in stock.

To guarantee a flawless process, knowing the exact profile type is essential. Since they are not yet coated, one cannot simply write or stick the profile number on it. The current state-of-the-art solution is having an order sheet placed in or around the profile.



Figure 2: Profil storage for powder coating – paper everywhere.

However, several problems arise with this approach: firstly, the sheets can get lost. Secondly, for some process steps, such as the coating with high temperatures, the sheets must be removed. Once a paper is lost, identifying the profile is tedious. Chances of taking the wrong profile are high, since they can look very similar and comparing them to the technical drawing needs time and concentration. This can lead to mistakes during the production process or even shipping the wrong profiles to the customer. Furthermore, printing and tracking all the papers are time and material consuming tasks.

To overcome these challenges, E. Luterbach AG teamed up with CSEM in an innovation project, partially funded by Innosuisse, to develop a robust and easy extendable solution. It consists of a Web App, hosted on Microsoft Azure cloud, which can be accessed by any mobile device or computer. The user can take directly with the smartphone a picture of the profile to be identified. The photo is then sent to the Cloud, where it is being processed by deep learning algorithms and compared to

references in the database. Finally, the result, such as profile type and number, is sent back to the user.

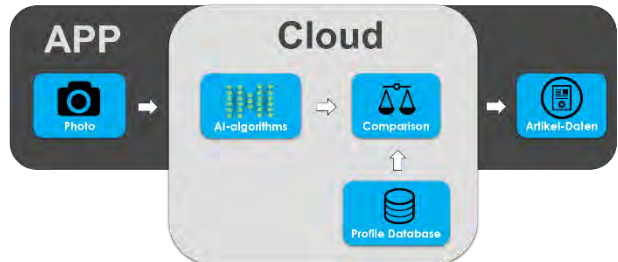
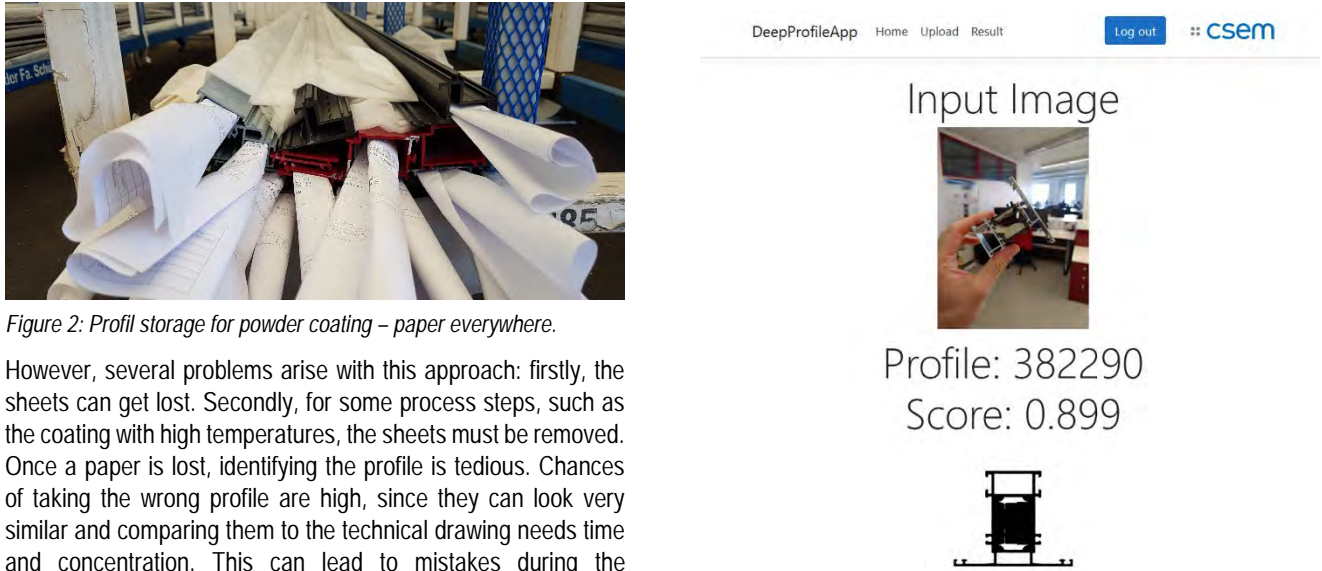


Figure 3: Process pipeline: from the smartphone to the cloud and back.

There are over 5'000 profiles registered in the databases and the resulting top score of finding the profile is currently over 97%.

Since storage and computing is completely hosted in the cloud, scaling is possible at all times. Due to the optimized architecture of the deep learning algorithms, new profiles can be added with minimal effort without compromising the performance and without retraining of the neural networks. New profiles can be added just through technical drawing or a photo. With the CAD drawing option, profiles can already be added to the database even before they have been produced the first time.



DeepProfileApp Home Upload Result Log out :: csem

Input Image

Profile: 382290  
Score: 0.899

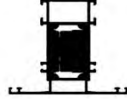


Figure 4: Smartphone app: picture with result - profile number and score.

To sum up, the provided solution enables a fast and reliable identification of profiles. Paper sheets in production environment are eliminated and mistakes are reduced. The next steps are extensive testing at customer's facilities and integrating the solution completely into existing software solutions (ERP, DCS, MES).

This work is supported by the Cantons of Central Switzerland.

# Gemstones, Place of Origin and Heat Treatments: Automatic Recognition and Classification using Deep Learning

T. Bendinelli, M. A. Kirschmann, M. Höchemer, P. A. E. Schmid

*Proof of authenticity renews the value of colored gemstones. In the framework of an innovation project partially funded by Innosuisse with Gübelin Gem Lab an AI system is under development to classify gemstones by authenticity and country of origin. The input data is highly multivariate, stemming from different optical and chemical spectroscopy methods, and microscopy observations with gemmologists' text descriptions. A wide variety of machine learning algorithms were applied to optimally utilize the different data sources. The classification system finally merges the different algorithmic approaches and gives unified predictions for a gemstone's country of origin and authenticity.*

For the jewelry and gemstone industry a gemstone's authenticity and country of origin are crucial characteristics, impacting the market value of the gemstone. However, these characteristics are not apparent and bad actors sell gems with false label of origin, or artificially treated gemstones as untreated in order to increase their selling value.



Figure 1: Colorful gemstones.

Gübelin Gem Lab, established almost a century ago, specialized in offering the service of analyzing and valuing gemstones for buyers and sellers. Gübelin Gem Lab issues an official certificate with the characteristics and findings. The gemmologists examine the gemstones with a quiver of different analytical methods, including optical and chemical spectroscopy. Visual peculiarities, which can be characteristic for certain origins or a sign of artificial treatment, are documented also by microscopic pictures and described by the gemmologists. Gübelin Gem Lab has ten thousands of (partially handwritten) reports in their database and thousands of reference gemstones that were acquired directly at the mines of origin providing further ground truth. Gübelin Gem Lab has teamed up with CSEM in an innovation project partially funded by Innosuisse to turn this data abundance into an objective, efficient, fast, and robust automated classification system. This system which is currently being developed combines all available data of a gemstone (analytical data from the different instruments and the written reports) and classifies the gemstone by origin and treatment status.

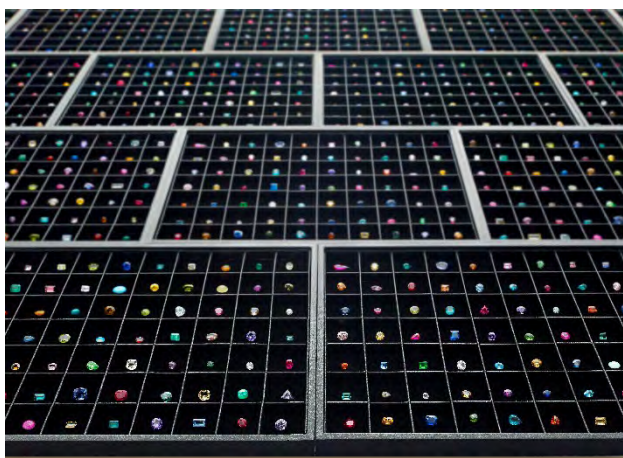


Figure 2: Gübelin Gem Lab reference gemstones.

CSEM's classification system is based on a series of statistical classifiers, one for each data source, which are combined to make a unified decision. Besides the classification result a confidence score is provided, which helps to understand if a gemstone clearly falls into one category or is ambiguous.

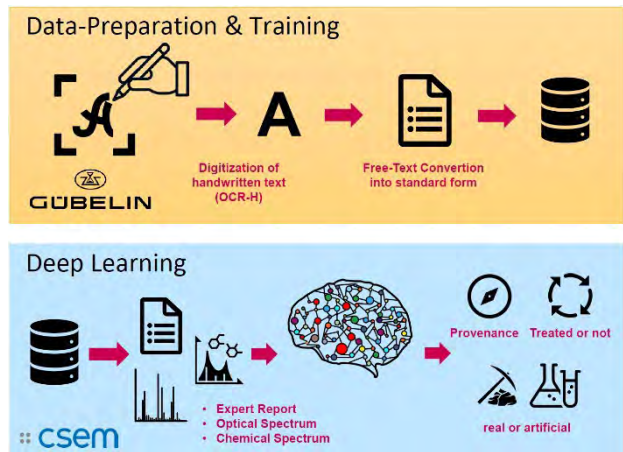


Figure 3: Schematic of data preparation and deep learning.

Each classifier is trained with a set of positive samples (gemstones originating from certain origins or treated with certain treatments) and a set of negative samples (gemstones of different origins or not treated). One big challenge that CSEM faced was integrating the data from the different instrumental sources and working with the varying formats of the data. While some data sources are based on text statistics, others are based on spectral data, others on image data, and others on chemical information. To tackle this challenge, CSEM has tested thoroughly many classification algorithms to find the best performing ones, giving the most robust results for each data source. The tested classification prototypes for the different types of data - spectral, chemical and text – include Random Forest, state-of-the-art convolutional neural networks, and natural language models.

Analysis methods from the field of explainable AI, showed that the ML algorithms had learnt to focus on features that gemologists also use in their decision-making process. With this approach there have been even new deciding features discovered which now the experts apply in their manual tasks.

The preliminary results are very promising, and it is planned to integrate the classification system in Gübelin Gem Lab's daily workflow to support gemologists' decision making.

This work is supported by the Cantons of Central Switzerland.

# Linear Adaptive Model Identification with Gaussian Processes

I. Sideris, F. Crivelli

We propose a scheme for learning probabilistic meta-models of linear system approximations for the identification of dynamical systems. Such models can be used for designing model predictive controllers and for online state estimation. The proposed model class combines the simplicity of linear models with a carefully increased representative power obtained by a data efficient optimization scheme.

System identification has been rigidly connected with the design and the robustness of controllers since the early days of automation. Indeed, having an optimization algorithm offering a good representation of a system's dynamics can prove to be very valuable. This is because it allows the design of high-performance model-based controllers as well as accurate state estimators for keeping track of the system's evolution. Moreover, precise system modelling provides the opportunity to capture the variability of the system and thus, strengthen the robustness of the overall control scheme.

The classical system identification theory mainly focuses on grey-box estimators for simple linear models<sup>[1]</sup>. This model class is suitable for control design. It allows the engineer to use standard tools for stability and performance, while also offering an intuitive and interpretable system representation. However, the hypothesis class of such models is limited, and as a result, these models are of reduced predictive performance. There are various approaches that extend the class of possible predictors to counteract this issue, with many researchers using schemes ranging from black-box models, like recurrent neural networks<sup>[2]</sup>, to statistical tools, such as Gaussian processes<sup>[3]</sup>. Though, these approaches to system identification result in highly non-convex optimization problems that have to be executed off-line. Also, they require extensive modeling and large amounts of data in order to be precise. As a solution to this problem, recent developments in the field of Online Learning have been targeting the construction of system representations through convex optimization using a limited amount of data points. This can be done either by introducing a set of convex relaxations to the system's state<sup>[4]</sup> or by targeting the Markov parameters of the system and then, obtaining a meaningful representation.

In comparison to the existing identification approaches, the proposed method tries to combine both the interpretability and the easiness of control-loop shaping that the linear models offer, while extending their capabilities. This is achieved by linking these models with non-linear, probabilistic tools while retaining the convexity of the optimization problem. The resulting model class is composed of ensembles of linear models, which are interconnected with Gaussian Processes. The statistical models themselves depend on the system parameters. As a result, the system dynamics change and readapt to any perturbation of the initial system configuration. This feature yields a very agile model class, and with the correct prior assumptions, it can describe a wide variety of interesting dynamical systems. Furthermore, by making sure that the linear models can be optimized in a convex

scheme, either by keeping them simple or by introducing convex relaxation terms, it is guaranteed that the linear models' optimization can also run online. This strengthens the robustness of the approach by giving the system the possibility to evolve over time.

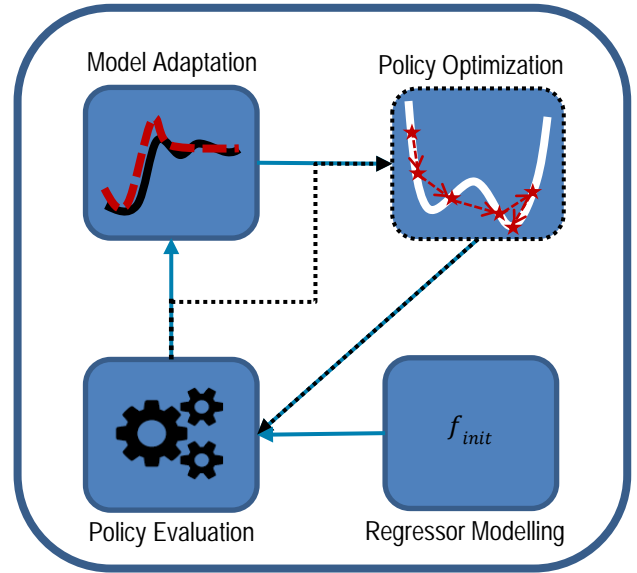


Figure 1: Schematic of the control optimization scheme. After initializing the model, use the obtained data to adapt the model if needed, and then optimize the policy evaluated on the system.

Subsequently, after coming up with an initial formulation for the equations driving the response evolution of a system, the model can be used for optimal control or parameter tuning, even before the learning phase is over. Simultaneously, by using the new information that is streamed in from the evaluation of the previous control inputs, the identification algorithm can learn in an incremental way the underlying dynamics of the system and, step by step, improve its performance.

The first steps of this method were tested and validated on a hydraulic tripod system with parallel cylinders driven by a single pump and one proportional valve at the entrance of each cylinder. Incrementally, an optimal controller design was learned with which the valves were regulated in a way that the movement of all the cylinders was synchronized. The learned controller was robust, and could attain a high level of performance even under different environmental conditions.

This work is supported by the Cantons of Central Switzerland.

[1] L. Ljung (1999). System Identification: Theory for the User.

[2] J. D. Rubio, W. Yu (2007). Nonlinear system identification with recurrent neural networks and dead-zone Kalman filter algorithm. *Neurocomputing*, 2460–2466.

[3] J. Kocijan, A. Girard, B. Banko, R. Murray-Smith (2007). Dynamic systems identification with Gaussian processes. *Mathematical and Computer Modelling of Dynamical Systems*, 411-424.

[4] E. Hazan, K. Singh, C. Zhang. (2017). Learning Linear Dynamical Systems via Spectral Filtering. Conference on Neural Information Processing System (NIPS).

# Uncertainty-Aware Prognosis via Deep Gaussian Processes

L. Biggio, I. Kastanis, P. A. E. Schmid

The task of predicting how long a certain industrial asset will be able to operate within its nominal specifications is called Remaining Useful Life (RUL) estimation. Efficient machine learning (ML) methods of performing this task promise to drastically transform the world of industrial maintenance, paving the way for Industry 4.0 revolution. However, given the safety-critical nature of maintenance operations on industrial assets, it's crucial that new ML-based methods be designed such that their levels of transparency and reliability are maximized. We address this challenge by investigating the performance of a recently proposed class of algorithms, Deep Gaussian Processes, which provide uncertainty estimates associated with their RUL prediction, yet retain the expressive power of modern ML techniques. Contrary to standard approaches to uncertainty quantification, such methods scale favourably with the size of the available datasets, allowing their usage in the "big data" setting. The performance of the algorithms is evaluated on the NASA N-CMAPSS (New Commercial Modular Aero-Propulsion System Simulation) dataset for aircraft engines.

Recently, predictive maintenance (PM) methods have been gaining popularity for many different industrial applications. PM aims at predicting the need for maintenance actions based on the information extracted from condition monitoring data describing the health state of the system. Efficient Remaining Useful Life (RUL) estimation is a key enabler of PM and the application of machine learning (ML) and deep learning (DL) techniques to RUL prediction tasks has been an active research area over the last several years.

While the majority of model-based prognostics approaches consider the associated uncertainty, only a few research studies on data-driven RUL prediction have tackled the challenge of quantifying the level of uncertainty associated with the predictions of the proposed techniques. Nevertheless, Uncertainty Quantification (UQ) is crucial in the context of PM because RUL models are used for critical decision-making and, therefore, need to be transparent regarding the level of uncertainty in their predictions. As a result, the deployment of ML techniques in real-world engineering scenarios cannot prescind from the design of reliable algorithms capable of providing a probability density function over RUL predictions instead of simple point estimates.

The main idea of our work<sup>[1]</sup> is to apply Deep Gaussian Processes (DGP) models to the problem of RUL estimation. Our main motivation is that DGP models combine the benefits of DL, via their expressive hierarchical representation, and standard Gaussian Processes, in light of their ability to perform UQ. We evaluate our DGP and a standard Feed-Forward Neural Network (FFNN) on a fleet of nine large turbofan engines under real flight conditions (the data is part of the new C-MAPSS dataset [2]). Overall, we split the full dataset into six training units (2,5,10,16,18,20) and three test units (11,14,15). Given are (input) multivariate time series of condition monitoring sensor readings and their corresponding (output) RUL values.

As shown in Figure 1, the predictions of the FFNN model tend to align to the ground truth towards the end of the units' lifetime. However, the network is overly confident in its RUL estimates, even when they significantly diverge from the ground truth (first predictions are far removed from the ground truth). In contrast, as shown in Figure 2, the predictions provided by the DGP model are supported by meaningful uncertainty estimates. In both cases, the confidence bounds show an important desirable characteristic for RUL models. The values of the predictive

variance decrease over time. This is physically meaningful since predictions are much more uncertain when the system is far from the end of its life. As a result, the confidence bounds associated with early operating times are significantly larger than those corresponding to the machine's end of life. Such a property has very important practical implications since it enables the design of risk-aware maintenance strategies.

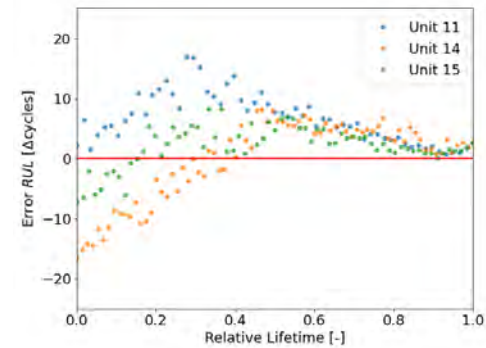


Figure 1: Prediction error of the FFNN model as a function of the relative lifetime.

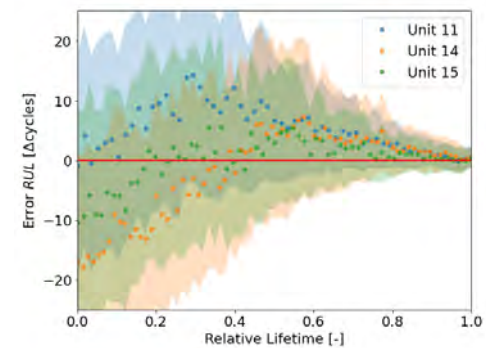


Figure 2: Evolution of predictive uncertainty (i.e.,  $\pm 2\sigma$ ) output by the DGP.

In the future, we plan to apply the same methodology to other industrial time series datasets to exploit its uncertainty estimation capabilities.

This work is supported by the Cantons of Central Switzerland.

[1] L. Biggio, A. Wieland, M. A. Chao, I. Kastanis, O. Fink, "Uncertainty-Aware Prognosis via Deep Gaussian Process", in IEEE Access, vol. 9, pp. 123517-123527, 2021, doi: 10.1109/ACCESS.2021.3110049.

[2] NASA C-MAPSS Aircraft Engine Simulator Data, <https://ti.arc.nasa.gov/tech/dash/groups/pcoe/prognostic-data-repository/>

# Cuffless 24-Hour Ambulatory Blood Pressure Monitoring

M. Proen  , J. Ambuehl\*, G. Bonnier, D. Ferrario, E. Rexhaj\*, M. Lemay

High blood pressure (BP), or hypertension, is the main risk factor for cardiovascular diseases and the root cause for approximately ten million deaths each year. Its formal diagnosis often requires 24-hour ambulatory blood pressure monitoring (ABPM), with cuff-based BP measurements cycling at 20- or 30-minute intervals. The procedure can be quite obtrusive, particularly during nighttime, where the inflation of the cuff can disturb sleep and lead to non-representative BP readings. In the present study, we demonstrate the feasibility of using a cuffless optical watch-like sensor for 24-hour ABPM, paving the way for a new branch of cuffless and patient-friendly solutions in the thriving market of hypertension diagnosis.

ABPM is increasingly used in clinical practice for the formal diagnosis of hypertension, and particularly indicated in cases of suspected white-coat effect, masked, or nocturnal hypertension. However, the use of cuffs for ABPM may be painful and cause discomfort, particularly at night, where it may even provoke arousal from sleep and lead to non-representative nighttime BP values<sup>[1]</sup>. The purpose of the present study was to investigate the feasibility of using a cuffless watch-like photoplethysmographic (PPG) sensor for 24-hour ABPM by comparing the PPG-based BP estimates with conventional cuff-derived ABPM values.

Our study (clinicaltrials.gov: NCT04119518) was conducted in 70 participants ( $43 \pm 18$  y, 35 with hypertension, 41 male) undergoing cuff-based ABPM. Systolic (SBP) and diastolic (DBP) BP values were estimated by our patented pulse wave analysis algorithm oBPM™<sup>[2,3]</sup> from the measured PPG signals. At the contralateral side of the cuff, a CSEM-designed PPG sensor was worn at the wrist or upper arm. Following a calibration procedure, the PPG-based daytime and nighttime BP estimates were compared to their cuff-based counterparts. The agreement between both methods was evaluated via the mean and standard deviation (SD) of their differences by Bland-Altman analysis. The agreement on the nocturnal dipping estimates of both devices was also assessed. Finally, the concordance rate was assessed as the percentage of dipping values showing a concordant direction (dipping vs. non-dipping) between both methods.

The data of 4 participants were incomplete due to technical issues and had to be rejected prior to analysis. In 4 additional participants, the PPG data quality was insufficient to provide enough BP estimates, probably due to poor sensor tightening. As shown in Table 1 and Figure 1, for the remaining 62 participants, we found differences between the daytime PPG-based and cuff-based BP estimates all falling within the limits required by the ISO 81060-2:2013 standard for non-invasive sphygmomanometers.

Good agreement was found between the PPG-based and the cuff-based daytime and nighttime BP averages, with generally negligible (~1 mmHg) biases. The direction of dipping was highly concordant between both methods. The estimation of its amplitude showed a low bias (~1%) but a non-negligible spread (SD), which can be in part attributed to the uncertainty on the cuff-based dipping estimates (95% confidence interval range of 12.5% and 16.5% on average for SBP and DBP, respectively).

more than twice than their PPG-based counterparts (5.7% and 7.8%). Although our study was designed as a method-comparison feasibility study, these results open the way for the development of highly demanded cuffless alternatives in the growing field of hypertension diagnosis.

Table 1: Agreement (bias and SD of the differences) between the PPG-derived BP values estimated by our pulse wave analysis algorithm oBPM91TPTMP91T compared to conventional cuff-based measurements.

BP	Daytime bias ± SD	Nighttime bias ± SD	Dipping bias ± SD (concordance rate)
SBP	-0.9 ± 3.6 mmHg	-0.8 ± 6.8 mmHg	0.1 ± 6.8% (97%)
DBP	-1.4 ± 2.9 mmHg	0.5 ± 5.3 mmHg	-2.0 ± 8.6% (97%)

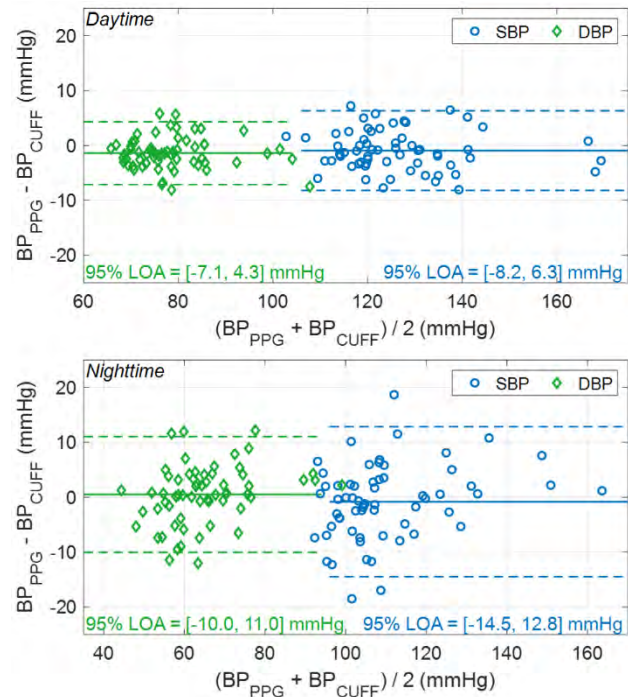


Figure 1: Agreement (Bland-Altman plots) between the PPG-based and cuff-based daytime and nighttime BP values. LOA: limits of agreement.

\* Departments of Clinical Research and Cardiology, Bern University Hospital, Inselspital, Bern, Switzerland

<sup>[1]</sup> R. Agarwal, R. P. Light, "The effect of measuring ambulatory blood pressure on nighttime sleep and daytime activity—implications for dipping", Clin J Am Soc Nephro, 5(2):281-285, 2010.

<sup>[2]</sup> M. Proen  , J. Sol  , M. Lemay, C. Verjus, "Method, apparatus and computer program for determining a blood pressure value", WO 2016138965 A1, 9 September 2016.

<sup>[3]</sup> Y. Ghamri, M. Proen  , G. Hofmann, et al, "Automated pulse oximeter waveform analysis to track changes in blood pressure during anesthesia induction: a proof-of-concept study", Anesth Analg, 130(5):1222-1233, 2020.

# VO2Max and Fitness Level Estimated with Speed and Heart Rate

C. Moufawad el Achkar, M. Gerber, P. Renevey, P. Theurillat, A. Lemkaddem, M. Lemay, D. Ferrario

Athletes and people looking to improve their health need an objective measure of their fitness levels. The maximal oxygen uptake or VO2Max is a direct measure of cardiorespiratory fitness that can reflect changes in endurance and overall exercise capacity. Existing methods of measuring VO2Max are either cumbersome (metabolic carts), test-specific (standardized tests), or insensitive to change (empirical models). We propose a method to automatically measure VO2Max when the user goes for a run. The method only requires a measurement of heart rate and speed and can be used with any wearable system that can provide both measures.

VO2Max is an objective measure of a person's cardiorespiratory fitness. It is the maximal oxygen volume achieved at exhaustion during incremental physical exercise. With proper training, an individual can increase their VO2Max, thus improving their endurance and physical capacity. VO2Max is crucial for athletes and is gaining interest with amateurs training to improve their fitness. In today's digital world, it is highly desirable to obtain such a measure automatically using connected wearables.

The standard way of obtaining VO2Max is through indirect calorimetry to measure oxygen volume. While this method is the gold standard, it suffers from setup complexity because it requires the user to wear a mask and bulky equipment, even in ambulatory measurement. Empirical models to estimate VO2Max from variables such as anthropometric parameters and heartrate (HR) are available, but they do not capture training-induced changes in VO2Max. Submaximal exercise tests such as the Cooper test provide a validated alternative, but they require specific conditions (e.g., fixed distance) and user interaction to input values into regression equations.

We propose a simple, automatic method to estimate VO2Max during running that only requires knowing the user's resting HR, maximum HR, and a measure of HR and speed during a run. The method is based on the linear dependence between HR and speed in running<sup>[1]</sup>. This relationship is depicted in Figure 1. The method expands on CSEM's previous work on VO2 estimation<sup>[2]</sup>.

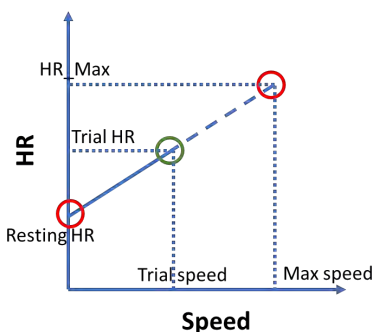


Figure 1. Relationship between speed and HR during running. The green circle represents the speed and HR obtained during a running trial.

The approach was validated on a dataset including 10 subjects (9 men and 1 woman), age range 30–49 years ( $35.40 \pm 6.47$  years), weight range 61–87 kg ( $73.80 \pm 7.71$  kg), and height range 1.64–1.95 meters ( $180.00 \pm 8.88$  cm). The subjects' fitness levels varied from poor to very good.

All subjects were asked to run on a treadmill at incremental preset speeds until exhaustion. Each speed was maintained for

[1] L. Léger, D. Mercier. Gross energy cost of horizontal treadmill and track running. Sports Med. 1984 Jul-Aug;1(4):270-7.

three minutes. HR was calculated from an ECG recording, speed was obtained from the treadmill, and VO2Max values were recorded using the Metamax spiroergometer (Cortex, Germany).

The proposed VO2Max estimation method is described as follows: when the user goes for a run, HR and speed values are recorded. Once a period of stable running (i.e., with low HR variability) is detected, the mean HR and speed are calculated (circle representing trial HR and speed on Figure 1) At the end of this step, maximum aerobic speed is calculated by extrapolating the line shown in Figure 1 to the maximum HR. VO2Max is then estimated from the maximum aerobic speed using a known relationship<sup>[1]</sup>.

The results (Figure 2) show that the VO2Max estimation error decreases as the users approach their maximum HR. Based on these results, a minimum ratio of 0.7 can be used to ensure a low-error estimation of VO2Max during a run.

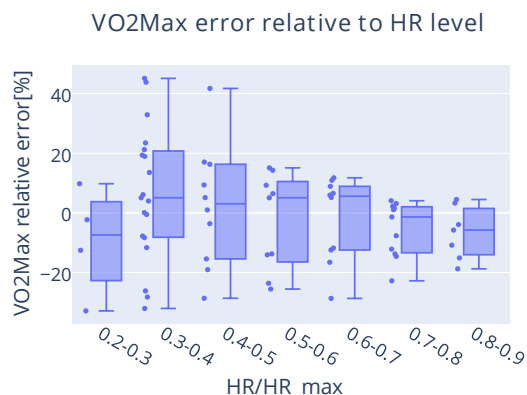


Figure 2. Boxplots of relative VO2Max estimation error as a function of the user's HR/HR<sub>max</sub> ratio.

The main limitations of the study are: 1) the protocol was performed indoors on a treadmill, thus not reflecting real-life running, and 2) each speed was held for 3 min, which might be a bit too short to achieve steady-state HR.

The advantages of the proposed method are: 1) it can be used with any device or system measuring speed and HR during running, 2) it is automatic and can be used in real time, embedded systems or in a backend/cloud, 3) it can capture changes in VO2Max induced by training improvements, and 4) the users only need to input their age (or maximum HR, if known).

Subsequent validations with a higher number of subjects and outdoor conditions are foreseen. The algorithm has a low memory cost and computational footprint and is therefore embeddable into any wearable device.

[2] C. Manzoni, A. Carrard, E. Fontana, M. Lemay, M. Bertschi, R. Delgado-Gonzalo. Towards VO<sub>2</sub> monitoring: Validation of a heart rate based algorithm. EMBC 2017.

# Measurement Location Influences Reflectance Pulse Oximetry During Sleep

F. Braun, G. Bonnier, P. Theurillat, M. Proen  a, Y.-M. Proust, F. Baty<sup>\*</sup>, M. Boesch<sup>\*</sup>, S. Annaheim<sup>\*\*</sup>, M. Brutsche<sup>\*</sup>, D. Ferrario, M. Lemay

*Peripheral oxygen saturation ( $SpO_2$ ) plays a key role in diagnosing sleep apnea (SA).  $SpO_2$  is mainly measured via transmission pulse oximetry at the fingertip, an approach poorly suited for long-term monitoring over several nights. In view of a more patient-friendly solution, we evaluated the accuracy of a proprietary watch-like device that measures  $SpO_2$  via reflectance pulse oximetry in a cohort of 9 patients with suspected SA. Two measurement locations were investigated: the upper arm and the wrist. The upper arm provided more robust and accurate  $SpO_2$  estimates than the wrist. These findings suggest that the upper-arm location is optimal for an unobtrusive and long-term SA detector using reflectance pulse oximetry.*

Sleep apnea (SA) has a high prevalence in the general population<sup>[1]</sup>, is associated with arterial hypertension, and contributes to the development of cerebral and cardiovascular comorbidities. The measurement of peripheral oxygen saturation ( $SpO_2$ ) via pulse oximetry is crucial for the detection and diagnosis of SA. However, state-of-the-art  $SpO_2$  sensors at the fingertip are not well suited for the long-term monitoring over several nights which is crucial to capture night-to-night variations and provide a correct diagnosis of SA<sup>[2]</sup>. In view of less obtrusive SA monitoring, we have evaluated our proprietary reflectance pulse oximeter (see Figure 1) at two body locations (wrist vs. upper arm) and compared to fingertip  $SpO_2$  in SA patients.



Figure 1: CSEM proprietary watch-like reflectance pulse oximeter device.

Our study (BASEC Nr. 2019-00450) was conducted at the sleep laboratory of the Cantonal Hospital St. Gallen (Switzerland) on 9 patients with suspected SA. Each participant underwent a full overnight polysomnography (PSG) recording, including  $SpO_2$  reference measurements via a fingertip sensor. In parallel, each patient wore two watch-like reflectance pulse oximeter devices, one at the wrist, and the other at the upper arm. The three  $SpO_2$  devices (2 watch-like devices at wrist and upper arm, 1 reference at fingertip) were placed on the same arm. The data were processed with CSEM's algorithm<sup>[3]</sup> providing  $SpO_2$  estimates together with a quality index (QI) indicating the reliability of the corresponding estimates. Unreliable  $SpO_2$  estimates with a QI below 75% were automatically rejected from analysis. This threshold represents the best trade-off between a high acceptance rate and a low  $A_{RMS}$  error.  $SpO_2$  estimates ( $SpO_2_{Est}$ ) were compared to fingertip  $SpO_2$  reference measurements ( $SpO_2_{Ref}$ ) using the amplitude of the root-mean-square error ( $A_{RMS}$ ) as recommended by ISO 80601-2-61:2017 standard.

Recordings on 9 SA patients led to a total monitoring duration of 51 h. After the automatic rejection of unreliable data by our algorithm<sup>[3]</sup> a total of 38.1 h (75%) and 41.1 h (81%) of data were

available for analysis from the wrist and upper arm, respectively (Table 1). When compared with the gold-standard fingertip, our  $SpO_2$  estimations showed an error of  $A_{RMS} = 2.5\%$  at wrist vs.  $A_{RMS} = 1.8\%$  at upper arm (Table 1 and Figure 2). Even though both are compliant with ISO 80601-2-61:2017 standard and FDA guidance for reflectance type sensors (acceptance limit at 3.5%),  $SpO_2$  data acquired at the upper arm are of better quality than those from the wrist and lead to more accurate estimations.

When combined with other vital signs, an upper-arm-based  $SpO_2$  sensor can allow for an unobtrusive solution for long-term monitoring of SA, as well as other diseases involving respiratory symptoms.

Table 1: Performance of  $SpO_2$  estimations at wrist vs. upper arm.

Performance Metric	Wrist	Upper Arm
$SpO_2 A_{RMS}$ Error	2.5%	1.8%
Acceptance Rate	75%	81%
Data Duration	38.1 h	41.1 h

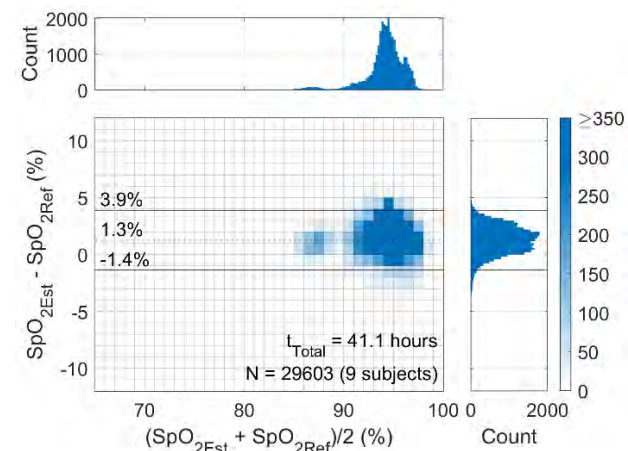


Figure 2: Bland-Altman analysis for  $SpO_2$  measured at the upper arm ( $SpO_2_{Est}$ ) compared to fingertip  $SpO_2$  ( $SpO_2_{Ref}$ ). The density of data points is highlighted using color-coded rectangles with their color saturation proportional to the number of data points (white: low density vs dark blue: high density, see color gradient bar). Less populated rectangles are emphasized by saturating the color scale at a superior threshold of 10% of the maximal number of data points of all rectangles.

- Cantonal Hospital St. Gallen, St. Gallen, Switzerland
  - Empa, St. Gallen, Switzerland
- [1] R. Heinzer, *et al.*, "Prevalence of sleep-disordered breathing in the general population: the HypnoLaus study". *The Lancet Respiratory Medicine*, 3(4), 310-318, 2015.

[2] L. Bittencourt, *et al.*, "The variability of the apnoea-hypopnoea index". *Journal of sleep research*, 10(3), 245-251, 2001.

[3] M. Proen  a, *et al.*, "Performance assessment of a dedicated reflectance pulse oximeter in a neonatal intensive care unit". In EMBC 2018, IEEE, 2018.

# Sleep Staging with Convolutional Recurrent Neural Networks

J. Van Zaen, F. Braun, P. Renevey, M. Lemay

The correct identification of sleep stages is of the utmost importance in the diagnosis of sleep disorders. The gold standard for sleep staging is polysomnography which is laborious and expensive as it requires several sensors and manual annotation by a trained specialist. To mitigate these issues, a neural network architecture was developed to classify sleep stages from a single photoplethysmogram signal. Such an architecture could be fed data collected with a wearable sensor allowing for the automatic and unobtrusive estimation of sleep stages over several nights in home settings.

Accurately identifying sleep stages is critical to diagnose sleep disorders. The current gold standard for this task is polysomnography (PSG) which records several signals over one night including electroencephalogram (EEG), electrocardiogram (ECG), electromyogram (EMG), respiratory airflow, and oxygen saturation via photoplethysmogram (PPG). These signals are then visually inspected by a trained specialist that annotates 30-second windows as wakefulness (WAKE), light sleep (N1 and N2), deep sleep (N3), or rapid-eye movement (REM). This approach has several drawbacks. First, PSG is expensive and time-consuming as it required specialized equipment and multiple trained professionals. Consequently, it is usually performed for a single night and often in a sleep laboratory which might not be representative of usual sleep patterns. It is also cumbersome for the subjects as they need to wear many sensors and electrodes during the night which might affect their sleep. Finally, since the data is annotated by visual inspection, annotations from different specialists can significantly differ.

To alleviate the issues of PSG, several approaches that combine a reduced set of sensors with machine learning have been proposed. A recent study<sup>[1]</sup> used a neural network to classify sleep stages from a single PPG signal. This network combines convolutional layers to automatically extract high-level features from the input signal and recurrent layers to consider time dependencies across 30-second windows. Using only PPG data enables cost-efficient, long-term monitoring of sleep.

In this work, a new neural network architecture is derived from the abovementioned study<sup>[1]</sup> and applied to the MESA dataset<sup>[2,3]</sup> which comprises 1698 PSG records. Each record includes a PPG signal recorded at the finger with a sampling frequency of 256 Hz and is annotated over 30-second windows with the five sleep stages (WAKE, N1, N2, N3, or REM). The dataset was split into three subsets: 60% for training ( $n = 1018$ ), 20% for validation ( $n = 340$ ), and 20% for testing ( $n = 340$ ). To prepare the data for training, the PPG signals were resampled at 64 Hz, filtered with a high-pass filter with a cut-off at 0.1 Hz, and scaled by the standard deviation estimated over the training subset. The proposed architecture takes 100 30-seconds windows of PPG data as input and yields the estimated sleep stage for each window as output. It is divided in three parts: a convolutional part to extract features, a recurrent part to consider dependencies

between successive windows, and a fully connected part for classification. The first part consists of six convolutional layers with max pooling followed by a global average pooling layer. The second part is composed of two bidirectional gated recurrent unit (GRU) layers. Finally, the third part includes two fully connected layers for classification. The network parameters were trained by minimizing the categorical cross-entropy with the Adam optimizer and an initial learning rate of 0.001. The learning rate was divided by two if the loss on the validation subsets did not decrease for five consecutive epochs. To limit overfitting, Gaussian dropout before and regular dropout after the recurrent layers.

The performance of the neural network was evaluated in terms of overall accuracy for 3, 4, and 5 classes:

- 3 classes: WAKE, NREM (N1, N2, and N3), REM
- 4 classes: WAKE, LIGHT (N1 and N2), DEEP (N3), REM
- 5 classes: WAKE, N1, N2, N3, REM

The accuracy values for the training, validation, and test subsets are reported in Table 1. There was some overfitting as shown by the difference between the training subset and the validation and test subsets. Dropout seems insufficient and additional regularization might help to bridge the gap between training and validation performance. However, the values obtained on the validation subset are close to the ones obtained on unseen data.

Table 1: Accuracy metrics.

Subset	3-class accuracy	4-class accuracy	5-class accuracy
Training	91.3%	86.3%	81.2%
Validation	86.7%	80.8%	76.1%
Test	76.1%	80.8%	75.7%

These results suggest that reliable automatic sleep staging with a single PPG signal is possible. This could pave the way towards the unobtrusive and long-term sleep monitoring using wearables.

<sup>[1]</sup> H. Korkalainen, J. Aakko, B. Duce, S. Kainulainen, A. Leino, S. Nikkinen, I. O. Afara, S. Myllymaa, J. Töyräs, T. Leppänen, "Deep learning enables sleep staging from photoplethysmogram for patients with suspected sleep apnea," *Sleep* 43 (2020).

<sup>[2]</sup> X. Chen, R. Wang, P. Zee, P. L. Lutsey, S. Javaheri, C. Alcántara, C. L. Jackson, M. A. Williams, S. Redline, "Racial/ethnic differences in sleep disturbances: the multi-ethnic study of atherosclerosis (MESA)", *Sleep* 38 (2015) 877.

<sup>[3]</sup> G. Q. Zhang, L. Cui, R. Mueller, S. Tao, M. Kim, M. Rueschman, S. Mariani, D. Mobley, S. Redline, "The National Sleep Research Resource: towards a sleep data commons", *J. Am. Med. Inform. Assoc.* 25 (2018) 1351.

# Miniature ECG Cooperative Sensors for Daily Monitoring

A. Fivaz, O. Chételat, N. Bonzon, K. Badami, M. Pons Solé, M. Crettaz, J. Wacker, S. Emery

Daily monitoring of electrocardiogram (ECG) at home, to be accessible to most people, sets many additional constraints to basic technical requirements such as user comfort, easy handling and setup. The solution described in this paper focuses on cooperative sensors that meet these needs by interconnecting miniature active electrodes with a single electrical connection, reaching a level of integration enabling creative designs of wearables with novel ergonomic and fashion opportunities.

Medical instrumentation for bio-potentials and bio-impedances has been for long built on the use of gel electrodes. Nowadays, active dry electrodes, i.e., embedding an electronic circuit, can outperform gel electrodes<sup>[1]</sup> but require to be powered. This simple requirement adds complexity and stiffness to an already cumbersome arrangement of bulky cabling, each electrode being attached to the central recorder by its own cable. Another solution is a battery at each electrode, which is undesired for many reasons, e.g., maintenance of the system, cost, weight, etc.

One feature of the prototype designed at CSEM to address long term ECG monitoring is to allow the health practitioner to freely position the ECG electrodes in a garment at the desired position without having to explicitly connect them by cables. As depicted in Figure 1, the system includes a recording device and several cooperative sensors as active dry electrodes. Each sensor has a pair of stainless-steel electrodes and embeds an ASIC (Application Specific Integrated Circuit) that has been designed at CSEM to lower the dimensions and the power consumption. The ASIC harvests power for the cooperative sensors and synchronizes the transmission of ECG signals through the body. This ECG belt was assembled using an electrically conductive textile on which four measuring sensors were fixed. The green, blue, and red active electrodes (seen from top) as well as a yellow one seen from below in Figure 1 are connected together by the textile, while the reference and guard electrodes (in black) are directly connected to the recorder.

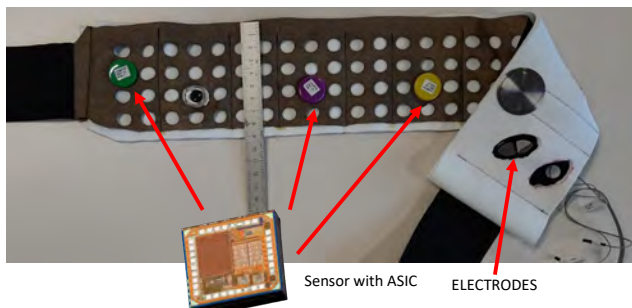


Figure 1: ECG belt with free positioning of active electrodes (cooperative sensors), mock-up of textile with electrically conductive top layer, and a ruler for size evaluation.

Figure 2 better illustrates the interconnection concept. All cooperative sensors and the recorder are connected to the same electrical connection. Each cooperative sensor and the master are connected to the body via two stainless-steel electrodes.

The recorder includes the battery to power all cooperative sensors. In addition, it also includes Bluetooth Low Energy wireless communication and a USB link to a computer.

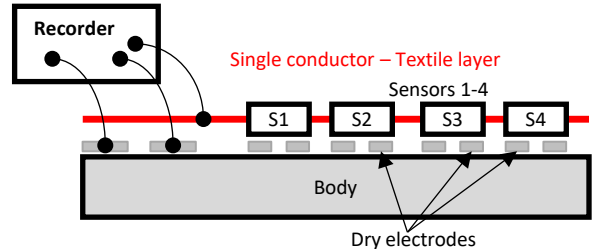


Figure 2: Interconnections between recorder, textile, and sensors.

An example of recorded signals is shown in Figure 3. The prototype was verified according to the IEC 60601-2-47 standard for ambulatory ECG systems and in its current version has a noise of 51  $\mu\text{V}$  pp, closely approaching the standard requirement of 50  $\mu\text{V}$  pp. Therefore, the prototype indicates that sufficiently low noise can be reached with the dry-electrode cooperative-sensor approach despite that the powering and measurement functions are shared by the same conductive textile.

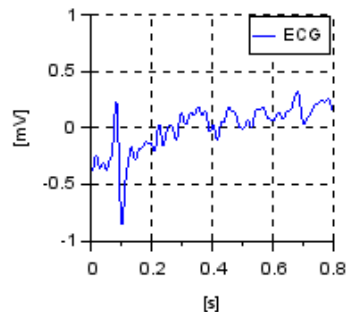


Figure 3: ECG signal measured on a subject.

Further noise optimization can be done by improving the filtering and lowering the flicker noise corner as shown in Figure 4.

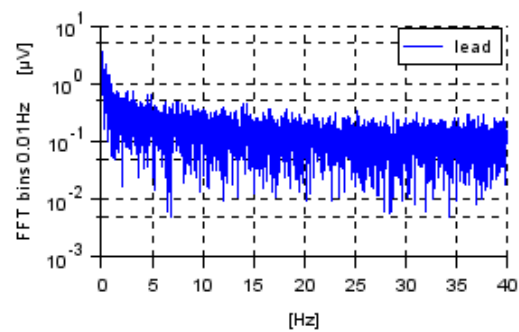


Figure 4: Noise spectrum in the ECG bandwidth.

This activity follows a set of achievements progressively obtained at CSEM with its patented cooperative-sensor technology that drastically simplifies the connecting complexity of devices acquiring biopotential signals with dry electrodes in wearables.

<sup>[1]</sup> O. Chételat, et al., 'Standalone dry electrode-sensors for multilead ECG monitoring in mobile patients', in 2014 8th Conference of the European Study Group on Cardiovascular Oscillations (ESGCO), Trento, Italy, May 2014, pp. 27–28. doi: 10.1109/ESGCO.2014.6847502.

# ULTEEM—Ultra-long-term EEG Monitoring

G. Yilmaz, M. Crettaz, L. Zhou, J. A. Lahera Perez, M. Frosio, A. M. de Sousa, O. Chételat, K. Schindler\*

*ULTEEM project showcases a sensor solution which transforms ordinary eyeglasses into smart glasses, by simply clipping two stand-alone devices onto the frame, to non-invasively record the brain activity generated by the temporal lobes. Temporal electroencephalogram (EEG) provides valuable information for long-term generalized epilepsy monitoring while electrooculogram (EOG) signals are commonly used in vigilance monitoring.*

Electroencephalography (EEG) is an electrophysiological monitoring method that is used to characterize the type of epilepsy syndrome and epilepsy seizures. A subset of these seizures, namely primary generalized seizures, is characterized by the bi-hemispheric simultaneous onset of epileptiform signals. Clinically they typically involve sudden impairment of consciousness. As patients often do not realize or remember that they had a seizure, the treating physician is faced with incomplete or inaccurate information. Reliable long-term monitoring of these seizures by EEG is therefore expected to significantly improve the personalized treatment of epilepsy patients by providing objective information about the individual pattern of seizure occurrence.

Patient compliance is the key factor for success to achieve reliable long-term EEG monitoring. In the context of epilepsy patients, who suffer a lot from social stigmatization, it is essential to provide an inconspicuous solution to ensure patient adherence (Figure 1). Today, neither bulky multi-channel EEG devices nor consumer-grade EEG headbands found in the market satisfy this demand. The project ULTEEM [1] sets out to address this unmet medical need by placing the patient and their comfort in the center of the solution. The proof-of-concept device (Figure 2) comprises two dry-electrode sensors that can be clipped onto the metallic frame of eyeglasses. Such a solution is only possible thanks to the unique technology of CSEM (EP2101408) allowing the connection of sensors using a single wire which does not need to be shielded nor insulated. Although the connection is simplified, the signal quality is not compromised. This feature differentiates the ULTEEM device from consumer-grade EEG solutions, providing the clinicians with a signal quality obtained with dry electrodes equivalent to clinical-grade EEG devices with gel/wetted electrodes. Applicable medical device standards (IEC 60601-1 and IEC 80601-2-26) were followed during the design and verification phases of the development.



Figure 1: ULTEEM device provides an inconspicuous solution to boost patient adherence, a key success factor for long-term EEG monitoring.

Using dry electrodes, ULTEEM device acquires 1-lead EEG between two temporal lobes. The sensors are powered by a rechargeable battery and communicate with portable devices via Bluetooth Low Energy, which allows recording and real-time visualization of the data.

The pilot study of the device was performed at NeuroTec [2] with 10 healthy volunteers (KEK Bern No 2020-01979). The objectives of the evaluation were to assess the usability of the ULTEEM device in clinical settings as well as benchmark the performance of the device with certified EEG devices used for clinical purposes. For each subject, brain signals were recorded simultaneously for 20 minutes with a certified EEG device using gel electrodes and with ULTEEM using stainless steel dry electrodes. Both signals were compared by an experienced neurologist from Sleep-Wake-Epilepsy Center (Inselspital, Bern) who concluded that measurements acquired by the ULTEEM device matches well with the measurements obtained with the reference device. Moreover, similarity analysis was performed between the two waveforms using Pearson's correlation coefficient. For the cases where the subjects were instructed to perform lateral eye movements, a very strong correlation was observed (Pearson's  $r > 0.97$ ). In the cases where the subjects were recorded still, similarly to clinical examination, a strong correlation was observed (Pearson's  $r > 0.80$ ). All the 10 subjects who participated in the study expressed that it was comfortable to wear the ULTEEM device and they did not develop any headaches or discomfort during and after the recordings.

In conclusion, by simply clipping the ULTEEM device onto ordinary eyeglasses, EEG signals comparable to clinical grade could be obtained in the absence of an explicit wired connection. This patient-centric solution holds great promise to address the unmet need for reliable long-term EEG monitoring, and thus to improve the personalized treatment of epilepsy patients. The outlook is to combine the ULTEEM device with a new form factor suitable for night-use to achieve 24/7 monitoring.



Figure 2: ULTEEM device clipped on eyeglasses with metallic frames.

This work was partly funded by European Space Agency (ESA). CSEM is thankful for their support.

\* Sleep-Wake-Epilepsy Center & NeuroTec, Inselspital, Bern

[1] <https://www.csem.ch/page.aspx?pid=161359>

[2] <https://www.neuro-tec.ch/projects/>

# Secure Ultra-long-term Ambulatory Monitoring of Subscalp EEG for Epilepsy Management

G. Banderet, M. Correvon, M. Crettaz, A. Falhi, R. Delgado-Gonzalo, P. Heck, J.-A. Porchet, R. Rusconi, E. Chanie •, G. Kouvas •

*Long-term brain activity monitoring could dramatically improve diagnosis and treatment of neuro-disorders, but there is currently no system capable of recording brain activity over months and years. One of the most prevalent chronic neurological disorders is epilepsy, which affects ~65 million people worldwide. Epilepsy is characterized by recurrent seizures generated by run-away neuronal excitation that causes a wide spectrum of clinical signs and symptoms. Identification of digital biomarkers through long-term brain monitoring with Epios is a first step towards personalized treatment and tailored therapies.*

The Epios system is being developed as an implantable 32-channel EEG Class-III medical device at the Wyss Center for Bio- and Neuro-engineering in collaboration with CSEM's ISO13485 certified Digital Health research activity.

The Epios system comprises a series of thin leads incorporating sensing electrodes and a miniature implant, inserted underneath the skin (Figure 1) behind the ear. The neural signals are wirelessly transmitted to an external receiver located over the implant and attached on the skin with a magnet. From there, the signals are relayed to a wearable data processor (Figure 2) and finally securely transmitted and stored in the Epios cloud – a data storage, analysis, and visualization software platform – via a docking station.

CSEM collaborated with the Wyss Center on the development of the wearable data processor integrated in a wearable textile 1-lead ECG harness and the docking station that provides a secure connectivity to the Epios cloud.

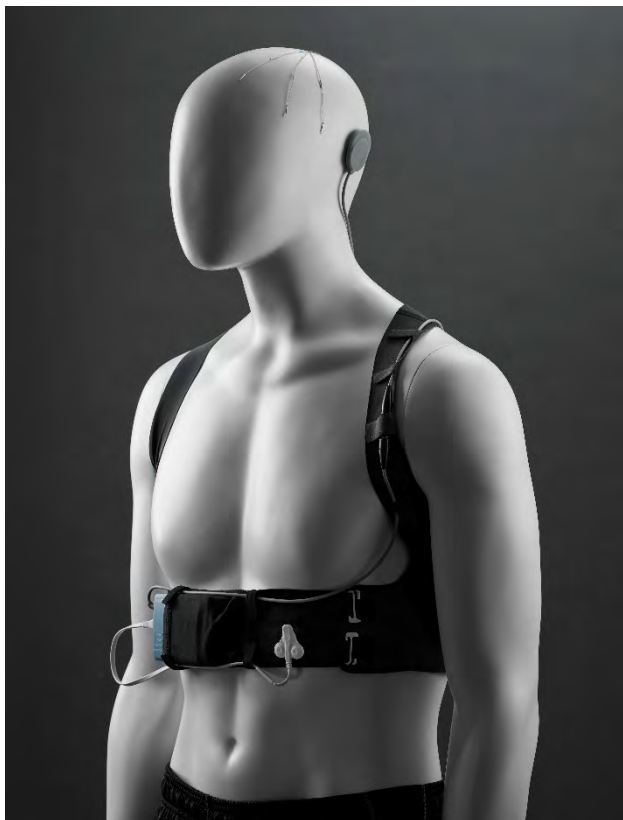


Figure 1: Epios wearable system including EEG subscalp electrodes (visible in the illustration above, but, in reality, between scull and scalp), transcutaneous wireless transmitter and receiver, and a harness integrating a wearable data processor and a 1-lead ECG belt.

The wearable data processor provides long-term recordings of biosignals over months while connected to the cloud by using two exchangeable wearable data processors. This enables remote access, retrieval, and review of the data by medical experts. The data processor also acquires non-EEG biosignals that have been shown to correlate with epileptic events, such as heartrate, vocalizations (ictal cries), spasms, and jerking.

CSEM focused its efforts on the miniaturization and ultra-low-power consumption of the data processor to achieve the longest possible autonomy. The second big challenge was the design of a secure and privacy preserving transmission channel based on advanced authentication and encryption mechanisms to transfer large quantities of sensitive data to the Epios cloud.



Figure 2: Wearable data processor recording 32 channel EEG, 1-lead ECG, surrounding sound, accelerometry, and patient induced events developed by CSEM according to its ISO13485-certified quality system for class-III medical devices.

The Epios cloud allows remote data access and provides a web interface for data visualization and analytics. A security solution to ensure the confidentiality, integrity, and non-repudiation of collected data was developed to ensure a secure transfer from the data processor to the cloud.

The first indication of the Epios system is epilepsy, but the Epios platform could have multiple potential indications that require real-time, long-term monitoring of brain activity. These include movement restoration for people with spinal cord injury and stroke, as well as Parkinson's disease, sleep disorders or pain management. This development is paving the way to enable long-term monitoring of brain activity, rendering it poised for future diagnostic and therapeutic applications in many neuro-disorders.

• The Wyss Center for Bio- and Neuro-Engineering, Geneva, Switzerland

# Collaborative Privacy-Preserving Training of Decision Trees

Y. El-Zein, R. Delgado-Gonzalo, K. Huguenin\*

As data generation becomes more ubiquitous, datasets are increasingly spread across several entities. Exploiting such distributed datasets simultaneously, by training machine learning models on them, can be beneficial to many fields, but also raises serious privacy concerns. In this work, a scalable protocol is designed, implemented, and evaluated, for training decision tree models collaboratively across mutually distrustful data providers, while ensuring privacy of each of the stakeholders' data.

Training accurate and robust machine learning (ML) models requires access to large datasets. Often, subsets of records of these datasets are held by different data providers (DPs). Due to privacy concerns and regulations, these records cannot always be shared among DPs, nor centralized in one common location, hindering the training of ML models on them. Privacy-preserving ML, more particularly federated learning, has emerged as a solution to this problem. However, federated learning solutions are mainly geared towards the training of neural network models. In this work, the focus is turned to privacy-preserving training of decision tree models. Contrary to neural networks, decision trees have the advantage of being interpretable white-box models. In domains such as medicine or finance, where every decision must be supported by a clear rationale, model interpretability is of utmost importance. To this end, a scalable protocol is designed, implemented, and evaluated for training decision tree models in a collaborative manner across different DPs, while maintaining the privacy of their data records.

In our implementation,  $N$  data providers are considered, each holding a subset of a horizontally partitioned dataset, whereby each DP holds a different set of records (of comparable size), with the same attributes as the others. Their goal is to collaboratively train a decision tree model that benefits from their joint data records, without disclosing the latter to each other. The training protocol also calls for a central coordinator (CC), who orchestrates the training process without contributing any data to training the model. In terms of threat model, we consider all involved entities to be honest-but-curious. An overview of the considered system model is given in Figure 1.

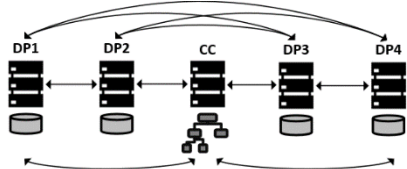


Figure 1: Overview of the different entities of the considered system model, and the different communication channels between them.

The protocol is designed to fit the following requirements. (1) The raw data of any DP is never shared with nor leaked to any other entity. (2) None of the exchanged messages between entities should leak information about the data distribution of a data provider's private dataset. The protocol is composed of two phases: the pre-processing phase and the training phase.

The goal of the pre-processing phase is to privately determine the optimal depth of the tree. Briefly, each DP computes, on their

local private dataset, the optimal tree depth and engages with the other DPs in an additive secret sharing subprotocol to compute the optimal tree depth. Following the pre-processing phase, the goal of the training phase is to select the best attribute to further split a given node in the decision tree. Each DP computes locally the information gain associated with the different attributes in their dataset and selects the best attribute for splitting the node accordingly. If the attribute is continuous, a numerical threshold for splitting is also computed by each DP. Using a proposed adapted variation of additive secret sharing, the attribute selected by most DPs is obtained and used to further split the node, without revealing the preferred attribute of individual DPs.

The protocol was implemented in Python and evaluated on 3 public datasets from the UCI (University of California, Irvine) machine learning repository [1]. It achieves privacy with a modest loss in accuracy compared to the privacy-breaching model, trained on all the data records centralized in one location, and consistently produces a decision tree model with better accuracy than the local models, trained separately by each DP. Figure 2 summarizes the model accuracy results.

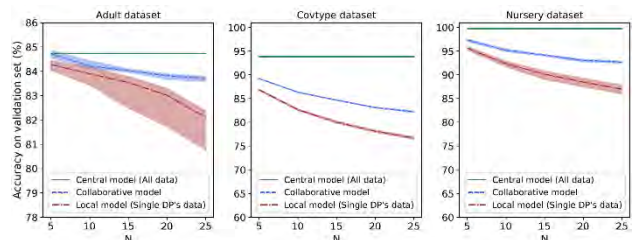


Figure 2: Accuracy of model trained on three datasets using the proposed protocol, compared to centralized and local models' accuracy.

Moreover, compared to existing solutions, the protocol is efficient in terms of communication and computation costs. For instance, training on one dataset, composed of 30'162 data records and 14 attributes, across 4 DPs each running on an AMD 2950X CPU at 3.5 GHz and using 128 GB of RAM, generates only 331.44 MB of exchanged messages, and requires 141.39 seconds of training time, including both CPU and communication time. This is an estimated 63 $\times$  speedup compared to the current state of the art for collaborative training of decision trees [2].

The presented work showcases an alternative to centralized training, that is privacy-aware, in the context of white-box models. The proposed architecture is scalable and easy to deploy, which can accelerate the introduction of ML into heavily regulated sectors (e.g., healthcare), where the data is considered extremely sensitive due to its nature.

\* University of Lausanne, Switzerland

[1] D. Dua, C. Graff, "UCI Machine Learning Repository", University of California, School of Information and Computer Science (2017) [<http://archive.ics.uci.edu/ml>]

[2] M. Abspoel, D. Escudero, N. Volgshev, "Secure training of decision trees with continuous attributes", Proceedings on Privacy Enhancing Technologies (2021).

# Improving Cockpit Safety through Real-Time Monitoring of Pilots with a Smart Vision System

S. Saeedi, E. Türetken, S. A. Bigdeli, P. Stadelmann, L. von Allmen, L. A. Dunbar

*Enhancing safety is a key target in transportation. Here we present how artificial intelligence can participate in increased safety for the next-generation cockpits. At CSEM, we developed a smart, real time at 60 frames per second, robust vision system for integration in airplane cockpits and cars to detect drowsiness-related features.*

Human fatigue is a serious issue affecting the safety of the traveling public in all modes of transportation. Nearly 20 percent of major US Transportation Safety Board investigations completed between 2001 and 2012 identified fatigue as a probable cause, contributing factor, or a finding<sup>[1]</sup>. There is evidence that fatigue reduces the capacity for situational awareness, impairs decision making and slows down reaction time.

The automotive industry is being legislated to install driver monitoring systems for the detection of drowsiness and distraction<sup>[2]</sup>. In the safety pioneering aviation sector, crew monitoring is seen as key to maintaining safety in case of incapacitation, stress, or exhaustion of crew members and in reduced crew operations. For any monitoring systems to be successfully adopted, an extremely high level of accuracy and robustness is required.

At CSEM, we are developing an intelligent vision system for the next generation aircrafts in the framework of the Clean Sky-sponsored project HIPNOSIS<sup>[3]</sup>. The goal of this tailor-made system is to monitor the pilots in the cockpit and to detect signs of drowsiness in real time to enhance fatigue-related safety.

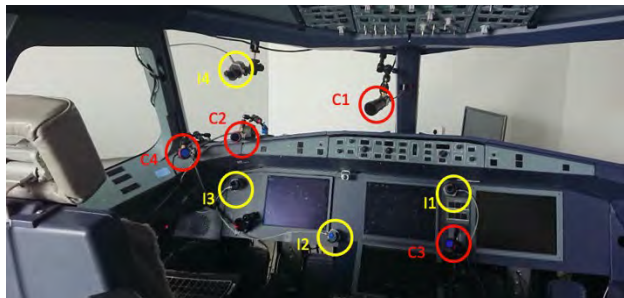


Figure 1: The HIPNOSIS vision system installed in a cockpit simulator, including 4 cameras (red outline) and 4 illuminators (yellow outline).

When designing a system for real-time operation in the cockpit, specific challenges and requirements in the aeronautics context should be addressed. For example, large field of view, the need for monitoring pilots at different seat positions and the necessity for high level of speed, accuracy, and robustness in various and extreme lighting conditions. CSEM, in collaboration with avionics experts, have designed and built a smart vision system for use in the cockpit. The multi-camera system includes 4 cameras and 4

illuminators (Figure 1), ensuring the face of the pilot to be covered during normal flight operations. Computer vision and machine learning algorithms detect behavioral features linked to drowsiness, such as percentage of eye closure (PERCLOS), blink duration, blink rate, 3D head pose, and pupil size.

The algorithmic pipeline for the detection of the mentioned behavioral features includes both data-driven and analytics approaches. To address the speed and accuracy requirements, resource-efficient algorithms for face detection and facial landmark localization were developed. The designed multi-camera system is calibrated and therefore allows for the facial features (the eyelids, eyebrows, mouth, and nose) to be accurately localized in 3D with an error less than 2 mm. Figure 2 shows the results of face detection and the 28 localized facial landmarks in one of the camera views.



Figure 2: Detection of face, facial features, iris and pupil using the HIPNOSIS vision system algorithms.

The remaining algorithms for the detection of blink information and eye closure, as well as the estimation of head pose were also developed. A model was trained to detect the iris, and a combination of classical data analytics and machine learning was used to accurately detect the pupil. These behavioral features provide insight into pilot cognitive states, such as fatigue.

The algorithmic pipeline is optimized for speed using a multi-threading software architecture. It runs in real time at 60 frames per second and provides the mentioned features with a latency of 32 ms. This is in line with the requirements identified for the pilot monitoring system.

Future directions for adopting such a vision system for monitoring drowsiness-related features would be in automotive context as well as medical applications.

[1] <https://www.ntsb.gov/Advocacy/mwl/Pages/mwl1-2016.aspx>

[2] Regulation (EU) 2019/2144 of the European Parliament and of the Council of 27 November 2019 on type-approval requirements for motor vehicles.

[3] This project has received funding from the Clean Sky 2 Joint Undertaking under the European Union's Horizon 2020 research and innovation program under grant agreement No. 821466.



# Live Analysis of Grains Morphology and Flowing Speed

N. Cantale, P. Pad, S. Blanc, C. Kündig, X. Zhou, M. Crettaz, E. Türetken

An industrial 4.0 vision system for the measurement of grain flow speed and their morphologies in milling machines was developed together with Bühler AG. Multiple algorithms were developed and embedded into the sensor, including displacement measurement, grain type detection, grain segmentation and grain shape analysis.

The high-precision quantitative and qualitative monitoring of grains moving through milling installation is a field in full development, due to its potential impact on an otherwise low profit industry. The current equipment uses flow balancers that regulate the flowing mass using load cells connected to impact plates on which the grains fall. However, such force measurements are imprecise at low speed when they are subject to vibrations and non-linearities. Moreover, these machines are unable to perform advanced measurement such as morphology analysis or other quality assessments.

In 2019 Bühler AG started a project with CSEM, its primary goal was to develop a compact low-cost smart vision system that can be placed on existing milling machines at Bühler to measure the flow speed and key morphological characteristics of flowing grains.



Figure 1: Prototype, during the commissioning at Bühler's facilities.

The project had two phases. The first phase consisted of a feasibility study during which a first prototype was designed and a test installation with a flow balancer and reference scales were built, for data acquisition with reference measurements. Following a data acquisition campaign involving several cereal types and multiple speeds, the feasibility was validated by estimating volumetric flow speed based on the prototype output. A very precise calibration considering all the deformations in the optical path (tube window, protection window, camera lens, perspective compensation, etc.) was developed and allowed the measurement of grain displacements lower than 40 microns for speed up to 2 m/s.

The second phase was dedicated to the development of grain detection, grain segmentation and shape analysis algorithms, based on the data collected from the first prototype. The grain identification is made through the color analysis of the grains in the image, each cereal types giving different signatures in the

hue, saturation and value (HSV) space. The grain segmentation is performed by a convolutional neural network, trained using weakly supervised learning. Indeed, a very small number of annotated images could be used, (e.g., only one image for the rice), which was sufficient due to smart data augmentation techniques and to the repetitive nature of the grains. The shape analysis was then performed by fitting ellipses on the individual grain masks and extracting the major and minor axis for statistics.

A second prototype embarking those algorithms was developed from learning of the first prototype and including all the processing and communication facilities needed. A complex illumination setup was designed and assembled; two rows of LEDs ensured a sufficiently homogenous illumination. The LEDs and camera are driven by a custom control board, that also distributes the power to the whole system. The computational capabilities are assumed by a Jetson Nano, which also hosts the graphical user interface, accessible through a web page. The prototype is designed to be easily installed on several tube diameters at any location of the facilities, with specific window adapters and a single power cable, the only outbound connection. This prototype was successfully commissioned by Bühler on a new test installation reproducing industrial conditions (up to 100 t/h).

The result of the project is a  $30 \times 20 \times 15$  cm device easily plugged on tube windows to perform flow speed measurements with an accuracy of 0.5%, down from 3%, and the statistical analysis of the shapes of 30 to 60 grains/s (for rice and wheat) or 15 to 30 grains/s (for corn). The device also hosts a web application accessible through WiFi by any browser. The final bill of material (excluding housing) of the device was maintained below 600 CHF.

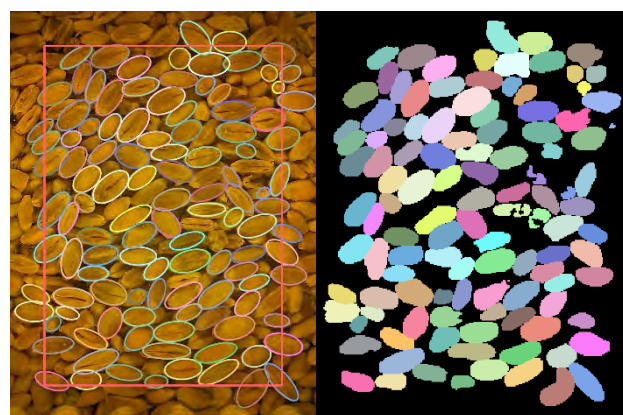


Figure 2: Example of instance segmentation that can be performed by the deep learning algorithm on wheat grains.

# Data Augmentation for Machine Learning Based Multi-illumination Defect Detection

D. Honzátko, E. Türetken, S. A. Bigdeli, L. A. Dunbar, P. Fua\*

*Detecting surface defects under different illumination angles using machine learning is a well-known approach in quality control systems. CSEM investigated increasing the number of illumination angles and then devised a novel data augmentation strategy; this significantly improves the defect detection performance and hence expands the possible automated quality control use cases.*

Automated visual inspection is a key element in both mass and high-end consumer product production. Existing systems often struggle with detecting defects on complex surfaces. One reason for this is that defects are only visible under specific illumination conditions. At CSEM we have introduced a system that inspects parts under several illumination angles, thus highlighting the illusive defects allowing automatic quality assessment.

Most techniques for surface defect detection use a small set of illuminations, often just three. We have conducted a study on the number of illuminations for different types of metallic watch parts – screws, gears, and washers. We have trained a machine-learning algorithm for each illumination configuration to segment out the defects. The results are pictured in Figure 1, they show a significant improvement in defect segmentation performance when increasing the number of illumination angles from 2 to 24.

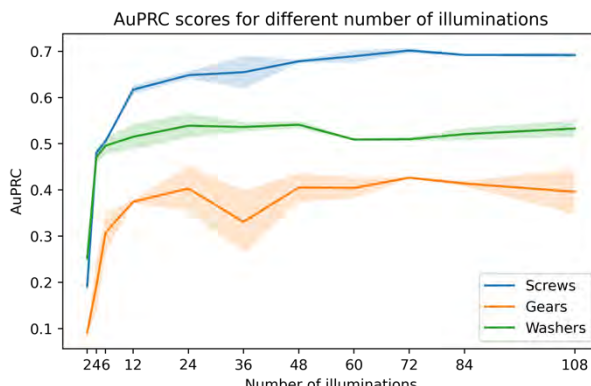


Figure 1: Defect segmentation performance measured as the area under the precision-recall curve (AuPRC), for a different number of illumination angles. 2 - 12 illumination angles share the same elevation, each additional 12 are placed under slightly lower elevation.

The increase in the performance with the higher number of illumination angles is principally caused by two factors. First, some defects are only visible under a very narrow range of illumination angles; more angles thus reveal more defects. Second, as we show further in the text, more illumination angles allow us to artificially generate more training data, which then improves the generalization of the machine learning algorithm.

We generate the data using the novel augmentation technique, which we call *illumination-preserving rotations*. It exploits the fact that by rotating the samples, we are effectively enriching the training dataset with new data. However, standard random rotations do not preserve illumination directions bound to the images. On the contrary, illumination-preserving rotations rotate the image only by multiples of the azimuth difference between two adjacent illumination directions and reshuffles the images

afterward so that the relative angles of illumination with regard to the image coordinates are preserved. An example of a 60° illumination-preserving rotation is depicted in Figure 2.

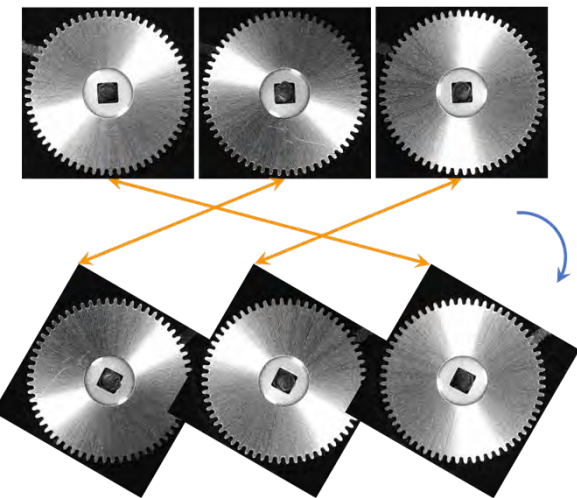


Figure 2: Illumination-preserving rotations for three illumination angles. Images are rotated and then shuffled such that the illumination angle with regard to the image coordinates is preserved.

To show the effect of the illumination-preserving rotations, we trained a defect segmentation algorithm with 24 illuminations with four distinct augmentation strategies: with no rotation-based augmentation, with arbitrary random rotations, with random 30° rotations, and with 30° illumination-preserving rotations. The results in Table 1 show that the illumination-preserving rotations significantly improve the defect segmentation performance irrespective of the dataset used. Conversely, arbitrarily random rotations can even deteriorate the performance as they degrade the samples with interpolation-related artifacts.

Table 1: Defect segmentation performance, measured as the AuPRC score, for 4 different augmentation strategies and 3 different datasets.

Dataset	Rotation-based augmentation strategy			
	None	Random	30°	Illumination pres.
Gears	0.28	0.20	0.27	0.40
Washers	0.29	0.39	0.50	0.54
Screws	0.30	0.25	0.54	0.65

The augmentation technique introduced together with the increased number of illumination angles brings a tangible boost in the performance of the automatic surface defect detection systems and may play a crucial role when moving from human-expert inspection towards the fully automated solution.25TP [1].

\* EPFL, Ecole Polytechnique Fédérale de Lausanne, Switzerland

[1] D. Honzátko, et al., "Defect segmentation for multi-illumination quality control systems. Machine vision and applications", Machine Vision and Applications 32, 118 (2021). <https://doi.org/10.1007/s00138-021-01244-z>

# Optical Neural Network for an Ultra-secure Vision System

Y. Sepehri, P. Pad, P. Frossard<sup>\*</sup>, L. A. Dunbar

*Preserving the privacy of users is an important issue in vision systems. For the first time, an AI-based privacy-preserving vision system is proposed which removes the sensitive content of users in the optical domain, before it even reaches the camera sensor. It is done without significantly affecting the performance of the target task. The proposed method is beneficial for feedback systems for smart TV content providers or outdoor广告ings, by measuring the users' satisfaction without threatening their privacy and identity.*

Deep Neural Networks have shown a state-of-the-art accuracy for a variety of vision tasks such as classification and facial recognition. Usually in such tasks, the user needs to load a standard image in a digital device which runs the relevant neural network. Preserving privacy in such systems is difficult as the images are rich in sensitive information and loading private images into the digital domain expose data to attacks. In most business cases, this sensitive information may not be needed to provide value. For example, to perform a facial detection task such as smile recognition or eye-gaze estimation, a high amount of information related to the person's identity or gender is loaded onto the digital device while it is irrelevant to the target task. Leakage of the private information is at greater risk if the user runs the desired task on cloud due to a possibility of untrusted connection or service provider.

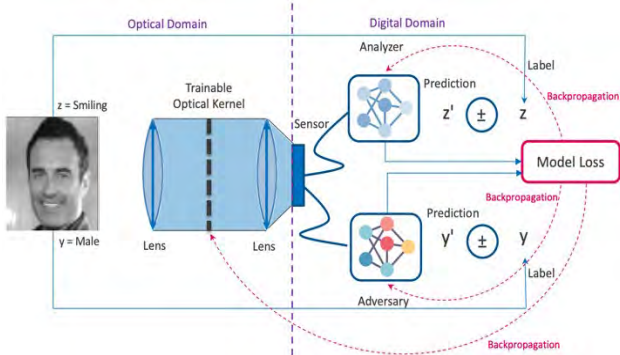


Figure 1: A schematic view of the optical kernel and the training setup. The analyzer classifies the desired attribute while the adversary attacks to extract the sensitive content. The optical kernel, the digital analyzer, and the adversary are trained.

A novel solution system for privacy-preserving artificial intelligence is shown, which helps to preserve the private information of users against all sorts of digital attacks, without significantly effecting the detection accuracy. A trainable optical front-end [1] is used as the privatizer in order to perform the privacy-preserving task in the optical domain before the data reaches the image sensor and therefore the digital domain (see Figure 1). Thus, with this optical front-end, the system is invulnerable against any attack in the digital domain (happening in the edge or cloud environment). A data-driven approach is pursued to optimize the optical front-end to let pass the predefined desired information while removing the sensitive one. Since this processing happens passively in the optical domain, it has no additional memory and computational cost for the edge device, which further saves energy and reduces latency on such devices with confined processing power. It is shown in a set of

illustrative tasks that the method can reduce significantly the amount of sensitive information from the face images without strongly affecting the performance of the target task.

It is ideal for use-cases like camera-based feedback systems for smart TV contents or billboard advertisements to recognize the satisfaction while not having access to the sensitive identity of users. This method can be further combined with methods of fully-digital privacy-preserving ecosystem to provide new features such as being resilient against direct attacks and increasing the total sensitive information blocking

The privacy-preserving optical convolution is trained using two methods of training of the privacy-preserving neural networks on CelebA face dataset [2]. It is proved that these methods, which were solely used to train fully-digital privacy-preserving neural networks with numerous layers until now, are also effective to train the new optical privacy-preserving system.

Extensive experiments are performed on different pairs of facial attributes and show the effectiveness of the method. As an example, it removes 65.1% of sensitive gender attribute while just losing 7.3% of the performance in an illustrative target task of smile detection. The method is also evaluated against deep reconstruction attacks, and it is shown that these attacks are unable to reconstruct the original signal and to restore the sensitive content that has been removed (Figure 2).

This novel method has been submitted as a scientific paper and the preprint is available online [3].

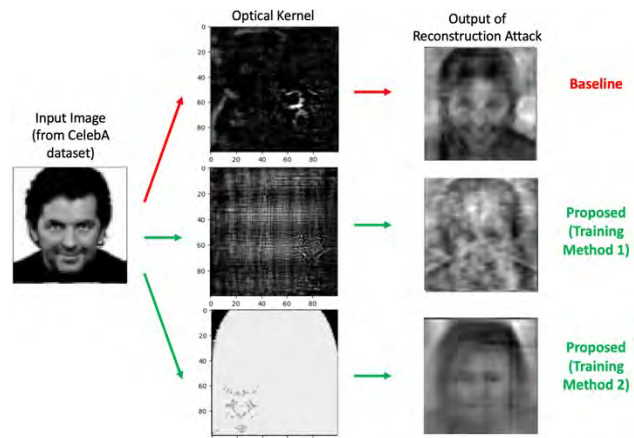


Figure 2: An input face image is convolved by the optical kernel for smile detection task and the reconstruction attack tries to regenerate the sensitive information (gender). In the proposed trainable optical kernels, the reconstruction attack fails to reconstruct the original gender identity.

[\*] EPFL, Ecole Polytechnique Fédérale de Lausanne, Switzerland

[1] P. Pad, et al., "Efficient neural vision systems based on convolutional image acquisition", 2020 IEEE/CVF Conference on Computer Vision and Pattern Recognition (CVPR), 2020, pp. 12282-12291, doi: 10.1109/CVPR42600.2020.01230.

[2] Z. Liu, et al., "Deep learning face attributes in the wild", arXiv:1411.7766v3 8 (2015).

[3] Y. Sepehri, et al., "Privacy-preserving image acquisition using trainable optical kernel", arXiv preprint arXiv:2106.14577 (2021).

# Distributed Encryption for Robust Data Confidentiality and Integrity for IoT

D. Vizár, R. Müller\*

The embedded IoT devices face attacks due to connectivity and physical exposure, such that a leakage of a device's secret key material may result in a long-term threat to the entire application, even if the original device is taken offline. The use of threshold cryptography can improve their resistance with groups of devices, whereby secret keys are partitioned into shares and exfiltration of a sub-threshold number of shares is as useless as having none. The recent designs of distributed encryption have a promise for practical implementations, which has been investigated and confirmed in this work.

Internet of Things (IoT) has a significant potential across the society in the industry, in the daily life of the population (home automation, consumer electronics, fitness wearables), increasing the efficiency of existing infrastructure (smart meters, intelligent buildings) or enabling new applications (real-time localization during evacuation) and business models (sensor network-based data gathering as a service). This broad adoption faces serious challenges. Among these is a tension between the exposure of embedded devices (a.k.a. Things), to potent attacks (through physical manipulation, wireless comm. channels and/or the Internet) and constraints of these devices in terms of pertinent power consumption, computational resources, or available HW security features. As a result, Things are often easily susceptible to attacks that only require moderate skills and effort, such that their long-term cryptographic secrets may leak. In that case, the device can be fully impersonated long after it is offline, and (depending on the security architecture), even other devices and data they produce may be in danger indefinitely.

CSEM uses distributed cryptography as a way to mitigate the impact of a secret-keys leakage from one or several Things, by partitioning secret keys into shares among devices of a group, making the exfiltration of a sub-threshold number of shares as useless as having none. A constant-time implementation suitable for an embedded application has been developed using the implementation of the elliptic curve group P256 (a.k.a. secp256r1) from mbedtls, as this group has a prime order (which is a prerequisite). The implementation has been integrated in CSEM's ultra-low-power RTOS μ111 and tested on the low-power HW platform Nordic nRF52840 (64 MHz).

Distributed (a.k.a. threshold) cryptography provides versions of primitives (authenticated encryption, pseudorandom function, etc.), with secret keys partitioned into  $n$  shares (for  $n$  devices), such that  $t$  of the devices must interact to apply the primitive, with  $n$  and  $t$  as parameters. If an attacker recovers  $\leq t-1$  key shares, the full key is still equally secure. Whenever multiple "Things" can establish point-to-point secure channels (e.g., sensor networks, smart home, or medical body area networks), this can be used to imbue the most critical keys of an application with an additional robustness to extraction attacks. Not directly depending on the security features of the Things' HW, this can increase robustness in virtually all devices. Not all distributed cryptographic primitives are suited for embedded platforms; e.g., secret-key distributed algorithms are much more tractable than distributed signature schemes, which are too computationally taxing. The distributed pseudorandom function (DPRF) construction by Naor, et al., [1]

allows an evaluation initiator to compute a pseudo-random image of an input  $X$  with help of  $t-1$  other key shareholders, who compute shares of the output to be combined by the initiator. When instantiated with an elliptic curve group, it has a complexity equal to a few times that of ECDH over the same curve (the latter being well-established as asymmetric key exchange primitive of choice for embedded platforms) and requires only two rounds of communication per each assisting shareholder. Agrawal et al. built on DPRF to create a practical distributed (authenticated) encryption scheme DiSE, [2] which preserves the single round-trip property, and only adds a small computational overhead (compared to the DPRF itself). DiSE is illustrated in Figure 1.

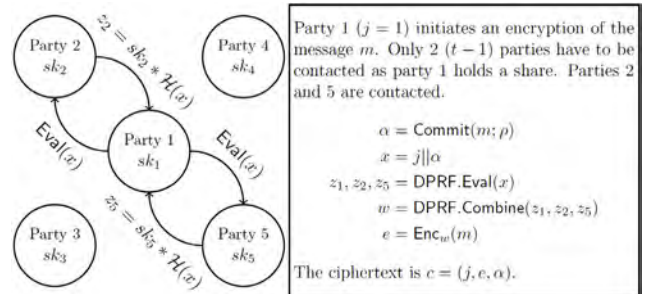


Figure 1: Distributed encryption protocol [3].

On our platform, with a threshold  $t=3$ , the running time of an evaluation (assisting party) is 2.3 s and that of combine (initiating party) is 13.8 s. According to the performance analyses, the main source of the computational complexity is the underlying scalar multiplication of elliptic curve points [2]. With suitable HW acceleration, it is expected to decrease by a factor of  $\approx 4$  (the nRF52840 does not expose APIs for all required operations). During the work on the implementation, two design flaws were discovered in the variants of the DPRF used in DiSE, [1] each invalidating the security proof in a different way. For both, simple fixes have been proposed and corresponding corrected analyses provided [3].

As this work shows, distributed cryptography can be practical in IoT (if used sparingly) and other embedded applications to increase the security level. for their most critical assets, such as the device firmware, datasets produced etc., or aid towards a representation of a group, rather than individual devices. The gains from using threshold crypto will be amplified in combination with an (autonomous) intrusion detection.

\* HEIG-VD, Yverdon-les-Bains, Switzerland

[1] M. Naor, B. Pinkas, O. Reingold, "Distributed pseudo random functions and kdc's", EUROCRYPT (1999), LNCS 1592 (1999) 327.

[2] S. Agrawal, P. Mohassel, P. Mukherjee, P. Rindal, "DiSE: distributed symmetric-key encryption", ACM CCS (2018) 1993.

[3] R. Müller, "Robust IoT security with threshold cryptography", Bachelor's thesis, HEIG-VD (2021).

# Hierarchical Machine Learning for Low-power IoT: Let's Exit Early!

J. Beysens, M. Sénéclauze

Traditional AI applications rely on the cloud to perform machine learning calculations. Introducing neural network processing in the IoT end devices allows for the decentralization of machine learning tools. CSEM develops a framework for hierarchical distribution between the Edge and End devices of neural networks exploiting the early exit mechanism, for lower latency, lower-power consumption and higher robustness.

Traditional AI applications run centralized machine learning (ML) computations in the cloud, which results in high latency, high sensitivity to connectivity failures and high energy consumption spent on communication. Moreover, privacy is at risk in cloud-based solutions. Recently, embedded ML such as STM32Cube.AI [1] allows for running AI in End devices. These are however typically limited in processing power and memory size, often resulting in low-quality output. To reach an acceptable accuracy, they still need to outsource part of the calculations.

CSEM develops a framework for IoT applications to efficiently distribute the inference performed by neural networks in a hierarchical manner. Processing more ML calculations on the IoT End device can reduce latency and energy consumption, as well as increase the application robustness. The typical low-power IoT system consists of 1) a resource-constrained End device, and 2) a more powerful Edge device, connected via a low-power wireless link (Figure 1). The End device includes a sensor generating data that needs to be classified (e.g., an image sensor detecting which object is in the picture). The End device runs the first part of the neural network until the *early exit*, and the Edge device continues with the second part.

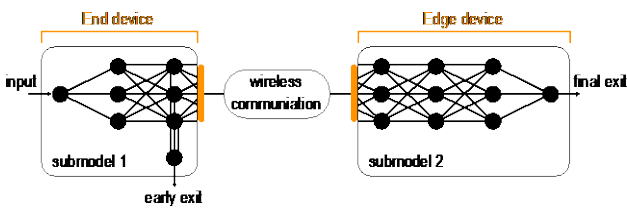


Figure 1: Hierarchical ML inference architecture.

This early exit mechanism allows to stop inference calculations already in one of the middle layers of the neural network, and thus not proceeding until the final layer. This is possible as not all inputs are equally hard to classify. Easy inputs can leave at the early exit, whereas difficult inputs require more effort and thus need to be processed until the final layer. The earlier an input exits, the lower the energy and latency on inference, but also on communication, as early exited inputs are not sent over the network (Figure 1). Lastly, the early exit allows to have a fallback in case of connectivity failure. We can control the probability of inputs leaving at the early exit, by setting a threshold on the confidence level at the early exit. The lower this threshold, the more inputs exit early, at the cost of potential accuracy loss.

Using this framework, we aim to answer following two questions. Firstly, what is the optimal layer depth for an early exit on the End device? And secondly, what is the optimal confidence threshold for the early exit? Intuitively, the optimal configuration depends on the network conditions and the application requirements. For example, a stringent latency budget might not allow communication with the Edge, whereas abundant latency budget favors processing on the Edge.

[1] "Neural network expansion pack for STM32CubeMX", <https://www.st.com/en/embedded-software/x-cube-ai.html>

In the example below, we run the framework using a Raspberry Pi, acting as End device, and a Nvidia Jetson Nano, acting as Edge device. We perform image classification using the well-known convolutional neural network (CNN) ResNet [2] with 32 layers trained on the CIFAR-10 dataset. After training for 50 epochs, this model achieves a top-1 accuracy of 87.5% on the test set. We compare the scenario in which we send and process all inputs on the Edge ('Edge-only'), with three early exit configurations on the End device: one after the 3rd, 7th and 11th layer of the neural network, referred to as exit 3, exit 7 and exit 11, respectively. All model configurations are quantized to 8-bit integers to minimize the processing time on the embedded devices.

We set the confidence threshold to maximize the overall inference rate, with a 2% maximal top-1 accuracy drop. The resulting inference rate in function of the link data rate is shown in Figure 2.

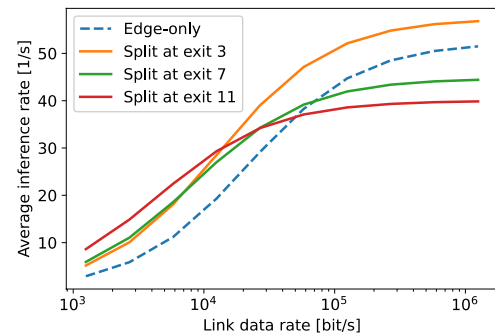


Figure 2: Early exits can significantly increase the inference rate.

This figure illustrates that selecting the right early exit can increase the inference rate compared to the Edge-only configuration. We observe that the later the exit is taken, the more confident the classification result is. This reduces the number of inputs sent over the network, which is especially interesting at very low link date rates. For example, at 1 Kbit link rate, exit 11 can speed up the inference rate by a factor of 3x. Remarkably, also at high link rate, an early exit can improve the inference rate. Now the earliest exit is preferred, as it can handle the *easy inputs* successfully with minimal resources, without processing them until the final layer. For example, for exit 3 the exit probability equals 46%, leading to a 10% higher inference rate at 1 Mbit link.

Further work will take energy consumption into consideration in the analysis and investigate the early exit mechanism on a variety of machine learning models, including resource-efficient CNNs and recurrent neural networks (RNNs).

[2] K. He, et al., "Deep residual learning for image recognition", (2015) arXiv:1512.03385.

# Ultra-low-power Networks for Neuromorphic Devices

S. Narduzzi, S. A. Bigdeli, L. A. Dunbar

Despite the advance of deep learning optimization techniques in recent years, embedding neural networks models on ultra-low-power devices remains challenging and hinders the uptake of AI at the edge. CSEM is tackling this challenge by developing techniques to design, train and benchmark efficient neural networks.

Edge computing, when data processing happens near the sensor, is creating new opportunities for Internet of Things (IoT) applications. Bringing most, if not all, of the computation to the sensor, allows local decision-making. The advantages of edge processing include reduced infrastructure, lower latency, increased energy efficiency, and improved privacy and security. Despite this most processing today still take place in the cloud.

The fact that edge computing can be energy efficient and scavenge energy locally means that it is one of the tools that can be used in creating a sustainable future. As such machine learning optimization techniques have been developed in the past few years to allow the deployment of neural networks with restricted resources. Quantization and pruning are some of the standard techniques used to reduce the memory footprint of deployed models.

An alternative emerging approach is based on spiking neural networks (SNNs). Inspired by biological neurons, SNNs only consume energy when they emit spikes to send information and not when they are silent, as opposed to deep learning neurons that are "always on" and processing. This computational efficiency is what makes our brain one of the most computationally powerful machines consuming only 20 W. CSEM has been contributing to the development of accelerators and processors specialized in supporting these SNN algorithms.

Most accelerators target generic applications and there are still many limitations on the hardware that make them suboptimal for specific tasks: speed, memory, supported operations (spiking or digital). This wide choice of embedded systems means its challenging to identify the ideal hardware for a particular application restricting the adoption and dissemination of ultra-low-power applications. In the EU project ANDANTE [1], CSEM aims to develop tools to help guide the choice of device as well as creating energy-efficient neural networks.

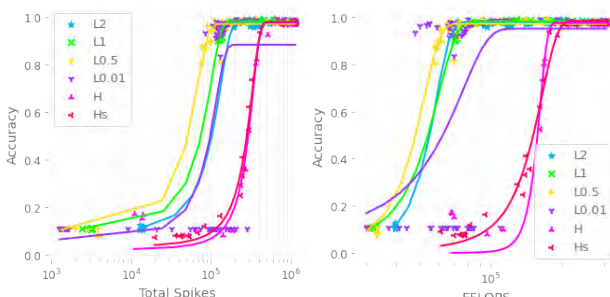


Figure 1: With increasing regularization, the number of spikes and EFLOPS are reduced while preserving the model's accuracy. L0.5 regularization has a good sparsity power, while L0.01 is not very stable and diverges, reaching worse performance compared to L2 regularization. Lines represent the interpolated values.

**Energy-aware training.** To reduce the consumption of artificial and spiking neural networks, we looked at training deep neural networks such that their equivalent SNN model emits fewer spikes. We trained the LeNet-5 network with different regularization techniques. Figure 1 shows the result of this experiments, where the regularization forced the neural networks to have sparser activations. Such sparsity is a significant advantage on hardware optimized to skip 0-value operations, as the model will require fewer effective flops (EFLOPS) compared to an unconstrained network. In Figure 1, we show that regularization indeed reduces the number of emitted spikes when the model is converted to a spiking neural network version.

**Energy-aware architecture.** An alternate direction for reducing the consumption of neural networks is to design architectures that are efficient due to their structure. As designing networks that are inherently efficient can be time-consuming for a human expert, computers become more and more successful in finding architecture that fits the task. They often reach above human-designed algorithm performance. The idea of using a Network Architecture Search (NAS) algorithm is to automatize the discovery of efficient structures in the network.

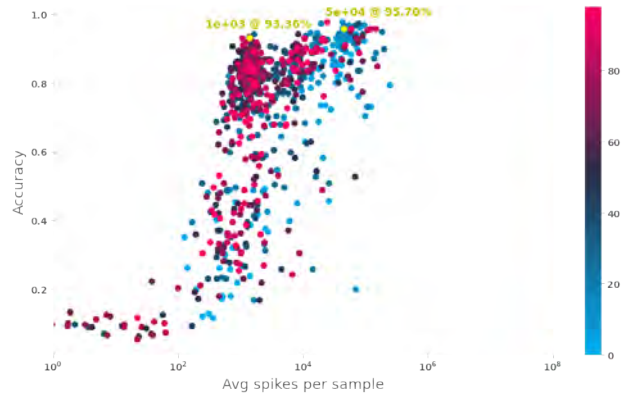


Figure 2: Evolution of the number of spikes across the generations. The color bar represents the generation index. Blue: old models. Red: recent models. We observe that our NAS algorithms successfully reduce the number of emitted spikes by 15x while only losing 1.34% in accuracy.

**Joint Optimization for Neural Network Parameters and Architecture.** We have integrated the two approaches of energy-aware training and the NAS techniques to further boost the performance of our models by first training the most efficient networks, and secondly finding the best model architecture that can further reduce the energy. We will deploy this technology to find best performing neural network for in-house and external hardware platforms for various applications.

Additionally, within the ANDANTE consortium, CSEM is developing a new benchmarking strategy that may facilitate the comparison of neuromorphic hardware and selecting relevant accelerators for each application.

[1] European Union ECSEL program grant agreement No. 876925

# SWISSMODICS—Toward Combined Visible, Infrared and X-Ray Imaging

P.-F. Ruedi, A. Paracchino, L. Lauber, R. Quaglia, S. Blanc

The Clean Sky 2 SWISSMODICS project is developing an ultra-thin wide spectral range image sensor to be inserted in the composite structure of airplanes to facilitate detection of defaults such as delaminations resulting from shocks or impacts on the structure during operation. This sensor will cover the visible, near infrared and x-ray ranges. In a first step toward this goal, detection layers optimized for near infrared and x-ray absorption have been developed and characterized.

Shocks or impacts on composite structures of an aircraft can generate delamination at a distant place. These events cause unscheduled inspections which always require immobilization of the aircraft and possibly disassembly of elements. Different techniques exist to detect these delaminations. The mostly used technique for composite structures of airplanes is based on ultrasound, but it can be very time consuming. The SWISSMODICS project aims to address the lack of efficient diagnostic tools by providing a miniature, ultra-thin camera that is sensitive to visible, infra-red and x-ray photons and that can be incorporated in the composite structure of an aircraft at places where delamination risks to occur. This will considerably facilitate diagnostic and reduce immobilization time.

Such a wide spectral range will be achieved by creating a detector made of a CMOS pixel array with configurable pixels to the specificity of each wavelength range. An absorber with areas sensitive to these three different wavelength ranges will be deposited on top of the pixel array, as illustrated in Figure 1. The top part of the Figure shows the pixel architecture. The top metal layer of the CMOS process is used to form an electrode in each pixel contacting the bottom of the photon absorber layer. A global counter electrode made of indium tin oxide (ITO), a transparent conducting oxide, is deposited on top of the absorber layer. Depositing the absorber layer on top of the pixel circuitry enables 100% fill factor (ratio of sensitive area to total area). The bottom part shows the pixel array with three different structured absorber layers.

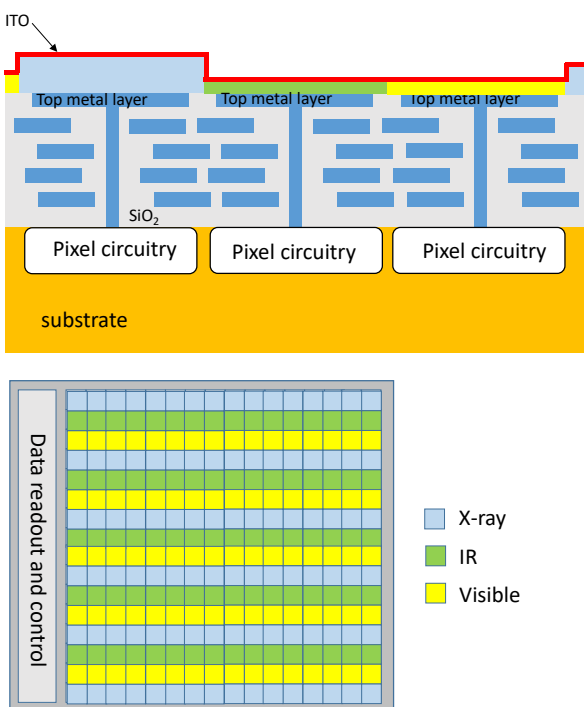


Figure 1: Sensor architecture.

Sensitive layers based on perovskite materials also used in the development of solar cells have been separately optimized for x-ray and near-infrared detection. Very promising results have been obtained. The spectral response of layers optimized for near-infrared light is illustrated in Figure 2. Sensitivity peaks around 800 nm and stays above half of its maximum up to 950 nm.

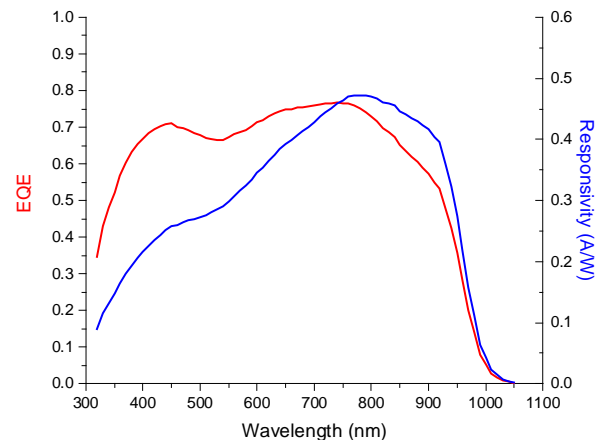


Figure 2: Spectral response of near-infrared optimized layer.

Figure 3 shows the response of x-ray optimized layers to the dose rate for different type of layers with a 100 kV x-ray source. A good linearity is observed on more than 4 decades of dose rate. Furthermore, the decrease of the response after a total irradiation dose of 55 kGy is less than 10%.

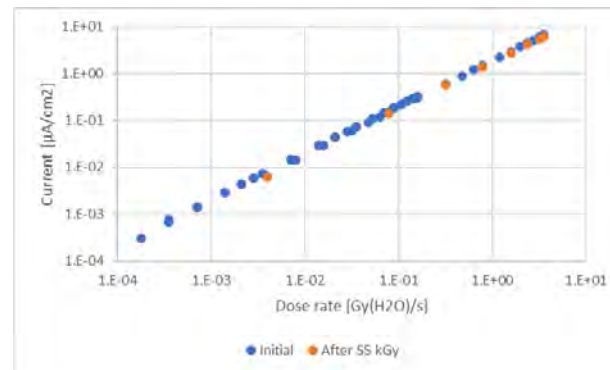


Figure 3: Response to x-ray dose rate.

This new sensor will be a breakthrough in non-destructive testing and will open the door to "intelligent" composite structures. In aeronautics, it will not only reduce immobilization time but also enable to reduce the security margin on composite parts thanks to continuous monitoring, resulting in economy of weight and fuel, thus bringing environmental benefits.

This work, which is led by CSEM, receives the support of the European Union Clean Sky 2 program under grant 887192. The consortium also includes the University Jean Monnet at Saint-Etienne (F) and Almay Technologies (F).

# PreciSense, a High-Performance, Low-Cost, Absolute Position Sensor

B. Schaffer, E. Azarkish, Y. Zha, B. Putter, J.-L. Nagel, P.-F. Rüedi, V. Moser, S. Emery, D. Manic, C. Monneron, P. Masa\*

A novel, generic, multi-dimensional, absolute position sensor ASIC prototype has been developed, offering higher-performance, one-fit-all solutions as a replacement of large variety of existing, highly specialized encoder sensors at a lower cost. The sensor has a resolution of  $2 \times 128 \times 128$  pixels and comprises two folded pixel fields that can be read out horizontally and vertically including random column and row binning for efficient absolute multi-dimensional code detection. In addition, the sensor includes a signal processor and a controller.

Encoder producers are facing difficulties to address the market needs of next-generation encoder products as e.g., compensation of mechanical tolerances, miniaturization or increased performance at a lower price. PreciSense facilitates a quantum leap in miniaturization, cost reduction, and speed. The pixel-based position sensor supports high encoder performance under extreme temperatures based on shadow imaging of patterns with absolute position encoding.

For this purpose several variants of smart codes (e.g., Figure 2) in combination with a sensor enabling successive readout of the same image with the capability of randomly binning rows or columns (Figure 2, 3) have been developed. Besides this specialized pixel field, the sensor, pictured in Figure 1, implements a high-performance DSP (icyflex4), a versatile controller (icyflex2) and standard interfaces allowing fast on chip position calculation and its communication to an external host.

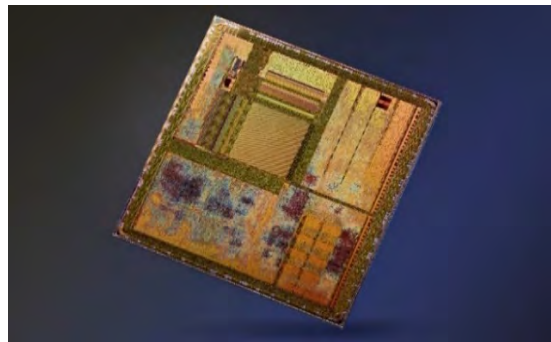


Figure 1: Microphotograph of the chip.

The structure of the codes allows the decoding of a very accurate relative position in the nm range by e.g., phase decoding (Step 1) as well as an absolute position calculation by the decoding of N-bits from the code image during step 2 to N. Figure 2 shows the binned pixels (dark shaded pixels) along columns and rows and their resulting summation values (bars).

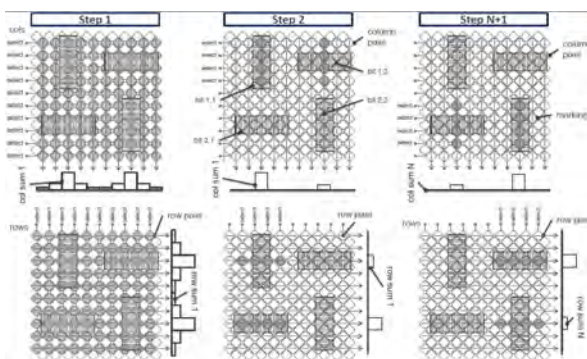


Figure 2: N-Step read out.

The sensor pixel field implements two pixel arrays folded into each other. This is realized via  $2 \times 128 \times 128$  90-degree rotated pixels (Figure 3). The readout circuitry is positioned vertically and horizontally around the pixel field. In contrary to standard pixel arrays columns or rows can be addressed in parallel and the output values are added.

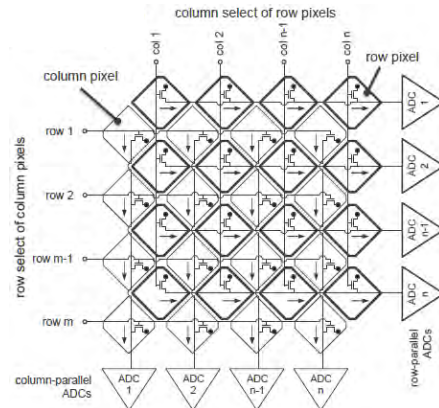


Figure 3: Folded pixel field.

In order to allow summation, the pixels include a sampling capacitor (C3), which is normally part of the adder (Double Sampling) stage (Figure 4). Special high-density caps with good matching performance have been used. The non-destructive read out is realized by adding an additional storage cap (C2) into the pixel which is not cleared during pixel reset. The "sel" switch controls the binning. The pixel diode is a pinned photodiode which is fully emptied into C1 during a transfer phase (TX). Because of the large variation (factor 128) of the charges pumped into the sampling cap of the analog adder, a gain control of a factor 1 to 32 has been implemented. With gain 32 and 4 rows selection the same swing can be achieved as with the selection of 128 rows at gain 1.

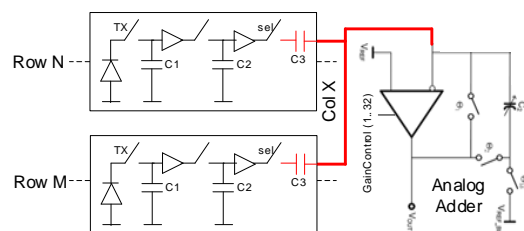


Figure 4: Pixel structure.

This industrial sensor has been tailored for low cost and ease of use. All needed references are generated internally. The chip can be supplied with only two voltages (1.8V/3.3V) and an 80 MHz clock. The chip is produced in 180 nm TowerJazz technology.

This work was done in collaboration with PreciLabs under the Innosuisse project name 28063.1 PFNM-NM. We thank Innosuisse for their support.

\* PreciLabs, Onnens, Switzerland

# Towards Battery-Less Machine Learning Inference at the Edge

P. Jokic, S. Emery

Processing machine learning (ML)-based image analysis algorithms is computationally demanding, requiring powerful hardware resources to achieve the required operational throughput for smart applications. Miniaturized devices are additionally challenged by limited battery capacities, leading to sub-mW power budgets to enable user-friendly battery lifetimes of multiple months. We demonstrate the feasibility of implementing battery-less ML inference using CSEM's ML system-on-chip (SoC), combined with solar energy harvesting on a miniaturized platform.

ML edge processing aims at performing ML-based tasks onboard a smart system instead of offloading the computation to cloud servers, so-called cloud computing. This offers reduced latency and avoids power-intensive communications as well as privacy concerns (for transmitting raw image data to the cloud). However, ML algorithms, like convolutional neural networks (CNNs), require millions of arithmetic operations to be performed for each image analysis. To enable responsive applications, frame rates of at least one frame-per-second (FPS) are necessary, making high computational throughputs essential, while the power budget is strictly limited by the miniaturized form-factors and mobility requirements. This work demonstrates the feasibility of performing complex ML inference on a battery-less solar-powered platform using CSEM's ML acceleration and ULP image sensing solutions. We implement a face identification application that runs at 1 FPS in indoor lighting conditions [1].

Figure 1 illustrates the main components of the demonstrated platform: a flexible solar panel, an ultra-low-power (ULP) ERGO320 image sensor, an electronic paper display (EPD), and the mentioned ML SoC. Its credit card-sized shape is less than 7 mm thick, showing the miniaturization possibilities of the system.

In Figure 2, the system architecture of the platform is shown, illustrating the connectivity between the functional sub-systems. The scene in front of the platform is captured by the image sensor and then transferred to the ML processing chip through an SPI interface, where the image is analyzed. Based on the result of the analysis, the EPD display can be updated through the second SPI interface. The entire system is powered by the on-board solar cell, which is feeding the power management system. More details on the main sub-systems are provided below:

- CSEM ML SoC [2]: This sub-mW SoC features a power-efficient 1.07TOPS/W CNN accelerator along with 1.2 MB of on-chip SRAM memory for buffering input images and storing all parameters. Controlled by its flexible RISC-V-based icyflex-V [3] core, the SoC allows to implement the entire end-to-end processing from image acquisition to ML processing, result evaluation, application control, and display actuation.
- CSEM ERGO320 image sensor [4]: The 320×320 pixel CMOS image sensor features a high dynamic range of 120dB, which enables the acquisition of high contrast images across a wide range of illumination environments. Due to its low-power design, it consumes merely 112 uW at 1 FPS.
- EPD display: This display type features zero-power image retention and high contrast, avoiding unnecessary power consumption during idle periods, whenever the same image

is displayed. Its on-board controller and DC/DC converter are only powered-up by the platform power management when the display is updated. However, the energy for a display refresh is significant and must be carefully balanced with low-power phases to avoid collapsing the supply voltage.

- Solar energy harvesting: Figure 1 shows the used flexible solar panel, which provides up to 1 mW in indoor lighting conditions and more than 50 mW in direct sunlight. To optimize the power extraction, a maximum power point (MPP) tracking circuit is used, which continuously adapts the harvesting current to the current lighting condition. A 47 mF super-capacitor is used to bridge short energy peaks (e.g., display updates). All main sub-systems can be separately power-gated to minimize leakage currents.

The demonstrator implements a 212 MOP CNN for recognizing the face presented to the image sensor, displaying a secret code upon positive identification. Running the imaging – CNN-processing – result evaluation pipeline at 1 FPS, consumes 0.68 mW using the ML SoC. This enables autonomous operation under indoor lighting conditions, providing 0.94 mW of harvested solar power. Proving the feasibility of running ML tasks on battery-less edge processing platforms opens the door for innovative future applications.

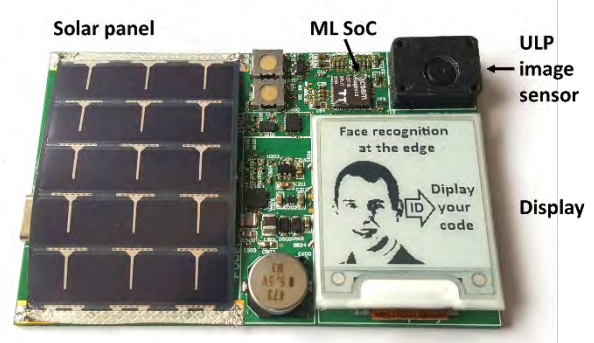


Figure 1: Credit card-sized edge ML platform.

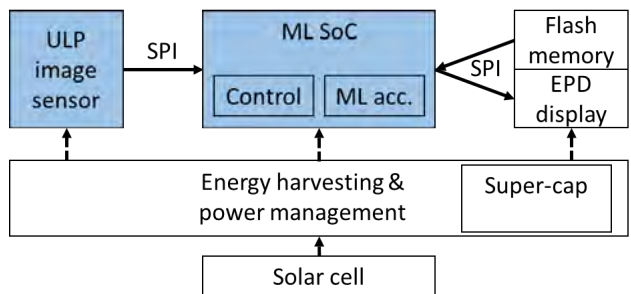


Figure 2: System architecture with CSEM's ML SoC and ULP imager.

[1] <https://ieeexplore.ieee.org/document/9462787>

[2] <https://www.csem.ch/pdf/159793>

[3] <https://www.csem.ch/pdf/51525>

[4] <https://www.csem.ch/pdf/167814>

# An Ultra-energy-efficient AI Chip for Next-Generation ICT Applications

E. Azarkhish, R. Cattenoz, M. Nair •, A. Aimar •, S. Emery

This report presents an overview of an AI acceleration chip under development as a joint collaboration of CSEM and Synthara AG for next-generation ICT applications such as wearable devices, augmented-reality and biomedical implants. The chip features two advanced technologies from Synthara: Watchdog analog mixed-signal (AMS) accelerator with in memory computation (IMC) capability; and NullHop, an ultra-high-performance CNN accelerator. CSEM builds a scalable SoC around the accelerators to support a wide range of requirements from a few microwatts of power consumption to beyond TOPS/W of performance and energy efficiency. The SoC aims to maintain a dynamic balance between performance and energy efficiency by smart management of power consumption and resources.

The Watchdog [1] and NullHop [2] accelerators (jointly known as the Adaptiva accelerators) address a wide range of requirements with two radically different architectures. Watchdog has a configurable topology of analog-mixed-signal (AMS) compute blocks with in-memory-computation capability, achieving up to 200 GOPS @ 50 TOPS/W. While NullHop implements a powerful CNN accelerator with zero-skipping and sparsity exploitation, achieving up to 6.5 TOPS @ 10.1 TOPS/W. Figure 1 illustrates an overview of the AI chip, including Watchdog and NullHop.

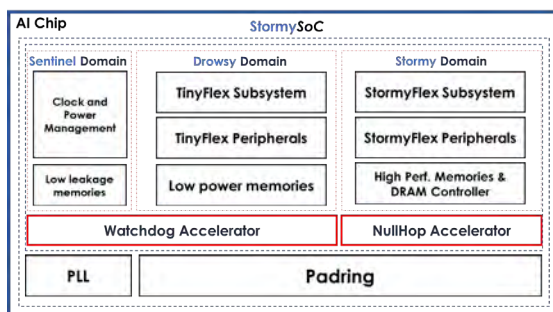


Figure 1: An overview of the AI chip.

The Adaptiva accelerators are coordinated by two RISC-V based processors (TinyFlex and StormyFlex), designed by CSEM. TinyFlex is a ULP RISC-V implementation (based on icyflex-V [3]) with a small memory footprint targeting sub-mW operation thanks to a light-weight operating system (OS) developed at CSEM. StormyFlex, an open-source core from Western-Digital [4], has a deeper pipeline with a 64-b memory bus interface, running a more powerful OS kernel to address the high-performance needs of the system. The chip features three operation modes: deep-sleep, wake-up, active. In 'deep-sleep' mode, it will be at lowest possible power consumption (<<100 uW), sensing and analyzing the environment through Watchdog. All other parts of the system are power-gated. As soon as Watchdog detects an interesting pattern, the chip will transition into the 'wake-up' mode, turning on the TinyFlex processor and boosting the performance of Watchdog (within a few milliwatts). In the extreme case where a thorough analysis is needed the NullHop accelerator is woken up by switching into the 'active' power mode, in which more than 10 TOPS of performance can be achieved (up to 1 Watt).

The 'clock-and-power-management-unit' (XMU) is responsible for handling power state transitions and generating clean clocks

• Synthara AG

[1] Design of low-power mixed-signal neuromorphic systems, <https://www.zora.uzh.ch/id/eprint/185720/>

[2] NullHop: A Flexible Convolutional Neural Network Accelerator Based on Sparse Representations of Feature Maps, 10.1109/TNNLS.2018.2852335

and resets in each mode. The generated clocks range from 32 KHz for always-on regions, up to 25 MHz for low-power sections, and to beyond 500 MHz for high-performance parts of the chip.

On-chip communication is handled by APB and icyflex-V [3] buses in low-performance regions, and by AXI-4.0 (64b) in high-performance domains. Full-bandwidth handshaking and fair arbitration schemes are implemented throughout the interconnection network to address communication needs.

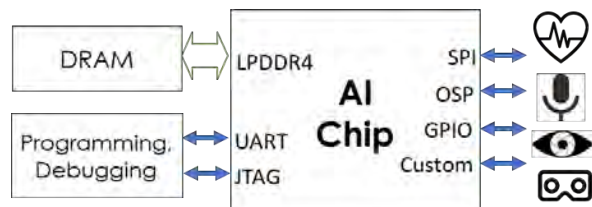


Figure 2: Planned system-level usage of the AI Chip in the demonstrator.

Off-chip communication is provided by SPI and UART for low-bandwidth scenarios, and OctoSPI (OSP) and LPDDR4 for high-performance modes (up to 8 GB/sec). A custom digital interface is implemented for lab evaluation, as well.

Memory is organized in a hierarchical fashion, with different flavors: low-leakage, low-power, and high-performance for different domains. A shared memory mechanism is implemented enabling communication between TinyFlex and StormyFlex.

JTAG is available for both cores. UART can be used for interactive debugging, and a tracing mechanism in TinyFlex allows for full instruction tracing. A flexible boot mechanism is implemented: A SPI flash is used to store TinyFlex boot code, while for StormyFlex, an OctoSPI flash stores boot code and system data. UART and JTAG boot are also supported for debugging.

The chip will be implemented in GF22FDX technology in 2022. Figure 2 illustrates a possible system-level instantiation of the AI chip. Access to DRAM will be provided through LPDDR4 interface, and access to various sensors, along with debugging, probing, and programming will happen through the other interfaces. A demonstrator is planned to be built in 2022, targeting various applications identified by Synthara.

[3] J.-L. Nagel, et al., "icyflex-V—a New Ultra-low-power Processor based on RISC-V Architecture", CSEM Scientific and Technical Report (2019), 116.

[4] EH1 RISC-V SweRV CoreTM 1.9 from Western Digital, <https://github.com/chipsalliance/Cores-SweRV>

# An Ultra-low-power Short-Range 60-GHz FMCW Radar in 22-nm FDSOI CMOS: Performance Characterization

S. Cerida Rengifo, F. Chicco, E. Le Roux

*Fully integrated RADAR-on-chip (RoC) systems have been developed particularly driven by automotive industry, where power consumption is not a tight constraint. There are however not yet many low-power solutions for mobile applications such as gesture recognition or vital signs monitoring. The first prototype of our 22 nm ultra-low-power RoC is characterized, operating from 57 to 66 GHz, with a minimum continuous power consumption of 40 mW.*

The report presents the design and characterization results of an ultra-low-power short-range frequency-modulated continuous-wave (FMCW) RADAR designed to operate in the 60-GHz band. The frequency synthesis is based on a quadrature digitally-controlled oscillator (QDCO) exploiting quadrature coupling to achieve a seamless and ultra-wide frequency tuning range [1]. Its frequency is tuned with a 10-bit current-steering DAC. The latter acts simultaneously in the current biasing of the cross-coupled pair and the coupling pair to obtain a fast and smooth sweep without wasting any current. In addition to the current-steering tuning, the DCO has 8 sub-bands controlled by capacitor banks. They are not meant to be used dynamically but to adjust the band in case of process variations. A wide-band and low-power divider chain is designed using dynamic topologies. The All-Digital Phase-Locked Loop (ADPLL) is closed off-chip by means of a FPGA platform providing flexibility for the design and test of the digital loop filter. The transmitter (Tx) path includes a BPSK modulator in order to implement a low-IF architecture minimizing the impact of LO-Rx leakage, DC offsets and flicker noise in the receiver (Rx) path. This also allows orthogonal modulations for Rx separation in MIMO operation. Furthermore, the Tx is optimized for short-range operation with 0 dBm output power [2]. The Rx path is designed as a low-IF I/Q mixer-first architecture optimized for low power with 30 dB noise figure (NF) and the down-converted signals are output through IF buffers.

The RADAR is required to operate across a very wide band, nevertheless, the FMCW signal is instantaneously narrow band. A band-tuning technique is used in Tx and Rx. to optimize the quality factor of the inductive loads for each stage and therefore the power consumption. This is particularly important for the Tx output stage loaded by  $50\ \Omega$  through a balun. The output impedance transformation network was designed for a 3 dB bandwidth of approximately 6 GHz. Moreover, every Tx and Rx stage is coupled using interstage transformers each one including a 3-bits thermometer capacitor bank designed to switch in 1 GHz steps. The band-tuning implemented in Tx and Rx operates synchronously with the DCO FMCW sweep to cover the entire 9 GHz bandwidth. The DCO signal distribution is designed in a modular approach to be able to extend the number of Tx/Rx paths for MIMO operation. RADAR sensing benefits from MIMO in terms of SNR and angular resolution. The 2-Tx & 2-Rx FMCW RADAR is integrated in GF 22-nm FDSOI CMOS technology and was tested mounted on a PCB through on-chip probing using 200- $\mu\text{m}$  pitch GSG probes. Figure 1 shows the RADAR microphotograph as well as other passive test structures. The total die size is  $2.5 \times 1.25\ \text{mm}^2$ .

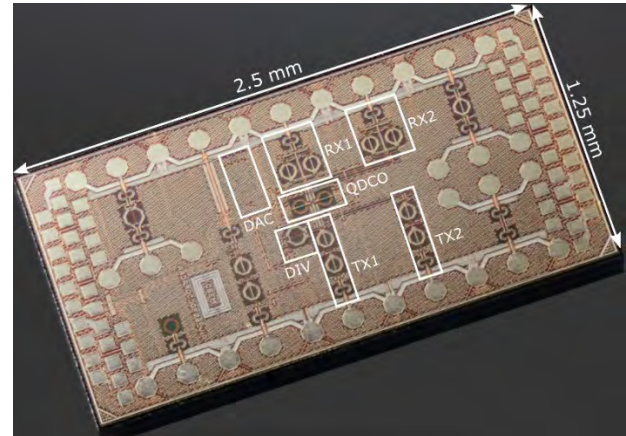


Figure 1: Chip microphotograph.

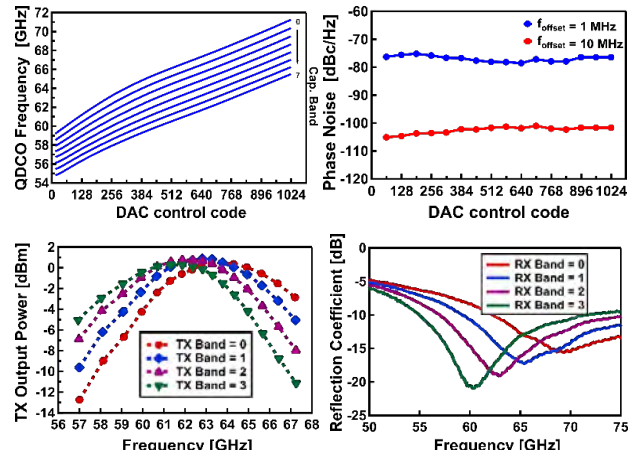


Figure 2: QDCO frequency and phase noise vs. DAC input code, TX output power and RX reflection coefficient vs. frequency.

Figure 2 shows the QDCO tuning range for the 8 sub-bands, each sub-band cover at least 10.7 GHz and the total tuning range is 16.7 GHz (26%), from 54.8 to 71.5 GHz. The measured phase noise at 1 MHz offset is -78 dBc/Hz. The TX output power varies from -5 to 1 dBm across the operating bandwidth. The RX shows good matching with a reflection coefficient below -10 dB. The average continuous power consumption is 40 mW and 61 mW for 1-TX & 1-RX and 2-TX & 2-RX, respectively. A second version is planned for Q1 2022 targeting lower power consumption and extending MIMO to 4-TX and 4-RX paths.

[1] F. Chicco, et al., "A 60 GHz QDCO with 11 GHz seamless tuning for low-power FMCW radars in 22-nm FDSOI", ESSCIRC 2021 - IEEE 47th European Solid State Circuits Conference (ESSCIRC), 2021, pp. 291-294, doi: 10.1109/ESSCIRC53450.2021.9567787.

[2] S. Cerida, et al., "An optimized low-power band-tuning TX for short-range FMCW radar in 22-nm FDSOI CMOS", ESSCIRC 2021 - IEEE 47th European Solid State Circuits Conference (ESSCIRC), 2021, pp. 467-470, doi: 10.1109/ESSCIRC53450.2021.9567815.

# An Ultra-low-power $\Delta\Sigma$ Analog to Digital Converter for High-Resolution Applications

A. Sukumaran, B. Putter, S. Emery

This work aims to build an ultra-low-power ( $<250\text{ }\mu\text{W}$ )  $\Delta\Sigma$  ADC for applications requiring resolutions up to 16/18 bits supporting different signal bandwidths. The architecture has been devised to operate from a 0.8 V (digital) / 1.2 V (analog) supply so that it can be easily adapted and portable across modern process nodes such as 28 nm and below. The resulting low-noise design targets a Noise Spectral Density (NSD) of  $-145\text{ dBc/Hz}$ . The proposed architecture adopts several state-of-the-art techniques such as FIR-DACs with optimal bit-weights, DRZ signalling to mitigate ISI, mildly multi-bit quantizers with DWA, dithering for idle tone removal and a fully continuous-time loop-filter architecture that does not require RC coefficient calibration.

$\Delta\Sigma$  ADC is the preferred architecture for high-resolution applications such as professional audio, precision temperature measurements, bridge sensors and more recently for biomedical applications. This work aims to use fully continuous time  $\Delta\Sigma$  modulators as they offer excellent power efficiency [1], resistive input impedance that is easy to drive and implicit anti-alias filtering that mitigates noise foldback from preceding stages. The architecture of the  $\Delta\Sigma$  ADC and the Pole-Zero (PZ) plot for the chosen Noise Transfer Function (NTF) is shown in Figure 1.

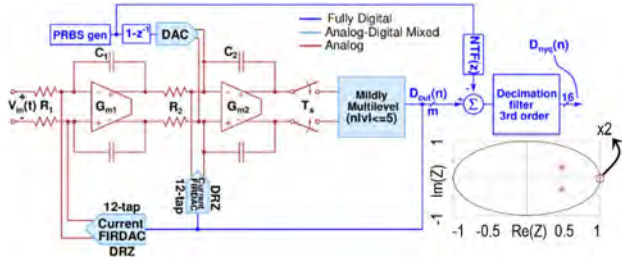


Figure 1: Architecture of the  $\Delta\Sigma$  ADC and PZ plot for the designed NTF.

The modulator consists of a second order loop-filter in the Cascade of Integrators FeedBack (CIFB) topology. A low order loop-filter is chosen to maximize the Maximum Stable Amplitude (MSA) of the modulator and to eliminate the requirement of calibrating the loop-filter coefficients against RC process spread. The second order CIFB filter is built using active-RC integrators which has good linearity as the opamps can have large output swings with almost no swing at their inputs. The loop-filter output is over-sampled by a multi-level quantizer. Using a multi-level quantizer improves the MSA, reduces quantization noise, effect of clock jitter and loop-filter non-linearity.

Slightly multibit quantizers are chosen as they allow for a high Maximum Stable Amplitude (MSA) while providing reasonably good static DAC linearity. The technique of Dynamic Weighted Averaging (DWA) is adopted to further improve the linearity of the multibit DAC. In this technique, the relation between the DAC input signal and the index of the DAC element that is chosen is decoupled. The DWA circuitry being present within the feedback loop degrades loop stability. However, quantizers with lesser number of levels leads to the possibility to use fast DWA circuit techniques thereby having only minimal impact on stability.

The quantized output is fed-back into the input integrator using Current-Source (CS) feedback DACs. This reduces the noise from the input integrator. Further, a Dual Return to Zero (DRZ) signaling is adopted to mitigate Inter Symbol Interference (ISI) by

ensuring the occurrence of a transition during every clock cycle. A Finite Impulse Response (FIR) low pass filter is integrated with the current source feedback DAC to filter the high frequency quantization noise [2]. This not only improves the immunity to clock jitter by reducing the foldback of far-off phase noise but also enhances the linearity of the input integrator [3]. This is illustrated in Figure 2.

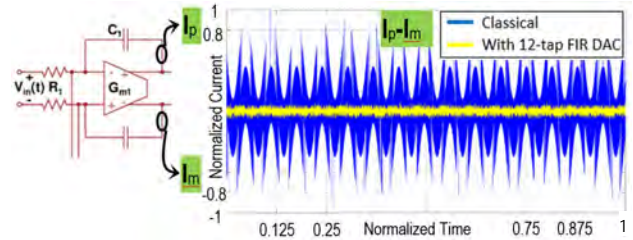


Figure 2: FIR-DAC reducing the current into the input integrator.

Specifically, a 12-tap FIR filter with an optimized transfer function is chosen to maximize the benefits from its usage. An FIR compensation DAC is added at the input of 2nd integrator to restore loop stability which would otherwise be jeopardized due to the insertion of the higher order FIR-DAC in the feedback path.

**Block-level simulations:** An example case of an audio bandwidth, 24 kHz,  $\Delta\Sigma$  ADC with an Over Sampling Ratio of 256 is chosen. Figure 3a shows the Power Spectral Density (PSD) at the output of the DSM while Figure 3b shows the overall Dynamic Range (DR) plot of the DSM in the presence of RC coefficient spread of the loop-filter. Figure 3b shows that the peak SNR remains well above 16-bit performance even with the coefficient spread. This eliminates the need for power-up RC calibration potentially saving significant bring-up time in volume production. Furthermore, the DR plot is linear, thanks to the dithering scheme which decomposes the spurious tones into the noise floor. Therefore, this solution makes an excellent candidate for several high-performance applications where non-harmonic tones are unacceptable and where low-power consumption is necessary.

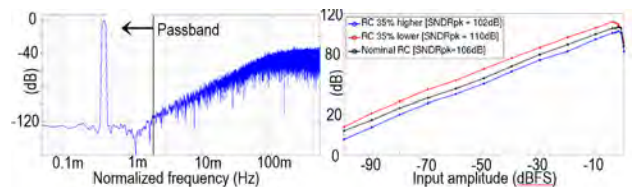


Figure 3: a) PSD at output of DSM; b) DR plot with  $\pm 35\%$  RC spread.

[1] R. Schreier, G. C. Temes, "Understanding delta-sigma data converters", Wiley Interscience (2005).

[2] B. M. Putter, "SD ADC with finite impulse response feedback DAC", 004 IEEE International Solid-State Circuits Conference (IEEE Cat. No.04CH37519), 2004, pp. 76-77 Vol.1, doi: 10.1109/ISSCC.2004.1332601.

[3] A. Sukumaran, S. Pavan, "Low-power design techniques for single-bit audio continuous-time delta sigma ADCs using FIR feedback", IEEE Journal of Solid-State Circuits 49, (2014) 2515.

# Miniature Quantum Sensor Prototypes: Development Status

L. Balet, S. Karlen, T. Overstolz, D. Grassani, G. Bergonzi, B. Gallinet, F. Lütfi, S. Dasen, S. Droz, S. Zabihzadeh, I. Marozau, J. Gobet, J. Bennès, M. Toimil, O. Hefti, J. Disser, G. Musy, L. Giriens, G. Perruchoud, O. Vorobyov, F. Droz, S. Lecomte, J. Haesler

The miniature vapor cells developed at CSEM are at the heart of different atomic quantum sensing technologies developed within the H2020 Quantum Flagship macQsimal project. In addition to custom cell production, CSEM is involved in the design, assembly and testing of system-level prototypes for miniature atomic clocks (MACs) and optically pumped magnetometers (OPMs).

The H2020 macQsimal project aims to make recent advances in atomic quantum metrology and sensing available to high-impact applications through microelectromechanical systems (MEMS) technology. Atomic sensors can exploit single-particle quantum coherence for extreme sensitivity to many physical quantities of interest and have the potential to harness multi-particle quantum coherence for still greater sensitivity.

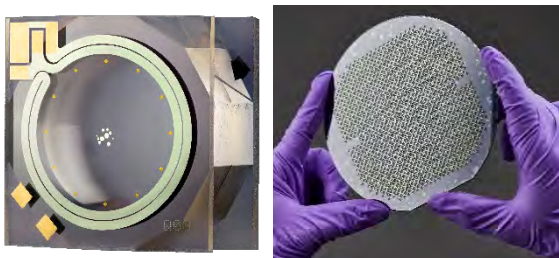


Figure 1: Typical  $4 \times 4 \times 1.9 \text{ mm}^3$  Rb vapor cell fabricated at the wafer-scale<sup>[1]</sup> for miniature quantum sensors.

MEMS devices leverage the fabrication techniques of the integrated circuit industry to offer a proven route to high volume/reliability and low-cost deployment. In the last decade, MEMS atomic vapor cells (Figure 1) enabled high-performance miniature atomic devices including atomic magnetometers, atomic gyroscopes, and atomic clocks. Applications such as autonomous navigation, non-invasive medical diagnosis, drugs/explosives detection, etc. are poised to incorporate such advances into practice.

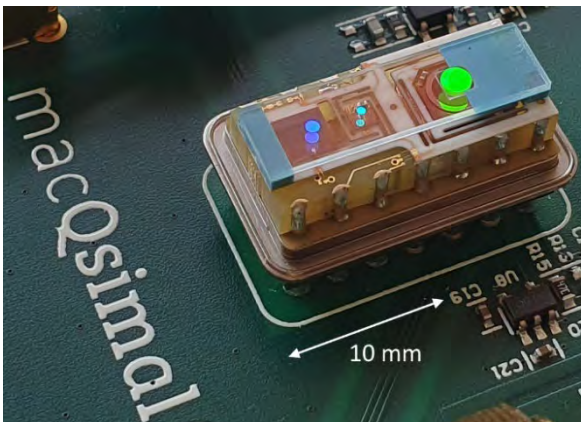


Figure 2: Evolution of the miniature atomic clock design towards a commercial DIL-14 package for straightforward integration.

CSEM acts as a cell provider and as a system level architect in the development of MACs (TRL6-7) and OPMs (TRL4-5) in collaboration with industrial partners.

CSEM could capitalize on decades of development to propose its patented flat form factor CPT based MAC prototype<sup>[2]</sup> shown in Figure 2 and adapt it to fit in a commercial and economically

more interesting DIL-14 hermetic package. Optimization of the MEMS cell design with the addition of patented nucleation site<sup>[3]</sup> for excess Rb, enhancement of the optical waveguide performances, and addition of in-package magnetic field generation allowed for the first prototypes under test to reach a short-term frequency stability below  $7 \cdot 10^{-11}$  at 1 second, well within the targeted specifications. Thanks to CSEM's MEMS atomic vapor cells with ultra-low drift measured well below  $5 \cdot 10^{-12}$  per day<sup>[4]</sup>, the prototype should allow surpassing state-of-the-art long-term MAC performances. Efforts to reduce the manufacturing costs have also been undertaken, e.g., by using standard PCB-flex for the structure of the physics package (Figure 2).

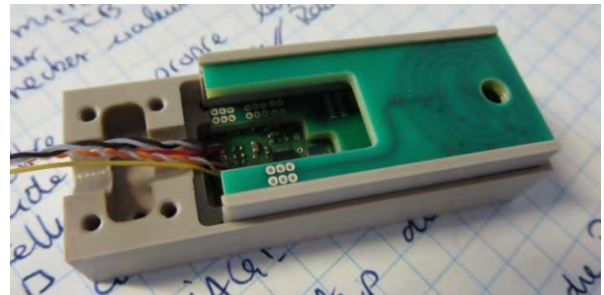


Figure 3: Inside view of the first  $20 \times 20 \times 55 \text{ mm}^3$  OPM prototype.

OPMs, even though being a rather recent field of activity for CSEM, benefits from many synergies with the MAC activities. By merging these synergies with knowledge shared by the macQsimal partners ICFO in Spain, as well as VTT, Aalto University and Megin Oy in Finland, a novel miniature OPM design could be engineered. Figure 3 shows an inside view of the prototype, the  $2 \times 2 \text{ cm}^2$  footprint of which should allow packing multiple sensors for brain imaging applications. The optical part, with VCSEL light source and optics, has been removed to show the top external magnetic field cancellation antenna visible on the right side of the top PCB. The atomic vapor cell, produced by CSEM with high buffer gas pressure up to 5 bars, heated to around 150°C and isolated from the environment in a vacuum sealed LTCC package, is placed just below the circular aperture on the right of the sensor prototype. The sensitivity of this prototype is expected to be in the fT range level, which imposes strict design rules, like e.g., the avoidance of metallic surfaces and magnetic materials.

The first OPM prototypes are being assembled and tested at CSEM, while their performances will be assessed by the University of Aalto and the Institute of Photonic Sciences (ICFO).

This work was partly funded by the EU with the Quantum Flagship H2020 project macQsimal under grant agreement No. 20393, and carried out in collaboration with Orolia Switzerland SA, MEGIN Oy, VTT and ICFO.

[1] CSEM patent n°US8906470 (B2).

[2] CSEM patent n°US10423124 (B2).

[3] CSEM patent n°US10461760 (B2).

[4] S. Karlen, joint EFTF-IFCS 2021, virtual conference (2021).

# Two-Photon Atomic Clock Targeting Miniature Dimensions and High Performances

S. Karlen, S. Kundermann, R. Blum, F. Droz, S. Lecomte

CSEM has developed its first optical atomic clock laboratory prototype based on a two-photon rubidium transition. This atomic technology has great potential in high-performance and/or miniature dimensions clocks for both ground and space applications.

In the last decade, the democratization of frequency combs has pushed forward the development of atomic clocks making use of optical transitions, the so-called "optical clocks"<sup>[1,2]</sup>. Among the broad variety of architectures, CSEM recently selected the rubidium two-photon atomic clock, which is based on the established hot atomic vapor cell technology. This type of clock offers a relatively simple architecture and is thus a good candidate for both high performance and miniature atomic clocks for space and ground applications. Based on CSEM's decades of expertise in the development of high-performance and chip-scale atomic clocks, stabilized lasers and frequency combs, development work has been started in collaboration with ESA on this technology.

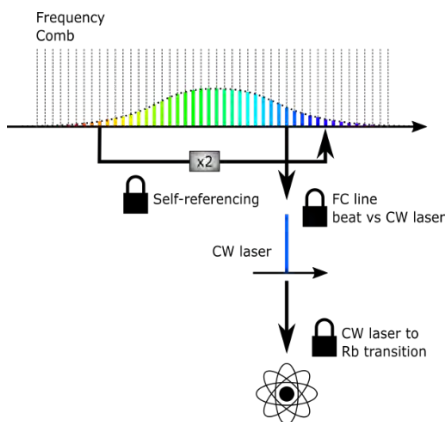


Figure 1: Two-photon atomic clock working principle: a continuous wave (CW) laser is locked to the two-photon atomic transition. The frequency comb (FC) acts then as a phase coherent frequency divider to transpose the relative frequency stability of the CW laser from optical to microwave frequencies and provides a stable output signal.

Two-photon rubidium optical atomic clocks consist of two main building blocks: an atomic vapor cell unit which provides a stable atomic reference at optical frequency and an optical frequency comb which allows to transfer the relative frequency stability from the optical to the more user-friendly microwave frequency domain. This working principle is described in Figure 1. A CW laser emitting a 778.1 nm is frequency locked to the  $5S_{1/2}$ ,  $F=2$  to  $5D_{5/2}$ ,  $F=4$  narrow two photon transition of  $^{87}\text{Rb}$ . The lock is realized by synchronous detection of the 420 nm fluorescence signal measured with a photomultiplier tube (PMT). This stabilized optical frequency is then divided by using the frequency comb: the carrier-offset frequency of the comb is self-referenced with an f-2f interferometer. One comb tooth is then locked to the CW laser atomic transition with a phase-locked loop (PLL).

CSEM is currently building-up experience in two-photon optical atomic clocks in the frame of two ESA projects: The project PHOTAC (Contract N° N°4000132895/20/NL/AS) where the

potential of high performance two-photon rubidium atomic clocks is explored for the next generation of Galileo satellites and in the frame of the ESA project A-CSAC (Contract N° 4000130251/20/NL/LW), the goal being to explore the miniaturization of a two-photon atomic clock. In this context, two aspects are being studied. On the one hand, a laboratory prototype experiment is realized with which the performance of a two-photon clock targeting compact dimensions is assessed. On the other hand, the further miniaturization of some of the functionalities in a silicon-nitride photonic integrated circuit (PIC) is studied. On Figure 2, the atomic vapor cell assembly of the A-CSAC project is illustrated. The current status of the clock frequency stability is reported on Figure 3. The short-term frequency stability of the clock is slightly above  $10^{-12} \tau^{-1/2}$ , averaging down to  $10^{-13}$  at 1'000s integration time.

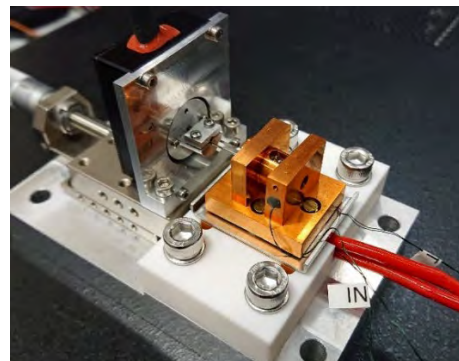


Figure 2: Two-photon atomic reference unit of the clock developed at CSEM: atomic vapor cell and micro photomultiplier tube.

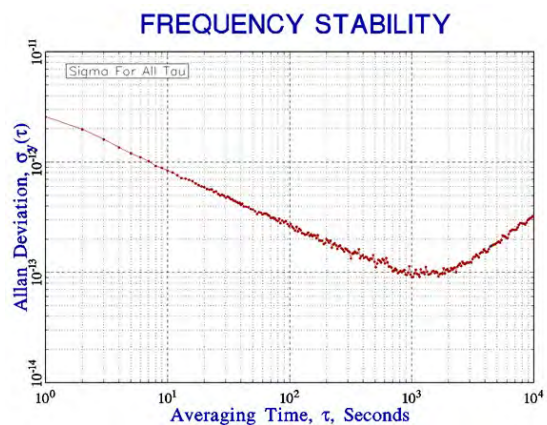


Figure 3: Allan Deviation of the CSEM two-photon atomic clock prototype. The short-term frequency stability is limited by the CW laser linewidth (here a Distributed Bragg reflector laser diode). The long-term stability is limited by the stability of the clock driving electronics.

These developments are ongoing with the objective to improve the long-term frequency stability of the clock prototype.

[1] K. W. Martin, et al., "Compact Optical Atomic Clock Based on a Two-Photon Transition in Rubidium", Physical Review Applied, 9(1), 2018.

[2] Z. L. Newman, et al., "Architecture for the photonic integration of an optical atomic clock", Optica, 6(5), 2018.

# Ultra-short Pulse Non-Classical Light Emitters Utilizing Multiple Wide Quantum Wells

N. Torcheboeuf, V. Mitev, L. Balet, P. Renevey, D. L. Boiko

A novel technology for a pulsed non-classical light source has been established. It can be used to build super-resolution instruments, e.g., optical quantum microscopes, and also to replace conventional ultrafast mode-locked lasers in numerous classical light applications.

The multiphoton quantum states keep the promise of growing importance in nowadays and future practical applications. In a series of European FET-OPEN (SUPERTWIN, RADIAL) and Quantum Flagship projects (PHOG), CSEM in collaboration with III-V Lab fosters a technology for a novel pulsed semiconductor light source by super-radiant emission.

The light source produces a pulse with 1.2 ps width (measured with a second-order autocorrelation technique based on two-photon interreference  $G^{(2)}$ <sup>[1]</sup>), 80 pJ energy and 67 W peak power at 800 nm wavelength, with a spectral FWHM of 1.3 nm in the pulse-on-demand mode. These optical pulse features are highly attractive in many applications of ultrafast lasers such as two-photon fluorescence lifetime imaging (2ph-FLIM). Yet, following the pioneering work of Dicke<sup>[2]</sup>, the cooperative superradiance (SR) originates from quantum correlations. The emitted super-radiant photon burst shall reveal non-classical correlations between photons, offering a potential breakthrough enabled by quantum properties of correlated photons surpassing the classical resolution and/or sensitivity limits. For instance, it can enable an optical imaging at the de Broglie wavelength<sup>[3]</sup> beyond the classical Rayleigh resolution limit, the frontier which is today accessible only with scanning near-field microscopy techniques.

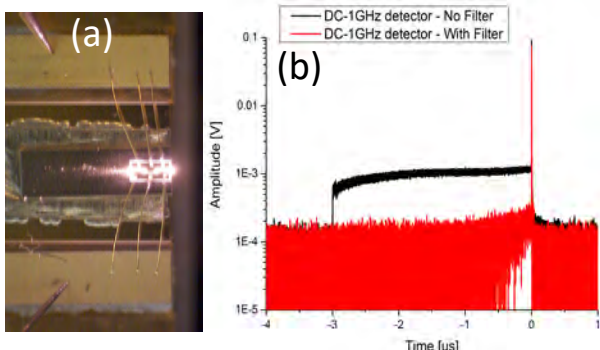


Figure 1: a) Microscope image of operating SR source. b) Spectral filtering to remove ASE. The waveforms are recorded with a slow detector without (black curves) and with (red curve) optical 10 nm bandpass filter.

The fabricated devices have much in common with multi-section ridge waveguide semiconductor lasers and have two p-electrodes on the top: one is dedicated to drive the two end-firing gain sections while the second one controls the middle absorber (Figure 1a). SR emission is achieved using a quantum-confined Stark effect in wide GaAsP/GaInP heterostructure quantum wells (WQWs) placed in the active region. Under bias field applied to the gain structure, the electron and hole envelop wavefunctions are spatially separated, quenching the lasing emission entirely for the duration of the current pulse (up to 7 μs, which is unusually long for semiconductor laser diodes). A single

optical pulse appears at the end of the current pulse (Figure 1b), when the external bias field is removed, enabling stronger overlap of carriers, and yielding a sudden increase in the radiative recombination rate.

With a positively biased absorber just above transparency the structure operates in continuous-wave (CW) lasing regime. At negative absorber bias, the structure operates as a laser and reveals self-pulsation (SP) at MHz frequencies. The first lasing pulse appears with unusually large delay of 7 μs preceded by a pedestal of amplified spontaneous emission (ASE). However, if the pump pulse is made shorter, we observe a drastically different dynamic regime. A narrow-width solitary light pulse of large amplitude emerges at the trailing edge of the current pulse, independently of the pump pulse duration. We apply an optical bandpass filter to remove the ASE (Figure 1b).

Using an interferometer with four single photon detectors at the output we measure the normalized correlation functions  $g^{(n)}(\tau)$  of the orders  $n$  from 2 to 4. For a reference mode-locked (ML) laser as well as for our sample operating in the ASE, CW or SP regimes, we obtain  $g^{(2)}g^{(4)} \geq (g^{(3)})^2$ . However in the SR regime, the criterion for non-classicality<sup>[4]</sup>  $g^{(2)}g^{(4)} < (g^{(3)})^2$  is fulfilled (Figure 2). In addition, the second-order spatial correlation patterns  $G^{(2)}(r,r)$  recorded with a dedicated 32×32 SPAD array sensor SuperEllen<sup>[3]</sup> revealed non-classical correlation features of the emitted photons in the SR regime as compared with lasing. We conclude that SR pulse is a mixed state with a large contribution from coherent classical state. The next step will be to filter out the coherent constituent using quantum-classical light discriminator, that has been validated in a model experiment<sup>[3]</sup>, in order to retain only non-classical light state.

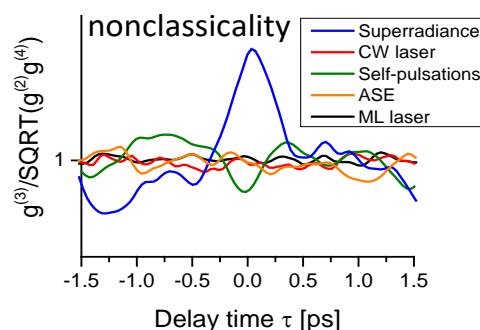


Figure 2: Verifying non-classicality of superradiance vs CW, SP and mode-locked (ML) laser as well as ASE. Indicative vertical axis scale.

The partners contributing to these results are Fondazione Bruno Kessler and Institute of Physics, National Academy of Sciences of Belarus. This work was partly funded by the H2020 program under grant agreement No. 820365.

[1] Y. Miyamoto, T. Kuga, M. Baba & M. Matsuoka, *M. Opt. Lett.* 18, 900 (1993)

[2] R. H. Dicke, "Coherence in Spontaneous Radiation Processes", *Phys. Rev.* 93 (1), 99 (1954).

[3] V. Mitev, L. Balet, N. Torcheboeuf, P. Renevey, D. L. Boiko, "Discrimination of entangled photon pair from classical photons by de Broglie wavelength", *Sci. Rep.* 10 (1), 7087 (2020).

[4] D. N. Klyshko, *Physics – Uspekhi* 39, 573 (1996).



# PRECISION MANUFACTURING

Michel Despont

The label "Swiss made" is associated with quality and precision. CSEM is committed to continue the valorization of this label by helping and supporting Swiss industry with innovative offerings and services in manufacturing technologies. This is particularly important in today's world, where industry is facing rapid changes in both manufacturing concepts (Industry 4.0) and the demanding requirements of the IoT (Internet of Things) which requires an ever-increasing performance and complexity of devices at the same time as decreases in their cost, form factor, and power consumption.

CSEM's developments in Precision Manufacturing are aimed at efficiently bringing new technologies to market. CSEM therefore not only develops new technology bricks, it also considers their implementation in an industrial environment as well as their integration into systems. It is by combining these aspects—and thanks to CSEM's understanding of industries' needs—that we will create value for Swiss industry. The research priority Precision Manufacturing therefore has both a technology-related focus—MEMS & Packaging, Additive Manufacturing, and Functional Surfaces, and a system-level focus—Photonics, Tools for Life Sciences, and Scientific Instrumentation.

## Focus Areas

In the Focus Area **Functional Surfaces**, CSEM provides its know-how in nano-structuration, surface modification, and interfacial engineering and assists its partners in manufacturing and up-scaling developed processes with its coating infrastructure and characterization platform.

CSEM provides under one roof MEMS and their associated packaging technologies—a one-stop-shop solution from development to small-scale production in an environment that fulfills sound quality requirement according to the ISO 9001 standard. CSEM's **MEMS & Packaging** technologies and versatile services are thus an essential element in the valorization chain of MEMS-based microsystems tailored for Swiss SMEs.

CSEM's **Additive Manufacturing** (AM) aims to develop the technologies necessary to take AM beyond its current uses, in particular extending it into applications that demand significant manufacturing precision. Our focus is on the use of high-performance materials, advanced design through topology optimization, the integration of functional elements such as built-in compliant structure or the printing of sensors, and the hybridization of AM technologies with other manufacturing technologies.

The Focus Area **Photonics** includes both the development of technology bricks such as free-form micro-optics and photonics integrated circuits (PICs) and system-level aspects such as the development of laser sources and laser-based systems, as well as camera solutions based on multispectral imaging.

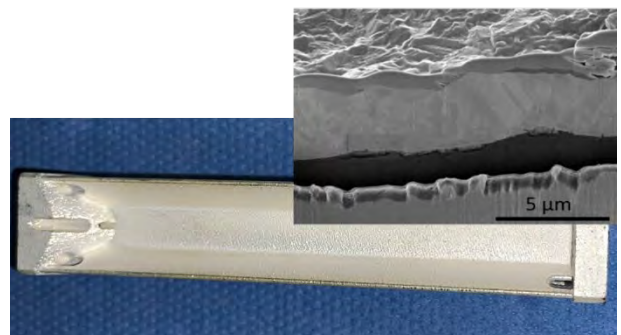
The **Tools for Life Sciences** Focus Area aims to provide the tools and devices necessary for the handling and monitoring of samples and biological entities. With a focus on human health, CSEM technologies aim at improving the quality of life of patients. From concept to prototyping and validation in biosafety level 2 laboratories, CSEM helps industry innovate and develop

new products across the application domains Organ-on-Chip & Organoids, Point-of-Care Diagnostics, and Lab of the Future.

The Focus Area **Scientific Instrumentation** targets meeting future demands for complex systems with ever-higher precision and new features in the fields of space, astrophysics, meteorology, watchmaking, and industrial instrumentation. CSEM's competences in the design, simulation, development, and testing of complex-, miniature-, and hybrid-precision systems have led to advantages in performance, including highly precise and reproducible motion patterns; a far smaller number of movable parts, enabling easier production at lower cost; and the absence of friction and wear.

## Recent highlights

The ever-increasing complexity of surfaces and interfaces developed using technologies such as additive manufacturing requires specifically adapted strategies for surface functionalization. During two successive Innosuisse projects with its partner SWISSto12, innovative metallization processes tailored to the novel materials and surfaces produced by 3D printing were developed to enhance the performance of SWISSto12's radio-frequency components. Swissto12 is a pioneer in the field of additively manufactured radio-frequency components. CSEM developed proprietary processes for metal adhesion and silver metal coatings. These processes enable the conformal metallization of intricate 3D-printed surfaces to a thickness of up to 10 micrometers. This particular process was then adapted to increase its lifetime from several hours to several days while maintaining the high quality and high rate of metal deposition. It also meets Swissto12's requirements for stability, speed, low cost, and environmentally friendly materials. The transfer of knowledge and technology is complete, and industrialization is underway in SWISSto12's facilities.



Silver coated 3D-printed waveguide using CSEM's process—SEM image of a conformally coated 3D-printed surface.

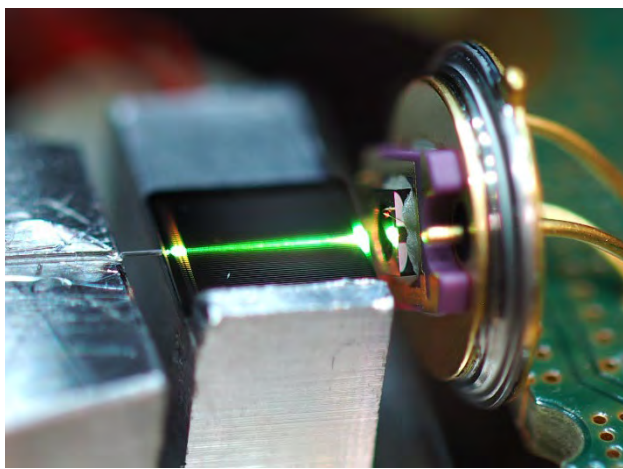
CSEM has established a road map for automated tools for regenerative medicine in fully closed systems. Burns are among the most devastating of all injuries. Each year, 11 million people require medical attention for burns that have a long-term impact on their physical and mental health. Funded through an Innosuisse project with the Swiss start-up CUTISS, denovoCast is the world's first automation platform for advanced tissue engineering for regenerative medicine. It allows four skin grafts to be grown in parallel (a total skin area of 400 cm<sup>2</sup>) containing both dermis and epidermis. The autologous skin grafts developed by CUTISS, named denovoSkin™, are bioengineered

from amplified fibroblasts and keratinocytes isolated from a patient biopsy. Performed in patented labware, the process is now fully automated for 10 days of tissue engineering, including hydrogel mixing and compression, cell seeding, media exchange, and environmental and process control.



*Personalized bioengineered human skin tissue.*

Based on CSEM's developments in photonic integrated circuits (PICs), a compact and direct self-referencing of a mode-locked laser has been demonstrated. Self-referencing turns a mode-locked, femtosecond pulsed laser into a metrological optical frequency comb. The conventional path to achieving self-referencing combines several traditional optical components, which results in high costs and larger sizes. Using CSEM's new lithium niobate on insulator (LNOI) PIC platform, a reduction in size and cost by one to two orders of magnitude has been achieved by combining the required components on a single PIC and increasing the energy efficiency. These results were published in the journal *APL Photonics*. This successful demonstration is the first step in CSEM's deployment of the new LNOI platform in many applications covering several domains, including quantum applications, environmental sensing, and highly nonlinear light sources.



*From a mode-locked, femtosecond pulsed laser to a metrological optical frequency comb. Right to left: optical input fiber, LNOI waveguide (glowing green), and Si-PIN photodiode.*

Using micromanufacturing techniques inherited from MEMS it is possible to batch process, with micrometric precision, centimeter-scale silicon parts featuring extremely fine mechanical functions comprising flexures (FlexMEMS). High-precision mechanical watches in particular can benefit from this approach, which fosters the emergence of novel ideas and allows their concretization at the watch scale. Combining its expertise in

microfabrication techniques and precision mechanisms, CSEM has, since the late 1990s, played a pioneering role in the design and production of novel and innovative watch mechanisms based on the FlexMEMS approach, paving the way for a new trend currently being taken up by several key players in the Swiss watch industry. This year, CSEM has revealed the so-called Double Hammer escapement, the latest FlexMEMS-based escapement designed, produced, and integrated into a watch caliber by CSEM, targeting very precise time keeping (typically +/- 2 s/d) with a regular power reserve. This innovative constant-force escapement is a perfect complement to CSEM's escapements portfolio, which address two complementary market segments: high power reserve and chronometric performance.



*The "Double Hammer" escapement integrated in a watch.*

The manufacturing of devices containing ultrathin walls and having consistent, homogenous mechanical and surface properties is a challenge for AM. In an Innosuisse that involved four partners (SIPPB and CSEM in research and ProtoShape and Medtronic as industrial partners), a full process chain for the custom fabrication of a pacemaker shield based on AM technology has been established using the Ti6Al4V biocompatible alloy. The project encompassed the adaptation of the design for laser powder bed fusion (LPBF), the definition of the raw material (powder), the LPBF process (with wall thickness as thin as 200 µm), and the post processing. This technology reduces shield development lead time and cost by around 80 percent, and the pacemaker shields fabricated cover all medical application specifications.

- |  |  |  |
|--|--|--|
| 1. Monolithically<br>fabricated case<br>- LPBF<br>- HIP/HT | 2. Case cutting<br>in 2 parts<br>- EDM | 3. Final device<br>- Assembling<br>- Welding |
|--|--|--|



*Process steps for manufacturing the pacemaker shield.*

# Advances in the Development of Highly Piezoelectric $\text{Al}_{0.7}\text{Sc}_{0.3}\text{N}$ Layers

M. Dubois, I. Marozau, O. Dubochet

*Summary of the work with examples of applications and/or business opportunities.*

There are many different piezoelectric materials used in all kinds of industrial applications. Many of those are however either bulk ceramics or single crystals. For example, proximity sensors or sonotrodes for ultrasonic imaging are made of bulk lead zirconium titanate (PZT) ceramics, whereas surface acoustic wave (SAW) devices are built on very specific cuts of single crystal quartz, lithium niobate, or lithium tantalate.

Most of the known piezoelectric materials have also been studied in the form of thin films, but only two have reached sufficient maturity to meet the requirements of high-volume production: PZT thin films are usually used in MEMS when large forces or displacements are required, for example in ink-jet printer heads; and aluminum nitride (AlN) is applied for any application demanding linearity or where losses need to be minimized. The best illustration of the latter is the large-scale manufacturing of the RF BAW filters necessary to operate today's multi-band mobile phones.

Despite their overall interesting properties, these two materials suffer from significant drawbacks, which prevents their use in many more applications. PZT is processed at high temperatures, and thus cannot be used on polymer substrates, it contains Pb which tends to be banned from the production lines due to its toxicity, and it is strongly non-linear and lossy. AlN exhibits rather low piezoelectric coefficients, which not only limits its use to very specific applications, but also restricts the miniaturization of devices. Indeed, in a sensor, a minimum area of AlN is required to collect enough electrical charges when the device is experiencing mechanical strain.

It has been shown a few years ago that partially substituting Al by Sc in the lattice improves drastically the performance of the piezoelectric layer, thus partially bridging the gap between AlN and PZT. AlScN with a Sc content lower than 10% is already industrially proven and used in mass-produced devices. However, depositing films with higher contents of Sc is much more challenging: e.g., abnormal non-piezoelectric grains tend to grow when the process conditions or the surface on which the film grows are not perfectly optimized. In addition, and depending upon the deposition method, internal stress can be quite high and even vary locally on the wafer, which negatively affects the fabrication yield of membrane-based devices: stress variations in the range of 1 GPa are quite common. Finally, films with a Sc content higher than 20% are very difficult to etch.

CSEM is tackling these different challenges and is working on the many process steps required to produce high-quality piezoelectric films with a Sc content of 30%. These steps encompass the bottom electrode material, the growth by reactive sputtering at moderate temperature of  $\text{Al}_{0.7}\text{Sc}_{0.3}\text{N}$  from a single alloyed target, and the etching of these layers.

Figure 1 shows the XRD analysis of a  $1\mu\text{m}$  thick  $\text{Al}_{0.7}\text{Sc}_{0.3}\text{N}$  layer. The width of the rocking curve measured around the c-axis of the  $\text{Al}_{0.7}\text{Sc}_{0.3}\text{N}$  exhibits a value of  $1.29^\circ$ , which underlines the excellent crystalline quality of the film.

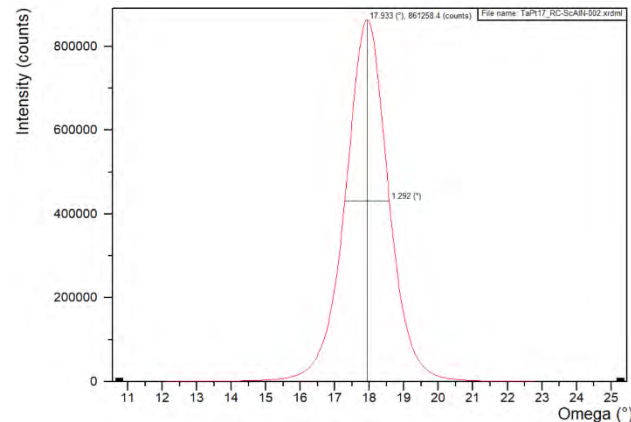


Figure 1: XRD rocking curve of  $\text{Al}_{0.7}\text{Sc}_{0.3}\text{N}$  showing the excellent crystalline quality of the layer.

Figure 2 shows the stress measured in the same layer. The latter is compressive, with a maximum variation of only 160 MPa, which is totally compatible with the fabrication of piezoelectric membranes.

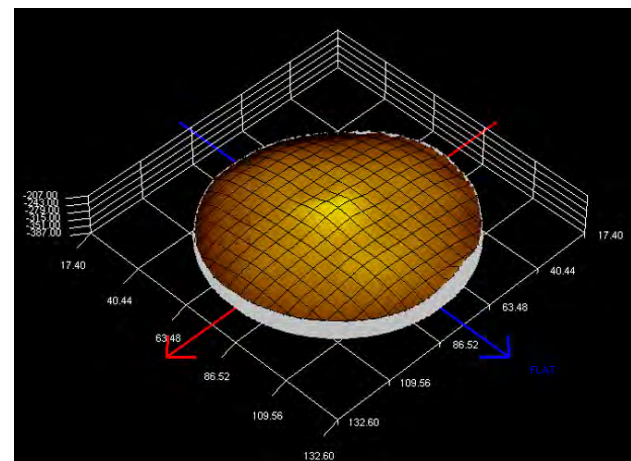


Figure 2: Stress uniformity across a 150 mm wafer of  $\text{Al}_{0.7}\text{Sc}_{0.3}\text{N}$ .

Due to the moderate temperature of the sputtering process, this material can be deposited on many different types of substrates or materials. For example, devices made of polyimide have been produced recently with CSEM's  $\text{Al}_{0.7}\text{Sc}_{0.3}\text{N}$  layers, which exhibit state-of-the-art piezoelectric properties. This is a clear advantage over PZT, and illustrates well the potential of this material.

# Silicon Carbide Pressure Sensor Characterization

A. Hoogerwerf, G. Choong

Piezoresistive-based silicon carbide pressure sensors can operate at temperatures of up to 650°C. This makes them excellently suited for the monitoring of, amongst others, gas turbines and airplane engines. The characterization of the first sensors has been done at room temperature and yielded linear responses.

Of all the physical parameters measured by sensors, pressure is one of the most important ones. Numerous pressure sensors exist for a wide variety of applications. Most of the micromachined pressure sensors in use today are made of silicon. Silicon is an excellent mechanical material and has therefore been widely used. However, the maximum operating temperature of silicon pressure sensors is limited by a number of factors, amongst which the plastic deformation of silicon above 300°C and 1 GPa<sup>[1]</sup>.

Silicon carbide (SiC) is much more resistant to high temperatures and does not deform plastically under 800°C<sup>[2]</sup>. It is therefore suited as a material for high temperature pressure sensors. The fabrication of the sensors needs to use processes and materials that are compatible with its high temperature operation. For example, the metal-to-SiC contact resistances should not drift at the operating temperature range of up to 650°C. We have developed a full fabrication flow for SiC pressure sensors that is compatible with this high temperature operation<sup>[3]</sup>. The fabricated sensor is shown in Figure 1.

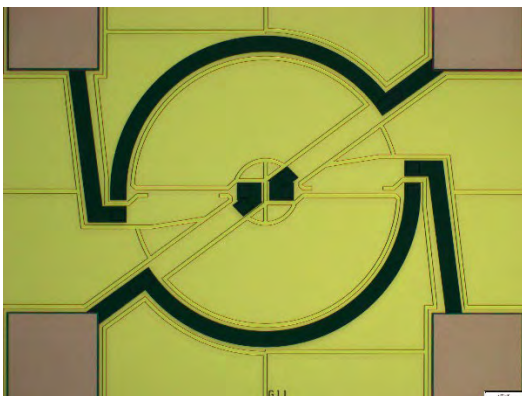


Figure 1: A SiC pressure sensor compatible with an operation temperature of 650°C.

The metallization of the sensor requires a careful choice of materials, as the metals need to withstand an operating environment of ambient air at 650°C. Platinum has therefore been selected as the material for the bonding pads. Not only is it resistant to the high temperatures, it is also compatible with the platinum wire bonding used for the sensors. For the interconnect, another metal has been chosen since platinum reacts with SiC at temperatures above 400°C. The metal forms a good contact with SiC above 1000°C and is stable enough to be passivated

with LPCVD silicon nitride, deposited at temperatures around 800°C. This is a clear indication that long term operation at the maximum operating temperature is feasible.

Apart from the metallization, the most important fabrication challenge has been the etching of membranes in SiC. Silicon carbide is a chemically very inert material and is not attacked by chemicals at temperatures below 100°C. We therefore use a dry etching process to etch 300 µm of SiC, leaving behind a 50 µm thick membrane.

The sensor that was thus fabricated was, for preliminary testing, glued to a backplate to obtain a closed reference cavity. The sensor was then measured at room temperature for its pressure response. The pressure response was measured starting at 0.1 bar, increasing to 6 bar, and then returning to 0.1 bar. The sensor has four piezoresistors connected in a Wheatstone bridge. The current supply to the bridge was 3 mA and the output voltage is shown in Figure 2. The sensors have a sensitivity of 130 µV/bar and the noise level is in the tens of µV.

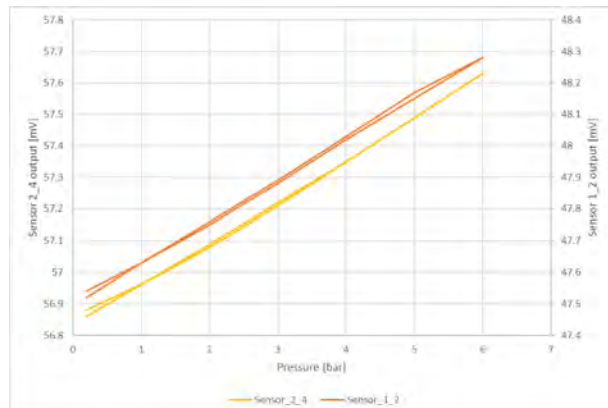


Figure 2: The pressure response of two SiC pressure sensors.

The closing of the reference cavity by gluing is not compatible with a high temperature operation. For this reason, the Laser Assisted Direct Bonding (LADB) method will be used to bond the sensor to a backplate. This bonding method is currently being evaluated for its long-term resistance to high temperatures in ambient air and will soon be used to bond the sensors to the back plates. This will allow the testing of the sensors at much higher temperatures.

[1] J. Castaing, P. Veyssi  re, L. P. Kubin, J. Rabier, "The plastic deformation of silicon between 300°C and 600°C", <https://doi.org/10.1080/01418618108235821>.

[2] K. Niihara, "Slip systems and plastic deformation of silicon carbide single crystals at high temperatures", [https://doi.org/10.1016/0022-5088\(79\)90161-9](https://doi.org/10.1016/0022-5088(79)90161-9).

[3] A.C. Hoogerwerf, *et al.*, "Silicon Carbide Pressure Sensors for Harsh Environments", <https://doi.org/10.1109/TRANSDUCERS.2019.8808586>

# Optoelectronic Packaging for Mid-IR OEM Laser Sources

M. Fretz, R. Jose James, G. Spinola Durante

*Spectroscopic analysis in the mid-infrared wavelength range is a key technology in industrial process control as well as environmental monitoring and medical diagnostics. We present a custom-designed package and corresponding assembly techniques for a temperature-controlled OEM laser source provided by Mirsense. The work was carried out with our partners in the EU project MIRPHAB.*

Fourier-transform infrared (FTIR) spectroscopy is a well-established analytical tool in the laboratory due to the unique absorption spectrum of many chemicals in this wavelength range. However, this technology lacks the compactness and robustness as well as cost-effectiveness for in-line or near-line measurement.

Tunable semiconductor laser sources and photonic integrated circuits (PICs) can fill this gap. The key to success is the integration of these components into a rugged package with small footprint and low power consumption.

Our integration approach is based on the so-called butterfly package made of solid metals (i.e., Kovar and CuW alloys) featuring hermetic electric feedthroughs. A custom-designed housing in combination with carefully selected assembly steps were devised.

The OEM laser source presented here contains following components (see Figure 1):

- Tunable laser source
- Thermistor
- Substrate (to accommodate laser source and thermistor)
- ASIC to control the tunable laser source
- Heat sink (CuW block)
- Peltier element (for temperature control)
- PIC
- Collimating lens
- Butterfly housing
- MIR transparent Window (in the housing)

Integration of all these components required the careful selection of bonding techniques and materials. The main challenges being the CTE mismatch between the bonding components (even though the materials were designed/selected for a reliable bonding) and the step soldering requirement due to the many components that need to be integrated serially. The sequence of assembly is follows:

1. Window to butterfly package bonding with AuSn solder,
2. laser diode to substrate bonding with eutectic AuSn solder,
3. Thermistor to heat-sink bonding with SAC solder,
4. Substrate to heat-sink boding with Sn-based solder,
5. Heat-sink to Peltier to butterfly package bonding with In-based solder,
6. ASIC to heat-sink bonding with conductive adhesive,
7. Establish electric connections between components with wire bonds,
8. PIC to heat-sink bonding with adhesive,
9. Collimating lens to butterfly package bonding with adhesive,
10. Package sealing with seam welding.

CSEM is a one-stop-shop for OEM devices. We provide or support you in establishing device concepts, designing device and assembly concept, procuring components, prototype assembly and testing.

Furthermore, we take care of heat-management issues by carefully selecting and designing the assembly components. If required, we can perform FEM simulations to optimise the design regarding heat dissipation requirements and thermo-mechanical stresses (see Figure 2). Optimisation parameters are bond and component materials and design considerations such as components' shape, size and placement positions. These simulations are validated themselves by comparison with optical thermal measurements to fine-tune the FEM model.

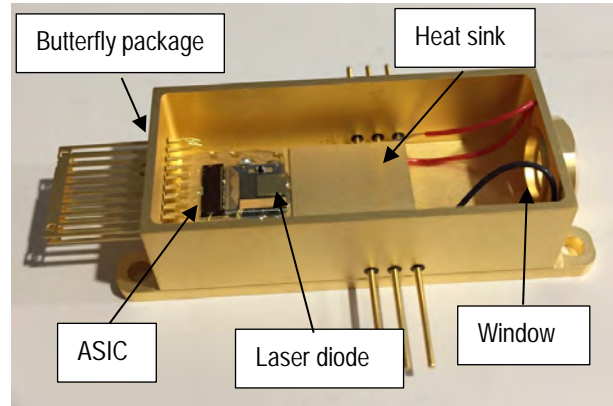


Figure 1: Integrated laser diode mounted on a AlN substrate, then placed on a heat sink made of CuW. The PIC and the collimating lens are not shown.

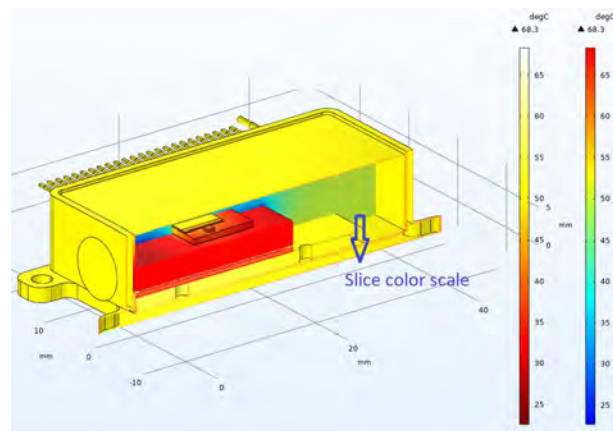


Figure 2: FEM simulation of a mounted laser source to assess the impact of design, component and bond material choices.

This project has received funding from the European Union's Horizon 2020 research and innovation program under grant agreement No. 688265.

# Thermal Management Simulations Based on Advanced Materials and Assembly Configurations

G. Spinola Durante, Rony Jose James, Mark Fretz, A. Hoogerwerf

Tailoring of the thermal budget is critical to achieve stable performances and long-term reliability of low-voltage and high-current DC-DC converters due to their intrinsic high-power dissipation. The proposed (low frequency) LF module package concept, developed in the Heatpack EU project, includes eight GaN switch chips. This Comsol™ study provides a basis both for deciding which technology will be chosen and it enables the path for assembly and integration.

FEM-based thermal simulations with Comsol™ have been performed to model the GaN switch chips mounted onto HTCC ceramic substrates (Figure 1) with dissipated power ranging from 1 W to 35 W per chip, which is in demand for several applications.

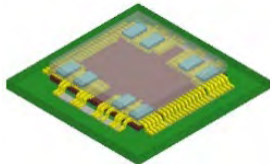


Figure 1: HTCC with 8 GaN chips with a transparent back-side SiC lid mounted on it.

A novel type of configuration for thermal management is shown in Figure 2, where the surrounding in air is also modeled and all the relevant materials and thermal interfaces for connecting the GaN chips on the backside to a SiC-lid. The silicon carbide (SiC) lid has the function of a heat-spreader with very low thermal expansion coefficient and high thermal conductivity, as described in a previous report<sup>[1]</sup>.

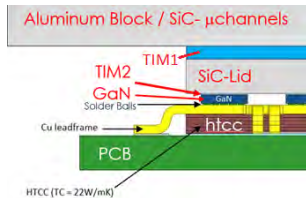


Figure 2: Cross-section of the fully packaged LF module DC-DC converter. TIM2 connection to the GaN chips back-side is emphasized.

To ease the benchmarking of the different thermal solutions we have set a worst-case scenario where all the thermal boundaries, both conductive (PCB/Aluminum block) and convective (ambient air) are set at Tref. = 80°C.

By using these boundary conditions, it is now possible to compare the maximum temperature increase compared to the reference temperature. Simultaneously we can check the percentage of heat flow towards the PCB and to the Aluminum block.

The TIM 2 material properties have been selected according to the Table 1 below. To make the comparison possible a thickness of 50 µm has been defined.

Table 1: TIM2 thermal properties.

Category	Material	Thermal conductivity
TIM2	Gap Pad	6 W/mK
TIM2	TIM2ATM	100 W/mK
TIM2	Silver sintering paste	150 W/mK

The thermal performance represented as  $\Delta T(K) = (T_{max} - T_{ref})$  helps to compare the different technology solutions independently of the reference ambient/heatsinks temperature. This value also scales linearly with the power dissipation.

In Figure 3 a typical cross-section is shown where the maximum temperature is indicated by an arrow (GaN chip active area).

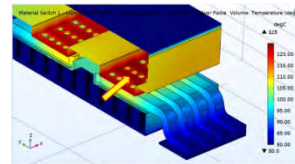


Figure 3: Cross-section of the LF module package simulation results.

In the summary Table 2, numbers for temperature increase ( $\Delta T$  in Kelvin) are shown in relation to dissipated power per chip and lid technology. Results are shown only for TIM 2 selected as Gap Pad with 6 W/mK.

Table 2: Thermal results based on a selection of material configuration and assuming TIM2 is defined as a Gap Pad with 6 W/mK.

Material - Thickness	$\Delta T(T_{max}, -80^\circ C)$		
	$P_{thermal} = 1W$	$P_{thermal} = 10W$	$P_{thermal} = 35W$
No-Lid	3.61	36.2	128.7
Kovar - 2mm	2.58	25.8	91.1
W90Cu10 - 2mm	1.77	17.7	62.2
Cu Diamond - 2mm	1.56	15.6	54.9
SiC - 0.35mm	1.87	18.7	65.7
SiC - 2mm	1.67	16.7	58.6
SiC $\mu$ -channels 2000W/mK - 0.9mm	1.55	15.5	54.3

Results show that the lid material and its thickness are limiting factors for the thermal budget only if heat dissipation per chip ( $P_{thermal}$ ) is  $\geq 10$  W. In this case a significant reduction of the maximum chip temperature of larger than 15 K can be obtained. The lid thickness has an impact since the thinner it is, the more difficult it becomes to spread the heat and to remove. As a side note the choice of an optimal lid solution is also affected by price and thermo-mechanical properties for reliability.

In conclusion the study enabled to select the following lids: a Kovar-lid was chosen as a baseline for production modules. Both SiC-lid with active micro-channel cooling and Copper-Diamond (CuD) lid were selected for demonstration purposes only. The latter SiC/CuD solutions come with a price-performance advantage, but these technologies are still in development.

CSEM acknowledges funding from the European Union's Horizon 2020, Space Research Program, Technologies for European non-dependence and competitiveness, under grant agreement No. 821963.

[1] G. Spinola Durante, et al., "Advanced Packaging for Simultaneous Hermetic Lid Sealing and Chip Backside Heat Removal", CSEM Scientific and Technical Report (2020), 24.

# Active Cooling-based Packages for Power Electronics

A. Hoogerwerf, R. Jose James

The ever-increasing power density of power electronics necessitates innovative solutions to remove the generated waste heat. We are currently working on using MEMS-based two-phase fluidic coolers that will have heat conduction properties that are better than copper or silver. Moreover, the MEMS-based technology uses silicon or silicon carbide substrates that match more closely the thermal expansion coefficients of the electronics than the metals do. The packages based on these coolers are aimed for use in satellites but will also find their way in terrestrial applications.

The evolution of semiconductor technology has led to ever-improving performances of the fabricated transistors. This leads to higher density circuits that switch even higher amounts of power with, as a consequence, high power density "hot spots" becoming more frequent in these circuits. An effective removal of this waste heat is necessary to limit the temperature rise in these areas, as the temperature increase leads to a degradation of the circuit and reduces its lifetime.

An effective way of removing heat is presented by oscillatory heat pipe loops. The functioning of such loops is schematically presented in Figure 1. The top side of the structure is attached to the heat generating device and the bottom one is attached to a heat sink. The structure is partially filled with a liquid under low pressure. Once the heat is turned on, a part of the liquid evaporates to form gas bubbles. The design of the loop with its alternation of wide and narrow parts, makes that the bubbles move back and forth in a chaotic way between the hot and the cold part of the structure. Each time a bubble reaches the cold side of the structure it condenses (partially), giving off the latent heat of evaporation of the fluid that it has obtained during the bubble formation on the hot side. The physical movement of the bubble therefore moves the heat from the hot side to the cold side. If the cross-sectional area of the loop channels is small enough, the effect of the orientation on the functioning of the structure is minimal and it can be used in micro-gravity environments, such as space. Moreover, the heat pipe loop can be made small enough, so that it has the size of a power electronics package and can therefore become a part of it.

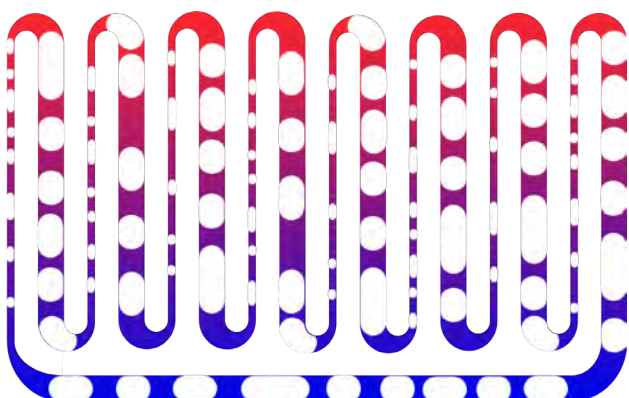


Figure 1: Schematic representation of an oscillatory heat pipe loop.

Within the EU project HEATPACK<sup>[1]</sup> (<https://heatpack.eu/>), the oscillatory heat pipe loop is pursued for two high-power electronics packages for use in satellites. In a first phase, test structures have been made out of silicon-glass sandwiches, as shown in Figure 2. Such structures are easy to fabricate and allow the observation of the filling and functioning of the devices, even though the heat conductivity of the glass is poor. The filling of the test structures and their sealing under low pressure has been a big challenge. This is due to the fact that silicon and glass

are both brittle materials that cannot be threaded or otherwise mechanically attached. The solution has been to metallize the silicon, fill the structure with the fluid through a small opening, and then solder a small solder ball onto the opening under a low pressure. The filling and soldering require careful control, since the fluid, when present in the opening area, has a tendency to evaporate and prevent a good solder joint from forming.

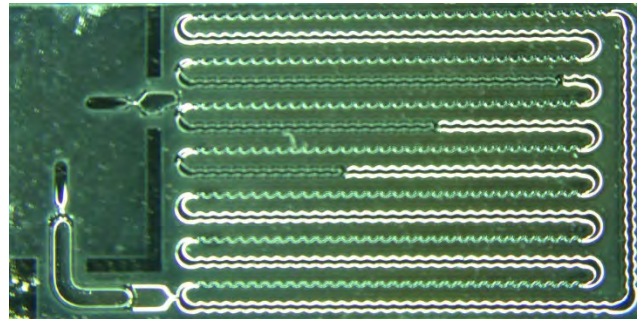


Figure 2: Silicon-glass structure partially filled with IPA.

Based on the successful tests of the silicon-glass structures, a new fabrication run has started with modified layout. Two layouts have been made, which are compatible with the two packages pursued in the HEATPACK project. The layout of the channels has been optimized to maximize the heat flow from location of the heat generating circuits to the cooler parts of the package. This time, the structures will be fabricated in silicon carbide, which is a good heat conductor itself and is also optically transparent to allow the monitoring of the device filling. A layout of the device for a radio-frequency power amplifier package base is shown in Figure 3.

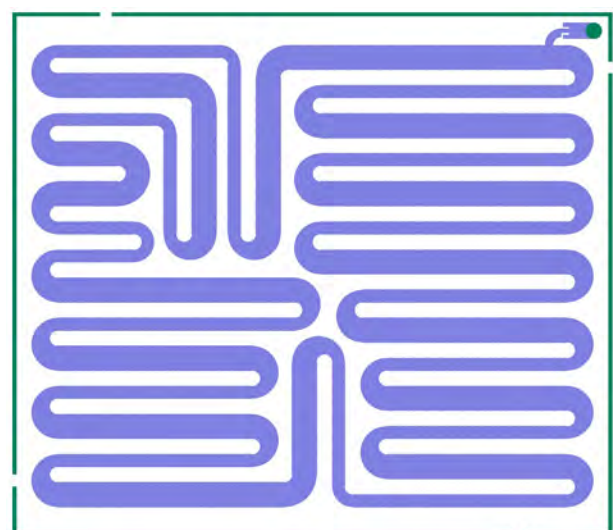


Figure 3: Layout of a RF package baseplate with integrated heat pipes.

<sup>[1]</sup> EC project funded under grant 821963.

# Reliability Assessment and Development of Qualification Standard for Miniaturized RF Electromechanical Relay for Space Applications

I. Marozau, S. Unterhofer, M. Dagon, O. Sereda, M. Berry\*, P. Gonin\*, G. Aubry\*, A. Flaceau\*, R. Enquebecq\*

A test program was developed for the reliability assessment and evaluation of radiofrequency (RF) miniaturized electromechanical relays (MEMR) as required for space application. The test program allows to carry out the required qualification of newly designed MEMR device for its use in space as well as in terrestrial applications (e.g., redundancy rings in telecom satellites or 5G technology equipment). It is aligned with the existing ESA standards for the direct current (DC) electromechanical relays. At the same time, the test and evaluation procedures are designed to meet specific needs and requirements of the RF application domain. The developed test procedure was successfully applied for the reliability evaluation of the MEMR developed within the framework of SELECTOR EU project (grant number 821973). The performed failure mode analysis allowed to improve the mechanical robustness of the device to match the qualification requirements.

The aim of SELECTOR project is to develop a miniaturized RF relay primarily for space applications, which shall replace the existing bulky electromechanical RF switches. The developed MEMR device must be qualified for the space domain. Up to date, there are no existing ESA standards for the qualification of RF relay components since the existing electromechanical RF switches are bulky and are therefore considered as systems, not as components. CSEM has developed a test program that can be used for the reliability assessment and evaluation of the RF MEMR components in the future. The test program will be presented to ESA as a basis for creating a new ESA qualification standard. The test program is aligned with the existing ESA standards for the DC relays. It addresses the main environmental and operational severities applicable for the usage in space:

- High and low operation temperatures, rapid temperature changes, thermal conditions for the reflow soldering
- Humidity
- Mechanical shock and vibrations (random and sine sweep)
- Electrical cycling with / without loads, voltage over-stresses

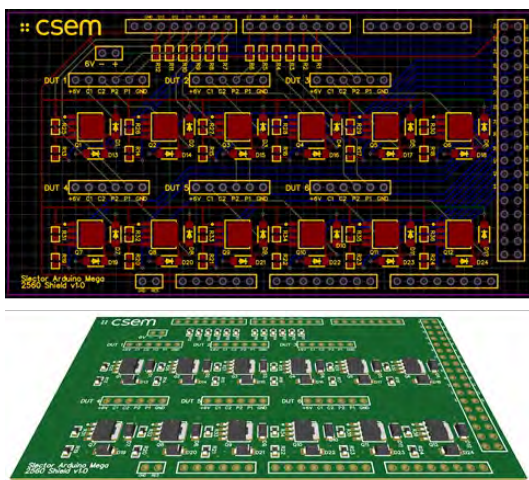


Figure 1: Developed test bench PCB and its schematics.

An innovative testing approach for the mechanical testing was developed. It allows to perform in-situ electrical characterisation by recording the relay state during the mechanical impact and detecting any micro-opening or micro-closing of the relay's contacts. Dedicated test benches were designed and constructed for these tests, as well as for performing the switching cycling tests at high and low temperatures (Figure 1). For the lifetime evaluation, CSEM has performed electrical characterisation during the high-temperature operation tests. In order to assess the degradation of relays with time, DC contact

resistance, RF insertion loss and isolation (for the frequencies up to 26.5 GHz), as well as switching time were measured. The obtained test data allows to elaborate a lifetime model that is based on the Arrhenius law for the temperature-accelerated life test:

$$R(T) = \gamma_0 \exp\left(\frac{-E_a}{kT}\right)$$

Lifetime estimation was performed for the developed MEMR products operating in various conditions (such as temperature of use and switching frequency). Figure 2 shows the obtained lifetime from the low current switching cycling test at 125°C.

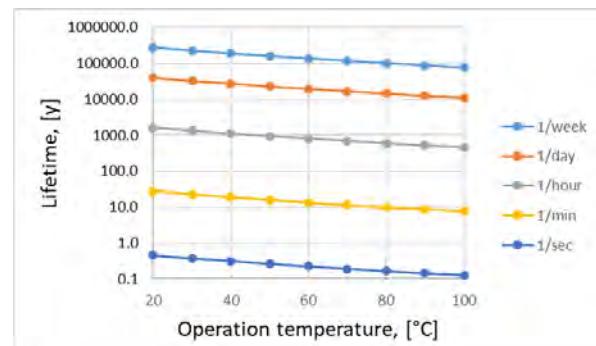


Figure 2: Estimated lifetime of MEMR devices as function of operation temperature and switching frequency.

As shown in Figure 2, the lifetime of about 10 years or more is achieved for the switching frequencies of 1 cycle per minute and less at any operation temperature up to the maximum MEMR rated temperature of +95°C. This is a good result for the dedicated space applications. However, to ensure even a higher level of reliability, additional long-term tests are planned.

The performed test campaign and subsequent failure mode analysis allowed to improve the resistance of the developed MEMR to the deteriorative effects of the mechanical shocks. After implementation of improvement solutions, a significantly better mechanical shock robustness was achieved. The improved MEMR can withstand mechanical shocks of up to 3000 g and continuous mechanical vibration with the acceleration levels of up to 50 g.

The classical reliability evaluation test program will be complimented with an innovative bi-parameter testing approach that will include simultaneous mechanical and thermal stresses. This will allow to evaluate the device reliability under the conditions closer to the real applications, where multiple stress factors may act on the device at the same time.

\* Radiall, Aubervilliers (FR)• EPFL

# Highly Efficient AM-based Cooling System for High-Power Electronics

H. Constantinou, F. Boudoire, S. Lani

One of the most relevant, effective, and important applications of industrial 3D printing is high-performance heat exchangers to manage extreme heat in the aerospace and energy segments. Taking advantage of CSEM 3D printing platform focused on small scale capability and precision manufacturing, a new generation of pulsating heat pipe (PHP) has been designed, produced, and tested including its fluidic and mechanical interfaces. PHP are typically used for cooling down high power electronics.

With its capability to produce complex shapes, additive manufacturing (AM) – also known as 3D printing – is offering the possibility to produce parts that were not possible to make before or to reduce the number of assembly steps by combining several parts together. One interesting functionality that can be easily produced in AM parts are channels, with the possibility to produce nozzles, fluidic manifold, and heat exchanger. Within this last category, pulsating heat pipe (PHP) are offering a very efficient way to transport the heat from a hot region to a cold region without the need of an external force, like pumps. They combine the principles of both thermal conductivity and phase transition and are constituted of a fluid sealed inside a metal enclosure, typically a pipe. PHP are typically made by a combination of machining and assembly; or by bending a tube to the desired shape. These manufacturing methods present the main disadvantage of coolant leakage and packing limitation.

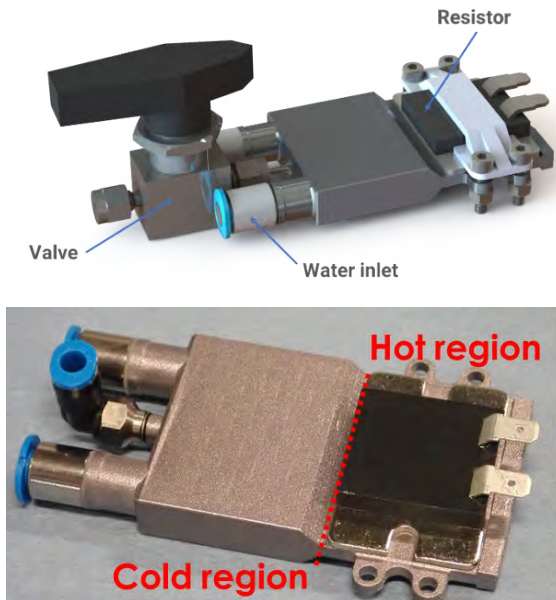


Figure 1: (top) CAD design of the PHP with illustration of the resistor and connector assembly; (bottom) manufactured PHP with connectors assembled.

Within the past few years, CSEM has developed the capability of producing AM parts embedding thin wall structures that can enable very efficient PHP as wall thickness is participating to the thermal resistance directly through its thermal conductivity or indirectly by reducing the volume/surface available for pulsating pipes. The evaluated PHP design is consisting of 48 channels of  $0.6 \times 1.7$  mm and a channels separation of 0.15 mm, corresponding to the minimum wall thickness in AISI12 material. In the cold region, an embedded water-cooling system condensate the refrigerant. All fluidic interfaces, for the condenser and PHP filling channel, are used with an as-built threading that does not require any post machining, reducing the cost per part. No leakage has been observed during testing, despite an internal PHP pressure rising to 20 bars.

The performances of the PHP have been evaluated in collaboration with JJCooling®. First the optimal filling ratio has been determined, with a value of 50%. With the combination of a thermal camera and temperature sensors, the thermal performances of the PHP were assessed. The PHP start pulsating at 10 W and a thermal resistance of 0.15 K/W was measured up to the dry-out of the system that happened around 440 W (average heat flux of  $49 \text{ W/cm}^2$ ). The PHP orientation is affecting the thermal resistance by only 10% in the worst case. In comparison, state-of-the-art commercially available PHPs have a thermal resistance of 0.11 K/W. Hence, 3D printed PHPs are close to outperform their equivalent produced by traditional manufacturing, considering that a wealth of improvements can be implemented, such as internal polishing. Moreover, additive manufacturing grants light weighting opportunities thanks to its design flexibility. Table 1 is presenting a comparison between the PHP, the PHP without refrigerant and the volume equivalent part in solid aluminium and copper, and reported to the mass of each part, the gain of the PHP is of 6 to 10 times more making it very interesting for application in aerospace.

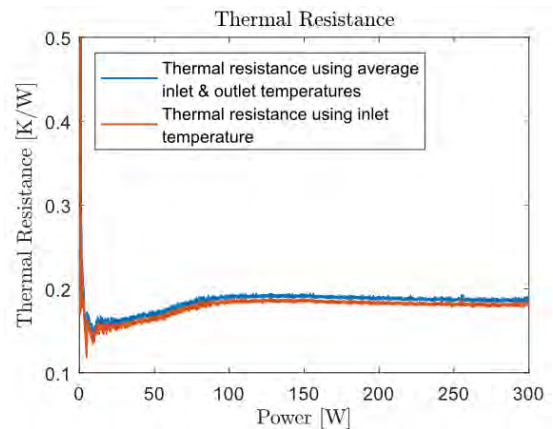


Figure 2: Thermal resistance of the PHP in function of the resistor input power.

Table 1: Comparison of the PHP with an aluminum and copper blocks.

Configuration	TR Thermal resistance [K/W]	Mass [g]	TRxM [gK/W]
PHP	0.15	20.6	3.09
PHP without refrigerant	1.09	19.2	20.93
Solid Aluminium	0.71	25.8	18.31
Solid Copper	0.37	87.3	32.3

# Promising Metallic Additive Manufacturing Technologies for 3D-shaped Millimeter-Wave Components Production

S. Unterhofer, A. Vorobyov, O. Sereda, M. Dadras

Laser powder bed fusion (LPBF) technology used for waveguide antenna manufacturing. Taking in consideration electrical conductivity, density and powder availability Cu10Sn, Al12Si, and Scalmalloy were investigated. Internal channel roughness found to be influenced by printed orientation related to build plate and alloy used. Al12Si showed the suitable alloy related to defined specifications.

Laser powder bed fusion (LPBF) technology is among additive manufacturing (AM) processes permitting fabrication of complicate metallic parts with nearly complete design freedom. This technology permits to manufacture very complex design with high precision 3D shape mm-waveguide antennas. The most important parameters for choosing the materials for high efficiency waveguide antenna defined as electrical conductivity, coefficient of thermal expansion, density and powder availability and printability for LPBF process. Three alloys were investigated for this purpose: CuSn Bronze, AISi, and Scalmalloy. The printing process focused on establish printing parameters to achieve high density, channel geometry and their roughness accompanying high electrical conductivity

## Materials and Methods

Three alloys were investigated: Cu10wt%Sn, Al12wt%Si, and Scalmalloy (Mg 7wt%, Sc 2wt%, Zr and Mn < 1wt%). TRUMPF TRUPRINT 1000 used for printing samples. Printed samples were investigated using Scanning Electron Microscope (FEI Scios2). Internal channel roughness measured using Keyence 3D laser Scanning Microscope. Mechanical properties measured on tensile test samples printed in Z direction.

## Results and discussion

The investigation, presented in this paper, focused on wave divider (Figure 1a) for all three alloys. The samples having different orientations related to built plate were printed (Figure 1b and 1c). All printed parts showed the density >99.5% in as printed state.



Figure 1: Wave divider antenna subject of present paper (a), different orientation related to build plate (b) and printed parts (c).

Cross section of printed samples prepared (Figure 2) and average internal roughness was measured.

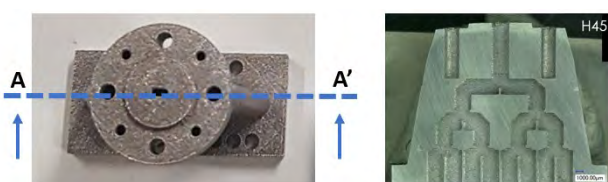


Figure 2: Example of printed sample with orientation of H45 (Figure 1b) and its cross section for internal channel roughness measurement.

Table 1 presents the average roughness measured for different alloys and different printed orientation. Al12Si showed the minimum of roughness in as printed state among other alloys. Cu10Sn found to be less suitable and controllable for internal

channel roughness. On the other hand, built orientation needs to be chosen correctly to achieve the optimal roughness.

Table 1: Internal roughness measured according to different printed orientation and different alloys.

Alloy	Cu10Sn				Al12Si				Scalmalloy			
	H45	HV45	V45	V90	H45	HV45	V45	V90	H45	HV45	V45	V90
Ra (μm)	18	17.9	17.2	18.1	9.1	9.2	7.5	8.1	16.4	17.4	12.7	12.8

Electrical resistivity of printed samples measured by four points methods and results presented by Table 2. The electrical conductivity is less than the bulk materials which related to presence of micropores.

Table 2: Electrical resistivity of as printed samples.

Alloy	Cu10Sn	Al12Si	Scalmalloy
Electrical resistivity ( $\Omega \cdot m$ ) $10^{-8}$	3.5	6.0	8.6-7.3*

\* After heat treatment 4hrs at 325°C.

In parallel mechanical properties was another issue for needed application. The mechanical properties measured and table 3 presents the obtained results for all three samples in as built state.

Table 3: Mechanical properties of as built samples.

Alloy	Young's Modulus (Gpa)	Ys 0.2% (Mpa)	Tensile strength (Mpa)	Elongation (%)
Cu10Sn	104±7	349±10	479±8	17.9±2.1
Al12Si	71±6	314±1	460±7	7.0±0.4
Scalmalloy	68±7	285±7	367±9	18.4±3.2
Scalmalloy*	61±7	478±13	516±13	12.7±1.3

\* After heat treatment of 3hrs at 325°C

The mechanical properties showed the deviation from existing bulk materials values which could be related to presence of defects in as built samples. Further post treatment as Hot Isostatic Pressure (HIP) would improve and adjust the properties.

## Conclusion

LPBF technology permitted to print waveguide antenna with complex design and geometry not affordable by any conventional classical methods. The internal channel roughness showed to be related to printed direction related to build plate. Among three investigated alloys, Cu10Sn, Al12Si, and Scalmalloy, bronze showed less suitable for this application. Al12Si showed to be best solution for controllable roughness in internal channels. Electrical conductivity is less than values announced for bulk material. This could be related to presence of microdefects in printed parts.

This project is supported by Clean Sky under grant agreement No. 886696.

# Development of Additively Manufactured Functionally Graded Components

V. Pejchal, H. Zhang, P. Bowen<sup>\*</sup>, O. Sereda

*Functionally Graded Materials (FGMs) are characterized by continuous or discontinuous gradients of composition, structure, and properties. FGMs can mitigate the strain accumulation within the gradient zone between dissimilar materials and reduce the risk of delamination. Steel-copper FGM is attractive due to the combination of good mechanical properties and the outstanding thermal conductivity. In recent years, the laser powder bed fusion (LPBF) is considered as a novel and attractive solution in FGMs fabrication due to its high flexibility. In this work we demonstrated the manufacturing of a 316L-pure Cu FGM using LPBF. As-built samples exhibited an ultimate tensile strength of  $218 \pm 19$  MPa, which is comparable to annealed pure Cu<sup>[1]</sup>.*

For FGM manufacturing, laser powder bed fusion (LPBF) system Trumpf TruPrint 1000 equipped with an infrared laser source (max. power 200 W) was first used to fabricate pure Cu, 316L, and three intermediate composites 316L-75 wt% Cu, 316L-50 wt% Cu, 316L-25 wt% Cu. Feedstock powder mixtures were prepared by mechanical mixing of 316L and copper powders with Dv(50) of 23  $\mu\text{m}$  and 33  $\mu\text{m}$ , respectively. For each composition, a Design of Experiment (DoE) approach considering several LPBF parameters such as laser power, scan speed, and hatch distance was performed to obtain the lowest porosity ( $\varphi$ ). Samples in the form of  $6 \times 6 \times 6$  mm<sup>3</sup> cubes were fabricated (Figure 1a) for further characterizations. Figure 1b shows vertical (parallel to the build direction) cross-sections of samples with the lowest  $\varphi$  in each composition. The lowest  $\varphi$  decreases with decreasing Cu content except for 316L-25 wt% Cu, in which the presence of solidification cracks along the build direction was observed.

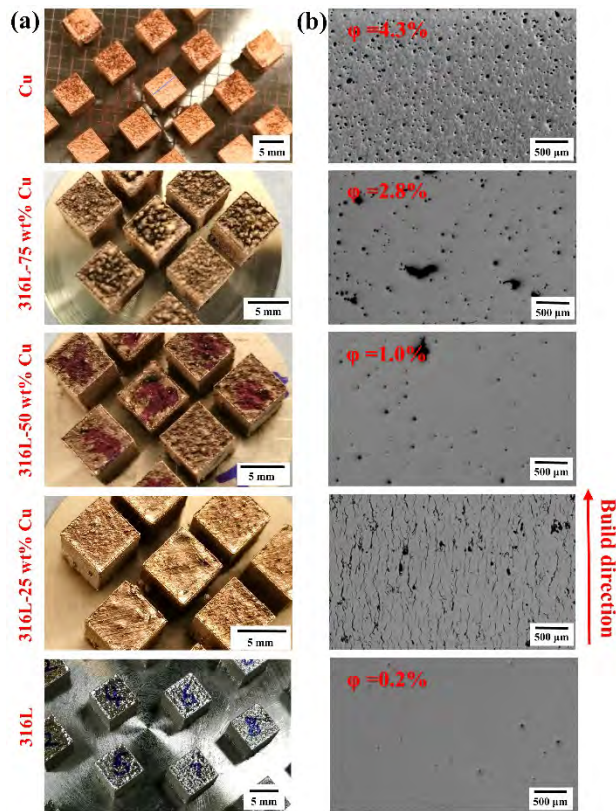


Figure 1: (a) As-built samples in different compositions fabricated using LPBF. (b) Optical micrographs showing vertical cross-sections of as-built samples in five different compositions with the lowest  $\varphi$ .

On this basis, FGM components with five sub-parts in the vertical (discontinuous) gradient were fabricated in the order from 316L to Cu (Figure 2a). Vertical cross-sections of these five parts are

presented in Figure 2(b-f) to compare with that of corresponding cubes. For 316L and 316L-50 wt% Cu, the  $\varphi$  of the FGM part and that of the cube were comparable. A 50% increase in  $\varphi$  was observed for the FGM Cu part, where irregular pores of few hundred micrometers can be observed (Figure 2b). On the contrary, for 316L-75 wt% Cu, there was a reduction in  $\varphi$  for the FGM part due to the reduction in the number of large pores (Figure 2c). The change in  $\varphi$  can be attributed to the change in thermal conditions during the manufacturing of FGM samples associated with the underlying material.

To evaluate the bond quality of the present FGM system, tensile samples with 2.5 mm diameter (Figure 2g) were fabricated with no observable delamination at all four interfaces. The fracture occurred within the 316L-25 wt% Cu part, which exhibited presence of microcracks. Nevertheless, the ultimate tensile strength reaches  $218 \pm 19$  MPa, which is comparable to that of annealed Cu (200 MPa).

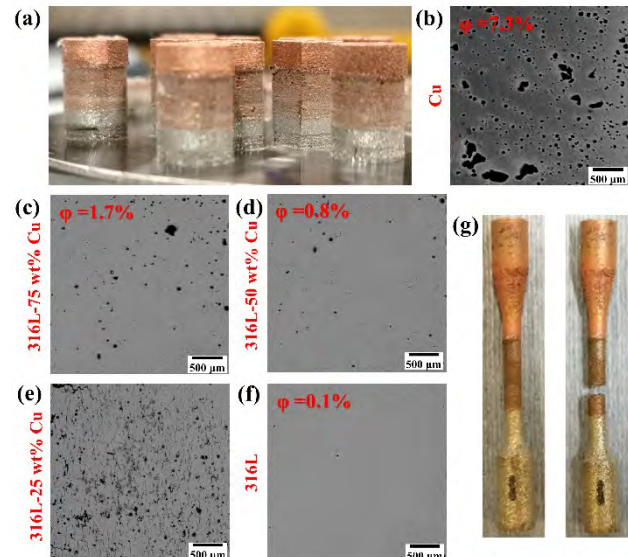


Figure 2: a) As-built FGM samples. Optical micrographs showing the vertical cross-section of b) Cu; c) 316L-75 wt% Cu; d) 316L-50 wt% Cu; e) 316L-25 wt% Cu, and f) 316L part within as-built FGM samples. g) As-built FGM tensile specimen before and after test.

In conclusion, feasibility of manufacturing of 316L-pure Cu FGM using LPBF was demonstrated. Porosity below 5% was achieved for all five studied compositions. Tensile strength of FGM samples is comparable to annealed Cu. The obtained results pave the way towards the fabrication of FGM components using LPBF. Combination with adapted post processing such as HIP could improve the mechanical properties of printed FGM.

\* EPFL

<sup>[1]</sup> E. Calla, et al., J. Therm. Spray Technol., 2006, 15, 255-262.

# Development of High-Specific Stiffness Composites by LPBF

V. Pejchal, C. Gremion, G. Bernard, R. Logé<sup>\*</sup>, O. Sereda

Metal Matrix Composites (MMCs) offer the toughness and ductility of a metal with the high stiffness and strength of a brittle reinforcement phase (usually ceramic) that allow to engineer the needed properties for a specific application. Especially, specific Young's modulus is improved since the applied load is borne by the stiff reinforcement<sup>[1]</sup>. Aluminium alloys are materials of choice due to their high-stiffness-weight ratio. Whereas alumina and titanium carbide are interesting as reinforcement because no fragile phases are formed, and good particle-matrix bonding can be obtained. The drawbacks of conventionally produced MMCs are the poor machinability and the difficulty to uniformly disperse the particle reinforcement. The advent of additive manufacturing and especially laser powder bed fusion (LPBF) delivers advantages to overcome these issues. The present study showed promising results with titanium carbide used as reinforcement. LPBF aluminium based MMC parts exhibited Young's modulus of  $115 \pm 5$  GPa ( $35 \text{ GPa} \cdot \text{cm}^3 \cdot \text{g}^{-1}$ ), an improvement of nearly 40% compared to the conventional aluminium alloys.

Selective laser melting (SLM) was conducted by TruPrint1000 (Trumpf GmbH, Germany) to produce A20X™ matrix reinforced with (i) 15vol.% of Al<sub>2</sub>O<sub>3</sub>, namely A20X-15P10, and (ii) 15vol.% of TiC, namely A20X-15TiC. The raw powders used were: (i) A20X™ gas atomized ( $D_{v50}=43 \mu\text{m}$ ), (ii) Polygonal Al<sub>2</sub>O<sub>3</sub> vapor deposited particles ( $D_{v50}=12 \mu\text{m}$ ), and (iii) TiC comminuted particles ( $D_{v50}=12 \mu\text{m}$ ). The powder blends were mechanically mixed.

The following section focus on development of A20X-15P10 MMCs. Firstly, single-line walls (consecutive layers of single-track) were studied to narrow down the laser power and laser scanning speed window (Figure 1a, b). Design of experiment (DOE) was performed to optimize the recipe and study the effect of laser power, laser scanning speed and hatch distance on the relative density of cube specimens (Figure 1a). Among the best parameters, several cubes were printed to assess the repeatability of the process. The porosity of material cubes with the highest overall density showed relatively high variability in the range of 1 to 10%. A representative microstructure is shown in Figure 1c where Al<sub>2</sub>O<sub>3</sub> is observed in both forms: (i) particles uniformly distributed and (ii) long-strip Al<sub>2</sub>O<sub>3</sub> oriented along the building direction. Particle size distribution analysis of the embedded particles within the matrix revealed a  $D_{v90} = 4 \mu\text{m}$ . Therefore, it was argued that larger Al<sub>2</sub>O<sub>3</sub> particles tended to be pushed along the melt pool boundary and fused together to form long-strip Al<sub>2</sub>O<sub>3</sub> while smaller ones are rejected by the solid/liquid front. This hypothesis was supported by the distribution of Al<sub>2</sub>O<sub>3</sub> within the single-line walls Figure 1b.

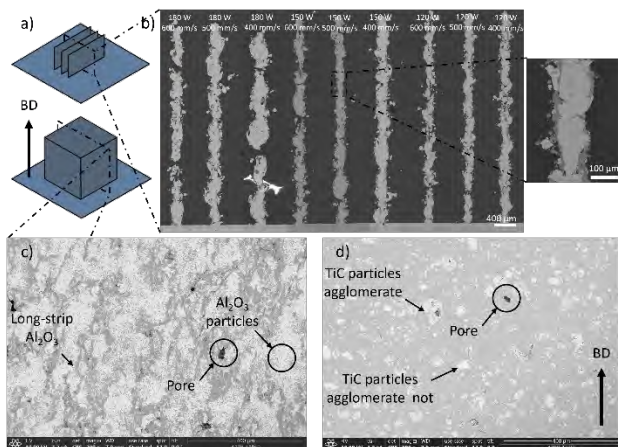


Figure 1: a) Schematic illustration of single-line walls ( $4 \times 6 \text{ mm}^2$ ) and cubes ( $7 \times 7 \times 7 \text{ mm}^3$ ); SEM micrographs of mirror polished cross section of b) single-line walls, c) A20X-15P10 cube and d) A20X-15TiC cube.

\* EPFL

<sup>[1]</sup> A. Hauert, et al., J. Mech. Phys. Solids 57 (2009) 473-499.

The formation of long strip Al<sub>2</sub>O<sub>3</sub> shows that the temperature reached was near the melting temperature of Al<sub>2</sub>O<sub>3</sub> ( $2072^\circ\text{C}$ ). Near this temperature two phenomena occur: (i) evaporation of aluminium (boiling temperature:  $2470^\circ\text{C}$ ) and (ii) the reduction of Al<sub>2</sub>O<sub>3</sub> by aluminium ( $1520^\circ\text{C}$ ). Both are known to destabilize the powder bed quality and thus hamper the processability.

A20X-15TiC MMCs were manufactured with the same optimal parameters previously studied for A20X-15P10 MMCs. The microstructure is shown in Figure 1d. The relative density measured from SEM micrographs was  $99.6 \pm 0.2\%$ . TiC particles embedded within the matrix were uniformly distributed and well embedded in the matrix showing improved wetting compared to MMC reinforced with Al<sub>2</sub>O<sub>3</sub>.

Young's modulus of as-built MMCs were measured from the tensile test experiments, see Figure 2. The Young's modulus of A20X-15P10 and A20X-15TiC were respectively  $52 \pm 18$  GPa and  $115 \pm 5$  GPa. The specific Young's modulus calculated for the later, using the theoretical density, was  $35 \text{ GPa} \cdot \text{cm}^3 \cdot \text{g}^{-1}$  which is nearly 40% higher compared to conventional aluminium alloys (near  $25 \text{ GPa} \cdot \text{cm}^3 \cdot \text{g}^{-1}$ ). The plastic deformation contained some discontinuity which was attributed to the Portevin-Le Chatelier effect<sup>[2]</sup>.

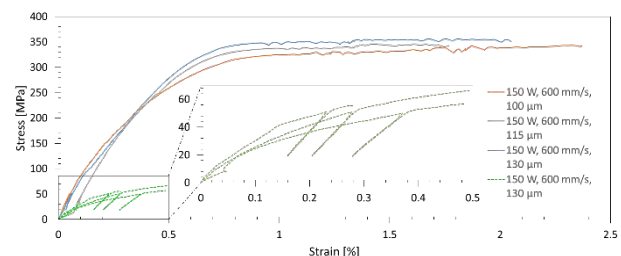


Figure 2: Stress-Strain curves of as-built MMCs with elastic unloading to determine the Young's modulus of a) A20X-15P10 (continuous line) and b) A20X-15TiC (dot line).

In conclusion, aluminium based MMC with uniform particle reinforcement distribution and high density were successfully manufactured using LPBF and 15vol.% of TiC particles as the reinforcement. Mechanical characterization showed outstanding specific Young's modulus of  $35 \text{ GPa} \cdot \text{cm}^3 \cdot \text{g}^{-1}$  which is 40% higher compared to the aluminium matrix. Results also show that using Al<sub>2</sub>O<sub>3</sub> micro-particles are less suitable as the reinforcement in LPBF process compared to TiC. This is mostly due to the lower wetting of Al<sub>2</sub>O<sub>3</sub> by molten aluminium and the potential reduction of Al<sub>2</sub>O<sub>3</sub> with aluminium and/or evaporation of aluminium at high temperatures reached during the process.

<sup>[2]</sup> P. Mair, et al., Materials Science & Engineering A 799 (2021) 140209.

# Validation of the Metal Additive Manufacturing Pilot Line Manuela

E. Onillon, D. Novo, G. Perruchoud, H. Saudan, V. Pechal, O. Sereda

Metal additive manufacturing (AM) allows, with the use of advanced design methods, the production of high added value components, at levels that cannot be reached with conventional manufacturing techniques. Still, the AM-based manufacturing sequence implies large amounts of critical steps – design for AM, AM fabrication, post processing, etc. – compared to conventional production sequences. In the frame of the H2020 research project MANUELA [1], an open-access metal additive manufacturing Pilot Line facility, was deployed covering the whole production sequence, to show the full potential of metal AM for industrial production. The pilot line was validated with the design and manufacturing of six use cases, covering a wide range of application fields.

Started in October 2018, The H2020 research project MANUELA deployed, with the collaboration of 20 EU partners, an open access pilot line addressing key limitations of metal additive manufacturing (AM) process, namely limited speed, limited capability of right first-time production, limited number of qualified materials, limited of further data analytics. It is mainly composed of a hardware and software layer as depicted in Figure 1.

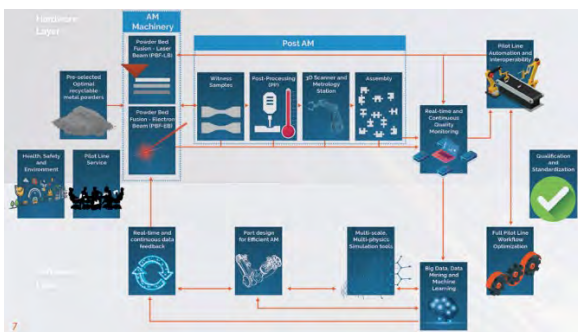


Figure 1: Manuela constitutive layer.

The pilot line's hardware layer covers two main state of the art metal-AM technologies – laser powder bed fusion (LPBF) and Electron Beam Melting (EBM) – as well as the post-treatment process, essential to complete the whole part production sequence, including control & shipping.

The pilot line's software layer strongly relies on improved design tools (Hexagon – MSC software suite), accounting for the manufacturing and post processing.



Figure 2: Manuela's software layer constitutive elements.

In order to ensure a zero-defect manufacturing, a precise design workflow was established, covering part optimization

(topological optimization) in terms of mass and eigen frequencies, AM optimization to avoid part deformation during the manufacturing process as well during the post processing.

Furthermore, to improve the reliability of the manufacturing process, an Artificial Intelligence based real-time feedback was developed (currently being implemented).

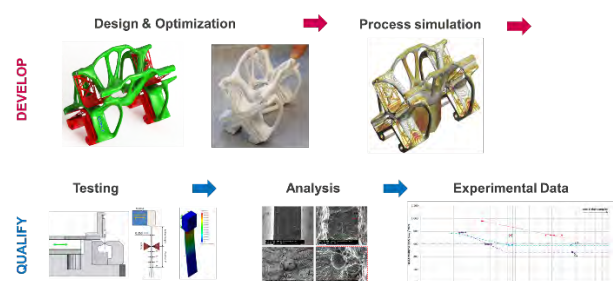


Figure 3: Design workflow.

In order to validate the pilot lines, six challenging industrial use cases were designed and manufactured, covering avionics (helmet display housing), space (slip ring rotor and stator), medical (cranial implant), power (gas turbine combustor and injector), automotive (rocker and brake support) and energy (fuel nozzle). Use cases allowed to commission the proposed software tools as well as the manufacturing logistics, such as the Manufacturing Execution System. At design stage, key challenges such as redesign for AM, optimization of the printing orientation, support design, deformation as well as accounting for postprocessing (such as subcomponents welding) were successfully overcome.

Manufacturing parameters were optimized accounting for novel materials such as copper.

Examples of produced use cases are provided in Figure 4.



Figure 4: Examples of produced use cases.

[1] European Union's Horizon 2020 research and innovation programme under grant agreement No. 820774.

# Towards Metal-Organic Framework based Field Effect Chemical Sensors for Pesticides Detection

A. Finelli, G. Andreatta, X. Lefèvre

Organophosphates are widely used as pesticides in intensive agriculture. Being strong nerve agents, they are one of the most common causes of poisoning in the world. Due to their adverse effect on health and environment, it is critical to develop a compact, reliable, fast, selective, and low-cost sensor able to detect pesticides traces in aqueous medium such as drinking water, foods, and soil samples.

Exhibiting a high surface area, metal-organic frameworks (MOFs) can be customized to adsorb efficiently the targeted analytes. Interest in integrating such porous materials as selective adsorbent layers in chemical sensors has increased recently.<sup>[1]</sup> Nevertheless, refinement of sensing materials and transducer mechanisms is still essential to increase the reliability, selectivity, and response kinetics to a level suitable for commercial applications. While MOFs seem excellent candidates for selective sensing, numerous studies demonstrate a higher response for the selected analyte compared to interferents because the compounds are tested each separately. In real-world applications, the sensor will be exposed to all components simultaneously, including some interferents present at much higher concentrations than the analyte. One way to address the selectivity challenge is to combine cross-sensitive sensors to form an array or "electronic nose" (e-nose)<sup>[2]</sup>. When the combined response of the array contains enough non-correlated information, the focused analyte can be monitored in a complex background via chemometric data analysis.

Due to the variety of organophosphate pesticides, nitro-based compounds have been focused on this study. Luminescent Zr-MOFs have been synthesized for the specific uptake of the toxic analytes from 1,2,4,5-tetrakis(4-carboxyphenyl) benzene and Zr(IV).<sup>[3]</sup> Characterization by X-ray diffraction (PXRD) and SEM (Figure 1) shows a flower-like morphology. Due to the luminescence properties of the MOF, the first sensing tests have been done by fluorimetry. Together with a surface area corresponding to 1453.2 m<sup>2</sup>/g and micropores size of about 0.60 nm, this MOF has shown a particular affinity with nitro-based family by the quenching of the luminescence of the fluorophore via adsorption (Figure 2).

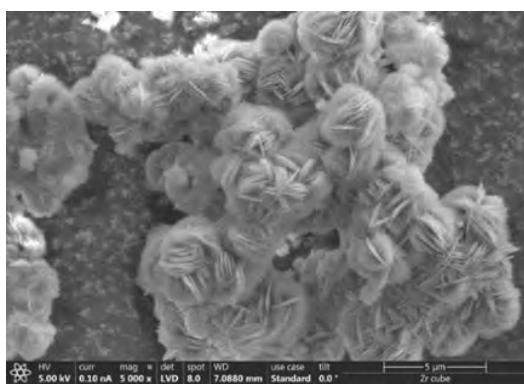


Figure 1: Scanning electron micrograph of flower-like Zr-MOF.

[1] H. Furukawa, K. E. Cordova, M. O'Keeffe, O. M. Yaghi, "The chemistry and applications of metal-organic frameworks", *Science* 30 (2013) 341.

[2] Freund R., et al. "The Current Status of MOF and COF Applications". *Angewandte Chemie International Edition* (2021).



Figure 2: Photoluminescence responses of Zr-LMOF against 6 organophosphates compounds containing nitro group. The final concentration of all the compounds is 0.012 mM.

In order to confirm such affinity, other chemical signals have been investigated. The selected Zr-MOF has been integrated as an active layer sensor on an electrochemical transducer. Preliminary tests have been undertaken by coating GCE electrode with Zr-MOF active layer to detect Methyl-parathion pesticide. A clear Methyl-parathion detection has been observed by DPV voltammogram (Figure 3) in particularly low-pesticide concentrations (0, 0.5, 1 and 5 ppm). Different patterning techniques as well as coating processes are also studied to ensure the reliability and the scalability of the deposition method whilst maintaining sensing efficiency of the active layer. Other electrochemical methods and detection limits are currently being tested for different nitro-based pesticides.

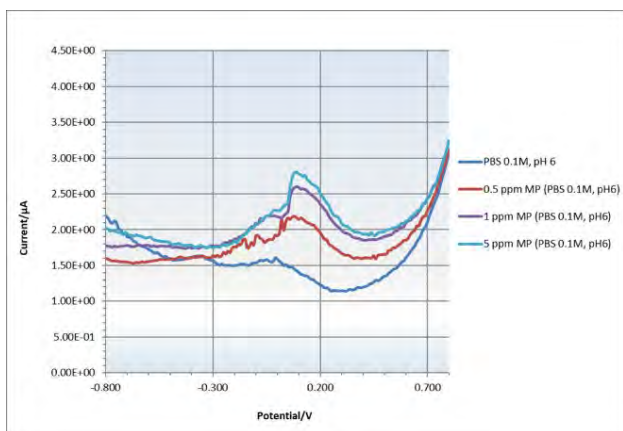


Figure 3: Preliminary DPV voltammograms of Zr-MOF active layer on GCE electrode with the varying concentrations of Methyl Parathion (0 to 5 ppm) in 0.1 M PBS, pH 6.

Further characterization will be carried out to evaluate and confirm the performance of the final array sensor. The reliability, selectivity and sensitivity will be measured and compared with performances measured by spectroscopy, including the calibration of the sensor.

[3] K. He, et al., "A water-stable luminescent metal-organic framework for rapid and visible sensing of organophosphorus pesticides", *ACS applied materials & interfaces* 11 (2019) 26250.

# Molecular Imprinted Polymer Sensor for Nicotine Detection

X. Lefevre, X. Bulliard, G. Voirin, M. Crenna, N. Glaser, M. Zinggeler, M. Palmieri, S. Steiner, R. Pugin

Nicotine is the main active component of tobacco. Its quantification in aerosols and particularly the amount delivered in lungs is of great interest to track its impact on health. Current detection methods rely on the use of mass spectroscopy coupled with liquid chromatography. However, this requires highly qualified personnel and expensive equipment. In this context, Molecular Imprinted Polymers (MIP) as sensing layer deposited on electrodes is a very promising alternative for the development of an efficient electrochemical sensor allowing fast and cheaper quantification of nicotine in aerosols.

Inhalation toxicological investigations and the development and pre-clinical testing of inhalable drugs require, in many instances, assessing the deposition kinetics of aerosol constituents on the epithelia of the respiratory tract or on in vitro models thereof. A commonly applied in vitro approach is the deposition of the test aerosol on a trapping surface under controlled conditions, followed by quantification of deposited individual targeted aerosol constituents. Particularly when working with complex aerosols such as smoke, this requires highly sensitive and selective analytical methodologies such as coupled chromatography - mass spectrometry. Such methodologies commonly require highly qualified personnel and expensive equipment and are not accessible in many instances. In this context, a promising technology for the quantification of aerosol deposition are chemically selective sensors and among them, molecularly imprinted polymers (MIP) showed very interesting abilities to selectively concentrate the target molecule for a better read-out. They could also be integrated in transducers to build a complete sensor that could be adapted to any detection measurement (from molecular spectroscopy like IR or NMR to optical detection or electrochemistry).

In our research, we developed an electrochemical sensor for the detection of nicotine in aerosols in the presence of various contaminants. MIP was used as sensing layer to selectively detect nicotine. MIP-based sensors are usually built by depositing preformed nanoparticles of MIP, but this leads to rather thick layers. We therefore focused on a polymer-based MIP formulation deposited as a thin film on the electrode and cured by UV exposure. Despite the polymer layer is insulating, we managed to deposit a very thin film (few 10ths of nanometers) to ensure sufficient recorded signal by using Pico-Pulse Jetting. Pico-Pulse Jetting ensured low volume and a precise control of the coated area as the response is optimal when the working electrode only is coated. Another way to polymerize the MIP directly on the electrode could be electrodeposition. This technique allows precise control of the material deposited on the surface, but also requires specific formulations comprising electropolymerizable monomers.

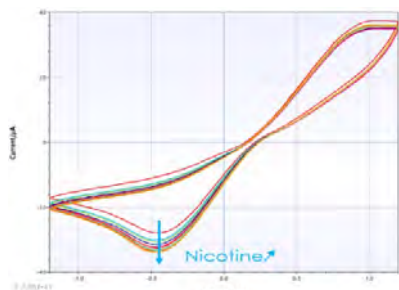


Figure 1: Detection of nicotine by MIP deposited on electrode.

MIP-based nicotine sensors were thus printed and further characterized. Direct monitoring of nicotine at its rather high redox potential was found to damage the sensing layer. Therefore, an indirect electrochemical measurement was

developed using Fe(II)/Fe(III) as probe, avoiding high potential and deterioration of the MIP layer. This Fe(II)/Fe(III) potential value is directly linked to the presence of Nicotine and Figure 1 shows an example of nicotine detection with this approach.

For such kind of sensors, calibration is then needed, and Figure 2 shows a typical calibration curve obtained with our sensor for successive runs. The linearity is sufficient over the nicotine concentration range of interest and allows nicotine quantification.

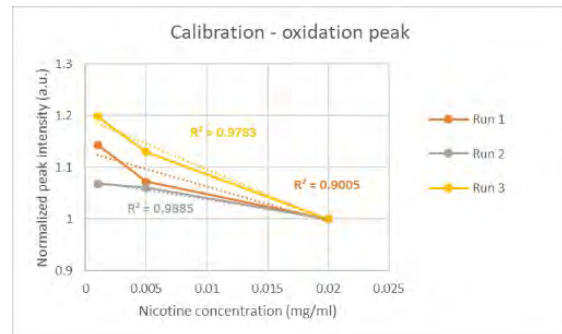


Figure 2: Calibration of MIP-based nicotine sensors.

Finally, as this sensor is meant to be used in various conditions including complex polluted media, we also investigated its sensitivity, its selectivity, and its stability. Very low amounts of nicotine (down to few ng/ml) were detectable in short times (10-15 min) allowing straightforward and fast measurements. The selectivity was very high even in presence of nicotine metabolites such as cotinine as illustrated in Figure 3. Regarding stability, the sensor was exposed to various pH, solvents and biological media conditions and showed sufficient reliability for the foreseen application.

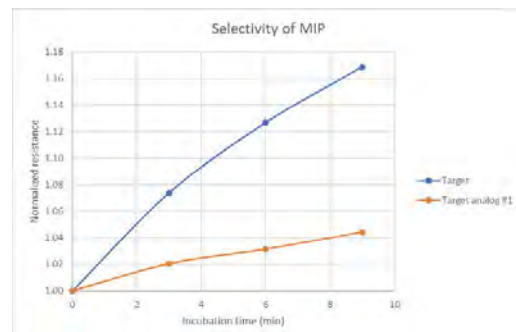


Figure 3: Selectivity of the MIP-based sensor.

In summary, we developed an efficient MIP-based electrochemical sensor for the quantification of nicotine in complex media. We adapted the MIP technology to our detection platform by formulating a new recipe compatible with our deposition process by Pico Pulse Jetting. We thus obtained robust sensors that could be further accommodated to a wide range of analytes. The number of applications that can benefit from this approach is thus large, and comprises fields as wide as biomedicine, environmental, chemical and safety monitoring.

# Barrier Treatment on Cellulose to Control Release of Elements in Blood Testing Device

X. Lefèvre, X. Bulliard, M. Crenna, M. Palmieri, R. Pugin, J. Déglon\*

In medicine, for blood analysis, an accurate quantification of several ions, such as calcium, is needed. DBS has developed a card to collect and store blood for further analysis. This device is composed of a microfluidic channel and a cellulose card, on which the blood sample is stored in a dry state until analysis by redissolution. However, the cellulose is exposed to calcium during manufacturing, and this calcium can be released during redissolution resulting in a contamination of the blood sample. It is therefore crucial to avoid this co-release. In this context different ways to block or get rid of calcium ions in the cellulose paper were investigated.

Blood analysis is common for health monitoring. Miniaturized collection systems based on the use of a single drop are of interest for the ease of use and the comfort of patients. DBS has developed such a system, as illustrated in Figure 1. Blood is collected through a microfluidic channel and stored in a dry state on a cellulose part. This card can be shipped to a laboratory where the blood is released by redissolution. Upon redissolution, the blood must not be contaminated by any constituents of cellulose. During manufacturing, cellulose is however typically treated with calcium sulfate, which can be trapped in the fibers and could potentially be co-released with the blood sample, interfering in the analysis. With our partner DBS, CSEM studied in detail this co-release and developed solutions to prevent it. For any treatments applied on cellulose, its blood adsorption property should not be degraded. It is to be noted that for all experiments, a substitute of blood with the same physical properties was used (Jonnin solution).

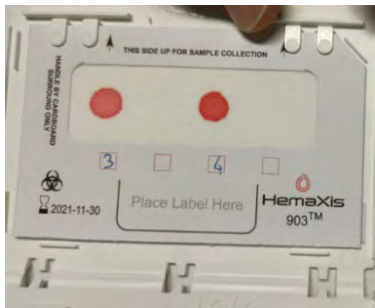


Figure 1: DBS blood analysis system.

Calcium release from cellulose can be detected by spectroscopic techniques, such as Inductively Coupled Plasma Mass Spectroscopy (ICP-MS). An alternative method based on colorimetry was developed to quantify calcium in the cellulose part and to follow its release in various conditions, underlying its possible interference with blood samples. A colorimetric titration based on a color-changing dye was used to determine the exact concentration of calcium within the fibers, as illustrated on Figure 2. This method highlights the shift and change of absorbance intensity as a function of Ca concentration. This type of experiment confirmed the release of Ca from the fiber to the blood sample, in proportion that would alter the real Ca measurement in the blood of a patient.

To prevent the release of Ca from the fiber, different strategies were investigated:

- Cleaning of calcium using acidic solution
- Trapping of calcium in cellulose using complexing agents
- Formation of a barrier layer on cellulose using sol-gel technology
- Combination of two latter techniques.

\* DBS System SA, Gland (CH)

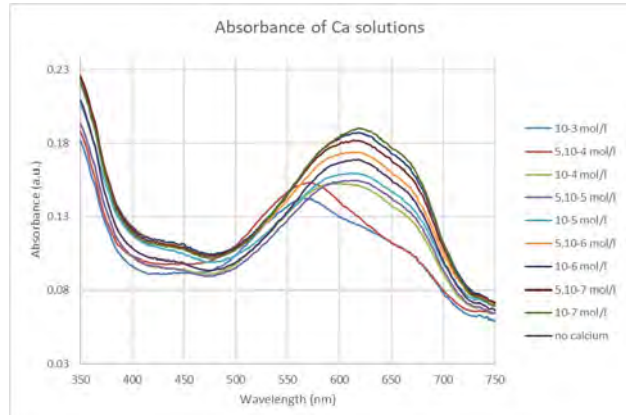


Figure 2: Colorimetric analysis of calcium.

By cleaning with an acidic solution, it was possible to remove most of the Ca in the cellulose fiber, but this cleaning step should be done ideally during manufacturing. We thus also explored the possibility to trap calcium within cellulose using complexing agents. We managed to fully complex calcium and avoid its release using EDTA. However, the excess of complexing agents in the fiber led to the absorption of calcium from blood samples. To prevent it, a sol-gel barrier coating was developed and deposited on the cellulose fiber by dip coating. The barrier layer proved sufficient to avoid the release of calcium as well as the adsorption of calcium from blood to cellulose. Best results were obtained by combining both approaches, i.e., the complexion with EDTA and the sol-gel barrier layer, for which the Ca release was below the limit of detection without any signs of absorption from the blood sample. In addition, the blood absorption capacity of cellulose was not altered by this treatment as shown in Figure 3.



Figure 3: Adsorption of blood samples on reference (left) and treated (right) cellulose.

In summary, an efficient barrier treatment to prevent calcium release from the cellulose was developed, enabling an accurate quantification of this ion in blood. This barrier coating can also be used to prevent the contamination from other elements, such as Al, and for the exact quantification of other elements in blood such as Se, Mg or Zn.

METEOR project is supported by the Interreg France-Suisse 2014-2020 program and has benefited from the European Regional Development Fund (FEDER), and on the Swiss side from federal and cantonal grants (Neuchâtel, Vaud). CSEM thanks them for their support.

# Selective Electroless Metal Deposition on Micropatterns Produced by Aerosol Jet Printing

G. Andreatta, N. Hendricks, M. Crenna

*Electroless plating of metals is an important industrial technique for metallizing insulators and objects with geometries that are difficult to coat by electroplating. Selective plating onto specific predefined areas of complex structures is advantageous in gaining higher design flexibility with applications from microwaves to optics but it remains challenging depending on the complexity of the structures and the nature of the substrate materials. CSEM has developed a versatile platform for localized metallization which combines the flexibility, high resolution, and materials availability of aerosol jet printing (AJP) with electroless metal plating.*

Direct integration of functional electronic circuits on complex three-dimensional devices responds to the growing demand for personalized and smart products. A variety of electronic components – for examples, conductive traces, antennas, sensors, transistors, batteries – could therefore be directly embedded into three-dimensional (3D) devices without the need for implementing large printed circuit boards, load-bearings, or protective structures [1].

Patterning high-resolution multi-metal layers without using subtractive lithography poses a substantial challenge. We report a generic and new additive manufacturing approach for the deposition of such layers by using a combination of aerosol-jet printing (AJP) and electroless plating (EP). EP is commonly used to metallize non-conducting surfaces. A wide range of metals and metal alloys containing copper, nickel, cobalt, gold, platinum, palladium, etc. can be deposited with this low-temperature, cost-effective, external field-free, chemical method. Two patents have been filed on the topic. AJP is a flexible and cost-effective technology that prints functional materials with high resolution on 2D and 3D substrates. It has been used for the development and prototyping of devices for consumer electronics, sensors [2], Medtech and life science [3].

In this approach, AJP is used to print patterns containing the catalytic particles that will induce the selective deposition of metal and metal alloys. Figure 1 shows catalysts seed lines printed on flexible substrates as well as the patterns obtained after selective electroless deposition. The thickness of the deposited electroless layer is tunable, from tens of nm to several micrometers.

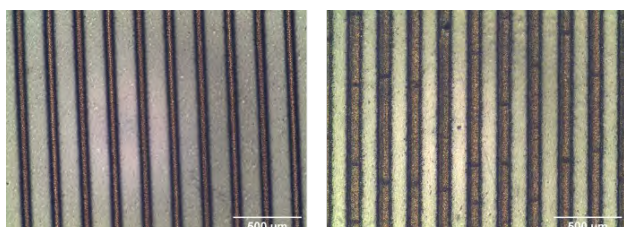


Figure 1: (left) Patterns obtained by AJP of inks containing catalytic nanoparticles; (right) The same patterns after electroless deposition of gold metal.

This method is highly selective, suitable for complex surfaces and can be easily scaled-up. The surface of the metal patterns obtained after electroless deposition is smooth; the metal layer

deposited by electroless deposition is dense and conforms to the surface of the initial pattern (Figure 2).

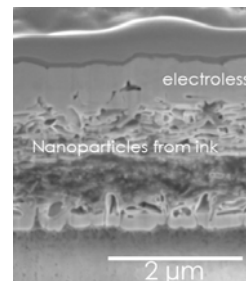


Figure 2: Scanning electron microscopy cross-section of gold deposited on silver-flake AJP ink. The electroless gold is conformal, dense and produces a smooth surface.

In addition to selective electroless gold plating, alloys of nickel and iron (NiFe) have been deposited on AJP-printed catalytic patterns (Figure 3). NiFe alloys are known to produce more robust diffusion barriers in microelectronic applications and have interesting magnetic properties.

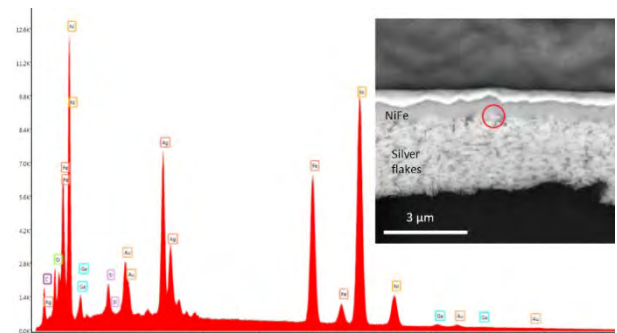


Figure 3: Energy-dispersive X-ray analysis of the silver-NiFe interface showing the presence of nickel and iron in the alloy. Inset is the corresponding scanning electron microscopy cross-section of NiFe deposited on catalytic AJP ink.

We demonstrated a method for the selective deposition of metal and metal alloys on AJP printed catalytic patterns. This approach can easily be translated on complex structures obtained by 3D printing. CSEM plans to further investigate these technologies for applications in the field of space and aeronautics, sensors and consumer electronics.

[1] S. Lee, M. Wajahat, J. H. Kim, J. Pyo, W. S. Chang, S. H. Cho, J. T. Kim, and S. K. Seol "Electroless Deposition-Assisted 3D Printing of Micro Circuitries for Structural Electronics", ACS Appl. Mater. Interfaces 11 (2019) 7123.

[2] S. Lani, N. Hendricks, O. Chandran, H. Saudan, L. Kiener, F. Cosandier, N. Marjanovic, J. Schleuniger, J. Kaufman, R. Jose James, "CHAMELEON—Compliant Mechanism with Embedded Sensing", CSEM Scientific and Technical Report (2019) 17.

[3] G. Voirin, S. Lani, A. Bionaz, R. Smajda, R. Pugin, "Aerosol-jet Printing, an enabling Technology for printing Electrodes, Interconnects, Sensors or Antennas on 2-or 3-D Parts", CSEM Scientific and Technical Report (2016) 63.

# Colored Surfaces Based on Micro and Nanoparticle Self-assembly

N. Blondiaux, X. Bulliard, G. Christmann, M. Crenna, J. Diaz

We report on the manufacturing of colored coatings based on micro-nanoparticle self-assembly. Three approaches have been investigated to produce omnidirectional structural colors. Particle diameters ranging from 100 nm up to 2.5  $\mu\text{m}$  were used to control interference and light scattering effects in the coatings. Small particles have been used to produce waveguiding effects leading to dark colors when combined with thin  $\text{TiO}_2$  films. Coatings based on larger particles allowed visible light scattering and lead to colored or white coatings.

There is a major trend in the manufacturing of micro and nanostructured surfaces and coatings to control the color of object. These so-called structural colors have the advantage of being non-fading, with an optical response that can be controlled via the materials employed and structure length-scales of the structures. Many examples can be found in nature (bird feather, butterfly wings, chafer's exoskeleton), which challenged many scientists for the understanding of the underlying physics [1] and inspired engineers to produce new types of colored surfaces (biomimicry).

During the past decade, CSEM has been developing processes to produce surfaces and coating with controlled length-scales at the micro and sub-micro scale. One of the main technique developed is colloidal self-assembly, which involves the use of organic and inorganic particles having well defined sizes. These have been used in past project (Interreg project Harissa) to produce opalescent surfaces [2].

The goal of present work is to investigate how particle self-assembly can be used to produce angle-invariant colors and how particle dimensions can be used to produce three types of colors.

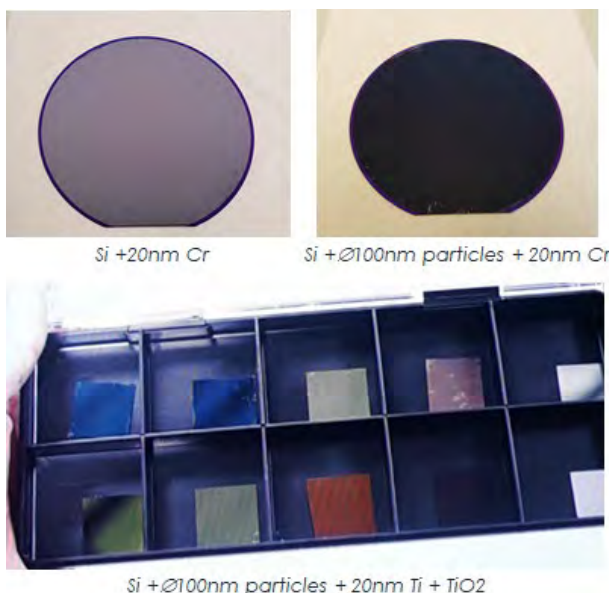


Figure 1: (top) Photos of silicon wafers showing the optical effect of  $\phi<100\text{ nm}$  particle coatings when combined with a Cr layer; (bottom) Photos of samples coated with  $\phi<100\text{ nm}$  particles, titanium and ALD  $\text{TiO}_2$ .

(1) **Nanoparticles ( $\phi<100\text{ nm}$ )**: monolayers of nanoparticles have been used in combination with metal and metal oxide thin films (Figure 1). At this scale, the particle monolayer is a dielectric cavity acting as a waveguiding layer, which leads to a strong light absorption by the covering metal thin film. A further layering of titanium oxide on top induces an additional interference effect. The contrast of the interference effect can be maximized when matching the reflectance at the air-titania and titania-metal interfaces.

(2) **Sub-microparticles ( $200\text{ nm}<\phi<300\text{ nm}$ )**: in this second case, micrometer thick amorphous colloidal array of particles doped with carbon black have been deposited on glass surfaces. Unlike opals, the lack of ordering in the layer produces angle-invariant colors (Figure 2). As the color arises from coherent light scattering by the particles, it can be adjusted by tuning their dimensions. The carbon black doping suppresses multiple scattering and enhance the structural colors.

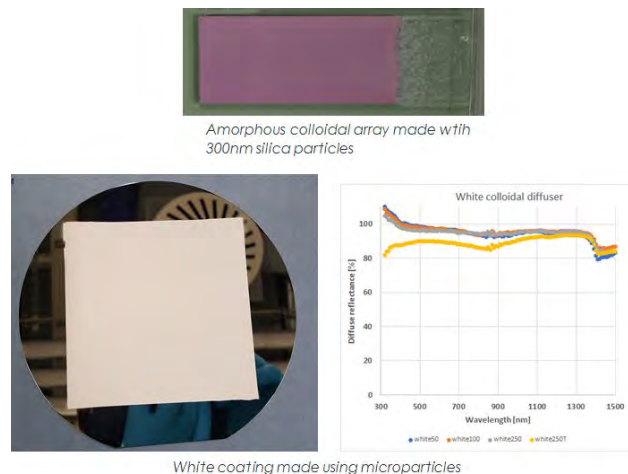


Figure 2: Photo of a glass slide coated with a silica amorphous colloidal array.

(3) **Coatings based on microparticles ( $1\text{ }\mu\text{m}<\phi<$ )**: in the last case study, formulations based on large particles have been developed to spray coat thick white layers. The particles were larger than one micrometer and the thickness of the layer was in the range of few tens of micrometers to be thick enough to maximize multiple light scattering.

To conclude, particle self-assembly was used in three different ways to produce various optical effect. The control of the length scale of the structures is made by tuning by the size of the particles. The main targeted application is to control the aesthetics of surfaces.

[1] C. Kilchoer, P. Pirih, U. Steiner, B. D. Wilts, "Diffusive structural colour in *Hoplia argentea*", Journal of Experimental Biology (2019) 222.

[2] N. Blondiaux, M. Crenna, P. F. Chauvy, M. Diserens, B. Oudot, R. Pugin, "Micro-nanostructuring of 3D Surfaces: on the Manufacturing of Functional Parts for the Medical and Watchmaking Industry", CSEM Scientific and Technical Report (2020), 34.

# Self-cleaning Surfaces for Optical Sensors in Harsh Environment

N. Blondiaux, M. Crenna, X. Bulliard

We report on the development of self-cleaning coatings for the protection of optical sensors operating in harsh environments. In the frame of the EU project CHARM, a vision system is integrated in a machine tool for in-line process monitoring. Several types of coatings have been developed to protect the optical window of the vision system from oil and cutting chips projections.

There is currently a global growth in the optical sensor and vision system markets for the development of connected product and processes. Such sensors are now widespread in engineered products and equipment such as cellphones, smart watches and are crucial components in the development of autonomous vehicle. In the manufacturing industry, vision systems and sensors are more and more integrated to improve process automation and quality control. However, one key point remains the acquisition of data or images reliable enough to be treated with advanced algorithms. For some applications, this is a challenge due to the harsh environmental conditions in which the sensor operates. Many technologies are thus being developed to improve the cleanliness of optical sensors, LIDARs and camera<sup>[1,2]</sup>.



Figure 1: Photograph of the Swiss lath from Tornos used in the project CHARM in which the vision system will be integrated.

CSEM is currently participating in the EU project CHARM (Figure 1)<sup>[3]</sup> which focuses on the development of systems for condition monitoring, predictive maintenance, automation, real-time manufacturing control, and optimization. In a use-case lead by the Swiss company Tornos, a vision system is integrated in a Swiss lath to perform in-line metrology of machined parts. The main objective is to avoid off-line, statistical characterizations of the produced part and improve the throughput.

One of the challenges for this integration is to keep the surface of the vision system clean and prevent the contamination due to cooling-oil droplets and metal chips produced during milling.

Two approaches are considered and will be combined in the project. The first, referred as passive solution, consists in the development of an oil repellent coating with very low oil wetting

<sup>[1]</sup> C. E Parker, J. Wasen, L. Munro, "Sensor Surface Active Debris Removal (SSADR)", SAE Technical Paper 2020-01-0081, 2020, doi:10.4271/2020-01-0081.

hysteresis (Figure 2). The main objective is to reduce the force necessary for oil droplets to slide on the surface. Several technologies based on sol-gel and silazane chemistries have been developed and are being tested.

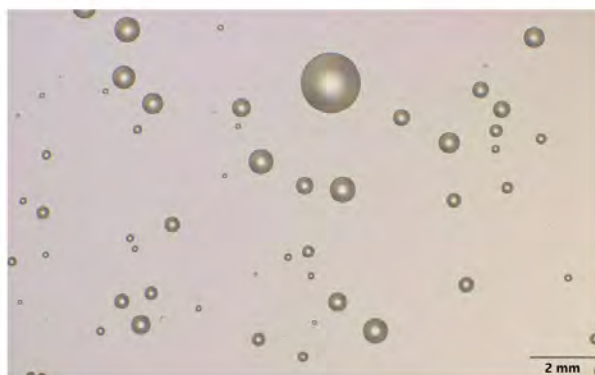
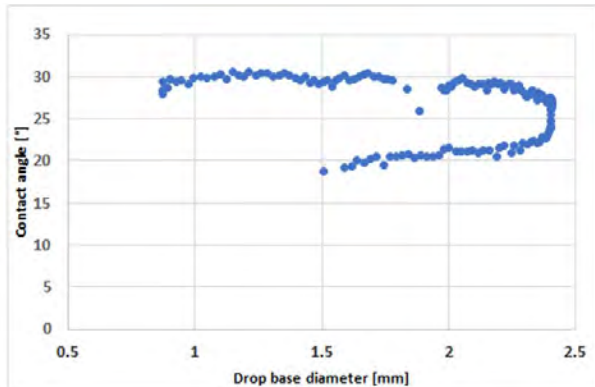


Figure 2: (top) Graph showing the wetting hysteresis loop during dynamic oil contact angle measurement. (bottom) Photo showing oil droplets on an oleophobic surface.

The second approach, referred as active solution, involves the use of external elements to clean the surfaces. The main objective is to induce the motion of oil droplets out of the field of view of the vision system, for instance by using centrifugal, acoustic, electrostatic forces or air flow. A first proof of concept for such self-cleaning optical windows has been done and will be integrated on a vision system in the next phase of the project.

<sup>[2]</sup> Project Oilguard: neue Technologie für höhere Umweltsicherheit auf Ölplattformen DURABEL no.11 (2018).

<sup>[3]</sup> <https://charm-ecsel.eu/>

# Anti-corrosion Coating by Liquid Deposition on Watch Components

X. Bulliard, M. Crenna, X. Lefèvre, M. Palmieri, R. Pugin, J. F Laithier<sup>\*</sup>, C. Storner<sup>\*</sup>

Anodized aluminum is protected by an oxide layer of alumina, which allows long-term coloration by dye encapsulated within its inherent porosity. Colored aluminum has numerous applications in consumer goods, automotive and watchmaking industry. To be competitive with other materials such as ceramic or stainless steels, and to extend the market to other applications such as tools for medical applications, the intrinsic protection against corrosion should be further improved, especially at extreme pH values. In this work, new protective coatings solutions based on liquid deposition have been validated for both acidic and basic conditions.

Anodization of aluminum alloys typically occurs in sulfuric acid bath, generating a nanoporous layer of aluminum oxide of 10 to 20 µm thickness (pore range Ø 10 to 20 nm). Coloring is performed by immersion in dyes solution, where the dyes impregnate the open porosity by diffusion. A final immersion in a hydrothermal bath modifies the surface chemistry generating a boehmite layer, which seals porosity and encapsulates the dyes. This process is widely used in the aluminum industry, with a focus, in this study, on watch components. The top boehmite layer offers a rather good protection to corrosion. However, to be competitive with ceramic parts as another class of material in the watchmaking industry, or to extend the market to new devices, such as tools for biomedical applications, the protection to corrosion of anodized aluminum should be further improved, especially at low acidic pH (>2) or at high basic pH (>11). Figure 1 below shows two examples of applications for the watchmaking industry and for biomedical applications.



Figure 1: Example of colored watch components and medical device in anodized aluminum.

To improve the resistance to corrosion of anodized aluminum, a protective layer can be added. However, this additional layer, in addition to the better corrosion protection, should also be mechanically-resistant, to scratches in particular, and should not change the aesthetics of the parts (such as the transparency). The mechanical resistance criterion eliminates a wide range of corrosion-resistant coatings, typically based on organic and polymers materials, due to the softness of these materials. In contrast, sol-gel chemistry offers a wide range of possibilities to tune many of the properties of the coating by changing the precursor types and concentration. In sol-gel chemistry, the precursor, often a silane molecule, is first hydrolyzed and form a 3-D network through condensation with a neighboring molecule. Based on the functional group grafted on the silane, a wide range of properties can be generated.

In this work, the sol-gel formulation was chosen to offer the appropriate protection to corrosion, without altering the other properties by using a mixture of different silanes, carrying

different functional groups. Figure 2 shows the protection to corrosion, on a non-colored samples for acidic conditions (pH >2) and on a colored samples for basic conditions (pH >11). These parts are round test samples, but of the exact same composition as a final watch component. Corrosion pits are visible on the samples without sol-gel layer, whereas no damage could be noticed with the protective layer.

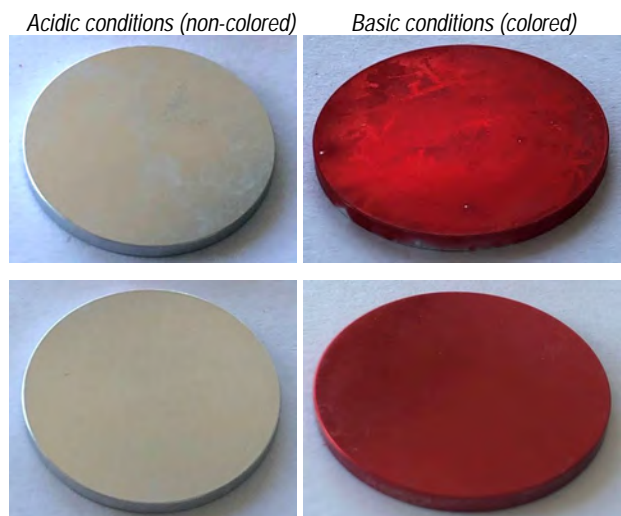


Figure 2: Example of sealed anodized aluminum test samples without (upper images) and with (lower images) sol-gel protective coating.

After checking the corrosion resistance, the samples were also tested against scratch resistance, by using diamond scratch tester and by checking the depth by profilometry. The coated anodized aluminum by sol-gel was as resistant as the bare boehmite sealing layer. Finally, the resistance to UV degradation was also checked, combined with humidity. No rapid color fading or damages in the coating could be detected.

Emphasis is now put on the deposition technique. Dip coating as well as spray coating techniques could be used for an easy processability. The developed sol-gel formulation is also stable several weeks in refrigerator allowing coating deposition at different intervals for the same performance.

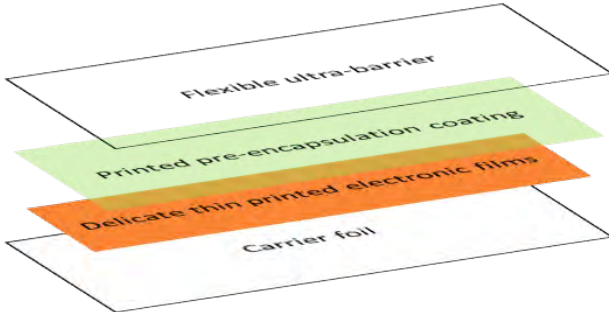
In summary, we developed a sol-gel protecting coating that shows a good corrosion resistance over a wide range of pH, from acidic to basic conditions. The resistance to corrosion is significantly improved as compared to the bare sealing layer of anodized aluminum. The mechanical properties could also be tuned based on the choice of sol-gel precursors molecules. In future, the properties of the coating could further be improved, for example by generating anti-bacterial properties.

\* Coloral SA, Cressier (CH)

# Inkjet Printable and Slot-Die Coatable Formulations for Pre-encapsulation of Solar Cells and Flexible OLEDs

T. Offermans, M. Zinggeler

Optoelectronic devices, which consist of delicate thin films deposited onto a carrier foil (typically PET), are prone to both physically (e.g., scratching) and chemically (e.g., degradation processes triggered by water or oxygen) induced damage. Therefore, such devices are typically produced in an inert atmosphere and encapsulated with a flexible ultra-barrier before going into application. In order to protect the delicate thin films already during production, an (inkjet) printable protection layer was developed.



Poly(vinylidene chloride) (PVDC) is known for its good barrier properties both against water and oxygen and good film forming properties. The material has found application in various packaging solutions and barrier films. Therefore, it was selected as a suitable base material for the inkjet printable protection layer. In order to formulate a pre-encapsulation ink suitable for inkjet printing, its solubility in different solvents was evaluated and the obtained solutions tested on chemical compatibility to the delicate thin films they were printed on. To improve the film properties of the inkjet printed film, glycol compounds were further studied as co-solvent, resulting in high quality films in both single and multi-nozzle inkjet printing.

The WVTR (water vapour transmission rate) of the inkjet printed PVDC coating was measured using an optical Calcium Test. In this test a Ca spot is evaporated on the coating and encapsulated with a glass plate. Moisture diffuses through the PVDC coated film and reacts with the metallic Ca into Ca oxide. In this reaction the initially reflective Ca becomes more and more transparent. From the change in transparency the WVTR is calculated.

The WVTR of a 125 µm thick PET ST-506 with and without the PVDC coating was measured. The WVTR measured at accelerated conditions (38°C 90%RH) without the PVDC coating was 1.28 g/m<sup>2</sup>/day and 1.06 g/m<sup>2</sup>/day with a 0.8 µm thick inkjet printed PVDC coating. This is a 20% reduction and implies that the thin PVDC coating has similar moisture barrier properties as a 25 µm thick PET film.

The coating quality of large area prints of the PVDC pre-encapsulation formulation was evaluated with an industrial scale inkjet printing platform (Figure 1) and a slot-die coater (nTact nRad). Using a 16 nozzle printhead, the appearance of the film was significantly improved compared to the prints made with a single nozzle printer. Thin PEF (polyethylene furanoate) films with thickness of 15 µm were coated with a 0.8 µm thick layer of the PVDC-ink obtained in 10 overprints. The WVTR of the pristine PEF film could be reduced by 80% from  $5.36 \pm 0.03$  to  $1.09 \pm 0.07$  (g/m<sup>2</sup>/day) with the PVDC coating. This WVTR is comparable to the WVTR obtained for an 8x thicker (125 µm) uncoated PET substrate. This implies that with the PVDC coating thinner packaging with PEF can be produced with comparable moisture resistance barrier as thick PET. Slot-die coated layers

of PVDC with a thickness of 1.2 µm obtained in a single pass yield a reduction of 25% of the WVTR of uncoated PET (ST.506 125 µm). This is a similar reduction as observed for the inkjet printed multilayer, which confirms the quality of the inkjet printed films.

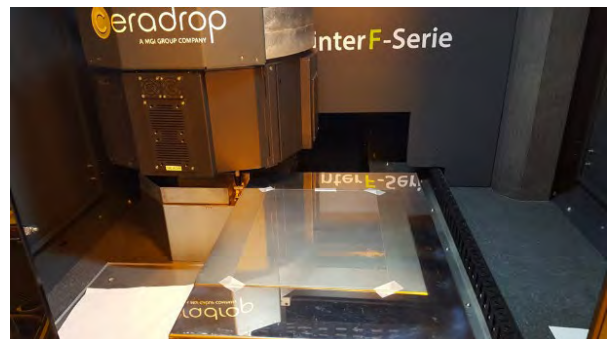


Figure 1: CeraPrinter F-Serie inkjet printing platform.

In order to improve both the moisture barrier property and the hardness of the printed PVDC coating the incorporation of different nanoparticles ( $\text{Si}_3\text{N}_4$ ,  $\text{SiO}_2$  and  $\text{Al}_2\text{O}_3$ ) and nano-clays was studied. Good quality layers without visible phase separation were obtained from inks with a low nanoparticle loading. The WVTR of the inkjet printed layer was reduced by 6% with the additional nanoparticles, and by 10% with the nano-clays.

Hardness tests were performed on the various formulations coated on glass following ASTM standards using the Pencil Test method (ASTM D3363).

The hardness of the PVDC coating compares favorably to other commercially available resins. Its hardness of HB, just a bit softer than F, places it right in the middle of the standardized hardness range (6H-5H-4H-3H-2H-H-F-HB-B-2B-3B-4B-5B-6B). The HB hardness of the PVDC coating makes it comparable to the reference material OrmoComp® (Microresist Technology GmbH). The hardness of the PVDC coating was improved by the addition of nano-clays to below 2H, which makes it harder than hard-baked OrmoComp®.

This work has been carried out within the OLEDSOLAR project, which aims to develop innovative manufacturing processes and in-line monitoring techniques for the OLED (organic LED) and thin film and organic photovoltaic industries (CIGS and OPV).

The OLEDSOLAR project has received funding from the European Union's Horizon 2020 research and innovation program under grant agreement No. 820789.



# Self-assembled Monolayers for Streamlined Process Flows in High-Efficiency Tandem Solar Cells

B. Kamino, G. Andreatta, A. Paracchino, F. Sahli, A. Walter, M. Dussouillez, S.-J. Moon, L. Lauber, S. Nicolay, R. Pugin, Q. Jeangros

The large-scale deposition of ultrathin contact layers for perovskite/silicon tandem solar cells presents a major challenge to their eventual industrialization. However, functionalized self-assembled monolayers present a unique opportunity to achieve this goal due to their self-limiting nature and flexible deposition routes. CSEM is actively exploring this concept by studying these materials as well their reaction dynamics.

Perovskite photovoltaics have already demonstrated significant potential to disrupt the photovoltaics market with either low-cost single junction modules or in the form of high efficiency tandem solar cells when combined with silicon technology. While many challenges still exist before market acceptance of this technology, scale-up of these structures to large area substrates remains one of the most pressing issues. One particularly difficult challenge is the large-scale deposition of efficient contact materials for perovskite solar cells. To date, the most efficient contacts for perovskite solar cells are based on very thin layers of organic semiconductors. When carefully chosen, such materials can present a near ideal interface for the perovskite absorber material resulting in a solar cell with exceptional performance. However, these same materials are poorly conducting and must be applied in extremely thin layers with thicknesses typically less than 20 nm. The application of these ultrathin layers over large area substrates presents a unique processing challenge whereby the layer must be thick enough not to present pinholes but not too thick to limit performance.

Recently, Self-Assembled Monolayers (SAMs) with organic semiconductor functionalities have been shown to form efficient contacts in perovskite solar cells leading to excellent efficiencies in both single junction structures as well as tandem structures. The application of these materials presents a unique opportunity to solve the problem of large area contact materials. As SAM materials can form a layer that is effectively self-limiting in thickness, ultrathin layers can be achieved without the same constraints as typical organic semiconductors. Additionally, there are multiple low-cost deposition methods for these materials opening up the possibility to lower processing costs.

To investigate the potential of these materials for large area solar cells, several scalable deposition techniques for forming SAM layers were explored and compared to a baseline process using spin coating. Specifically, both spray coating and immersion coating were explored as they rely on inexpensive process equipment. Successful formation of the SAM layers was analyzed by water contact angle measurements (dynamic and static, FTIR-ATR, as well as quartz crystal microbalance studies on functionalized surfaces.

Initial studies of the application of these layers by both spray-coating and dip coating demonstrated that successful functionalization of the electrode's surfaces was possible with both techniques. However, when solar cells were fabricated on these functionalized electrodes, the devices performed poorly in comparison to the baseline devices using spin coating. By analyzing the adsorption kinetics of the SAM on electrodes with different surface preparations, we found that the SAM adsorption could be greatly improved with careful preparation of the electrode surface. The result of this preparation was the demonstration of single junction perovskite solar cells with both spray-coated and dip coated electrodes having equivalent performance characteristics to the baseline spin coating

conditions (Figure 1). This result greatly opens up the potential to apply these materials to large area substrates.

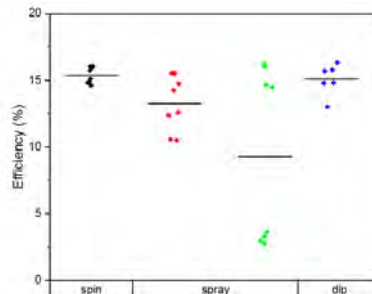


Figure 1: Device efficiencies of single junction perovskite solar cells using SAM contact layers deposited by different methods demonstrating the ability to use dip or spray coating to achieve efficient cells.

To this end, large area perovskite solar cells were tested with these SAM contact materials by fabricating laser interconnected mini-modules and perovskite/silicon tandem solar cells based on a textured bottom cell (Figure 2). Such devices were able to achieve efficiencies up to 14.7% and 25.5% demonstrating the validity of this concept.

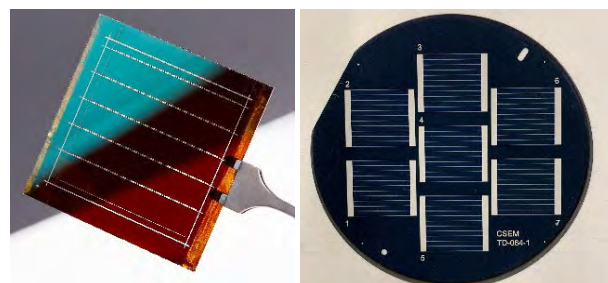


Figure 2: (left) Image of fully laser interconnected perovskite single junction mini-module with a SAM contact layer based on  $5 \times 5 \text{ cm}^2$  substrate; (right) Fully textured perovskite/silicon tandem solar cell with SAM contact layer with an active area of  $4 \text{ cm}^2$ .

Future investigations will focus on further scale-up to even larger substrate sizes as well as the development of SAM materials based on different chemistries to specifically target tandem solar cell interfaces.

This work was financed in part by the SNF projects POWER (20B2-1\_176552), PAPET (200021\_197006), and EPISODE (CRSII5\_171000).

# SMART LIDS—Standardized Cell and Tissue Culture in Multi-well Plates

S. Heub, S. Graf, N. Schmid, R. Ischer, H. B. Atakan, D. Migliozi, S. Boder-Pasche, G. Weder, V. Revol

The development of complex *in vitro* models is driven by the ultimate objective of personalized medicine to match the right patient with the right treatment at the right time. Organoids and organ-on-chip systems are used for drug discovery, diagnostics, and therapy planning. The adoption of these new laboratory models by the life science industry requires standardized and affordable processes. In this context, CSEM is providing Smart Lid solutions for the standardization of cell and tissue culture of biological models in both universal and proprietary labware formats.

Personalized medicine drives the development of new 2D and 3D *in vitro* models, constantly adding more complexity to the labware to recreate physiological microenvironments. The multi-well plate (MWP) is an international standard, increasingly adopted by organoid technology and organ-on-chip testing platforms. In addition, advanced co-culture and multi-tissue systems require the integration of non-conventional modules (actuators, sensors, etc) but always with the common need for precise liquid handling and control of the environmental conditions.

Whether developed on standard MWP format or specific organ-on-chip devices, their implementation into the life science industry remains slow due to the gap between research laboratories and industrial requirements, and regulations. In this context, and as part of the technology platform YOU-ON-CHIP™, CSEM is developing Smart Lid solutions for the standardization of basic cell culture processes (Figure 1).

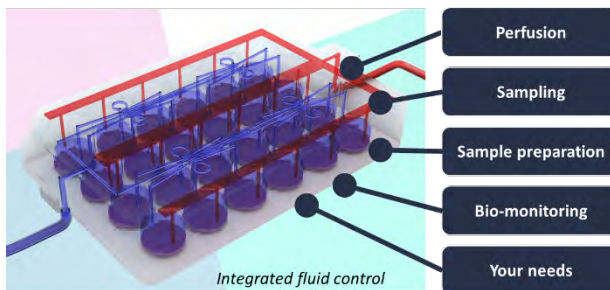


Figure 1: CSEM's Smart Lid program offers the possibility to integrate fundamental functions required for standardized cell and tissue culture.

CSEM Smart Lids are automated tools for parallel and long-term cell and tissue maintenance while ensuring sterility, controlled gas exchange, temperature and humidity, optical readout, and small footprint. They are designed and prototyped in compliance with industrial-scale manufacturing processes and validated in our Biosafety Level 2 laboratories.

CSEM has recently achieved the development and industrial production of a lid for automated and parallelized medium exchange in 24-MWP (Figure 2a). This disposable injection-molded polystyrene lid and its control system enable a regular supply of fresh nutrients and oxygen to the cells over several weeks. The lid comprises a single liquid inlet and one outlet to control 24 liquid channels in parallel with  $\leq 6\%$  volume precision on the exchanged liquid volumes. The platform has been validated through the differentiation and maturation of mouse embryonic stem cells into neurons over 2 weeks (Figure 3). Evaluation for the culture of human 3D cell culture models over several weeks is currently ongoing.

In the ECSEL project Moore4Medical<sup>[1]</sup>, CSEM is developing a smart lid for automated sampling and glucose sensing to standardize the monitoring of 3D liver and kidney models in MWP. The prototype (Figure 2b) enables automated sensor calibration, 10  $\mu\text{l}$  sampling steps, and sequential glucose measurement on 24 wells (384-array) for several hours. It comprises disposable and reusable parts to facilitate the sterilization and handling of the system and operates in a classical incubator for cell culture. After validation, CSEM will produce the lid in collaboration with the international consortium partners.

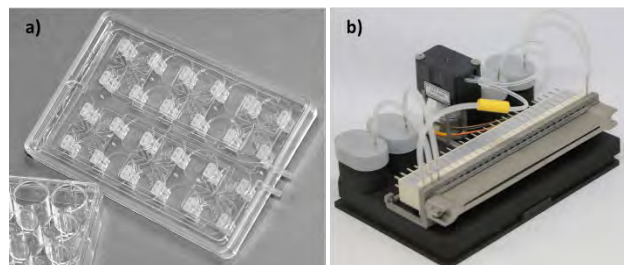


Figure 2: a) CSEM's injection-molded lid for automated medium exchange on 24-MWP; b) CSEM's lid prototype for sampling and glucose sensing developed in Moore4Medical.

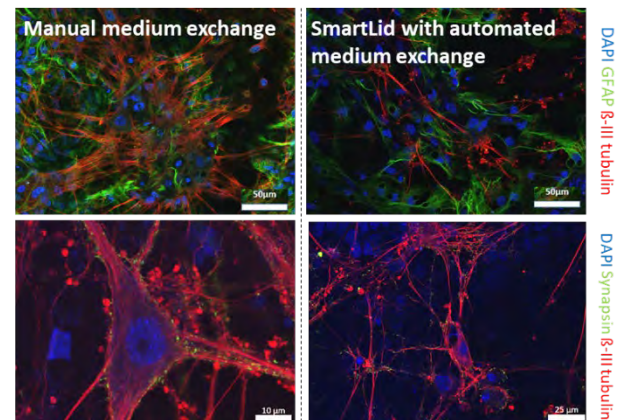


Figure 3: Microscopy images of neurons showing similar differentiation and maturation signs after 16 days of manual medium exchange and automated medium exchange using our 6-MWP Smart Lid platform.

In the EU project OrganTrans<sup>[2]</sup>, CSEM aims at developing a Smart Lid that is compatible with 6-MWP for the maturation of bioengineered liver tissues. It enables automated and standardized medium perfusion including sampling for regenerative medicine applications.

Thanks for this novel approach to cell culture, CSEM is supporting industrial partners for the development of customized organ-on-chip labware.

[1] <https://moore4medical.eu/>

[2] <https://organtrans.eu/>

# Microtissues and Organoids High-Throughput Histology

S. Heub, J. Goldowsky, D. Migliozi, F. Navaee, M. Despont, V. Revol, G. Weder

Precision and stratified medicines are medical approaches that seek to exploit patient- or group-specific therapeutic strategies. Microtissues and organoids harboring in vivo architecture and functions are a milestone in the development of the ultimate personalized healthcare. CSEM is developing tools for organoid technology: production, sorting, placing, maturation, monitoring and testing. Histology is the examination of the anatomy of cells that remains a gold standard during the whole life cycle of organoids. A new discipline, named microhistology, is emerging to align, embed and section organoids in high-throughput sample processing.

Organoid technology is revolutionizing drug discovery, disease modeling, tissue engineering, regenerative medicine, and precision/stratified medicine. These mini-organs, based on embryonic or adult stem cells, exploit the potential of multicellular assemblies to self-organize into three-dimensional structures that mimic in vivo architecture and functions. By recapitulating the complexity of organs, these in vitro models enhance the translation of drugs from preclinical to clinical phases. Organoids made from patients can allow for a personalized medicine with the potential to pre-test medical treatments on organoids rather than directly on people.

Within the Tools for Life Sciences, CSEM has established a roadmap towards tools for organoid technology in drug testing and regenerative medicine (Figure 1). The examination of the anatomy of cells is required throughout the global 3D cell culture value chain including production, sorting, placing, maturation, monitoring and end-point analysis<sup>[1]</sup>.



Figure 1: CSEM roadmap on tools for organoid technology showing the increasing need of histological analysis from production to endpoint analysis.

In microhistology, tissue processing starts with the fixation of the organoids (formalin) followed by their embedding in hydrogels to facilitate further dehydration, clearing with xylene, and infiltration and embedding with paraffin. Finally, the samples composed of multiple organoids are sectioned, stained, and observed under the microscope.

The current limitation for high-throughput microhistology remains the alignment of hundreds of organoids in one focal plane to parallelize their processing, imaging and analysis.

In collaboration with the School of Life Sciences FHNW which provides the biological requirements and tissues<sup>[2]</sup>, CSEM Tools for Life Sciences are developing strategies for placing multiple organoids with an accuracy of  $\pm 20 \mu\text{m}$  (Figure 2). This positioning is performed between the fixation and dehydration steps.

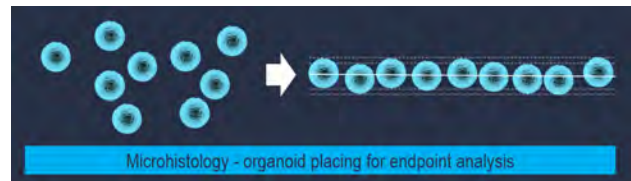


Figure 2: High-throughput microhistology requires the placing of the organoids in one plane with an accuracy of  $\pm 20 \mu\text{m}$ . The objective is to section all the organoids at the same height.

Several concepts were investigated and tested including open microwells and microfluidics approaches. All platforms enable either user-friendly bench top or fully automated sample processing. For example, the HistoBrick is a hydrogel microwell device enabling the positioning of organoids or microtissues on a 24 or 96 array in a single plane for high throughput histology (Figure 3).

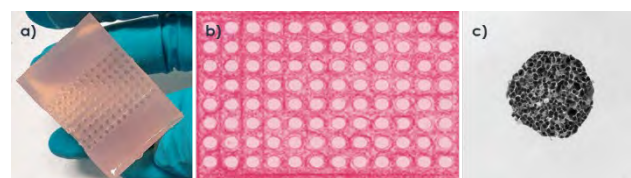


Figure 3: a) 96-well HistoBrick before embedding; (b) 4  $\mu\text{m}$  slice obtained after sample processing; c) typical resulting microscopy image of a 200  $\mu\text{m}$  HepG2 spheroid.

The main challenge is the accurate alignment of the 3D models in a defined plane so that many replicates of an experiment are cut through the same height/radius for direct comparison side-by-side. The positioning of the microtome is also of particular importance.

In combination with camera-based fluorescence microscopes, microhistology is the endpoint analysis of advanced cell culture assays in pharmacological and toxicological applications. A solution for a full traceability from cell culture systems to histology microscope slides is under evaluation.

This work is partially funded by Innosuisse under the grant No 39848.1 IP-LS.

<sup>[1]</sup> S. Boder-Pasche, et al., "Organoid Technology Platform for Tissue Engineering", CSEM Scientific and Technical Report (2020), 44.

<sup>[2]</sup> Fachhochschule Nordwestschweiz, Institute for Chemistry and Bioanalytics, Prof. Dr. Laura Suter-Dick

# denovoCast—Automated Skin Tissue Formation Machine

G. Weder, C. Beyer, S. Boder-Pasche, C. Coen, D. Ledroit, K. Krasnopski, S. Graf, R. Ischer, M. Jungo, N. Schmid, T. Valentin, T. Volden, V. Revol

Regenerative medicine is focused on the development of new treatments to restore tissues' and organs' function lost due to aging, disease, damage or defects. Various regenerative therapies are currently being developed thanks to advances in gene editing, cell isolation and tissue engineering. Despite great promise in clinical studies, such therapies face difficulties to reach the market due to the highly manual processes, requiring expensive cleanroom environment and highly skilled personnel. Together with CUTISS, CSEM developed a fully automated skin engineering machine producing 400 square centimeters in parallel – a first of its kind worldwide.

Every year millions of people suffer from severe skin defects, such as burn injuries. Treatment options are limited particularly for large burn victims. With current standard of care, patients are often left with disfiguring and debilitating scars. Scars can impair mobility requiring follow-up surgeries, intense homecare and psychosocial rehabilitation. Zurich-based Cutiss AG, a spinoff of the University of Zurich has worked on developing a personalized, permanent skin graft produced from the patient own cells. denovoSkin™ minimizes scar after transplantation and is now being tested in a multi-centric phase II clinical trials in Switzerland and Europe.

The overall goal of the denovoCast project between CSEM and CUTISS was the automation of the denovoSkin manufacturing process with a focus on scalable 3D engineered tissue production. One major result is the bioengineering of the skin grafts in a closed system, which resulted in a dedicated labware named GraftBox. This innovative single-use labware allows the injection of biomaterials including cells, gel compression and media exchange and facilitates the formation and cultivation of denovoSkin grafts. After 10 days of automated operation, the skin grafts can be harvested by the surgeon to be implanted on the patient (see Figure 1).



Figure 1: Picture of the skin graft after engineering and maturation in the patented labware - so-called GraftBox. The GraftBox was developed to allow the automation of all tissue engineering operations in a fully closed system.

A GraftBox set composed of four GraftBoxes in parallel, is mounted on the so-called demonstrator (Figures 2 and 3). This machine is composed of hardware for injection and mixing, compression, fluid control, imaging, and a software control system that oversees the production of four denovoSkin in parallel. The biovalidation of this innovative technology including cell morphology, cell proliferation, cell viability as well as histological analysis showed similar results compared to the manual process (see Figure 4).



Figure 2: Picture of the GraftBox set including all disposable parts (bags, tubings, connectors) before gamma sterilization. GraftBox units are manufactured by injection molding allowing for a quick scale-up.



Figure 3: Picture of the patented denovoCast machine with four installed GraftBoxes allowing for complete automation over 10 days.

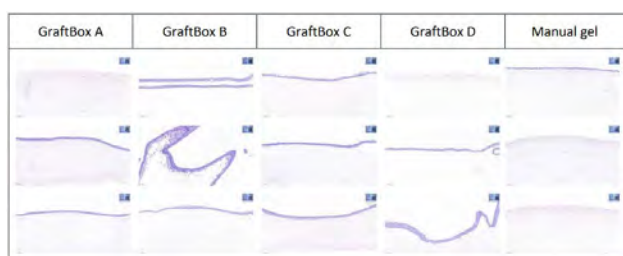


Figure 4: Result of the histology analysis on three different positions of the skin graft produced by the denovoCast machine (GraftBoxes A to D) and by a manual operator. The results show identical formation of the dermis and epidermis.

CUTISS and CSEM thanks InnoSuisse - Swiss Innovation Agency for their financial support under grant 35855.1 IP-LS.

# Deep-Learning Powered Organoid Handling and Sorting Platform for Liver Tissue Engineering

S. Boder-Pasche, T. Valentin, B. Atakan, M. Blache, J. Goldowsky, S. Heub, F. Luongo, F. Navaee, C. Netsch, C. Sampaio Da Silva, N. Schmid, V. Revol, G. Weder

Organoid technology has emerged to play a central role in the new generation of complex human *in vitro* models. Relying on self-organization of stem cells, organoids can also be used as building blocks to engineer organs and show therefore great therapeutic potential for regenerative medicine. The transition from lab to clinic requires standardized processes, aiming at high-throughput handling and sorting of organoids. In this context, CSEM is developing automated tools combining digital and micro technologies to classify and sort organoids.

Organoids are 3D multicellular *in vitro* tissue constructs derived from stem cells, which mimic their corresponding *in vivo* organs. Beyond their use as *in vitro* models for drug testing, the therapeutic potential of these mini organs is increasing, using them as building blocks for tissue engineering. The use of organoids in regenerative therapies requires large-scale organoid production with minimal variability and high-throughput methods to eliminate risk for tumorigenicity, relying on automated organoid sorting and handling. The lack of standardized and automated processes is one of current limitations that prevent the clinical use and adoption of organoid technologies in regenerative medicine.

In this context, CSEM is coordinating the European project OrganTrans [1] to develop an automated and standardized tissue engineering platform capable of fabricating a liver construct from donor cells, thereby presenting a disruptive alternative to donor organs [2]. Liver tri-culture organoids are produced in a standardized protocol developed in the OrganTrans project, before being sorted to eliminate unhealthy spheroids.

Our approach for organoid sorting builds on previous expertise at CSEM for the sorting of other biological entities [3]. The technology relies on high-resolution microscopy video sequences, classification based on deep-learning algorithms, followed by extraction of unhealthy organoids, and finally harvesting of healthy organoids.

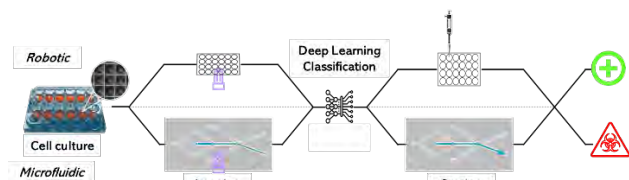


Figure 1: High throughput automated processing for organoid handling and sorting, based on self-learning vision algorithms.

The platform is compatible with biosafety cabinets, microwell plates, and enables sorting of 80,000 spheroids within 2 hours. The deep learning algorithm demonstrated a classification accuracy of >98%. The platform extracts unhealthy spheroids using a 300 µm capillary needle, followed by a simultaneous washing & harvesting step. Organoids are then concentrated using cyclonic separation before resuspension in hydrogel precursor solution used to manufacture the bioconstruct.

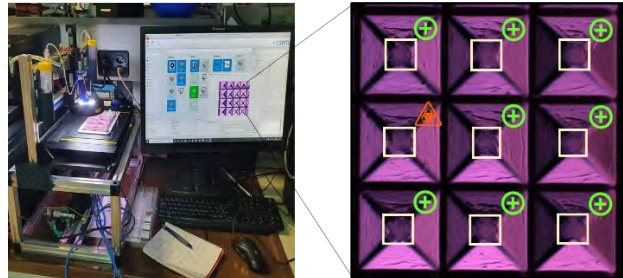


Figure 2: Robotic unit for imaging and classification of organoids produced in the Kugelmeiers Spherical 5D plate (left), with an example of the organoids bounding boxes from the deep learning model (right).

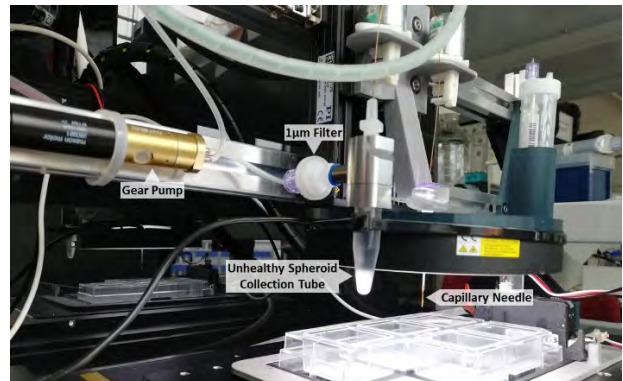


Figure 3: Robotic unit using a capillary needle for removal of unhealthy organoids, followed by harvesting of healthy entities.

This novel automated platform therefore enables precise sorting of organoids in a non-destructive way while predicting and minimizing the risk for tumorigenesis.

We are currently exploring microfluidic strategies for organoid sorting using deep learning and intersecting flow separation in a controlled environment, relying on similar imaging and classification methods. Combined with current tools for large-scale and standardized production of organoids, our sorting technologies open new perspectives for the use of organoids in regenerative therapies.

[1] [www.organtrans.eu](http://www.organtrans.eu) (grant agreement No. 874586 funded by the EU Horizon 2020 research and innovation program).

[2] S. Boder-Pasche, et al., "Organoid Technology Platform for Tissue Engineering", CSEM Scientific and Technical Report (2020), 44.

[3] Graf SF, et al., "Image-based fluidic sorting system for automated Zebrafish egg sorting into multiwell plates", J Lab Autom. 2011;16(2):105-111.

# Cell Culture Monitoring

F. Kurth, S. Graf, N. Glaser, L. Burr, S. Sattayasamitsathit, M. Zinggeler, H. Chai-Gao, N. Schmid, D. Migliorelli, S. Generelli

With the increasing complexity of cell cultures in Organ-on-Chip and complex in-vitro models, the assessment of specific culture parameters becomes crucial. Parameters like pH, glucose, and lactate can be measured label free with electrochemical sensors. At CSEM, such sensors are developed and integrated in compact microfluidic systems enabling automated cell culture monitoring to improve, for instance, future drug development tests.

Monitoring of cell culture progression over time is an essential tool for quality control as well as one way of determining the effect of varying test parameters, such as the effect of a drug during early development. Novel culture platforms, for instance, Organ-on-Chip devices are moreover accompanied by a higher system complexity compared to conventional 2D cell cultures, which consequently renders the understanding of cell behavior more difficult. Therefore, the assessment of specific culture parameters becomes even more valuable.

In general, approaches using labels and label-free methods exist for cell culture monitoring, whereby monitoring of introduced labels is either prone to interfere with the biology (fluorescent labels) or can only be used in restricted laboratory settings (isotope labels). A strategy to monitor cultures over time without interfering with the experimental trial itself is the quantification of target molecules in the cell culture medium. Although standardized chromatographic assays are well-established, instrumentation is still expensive and bulky as well as depends on a sampling strategy. In contrary, electrochemical sensors are small devices that can quantify molecules of interest with high specificity and accuracy using comparably small periphery equipment. To overcome the considerable costs for materials still used for the fabrication of electrochemical sensors, CSEM develops such sensors by a combination of screen printing and liquid deposition, both cheap fabrication technologies and highly scalable in production. Examples for developed CSEM sensors compatible with cell culture applications are pH, ion-specific, and enzymatic sensors (Table 1).

Table 1: Overview of CSEM electrochemical cell culture sensors. The sensors are developed to be compatible with industrially relevant sterilization processes, such as gamma and X-ray sterilization. RPMI, DMEM: cell culture media (with and without serum); PB, PBS: phosphate buffers and phosphate buffered saline solutions.

Analyte	Dynamic range	Tested media	Operation time
pH	pH 5-8	RPMI, PB, PBS	>48 hours
Glucose	0-20 mM	RPMI, DMEM, PB, PBS	>24 hours
Lactate	0-15 mM	RPMI, PB, PBS	>12 hours

Electrochemical enzymatic sensors selectively quantify, for instance, glucose and lactate, provide essential information on cell metabolic activity, and can be fabricated using different

[1] V. Zubkovs, et al., "Coatings for SWCNT-based Glucose Biosensors Applied in Cell Culture Monitoring", CSEM Scientific and Technical Report (2021), 90.

[2] S. Heub, et al., "Non-invasive Optical Oxygen Sensing for Life Sciences and Environmental Monitoring", CSEM Scientific and Technical Report (2019), 45.

materials, technologies as well as can depend on different molecular sensing principles. Several sensing strategies have been investigated, in order to target the optimal results for cell culture monitoring, specifically long-term detection and minimization of interferences. Another important parameter to precisely control in cell culture environments is pH. Electrochemical pH sensors hereby have the advantage that by employing the potentiometric measurement principle, no current interferes with the liquid environment. Other CSEM sensors for monitoring cell cultures comprise enzymatic sensors with optical readout<sup>[1]</sup> and optical dissolved oxygen sensors<sup>[2]</sup>.

Since biological processes are very sensitive towards external perturbances, CSEM sensors are validated in their cell toxicity and only integrated in direct cell contact upon proven non-toxicity for the individual process. Due to the sensitive nature of cell biological processes, such immediate integration is however very often not feasible. A specific requirement of automated cell culture monitoring systems is thus the integration of sensors into microfluidic channels of liquid sampling routes. As the CSEM electrochemical sensors are based on functional printing and functionalization onto a polymer sheet with individual sensing areas of two square millimeters or less, they qualify naturally for such microfluidic integration. Figure 1 presents two of these automated monitoring systems with integrated sensors, which are currently employed for the development for the BRIDGE project "AOP Plug 'n Play" (AOP) and the EU project "Moore 4 Medical" (M4M), both of which depend on sampling of microliter volumes in conjunction with real-time electrochemical quantification of cell metabolic relevant parameters.

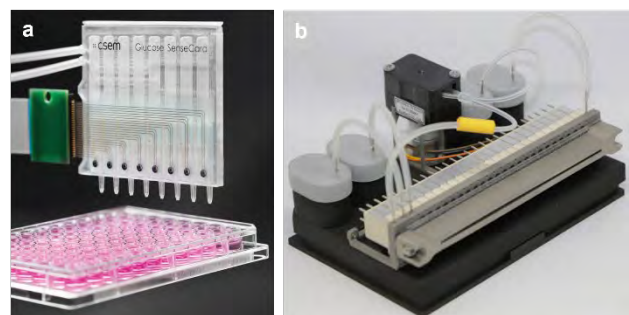


Figure 1: a) The BRIDGE project AOP develops a miniaturized version of the CSEM SenseCard<sup>[3]</sup> shown here to quantify pH, glucose, lactate, and reactive oxygen species in a liver Organ-on-Chip model. b) The fully automated sampling lid (SmartLid) for the EU-project M4M is equipped with an integrated glucose sensor is optimized for the InSphero Akura™ Flow 384 and can be customized to other well plate formats.

[3] S.F. Graf, et al., "SenseCard—a Disposable Parallel-sensing Card for Advanced In-vitro Models", CSEM Scientific and Technical Report (2019), 53.

# PEPS—Printed Electrochemical Protein Sensor

S. Schär, H. Chai-Gao, N. Glaser, C. Hilty, C. Seitz, L. Burr, S. Fricke, S. Generelli, M. Zinggeler

In the PEPS project we are developing nanocomposite electrodes for highly sensitive protein sensing applications at the point-of-care (POC). The electrodes consist of an antifouling polymer network with embedded carbon nanotubes (CNTs) with high electrical conductivity. The electrodes are fabricated using highly scalable printing processes and retain >95% of their initial electroactive surface area (EASA) after 1 h of incubation with concentrated bovine serum albumin (BSA) solution, whereas standard carbon electrodes drop to 50% within a few seconds. A first sensor demonstrator was successfully realized, enabling the rapid detection of a protein biomarker with a concentration in the ng/mL range in undiluted human blood serum.

Electrochemical protein sensors could revolutionize the diagnosis and monitoring of various diseases, making testing as convenient and effective as monitoring diabetes with a glucose meter. However, the industrialization of such sensors is hampered, mainly because of problems with unspecific surface fouling, low POC compatibility of the devices and/or expensive sensor fabrication. To address these limitations, we are studying the development of conductive nanocomposite electrodes with strong antifouling properties that can be prepared using cost-effective and highly scalable printing processes.

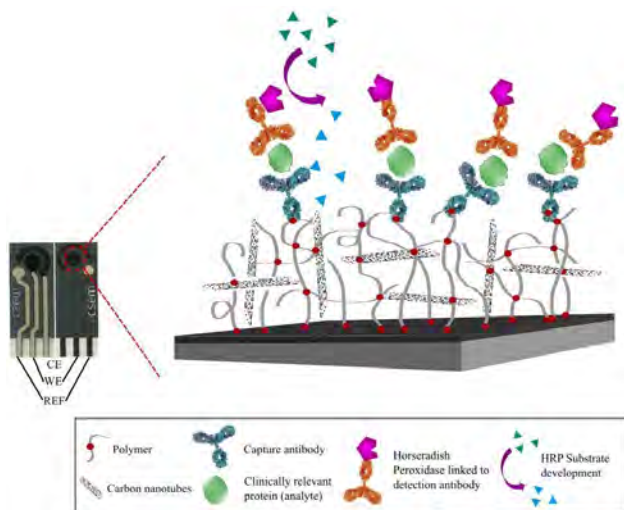


Figure 1: Schematic of a printed three electrode setup with nanocomposite working electrode (WE) for protein sensing. The analyte is bound to the immobilized capture antibody followed by enzymatic (HRP) labelling using a detection antibody. Read-out is performed in the presence of an enzyme substrate which can be measured electrochemically after conversion by the enzyme.

Surface fouling due to unspecific protein adsorption was determined by measuring the electroactive surface area (EASA) decrease after incubation with 40 mg/mL BSA solution.

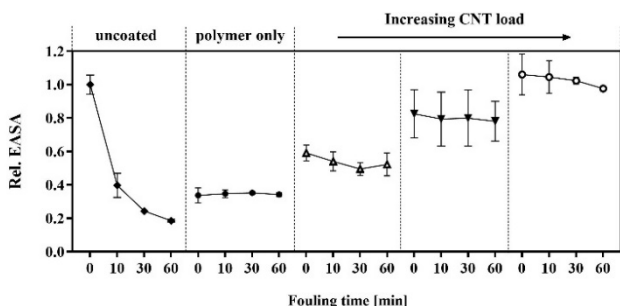


Figure 2: Fouling effect on uncoated electrodes, with polymer only and polymer with increasing CNT content.

Under such conditions, standard carbon electrodes showed an EASA decrease of about 50% on mere contact with the fouling solution. Printing of increasing loads of polymer onto carbon electrodes increased their antifouling properties, however, at the cost of a decreased EASA due to the insulating nature of the polymer. By incorporating conductive CNTs into the film, this limitation was overcome (Figure 2). Optimized parameters enabled to obtain a high and stable EASA over 1 h in the fouling solution.

Nanocomposite electrodes were functionalized by immobilizing an antibody against C-reactive protein (CRP). Electrodes were immersed for 10 min in undiluted human blood serum spiked with different CRP concentrations. The binding assay was completed by incubation with an HRP labelled detection antibody followed by electrochemical read-out in presence of an enzyme substrate. The assay showed a wide dynamic range (3-4 order of magnitude) and a LOD of 3.8 ng/mL (Figure 3).

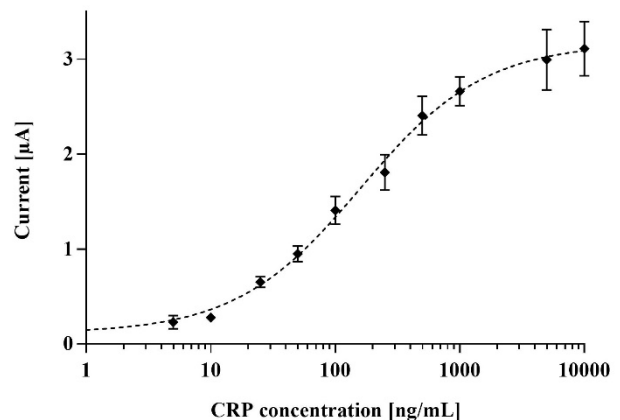


Figure 3: Results of the electrochemical immunoassay for the detection of CRP in blood serum.

The immediate, strong, and unspecific adsorption of bio-foulants on electrode surfaces can effectively be prevented using an antifouling polymer coating. However, the insulating nature of such coatings interferes with most electrochemical read-out principles. To overcome this limitation, conductive CNTs can be incorporated into the film, forming a nanocomposite. Such composite electrodes enable highly sensitive electrochemical assays for protein detection and could pave the way for next generation digital POC devices.

We thank the Swiss Nanoscience Institute (SNI) for funding our "PEPS" project.

# DigiLab—Automated Calibration Platform for Liquid Handling Systems

J. Goldowsky, P. Cristofolini, R. Limacher, N. Schmid, V. Revol

In the recent years CSEM has built wide knowledge on dispensing applications, various ways of measuring dispensed liquid amounts for process control as well as the calibration and verification of such methods. Especially for low-volume droplets and/or low flow rates, the precise measurement itself is challenging and may lead to erroneous calibrations of the investigated systems. To address these challenges, an automated (calibration) platform for liquid handling systems has been built. It combines precise measurement technologies – composed of off-the-shelf and CSEM developed solutions – allowing for the characterization of liquid handling systems in terms of flow rate and droplet volume.

The handling of small liquid quantities is a critical process step in many clinical, pharmaceutical, bio-technological, and industrial applications. Regular calibrations are performed to guarantee the correct behavior of the dispensing systems especially when it comes to low volumes and flow rates. For on-site droplet volume verification, the "DropWatch" system has been developed in cooperation with our partner Hamilton AG in Bonaduz GR, which enables the characterization of nano- and pico-liter droplet volumes and the detection of potential satellite droplets, including their flight trajectories.<sup>[1]</sup>

In parallel CSEM has been developing calibration free, liquid class independent metering solutions for bio-technological and microfluidic applications. Even though such systems are calibration free during usage, their development and characterization requires profound studies on their performance in the targeted droplet volume ranges and flow rates. It is therefore crucial to perform correct reference measurements during system development.<sup>[2]</sup>

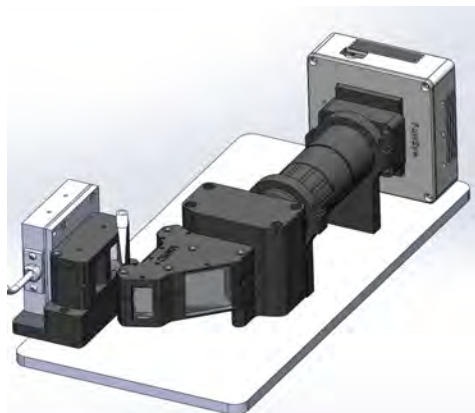


Figure 1: CAD drawing of advanced "DropWatch" system using optics to generate a 90° angled view image on one FastEye camera module.

To perform such reoccurring reference and calibration measurements effectively, a calibration platform has been developed comprising an advanced development of the "DropWatch" system in combination with a Mettler Toledo WMC15-SH module for precise evaluation of micro to pico-liter droplets. The original "DropWatch" system has been reduced in size by developing advanced optics that project 90° angled views of the droplet onto one camera sensor. Thus, camera synchronization is avoided, and system weight and size are reduced. By combining optical droplet measurement and Mettler Toledo scale into one module both measurement principles can be compared to each other for droplet sizes in sub-microliter

range. While the weight scale is applicable for higher droplet volumes its results get less reliable the smaller the droplet volume is. Therefore, measuring nano and pico-liter droplets is preferably done with the optical setup only.

Besides the characterization of droplets, verification of flow rates is a reoccurring challenge in many applications. Based on commercial flow sensors (Fluigent FRP S, M, L) modules have been developed that allow the measurement of flow rates between 0.1  $\mu\text{l}/\text{min}$  and 10  $\text{ml}/\text{min}$ . Especially for low flow rates it is essential to account for tubing expansion and possible air encapsulation within the measurement channels. Hence, the integrated modules are placed downstream the main flow restriction (i.e., the dispensing needle) to create as little pressure difference between measurement channel and atmosphere as possible. Pierceable membranes enable the automated switching between the different sensors.

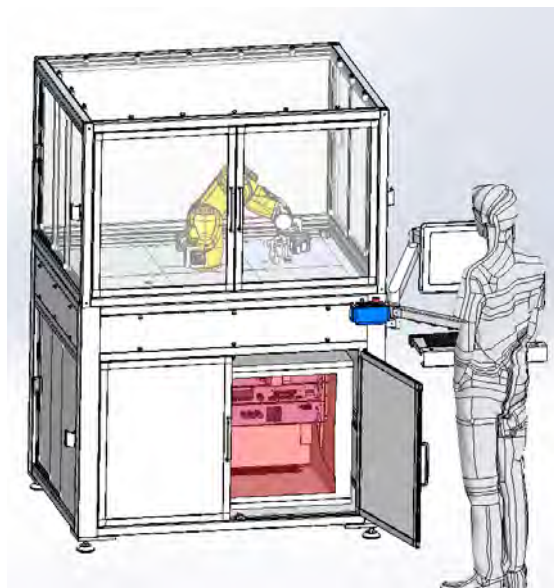


Figure 2: Automated calibration platform for liquid handling systems.

In the overall system design six replaceable measurement modules can be arranged in the working space of a Stäubli TX2-40 robot onto which various dispensing systems can be mounted for evaluation. Equipped with the previously described droplet and flow rate modules a broad range of dispensing systems can be evaluated in terms of performance, repeatability, and accuracy.

[1] P. Cristofolini, et al., "DropWatch—High-speed Volumetric Measurement System for Nanoliter Droplets in Flight", CSEM Scientific and Technical Report (2020), 47.

[2] J. Goldowsky, et al., "Calibration-free Liquid Dispensing of Microliter Volumes", CSEM Scientific and Technical Report (2018), 47.

# Coatings for SWCNT-based Glucose Biosensors Applied in Cell Culture Monitoring

V. Zubkovs, E. Vuille-dit-Bille, H. Chai-Gao, M. Zinggeler, M. Markocic, G. Orawez, X. Bulliard, X. Lefevre, R. Pugin, S. Cattaneo

*Bio-inspired functional materials play a central role in optical and electrochemical sensing. CSEM experts can tailor functional coatings towards the need of specific applications for biosensing. In this project, we investigate the integration of single-walled carbon nanotubes (SWCNT) in hydrogel and sol-gel thin films and we evaluate their performance for continuous glucose monitoring. The composites are deposited onto an optical reader, creating stable, porous sensing layers with a thickness of a few hundreds of micrometers.*

Monitoring of bio-analytes, such as glucose, is a crucial factor for the optimization of cell culture growth conditions and cell viability control. It is vital for cell health that glucose levels are maintained within a certain range during cell growth. That is particularly relevant for cultures used for biopharmaceutical production, regenerative therapies, organ cultures, and personalized tissue engineering. Glucose monitoring in cell cultures is typically performed by a manual sampling of cell culture media. These frequent interventions increase the risk of contamination. A recent survey, published in *Nature Biotechnology*, has shown that 45% of the global biotech companies (comprising >75% of mammalian cell culture manufacturers in the world) have experienced at least one contamination event, causing losses between 1 and 10 million dollars [1].

An alternative to manual sampling is continuous monitoring of bio-analytes in cell cultures using autonomous sensors. This allows decreasing the risk of contamination during manual handling and reduces the workload of laboratory assistants.

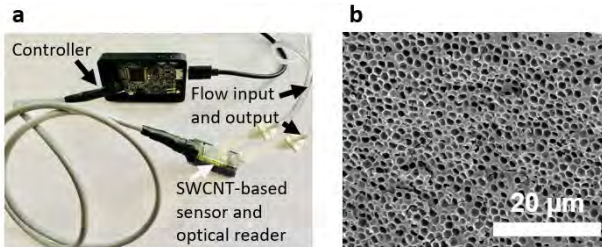


Figure 1: a) Miniaturized optoelectronic SWCNT-based sensor for continuous monitoring glucose in physiological liquids. b) Electron microscopy image of a thin film sol-gel coating.

As reported earlier [2], CSEM has developed a continuous glucose monitoring sensor based on a fluorescent SWCNT material (Figure 1a). A central component of the sensor is a thin film coating, which serves as the scaffold for the sensing material and as a barrier for larger biomolecules and cells. CSEM investigated several options to stabilize the nanomaterial and create a functional coating, such as hydrogel and sol-gel membranes. An example is shown in Figure 1b.

The thin film coatings offer several advantages:

- The pore dimensions can be tuned to optimize the sensor response.
- The structure allows immobilization of multiple layers of the fluorescent material, increasing the active sensing surface and the signal intensity.
- The hierarchical porosity improves the linearity of the response as well as the sensor stability.

[1] P. W. Barone, et al., "Viral contamination in biologic manufacture and implications for emerging therapies", *Nature Biotechnology* (2020) 38, 563-572.

We characterized the responsivity of the various sensing layers to glucose in a fluidic setup (Figure 2a). The thin film coatings with incorporated SWCNTs were deposited on the surface of a poly (methyl methacrylate) (PMMA) chip. The device was illuminated with 660 nm light and fluorescence of SWCNT-sensors was monitored between 1000 and 1200 nm. Cell culture media supplemented with or without glucose was administered into the fluidic setup in alternating cycles. Figure 2b and 2c show the results obtained with a copolymer hydrogel, demonstrating the stability of the biosensor-hydrogel composites and their response to 10 mM glucose for more than 40 h.

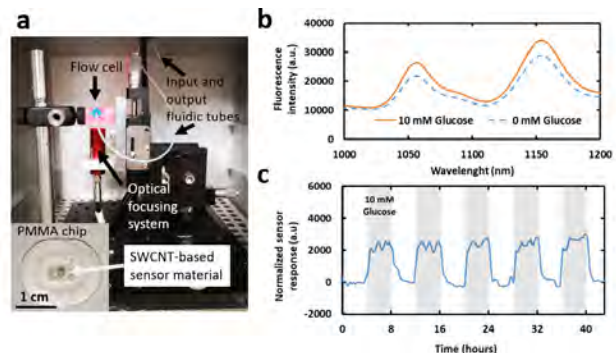


Figure 2: a) Fluidic setup for continuous glucose monitoring using SWCNT/GOx sensors. b) Fluorescence spectra of SWCNT/GOx sensor exposed to 10 mM glucose in cell culture media. c) Continuous monitoring of 10 mM glucose in cell culture media (grey areas), administrated in alternating cycles with cell medium without glucose (white areas).

In conclusion, hydrogel and sol-gel thin films allow realizing suitable scaffolds for SWCNTs based sensors. Such thin film matrices can be either integrated onto an optical sensor head or can be applied inside cell culture flasks creating glucose-responsive layers, which can be monitored using an external optical reader. Due to the versatility of the SWCNT-based sensing platform, the technology could in the future allow the realization of multiplexed biosensors for the simultaneous detection of several analytes which are relevant for in vitro and in vivo applications, such as lactate, nitric oxide, hydrogen peroxide, and micro-RNA molecules [3].

[2] V. Zubkovs, et al. "Optical sensor for glucose monitoring in cell cultures", CSEM Scientific and Technical Report (2020), 49.

[3] S. Kruss, et al., "Carbon nanotubes as optical biomedical sensors", *Advanced Drug Delivery Reviews* (2013) 65, 1933-1950.

# Enhancing the Performances of Lateral Flow Assays

H. Chai-Gao, F. Kurth, Y. Tang, M. Wipf\*, C. S. Wood\*\*, N. Marjanović, J. Disser, F. Lütfolf, C. Seitz, M. Fretz, S. Generelli

The present work reports strategies for quantitative analysis with an improved working range and lower limit of detection of lateral flow immunoassays (LFIA) strips. To achieve this, a nanocellulose aerogel pad incorporated into a conventional LFIA strip delays the fluid sample flow by increasing the fluidic resistance and thus extends the reaction time between the antibody and the analytes, which consequently improves the limit of detection. Another LFIA technology co-developed with Momm Diagnostics is an enzyme-linked lateral flow immunoassays (ELLFIA) that in combination with a quantitative electrochemical readout enables rapid biomarker quantification down to sub-picomolar concentrations.

Lateral flow immunoassays (LFIA) have become an increasingly important Point-of-Care (POC) device in medical diagnostics and at-home testing due to their ease of use, low costs, and portability. For instance, and in relation to the current COVID pandemic, LFIA are developed to enable fast and qualitative detection of IgM and IgG antibodies and antigens in suspects in response to a SARS-CoV-2 infection.

One of the major limitations of LFIA is that they only provide qualitative and/or semi-quantitative results and have a relatively low analytical sensitivity, i.e., high limit of detection (LOD). The latter is mainly caused by the small and poorly controlled sample volume as well as the short reaction time between the detection antibody and analytes of interest. Changes in the lateral flow strip design primarily aim at prolonging the sample flow time, which leads to a longer reaction time between detection antibodies and target analytes, improves the binding efficiency between them, and ultimately enhances the analytical sensitivity of LFIA. Analytical sensitivity can be ameliorated by introducing new label-detection antibody conjugates. In case such conjugates actively amplify the signal output, e.g., by introducing enzymatic labels, the analytical sensitivity can be further optimized.

A study recently published by CSEM focused on designing a novel strategy to decrease the LOD of LFIA as well as to render a quantitative analysis possible.<sup>[1]</sup> Both were achieved by incorporating a cellulose nanofiber (CNF) aerogel in between the conjugate pad and the nitrocellulose strip of a conventional lateral flow device to extend and better control the sample flow time (Figure 1).

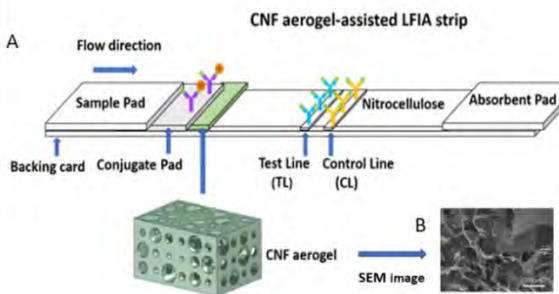


Figure 1: a) Schematic of the CNF aerogel-assisted LFIA strip design. b) SEM image of the CNF cellulose aerogel pad. The pore sizes are very heterogeneous and range up to approximately 200 µm in dry state. A and B adapted from [1].

The potential of the CNF aerogel-assisted lateral flow strip was evaluated targeting mouse IgG as a model system. The results show that the CNF aerogel-assisted LFIA allowed for quantifying even small concentrations (Figure 2a) and improving the LOD by

a 1000-fold compared to a conventional LFIA (Figure 2b). The potential of the proposed method for detecting COVID-19 antibodies is currently under evaluation.

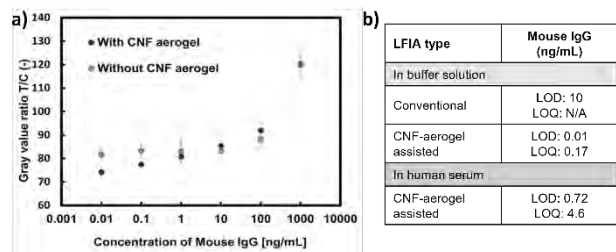


Figure 2: a) Comparison of the calibration curves of the LFIA with (blue) and without (gray) CNF aerogel. b) Comparison of the LODs and limits of quantification (LOQs) for the conventional and the CNF-aerogel assisted LFIA.

Supported by CSEM, the company Momm Diagnostics is developing point-of-care diagnostic technology with superior analytical sensitivity to streamline blood testing procedures. The first test under development is a rapid test for preeclampsia, a dangerous pregnancy condition. Momm's test will assist doctors on-site to optimize interventions and save the lives of mothers and babies.

The technology is based on enzyme-linked lateral flow immunoassays (ELLFIA), for signal amplification, in combination with a quantitative electrochemical readout, by integration of low-cost ion-sensitive electrodes in single-use test cartridges. The approach enables rapid biomarker quantification down to sub-picomolar concentrations and opens previously laboratory-based diagnostic tests to point-of-need and self-testing (Fig.3).

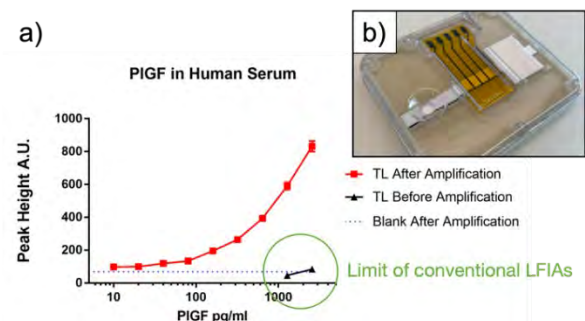


Figure 3: a) Comparison of the colorimetric readout of the test line (TL) of an ELLFIA (red) and a conventional LFIA (black) for placental growth factor (PIGF) in human serum. Through enzymatic amplification, the LOD can be improved by three orders of magnitude compared to conventional LFIA. b) Prototype cartridge with ELLFIA test strip and printed ion-sensitive electrodes for quantitative electrochemical readout.

\* Momm Diagnostics GmbH, Basel (CH)

\*\* Hochschule für Life Sciences FHNW, Muttenz (CH)

<sup>[1]</sup> X. Ye, et al., Biosens. Bioelectron. (2021), 192, 113491.

# Cartridge for Digital Urine Analysis with Electrochemical Sensors

N. Glaser, D. Migliorelli, M. Zinggeler, L. Burr, I. Stergiou, G. Orawez, H. Gao, L. Mühlbach, R. Junuzovic, N. Schmid, K. Krasnopsolski, R. Krähenbühl, C. Seitz, F. Geister, S. Fricke, S. Paoletti, C. Abongomera\*, D. Paris\*, S. Generelli

There is a need for developing new solutions that enable rapid diagnostic tests in low-resource settings. CSEM has realized a printed sensor array for urine diagnostics with a disposable cartridge and a pocket-size reader. An array with a glucose, pH and a sodium sensor was developed for the Swiss TPH. Other analytes for urine diagnostics like  $K^+$ ,  $Cl^-$ , creatinine and protein content will be added to the device in the future.

The Swiss Tropical and Public Health Institute (Swiss TPH) aims to develop a diagnostic tool for the most common pathogens and febrile illnesses, to fight migrant diseases. Nowadays, basic urinalysis is done with urine paper dipsticks with color indicators, which are prone to misinterpretation. Our solution is based on quantitative electrochemical sensors providing digital data. We have developed a low-cost sensing array for a first set of three relevant urine markers (glucose, pH, sodium). Additional sensors will be added to the device in the future, these may include additional ions ( $K^+$ ,  $Cl^-$ ), creatinine, urea, and full protein content in urine.

Once more sensors are added to the device, cloud-based algorithms can assist clinical decision making in low-resource settings, where high-throughput laboratory analysis in professional diagnostic centers is not available. Furthermore, we believe that the regular monitoring of urine markers will also emerge for the monitoring of at-risk patients in European settings.



Figure 1: The disposable sensor cartridge with a printed sensor array attached to the custom-made reader.

The cartridge is fabricated using sensing solutions based on printing and depositions techniques which keep the solution low cost. The assembly of the fluidic cartridge and liquid pouches is equally in line with industrial fabrication techniques.

The cartridge we developed is plugged into a pocket-size reader and an intuitive software guides the user through the calibration and sample measurement. For the validation of our device, we used 21 urine samples of healthy donors. The samples were spiked with additional glucose and sodium to record the full spectrum of the desired physiological range, covering healthy and pathological ranges. The results were calculated with an individual calibration per sensor and with a single averaged calibration function for all sensors. We show that the pH and glucose sensor could be fabricated reproducible enough for a calibration free measuring method. The sodium sensor still requires 1 calibration point per sensor. Additional work is ongoing

to further simplify the sensor cartridge and lower its fabrication cost and for the development of additional sensors.

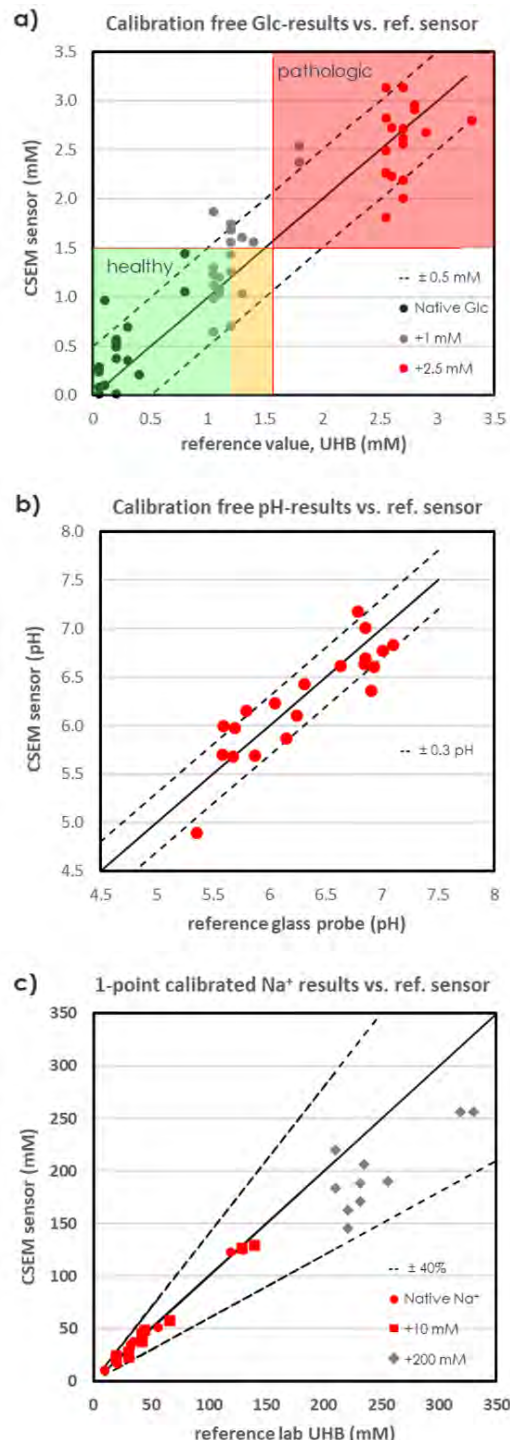


Figure 2: Results of the printed sensor array. Validation with urine samples from healthy volunteers. Each point represents a different urine tested with the single-use cartridge. 1-cartridge per urine sample.

\* Swiss TPH, Basel (CH)

# Modular Electronic Readout Platform for Electrochemical Sensing

I. Stergiou, G. Oravez, M. Markocic, D. Migliorelli, L. Burr, S. Generelli, S. Cattaneo

Concentrating on human health, CSEM's technology platforms address the evolving needs of the life science domain by utilizing the latest advancements in biomonitoring. One such platform is the instrumentation for electrochemical applications and sensors, where CSEM is developing readout electronics based on a versatile and powerful platform, to accommodate broad or turn-key needs, narrowing the gap between applied sciences and industrialization. At present CSEM has successfully established a robust potentiostat with an outlook to complement this platform with galvanostatic and impedance analyzing capabilities.

Innovations in diagnostics and consumer health that provide precise digital data in sports, patients or disease monitoring are in great demand for rapid measurements in everyday life, outside of the lab environment where typically costs are high, and the turnaround time is inefficient. CSEM meets these demands not only by developing low-cost disposable electrochemical sensors, but also the necessary electronic readout. CSEM has developed a modular and low-cost readout platform for electrochemical sensing applications and is continuously developing its core functionalities. Additionally, the reader's core functionality, which is to perform various electrochemical measurements, is paired with other modules such as communication or fluidic control and others.

## Analog-Front-End (AFE):

- Amperometric
- Chronoamperometric (Pulse Test)
- Cyclic Voltammetry
- Square Wave Voltammetry
- Impedance Spectroscopy

## Communication:

- Bluetooth
- UART (USB)

## Extras:

- Battery (on the back)
- µC for script-based autonomy
- On-board flash memory (on the back)
- Fluidic control (pumps & valves)

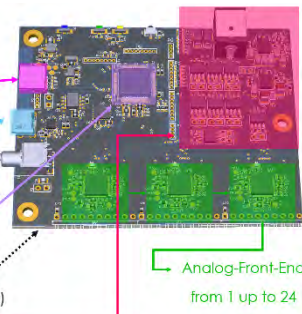


Figure 1: Modular electronic readout platform for electrochemical sensors.

Starting from this general platform, different use case scenarios and readout implementations are currently being targeted by CSEM and its industrial partners. Examples of such scenarios are shown in the Figure 2, showing (from left to right) a 1-channel handheld reader when wireless portability is requested; a fully autonomous device including fluidic control for in-line quality control measurements in a production line; and a cost effective miniaturized 24-channel electrochemical reader (footprint  $100 \times 45 \times 42 \text{ mm}^3$ ) for biomonitoring applications.

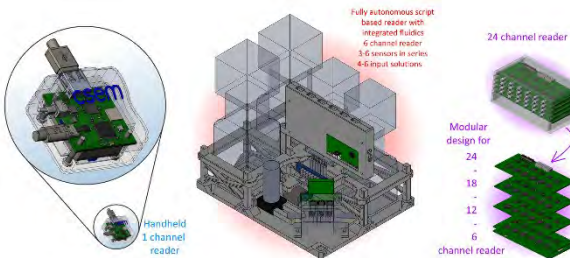


Figure 2: Examples of electrochemical readout implementations, tailored to specific applications.

The user interaction with each device is either connected via cable to a computer or wirelessly connected to a smartphone or tablet, depending on the application. CSEM also developed basic software user interfaces for these devices, with the option of a graphical environment and data-analysis scripts on open-source

platforms such as python. Screenshots of various available GUIs are shown below.

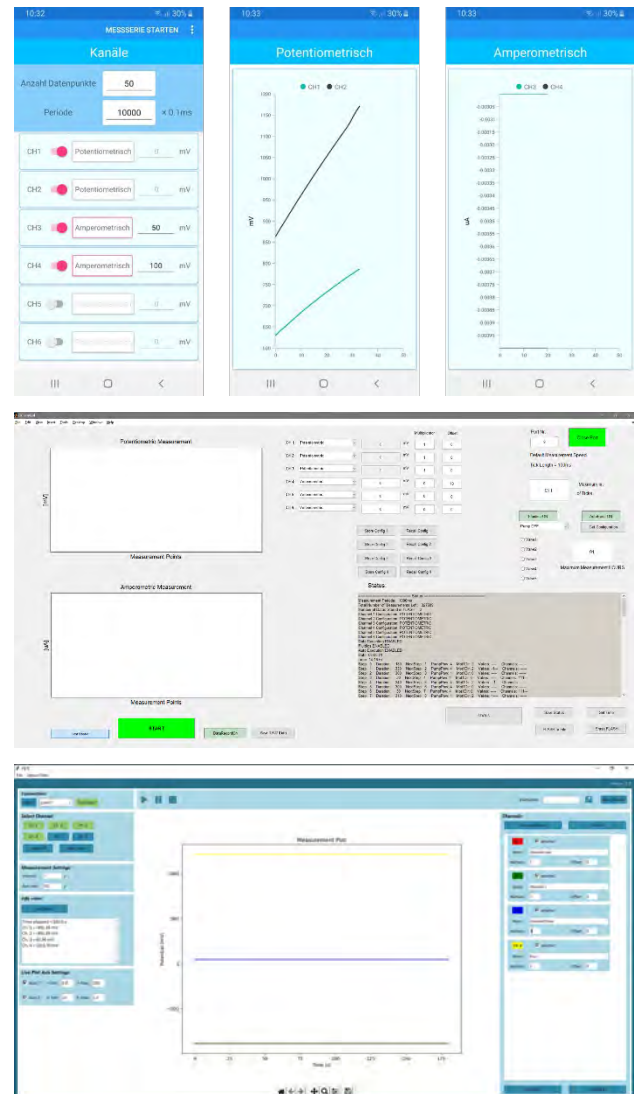


Figure 3: Screenshots of GUIs for electrochemical sensing applications. Mobile GUI for Android smartphones (top), PC GUI based on MATLAB (middle) and Python (bottom).

The analog front end used in our reader platforms supports a wide range of electrochemical measurements, as shown in Figure 1. Currently, the commonly requested types of measurements such as open circuit potentiometry (OCP) and amperometry have been developed on the platform and validated by benchmarking with laboratory grade potentiostats. Other measurement modalities such as square wave voltammetry and impedance spectroscopy will be targeted in the future. In parallel, the device firmware is continuously being improved to support these modalities and to further enhance the hardware's capabilities.

# LEDLight—Multiwavelength Imaging System for Security Feature Inspection

P. Cristofolini, G. Oravez, S. Cattaneo, M. Eichenberger\*

CSEM has developed a standalone visual inspection system for fluorescent security features. It includes UV, NIR and visible light illumination and an automated camera controlled by an integrated computer. LEDlight is used to inspect print quality of security features by the printing technicians and can be customised for other fluorescent illumination/imaging applications.

Fluorescent tags are well-known security elements, often encountered in banknotes, official documents, and luxury goods. Orell Füssli Ltd. Security Printing (OFS), the company renowned for producing the new Swiss banknotes<sup>[1]</sup> and many other currencies, has commissioned CSEM with the development of a visual quality inspection system for fluorescent and infrared security features. The LEDlight system was developed as a small standalone illumination and imaging system, including a single-board computer. It fits seamlessly into OFS' existing quality control setup and is used to inspect print quality of security features by the printing technicians.

LEDlight consists of a multicolour illumination system and an automatic camera for recording fluorescence and brightfield images of the security features. The illumination can be switched between UV-C, UV-A, D65 reference white light and NIR light with a rotary switch. Two programmable push buttons allow for quick access to important visual comparison and inspection tasks of the recorded images.



Figure 1: (top) LEDlight standalone system for visual inspection of fluorescent security features. (bottom) The heart of the LEDlight, the electronics board with UV-C, UV-A, NIR and white light illumination and Raspberry Pi interface.

- Orell Füssli Ltd. Security Printing, Zurich (CH)

The integrated Raspberry Pi runs the quality control software developed by OFS. It can communicate with the LEDlight electronics board, an in-house development, via the GPIO ports. This allows the single-board computer to register the colour of the illumination and pushbutton press events, and further to switch a blocking filter for visible light in the camera on or off.

Special attention was required to achieve a homogenous illumination in the camera's field of view. Each LED group has a dedicated adjustable power supply and LEDs are connected in series. The imaging camera, the computer, the illumination, and the heat management system for the UV-C LEDs could be integrated in a small housing of 140 × 100 × 55 mm with full access to all connection ports and the SD card of the Raspberry Pi. Requirements included low overall mass and a well-balanced mounting bracket to eliminate torque on the linear motion arm.



Figure 2: Optical security features of a 20 € banknote recorded with the LEDlight system. Fluorescence images with illumination light: UV-C (top left), UV-A (top right), white light (bottom left) and NIR (bottom right).

A number of LEDLight devices have been delivered to OFS and were installed in the print production and laboratories.

Applications of LEDlight are not limited to security features and could range from glue curing with live visual feedback, microplastic detection via autofluorescence, or inspection of surfaces after UV-C disinfection. The four high-power LED groups can be customised to the application and the housing is futureproof so that other camera/objective combinations can be fitted.

<sup>[1]</sup> <https://www.ofs.ch/products-services/banknotes>

# Nanoimprinted Diffractive Waveguides with Refractive Index above 1.9 for Augmented Reality

A. Luu-Dinh, F. Lütolf, F. Herzog, R. Krähenbühl, R. Ferrini, B. Gallinet

Augmented reality combiners based on diffractive waveguides can transport light from a miniature projector to the eyes of the user. The projected picture is overlaid on the background image. Augmented reality headsets find a manifold of application from product design to the medical field. We report on nanoimprinted diffractive waveguides with refractive index above 1.9 and a high efficiency grating couplers over a field of view of 60°.

High-refractive index (HRI) materials for UV Nanoimprint Lithography (UV-NIL) have a huge potential for several application domains, notably for augmented/mixed reality (AR/MR) devices, whose market is foreseen to grow at high rate in the next few years. Aim of this project is to overcome barriers preventing mass adoption of this manufacturing platform, thus bringing it closer to industrial uptake and demonstrating a diffractive waveguide with high refractive indexes. Figure 1 shows a standard UV nanoimprint process which replicates the structure from a mold into a UV curable material. The mold can be fabricated using a variety of approaches, such as laser interference lithography or electron beam lithography. We designed a high field of view diffractive combiner based on a waveguide with refractive index above 1.95 and a high efficiency grating incoupler. We also developed a UV-NIL process specifically suitable to their fabrication.

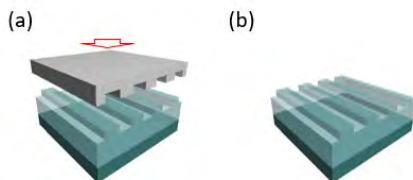


Figure 1: UV imprint process. a) A stamp is used to replicate micro- or nanostructures in a UV curable hybrid polymer. b) Structure after the stamp release.

Figure 2 shows the working principle of a diffractive waveguide combiner. Light projected by a miniaturized light engine is incoupled by a diffraction grating into a glass slab. It is then outcoupled by another diffraction grating to reach the eye. The projected image is overlaid with the background, yielding an augmented reality experience for the user. In such a waveguide combiner, the field of view of the projected image that can be guided is directly determined by the refractive index of the waveguide. It is therefore extremely important to have it as high as possible, while keeping the other optical performances (e.g., efficiency, light scattering) within the required device specifications.

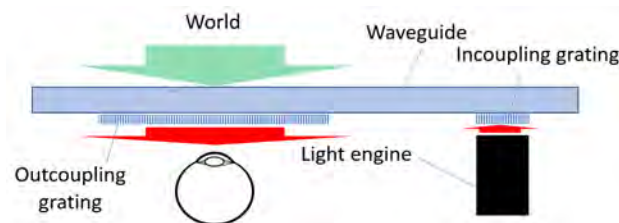


Figure 2: Functioning principle of a diffractive waveguide combiner for augmented reality.

The nanoimprint master was realized with electron beam lithography. The gratings were imprinted on the waveguide substrate. In order to guarantee the incoupling of a full image in

the waveguide, the refractive index of the imprint material must be matched with the one of the waveguide. We used the IOC-133 UV-NIL material developed by Inkron. The resulting combiner is shown in Figure 3. It has a butterfly-like geometry, where the incoupling grating is located at the bottom center, while the outcoupling grating is at the top of the image. The diagonal field of view was increased from 35° to 60° with the use of a high refractive index waveguide and UV-NIL material.

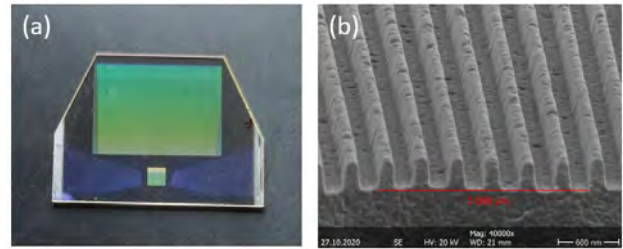


Figure 3: a) The 60° augmented reality combiner with waveguide refractive index above 1.9. b) Scanning electron micrograph of the incoupling grating before thin film coating.

The incoupling grating was coated with a thin dielectric film to increase its efficiency with the aim to the device consumption [1]. At the same time, the grating aspect ratio remains low, which guarantees the manufacturability by UV-NIL. Figure 4 reports measurements of the incoupling efficiency as a function of the incidence angle.

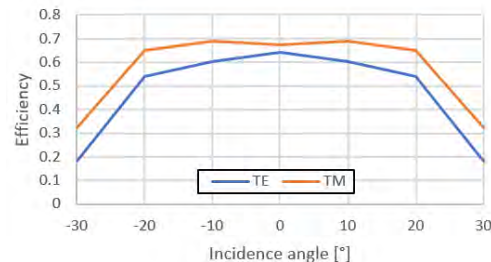


Figure 4: Measured incoupling efficiency as a function of incidence angle, for TE and TM polarizations.

Using this approach, the measured incoupling efficiency is above 50% in average over both light polarizations and over the entire field of view, maintaining a very good homogeneity.

We have reported on a high field of view augmented reality waveguide combiner manufactured by UV-NIL, as well as strategy for a high-efficiency incoupling grating. The field of view can be further increased with appropriate design of the diffraction gratings. Note that the current version applicable to monochromatic green light can be extended to full RGB imaging using two or three stacked waveguides.

Funding from Innosuisse 38832.1 IP-ENG is gratefully acknowledged.

[1] US Patent 9'739'950

# Narrowband Spectral Filters Based on Nanostructured Arrays

C. Schneider, J. Hadler, R. Krähenbühl, B. Gallinet

*Filter arrays based on a combination of plasmonic and dielectric guided mode resonances are presented. This approach is foreseen to find applications in compact and mass manufactured miniature spectral sensors and multispectral cameras.*

Recently, there has been an increasing interest in miniature devices performing spectral measurements for a variety of applications such as photography or food analysis via consumer electronic devices, as well as human centric lighting and industrial quality control. Interference filters for on-chip spectrometers or multispectral imagers show high performance but require a very large number of process steps, which scale with the number of spectral channels. Nanostructured filters have the potential to overcome these constraints, as they can be manufactured with a low amount of process steps which does not scale with the number of spectral channels. We report on the design and fabrication of band-pass filters with a bandwidth of 20 nm in the visible range, based on hybrid plasmonic-dielectric thin film waveguides<sup>[1]</sup>.

Figure 1 shows the working principle of the proposed filtering approach. The incident light (orange arrows) is initially coupled as plasmonic resonances in the metallic top coating, into a resonant waveguide grating consisting of a ZnS core (green) conformal to a periodic corrugation, and finally coupled out (black arrows). It interferes with directly transmitted light (red arrows) to generate a Fano-like resonance. A silica spacer (blue squares) is deposited between the metallic layer and the waveguide core.

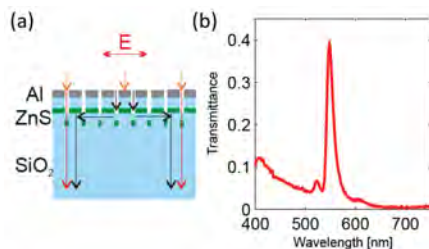


Figure 1: a) Light propagation in the proposed hybrid plasmonic dielectric corrugated waveguide system. b) Measured transmittance spectrum of TM-polarized light.

Figure 2 summarizes the process flow applied for the fabrication of the filter array. UV NIL is first performed from a master containing 10 different linear binary grating profiles. The waveguide core material is coated (ZnS, green arrows), followed by the cladding, the spacer material (SiO<sub>2</sub>, red arrows) and an oblique aluminum metallization (gray arrows). This method allows for the fabrication of an arbitrary number of filters at the same time, thus reducing dramatically the production costs with respect to interference filters.

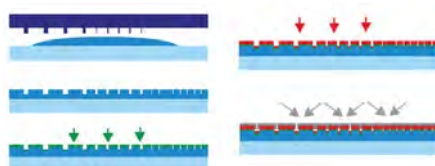


Figure 2: Fabrication process flow of the filter array.

<sup>[1]</sup> B. Gallinet, G. Quaranta, C. Schneider, "Narrowband transmission filters based on resonant waveguide gratings and conformal

The transmission spectrum of a set of filters has been measured in the visible and near infrared spectral range (Figure 3). The thin film parameters have been chosen in order to maximize the peak transmission of all 10 filters at once. Each filter has a lateral size of 3 mm. The transmission amplitude off-resonance is generally below 10%, which is lower than other approaches based on nanostructuring (e.g., plasmonic filters).

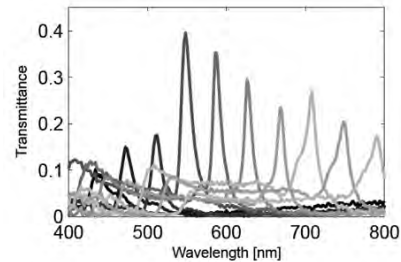


Figure 3: Measured transmittance for TM-polarized light. From left to right: periodicity of the corrugation of 260, 288, 316, 344, 372, 400, 428, 456, 484 and 512 nm. The coatings were applied simultaneously to all gratings.

Since the filter effect is based on laterally propagating guided resonances, we have investigated the effect of downscaling the filter lateral size on the resonance amplitude (Figure 4).

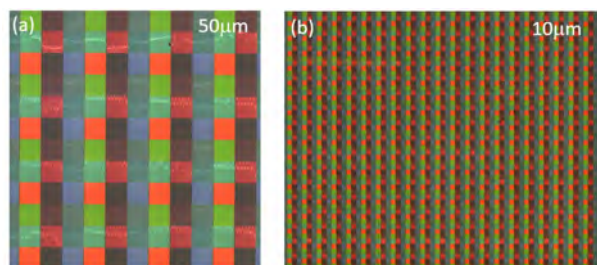


Figure 4: Microscope images of fabricated filter arrays. a) Pixel size 50  $\mu\text{m}$ . b) Pixel size 10  $\mu\text{m}$ .

Measurements of the pixel transmission show that the resonance amplitude, determining the filtering efficiency, is not affected by the size reduction down to 10  $\mu\text{m}$ . This is in agreement with the results of full field electromagnetic finite differences in time domain (FDTD) simulations.

We have reported on nanostructured bandpass filters fabricated by UV-NIL and metallo-dielectric coatings. They have a bandwidth of 20 nm in the spectral range between 400 nm and 800 nm. We have shown that they can be pixelated down to 10  $\mu\text{m}$  pixel size without compromising their efficiency. The presented filter approach is foreseen to find applications in compact and mass manufactured miniature spectral sensors and multispectral cameras.

dielectric-plasmonic coatings", Adv. Opt. Technologies (Nov. 2020), 10 (1), 31-38. <https://dx.doi.org/10.1515/aot-2020-0049>

# Femtochip—Electro-Optic Frequency Combs and Integrated Photonic Circuits

V. Brasch, T. Herr<sup>•</sup>, E. Obrzud, S. Lecomte

Integrated photonic circuits (PICs) have clear advantages over traditional bulk or fiber optics because of their small size, scalable fabrication and the resulting low costs. In the project Femtochip such integrated optical structures were combined with the electro-optics frequency comb technology that was developed at CSEM for astronomical and industrial applications. The results did not only lead to several publications but also built the foundation for present and future activities in PICs and astronomical frequency combs.

Electro-optic frequency combs (EO combs) have been developed at CSEM for several years now. With their large line spacing (tens of GHz) and easy translation of the center wavelength (or offset frequency), they complement CSEM's mode-locked laser technology (line spacings of hundreds of MHz) very well. The large line spacings are required for example in astronomy, where electro-optics frequency combs are used to calibrate spectrographs. On the other hand, the tunable center wavelength makes such systems also a good candidate for frequency comb spectroscopy. Other applications of EO combs are in material processing and telecom.

Similarly, photonic integrated circuits (PICs) have been used at CSEM for a few years now in particular in the context of Kerr frequency comb generation in optical microresonators and to generate supercontinua from mode-locked lasers. PICs enable the integration of several optical elements on a small chip, similar to electrical integrated circuits (ICs). For nonlinear processes the small size of PICs has the additional advantage that such processes become more efficient compared to fiber optics or bulk optical elements such as lenses and optical crystals.

With EO combs and PICs as very relevant topics at CSEM but also in photonics in general, Femtochip was a great opportunity to unite these two developments in one project. Femtochip was one of the first Bridge Discovery project at CSEM and was a collaboration with Tobias Kippenberg at EPFL, who provided the silicon nitride (SiN) PICs for some experiments.

There are several key results that have been achieved in Femtochip. One result used SiN waveguides to generate a visible supercontinuum from an EO comb pulse source. These results were published in Optics Letters [1]. One key feature was that due to the high third-order nonlinearity (also known as Kerr nonlinearity) of the SiN PIC, the mechanism of triple-sum frequency generation played a significant role in the generation of these spectra. The output spectrum from this publication is shown below and spans the full visible wavelength range.

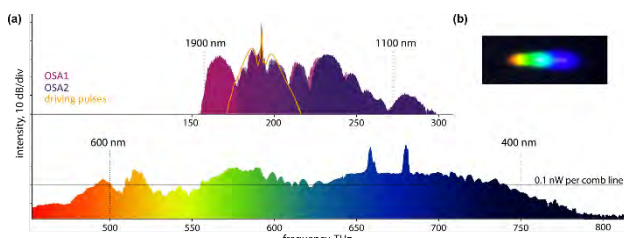


Figure 1: Visible supercontinuum spectrum generated from an electro-optic frequency comb inside a silicon nitride PIC.

• Center for Free-Electron Laser Science (CFEL), Deutsches Elektronen-Synchrotron (DESY), Hamburg (DE)

[1] E. Obrzud, et al. . Optics Letters 44, n° 21 (2019): 5290-93. <https://doi.org/10.1364/OL.44.005290>.

Another result, published in Optica [2], showed for the first time the mechanism of nonlinear filtering of a pulse train timing jitter in optical microresonators. For this work the microresonators were not PICs but microresonators realized in CSEM's proprietary fiber-based technology. However, the results can be transferred to any other type of microresonator, including PIC-based ones. In the experiment, the carefully characterized pulse train generated by an EO comb was sent to the microresonator. Because of nonlinear optical effects inside the microresonator, the pulse train was modified. Surprisingly, when characterizing the pulse train after the microresonator, it was measured that the timing jitter properties of the pulse train had improved by more than one order of magnitude beyond what was expected from the linear optical properties of the microresonator. The theory behind this novel concept of nonlinear filtering is explained in the publication, which is Open Access and free to read for anyone.

Lastly, combining the capabilities and experience also gained in Femtochip with the expertise in microfabrication at CSEM, we could demonstrate the first lithium niobate on insulator (LNOI) PICs at CSEM in experiments for supercontinuum generation of frequency combs. This was a substantial first steps for CSEM's own PIC platform, currently under development.



Figure 2: A lithium niobate on insulator (LNOI) PIC fabricated at CSEM generates a broadband supercontinuum including visible light.

Beyond the publications, the results of the project have been the basis for new projects and proposals for both, the electro-optic frequency comb as well as the PICs. Another Bridge Discovery-funded project has started in 2021 using LNOI PICs to build gas sensors. The electro-optic frequency combs have been demonstrated as a turn-key technology for applications in astronomy and several other proposals for European and Swiss funding instruments have been submitted or are in preparation.

[2] V. Brasch, et al. Optica 6, n° 11 (2019): 1386-93. <https://doi.org/10.1364/OPTICA.6.001386>.

# Microlenses: Capability Overview

F. Zanella, G. Basset, C. Schneider, R. Ferrini

*Microlenses, and especially microlens arrays (MLA), are commonly used as stand-alone optical components, for beam homogenization and shaping, or integrated as wafer-level optics (WLO), either on top of light sources (VCSEL, micro-LED), for beam shaping, or on top of light (photodiodes) or image (CMOS, CCD, SPAD) sensors, as light concentrators. In the latter case, each microlens of the MLA, also known in the photography domain as On-Chip Lens (OCL), redirects the light to the active volume of the pixel located underneath (see Figure 3) which increases the external quantum efficiency (EQE), especially for front-illuminated image sensors and their limited pixel fill-factor. CSEM offers to its customers a microlens origination and replication service ranging from design and prototyping up to small-series production.*

The footprint of the microlenses – circular, square, hexagonal, elliptical or cylindrical, see Figure 1 – and their shape – sag, diameter, and gap, see Figure 2 – are originated at CSEM by a photolithography step to get photoresist pillars, followed by a thermal reflow process which melts those pillars into microlenses. This wafer-level process is usually performed on glass wafers, resulting in the so-called master, and can also be performed directly onto the final substrate when the microlens shape cannot be UV-replicated, e.g., sup-hemispherical microlenses.<sup>[1]</sup> This origination method allows extremely low surface roughness, better than for example laser ablation or multi-photon polymerization. Next, the negative of the microlens master is realized by UV nanoimprint lithography (UV-NIL or UV replication) in a mask aligner and on a photomask, resulting in a so-called mould or stamp. Finally, the same UV-NIL process is used to replicate the microlenses of the mould onto the final substrate in an aligned way ( $< 2 \mu\text{m}$ ). During that process, the UV-curable microlens material is dispensed in liquid state, which allows replicating microlenses on complex topographies. An advantage of this approach is that the mould can be re-used multiple times. A residual layer remains under the replicated microlenses, see Figure 2, which thickness can be tuned from hundreds of micrometers down to around 10  $\mu\text{m}$ .

The substrates on which CSEM can replicate MLA are wafers up to 150 mm diameter, bare dies down to  $2 \times 2 \text{ mm}^2$  or even packaged dies<sup>[2]</sup>. Various lens materials can be used, inorganic-organic hybrid (sol-gels) or organic (PMMA, PU) polymers, depending on the application requirements, e.g., space<sup>[2]</sup>.

CSEM is constantly evolving its processes and expertise to meet unmet needs of new and demanding photonic solutions.

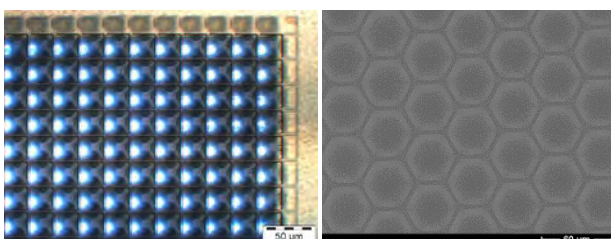


Figure 1: MLAs with square (left<sup>[3]</sup>) and hexagonal (right) footprints

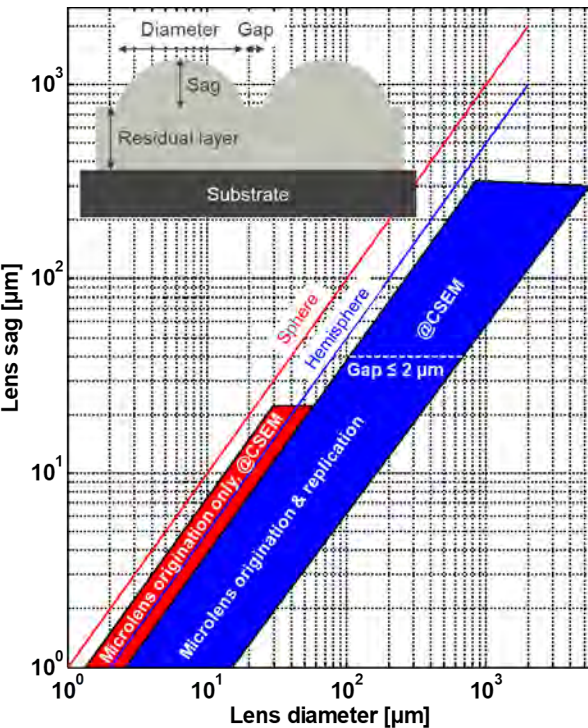


Figure 2: Microlens geometrical parameter space available at CSEM.

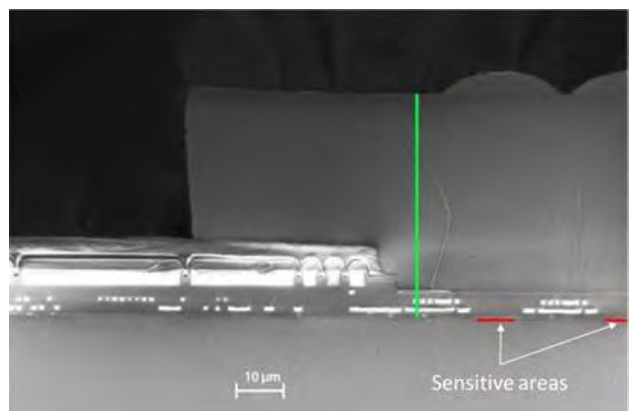


Figure 3: Cross-section of a front-illuminated image sensor equipped with CSEM's microlenses focusing light onto the sensitive areas<sup>[4]</sup>.

<sup>[1]</sup> G. Basset, et al., "Fabrication of Arrays of Quasi-micro-beads for Parallel Nanojet Super-Resolution Imaging", CSEM Scientific and Technical Report (2021), 99.

<sup>[2]</sup> F. Zanella, et al., "Microlens testing on back-illuminated image sensors for space applications", Applied Optics 59 (12), 3636-3644 (2020).

<sup>[3]</sup> I. M. Antolovic, et al., "Optical-stack optimization for improved SPAD photon detection efficiency", Proc. SPIE 10926, Quantum Sensing and Nano Electronics and Photonics XVI, 109262T (2019).

<sup>[4]</sup> J. Mata Pavia, et al., "Measurement and modeling of microlenses fabricated on single-photon avalanche diode arrays for fill factor recovery", Optics Express 22, 4202-4213 (2014).

# Fabrication of Arrays of Quasi-micro-beads for Parallel Nanojet Super-resolution Imaging

G. Basset, A. Luu-Dinh, C. Schneider, D. Schlup, S. Perrin<sup>•</sup>, W. Fangting<sup>•</sup>, S. Lecler<sup>•</sup>

Many industries face the challenge of observing submicron objects quickly and reliably. It can be the inspection of micromechanical parts for quality controls, cell imaging for the analysis of the reaction of cells to external agents, typically future drugs to be tested, or quality control in microelectronics or in photonics. The techniques used today are optical microscopy (confocal, SNOM), electron microscopy, AFM and fluorescence microscopy in biology. These techniques have made a great deal of progress but have various limitations. Some are not sufficiently resolved while others are too long/complex for industrial processes. It is of high interest to make accessible a simple technique of super-resolved optical microscopy in 2D and 3D that can meet the current requirements of the industry. CSEM is producing sup-hemispherical microlens arrays to enable such fast and versatile super-resolution imaging.

Optical super-resolution imaging techniques allow to obtain a finer effective imaging resolution than the limit due to the optical wavelength of the imaging light. Photonic jet imaging has been developed in the last decade for super-resolved imaging under an optical microscope using microspheres made of silica or of a high-refractive index transparent metal oxide. This technique allows the fast imaging in 2D or 3D of organic or inorganic objects with super-resolution at various wavelengths and without fluorescence. However, it is limited by the small field of view located below the microsphere, or the few microspheres, used.

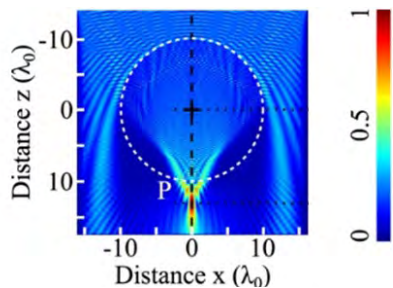


Figure 1: Electromagnetic field intensity near a microsphere and its photonic jet. Scales in the super-resolution-imaging wavelength.<sup>[1]</sup>

A possibility to overcome this limiting factor is to fabricate dense arrays of quasi-microsphere: sup-hemispherical microlens arrays. As most microlenses, these special shape microlenses are manufactured using a photoresist which is patterned in pillars by photolithography. The pillars are then melted during a thermal reflow. High-microlens shapes are not possible with this process except with a CSEM-developed local modification of the surface energy between the photoresist pillars. It fixes the photoresist footprint and enables reaching the needed shapes.

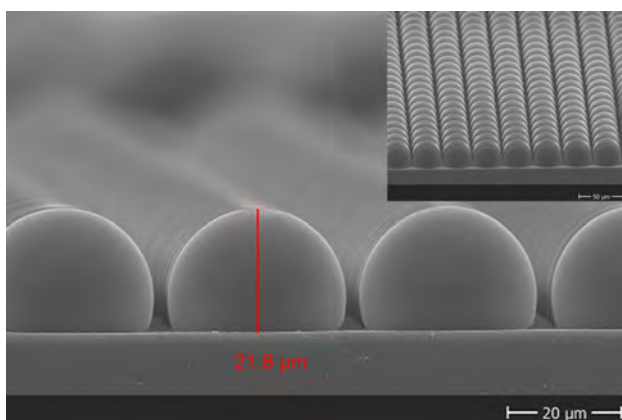


Figure 2: Arrays of sup-hemispherical microlenses.

The fabricated sup-hemispherical geometries can be tuned easily and have very high quality and low-surface roughness. Thousands or millions of such microlenses can be fabricated simultaneously in parallel on glass substrates using conventional microtechnology production equipment, making such arrays potentially affordable to fabricate.

Imaging in a conventional optical microscope using such an array of quasi-microsphere allowed to demonstrate optical super-resolution imaging without scanning and simultaneously in an array of fields of view.

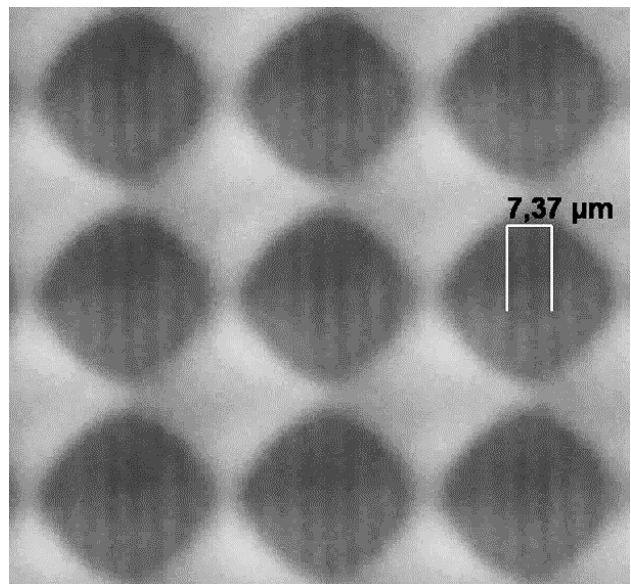


Figure 3: Arrays of super-resolved field of view of a grating (400 nm linewidth) with a quasi-microsphere additional magnification of ~4.6 using an optical microscope. The magnified grating period is observed at 3.7 μm.

The adjacent fields of view are super-resolved without generating crosstalk and allow to reconstruct a much larger synthetic super-resolved image than with a single microsphere. This makes this photonic-jet super-resolved imaging much faster as tens or hundreds of quasi-microspheres can be used in parallel to reconstruct a complete image.

Further work is on-going to optimize the shape of the sup-hemispherical microlenses and of the substrate supporting them. This targets to further improve the imaging contrast and the super-resolution.

• ICube Laboratory, Illkirch, France

[1] S. Lecler, Photonic jet lens, Scientific Reports, vol 9, (2019).

# Design for Manufacturing Tools: Freeform Micro-optics

O. Fernandez, T. Aderneuer, T. Offermans, R. Ferrini

Freeform micro-optical arrays (FMOAs) gain increasing interest because they can overcome some limitations of rotationally symmetric optical components and because of the benefits of their microscopic dimensions. They enable better performance and compactness of optical devices. However, the complex and segmented surface shapes bring many challenges, from design to fabrication to quality control. Especially for FMOA designs that contain many individual freeform elements, their manufacturability assessment is far from trivial. Here, we present computer-aided design (CAD)-based tools that analyze FMOA designs for manufacturing constraints so that critical parts can be identified at an early stage, reducing time-consuming and costly adjustments at a later stage.

Optical designs optimized only based on performance without considering manufacturability limits will likely turn out expensive or simply unfeasible. In many cases the achievable quality is limited by the precision and limitations of the manufacturing technologies. Hence, the optical solutions must be designed in such a way that they are easy to manufacture using design approaches that automatically account for the fabrication tolerances and manufacturing limitations. Freeform optical components, with non-isotropic tolerances, can hardly benefit from classical tolerancing practices and require innovative solutions.

With this objective the PHABULOUS Pilot Line (<https://phabulous.eu>) is developing tools that facilitate and speed up the assessment of FMOA designs from a manufacturing perspective. The feedback received by most PHABULOUS manufacturers indicate that the local surface slope, height, and aspect ratio are some of the most important parameters to consider in such assessment. Here we present three CAD-based tools that, for given manufacturing constraints, quickly identifies, and clearly visualize the problematic parts of the investigated FMOA design (Figure 1).

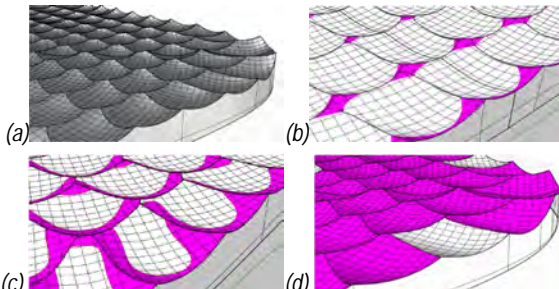


Figure 1. (a) Example FMLA design © LIMBAK 4PI SL (b-d) CAD tool-based analysis against (b) height, (c) slope, and (d) aspect ratio constraints. The visualization is done with a two-color scale, with areas colored white indicating areas within the user-defined limit and magenta areas indicating critical areas outside the limit. The tools were created with Grasshopper, a visual programming environment within the Rhinoceros CAD modelling software.

In Figure 2(a-e) we illustrate the various the main steps of the implemented algorithm for the slope tool. First, a uniform point grid is generated on each surface (Figure 2a). Then, the surface slopes are calculated at the locations of the point grid on the surfaces. Subsequently, another point grid is generated with the same x and y coordinates and new z coordinates whose z values correspond to the slope values (green points). From these points, new surfaces are generated (shown in red). Next, a plane surface is generated whose z-value corresponds to a user-defined limit for the slope angle (green, Figure 2b). The intersection between the generated plane and the surfaces is calculated. The isocurves thus correspond to the limits of the surface parts that lie outside and inside a defined limit of the surface slope. These isocurves are projected onto the original surface (green,

Figure 2c). From these boundaries, intersection planes are generated (shown in red, Figure 2d) which cut the original surfaces. The resulting surfaces (cutting boundaries shown in green) are processed with an algorithm that assigns them a color (Figure 2f).

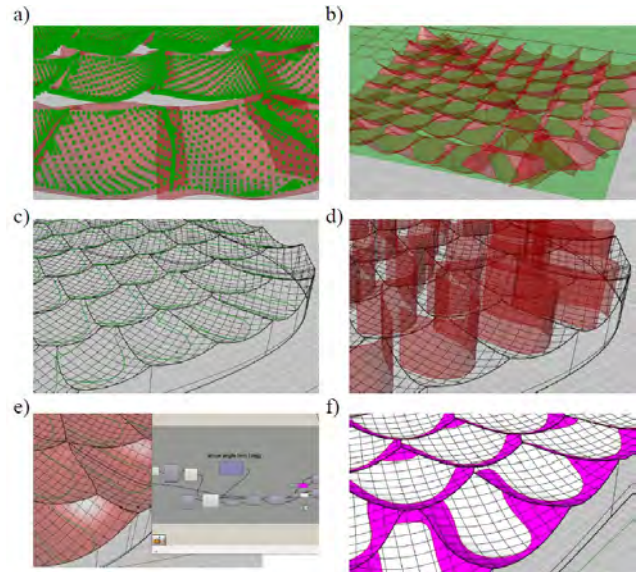


Figure 2. CAD-based analysis of the surface slope. (a)-(f) visualize the main steps of the implemented algorithm. The structure of the algorithm implemented in Grasshopper is shown in the image with each box corresponding to a command (e, inset).

We have shown how freeform optical designs comprising differently shaped surfaces can be analyzed in a fast and comprehensive way from a manufacturing perspective. The presented tools make it possible to evaluate designs at an early stage which speeds up the manufacturing assessment and facilitates the necessary corrections before proceeding with (often expensive) manufacturing trials. In comparison with built-in CAD tools can be easily customized according to the needs which represents a real advantage. As such, the presented tools can serve various manufacturing technologies with various manufacturing constraints.

This work has been carried out within the PHABULOUS project (<https://phabulous.eu>) and was published at the SPIE (doi: 10.1117/12.2597089). The project has received funding from the European Union's Horizon 2020 research and innovation program under grant agreement No. 871710 in a public-private partnership with Photonics21.



# Surface Topology and Functionality of Freeform Micro-optical Arrays

T. Aderneuer, O. Fernández, R. Ferrini

Freeform surfaces are surfaces designed with no symmetry constraints; thus they increase design freedom and consequently allow to effectively achieve non-symmetrical light distributions. However, the complexity in shape introduces additional manufacturing and characterization challenges. Here we report on a new characterization approach based on the generation of 3D CAD models with data of experimentally measured surface topology, contribute for an improved computational analysis of microscale components.

Freeform micro-optical components have recently raised considerable scientific and industrial interest. On the one hand, they enable optical systems with lower number of components, smaller size, improved optical performance and higher efficiency. On the other hand, freeform micro-optical arrays (FMOAs) can foster system miniaturization even further and are compatible with large area manufacturing.

The characterization of FMOAs is not yet standardized and still a challenge. A main objective of CSEM in the domain of freeform micro-optics is to accelerate the manufacturing chain and improve quality control. Here we report on an innovative approach that we developed for improved quality control of FMOAs by creating virtual 3D CAD models using NURBS surface representation.<sup>[1]</sup>

**Method:** To measure the surface topology a laser scanning microscope (Keyence VK-X1100) was used. The surface shape, provided as point cloud (XYZ coordinates) was segmented to overcome the limit of the CAD software, which can transform only a maximum number of points at once. The segments were then converted into so-called NURBS surfaces using the CAD software Rhinoceros and inhouse developed python scripts. Finally, they were merged to have the full surface and converted to a solid, which was imported in the ray-tracing software LightTools.

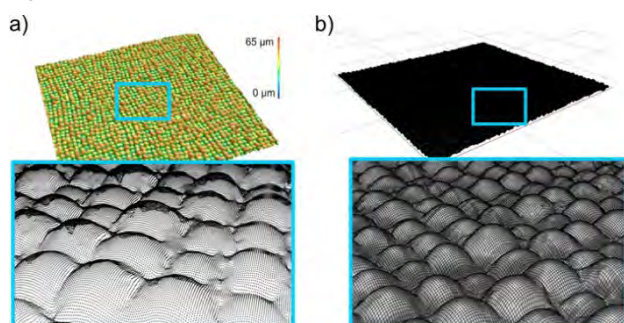


Figure 1: Creation of 3D CAD model of FMOA. a) Experimentally measured surface topology in point cloud format b) NURBS surface created from point cloud data.

**3D CAD model of FMOAs:** It was reported that computational surface models with accuracy in the order of tens of microns can be insufficient for analyzing the optical performance.<sup>[2]</sup> CAD models with high accuracy are therefore important for reliable analysis of micro-optical components. Creating 3D CAD models

using NURBS surfaces enable higher accuracy than polynomial fitting. We used different FMOA samples to generate such 3D CAD models. Figure 1 shows a diffuser sample with thousands of individual shaped elements and the respective NURBS surface created. More than one million points were processed. The standard deviation is below 0.2 μm and shows thus excellent accuracy. Figure 2 shows the concept of implementing these CAD model in optical simulations, which allows to link the surface form to the light distribution pattern. The ray-tracing software allows to identify rays responsible for a certain part of the light pattern. If the computational model has sufficient accuracy, critical parts of the surface can be identified, which may cause a decrease in the optical performance.

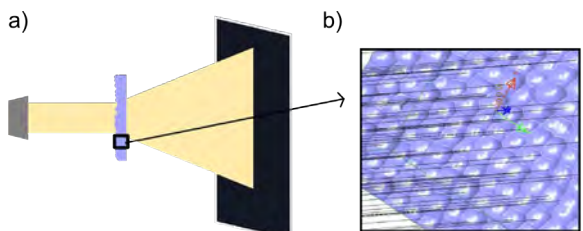


Figure 2: a) Sketch of an optical simulation configuration with a light source, FMOA placed into the optical path and a black rectangle representing a detector for analysis of the light distribution pattern. b) Close view an 3D model of the diffuser structure imported in LightTools with the black lines representing single light rays.

**Conclusion:** We presented an innovative method for characterizing manufactured FMOAs based on experimentally measured surface topology and ray-tracing optical simulations. Surface fitting of FMOAs with submicrometer accuracy was achieved. Using the created 3D CAD models enables to overcomes limitations of experimental optical setups.

**Acknowledgements.** This work was done in the framework of the Innosuisse project 30049.1 together with the Fachhochschule Nordwestschweiz, School of Engineering Institute of Polymer Nanotechnology (INKA). Further, we would like to thank the SNI Imaging Lab for providing access to their confocal laser scanning microscope.

[1] T. Aderneuer, O. Fernández, A. Karpik, J. Werder, M. Marhöfer, P.M. Kristiansen, R. Ferrini, "Surface topology and functionality of freeform microlens arrays", *Opt. Express* 29, 5033-5042 (2021).

[2] I. Sieber, A. Yi, U. Gengenbach, "Metrology Data-Based Simulation of Freeform Optics", *Appl. Sci.* 8, 2338 (2018).

# Wearable Temperature Sensor based on Photonic Technologies for Blood Composition Measurement

R. Krähenbühl, F. Zanella, N. Marjanovic, S. Fricke

To non-invasively measure the blood constituents (i.e., glucose), without the need for a finger pricking, we proposed and demonstrated the basic functionality of an innovative, minimized, wearable device. The concept is based on infra-red (IR) spectroscopy (the optical measurements of the wavelength-dependent temperature increase), exploiting a Mach-Zehnder Interferometer (MZI) device on a photonic integrated circuits (PIC) platform.

Currently, the measurement of the concentration of different constituents in human blood is mostly done by invasive methods (taking blood and its analysis in a laboratory). Non-invasive methods, however, allow for pain free examination with minimum risk of infection, as well as the possibility for real-time data monitoring for immediate clinical reaction.

The here proposed concept is an integrated device fabricated on a silicon-on-insulator (SOI) PIC. It can measure the concentration in the blood by placing a finger on top or wearing the device on the patient's skin. The core of the device is an innovative SOI Mach-Zehnder Interferometer (MZI), which is highly sensitivity to temperature changes and therefore able to measure the absorption spectrum of the blood. The wavelength dependent temperature change is possibly produced by a tunable quantum-cascade laser (QCL) beam which interacts with the blood capillary within patient's finger/skin. To realize the device on the backside of the chip (not interfering with the skin) required compact, precise in-plane fiber interconnects, waveguide grating couplers together with CSEM's previously published folded micro-optical elements are foreseen.

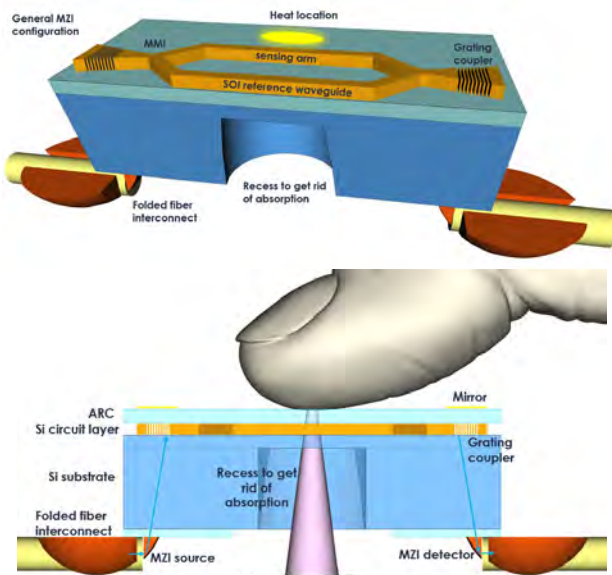


Figure 1: Concept (3D view, cross section) of the photonic integrated circuit (PIC) with a standard Mach-Zehnder interferometer (MZI)-sensor, as well as the micro-optical elements for compact in plane fiber interconnects.

To fabricate the MZI PIC, our collaboration partner Interuniversitair Micro-Electronica Centrum (IMEC) employs electron beam (e-beam) lithography which enables fast prototyping on 220 nm silicon-on-insulator devices. To create the folded micro-optical elements, we make use of the UV-replication process into polymers, which produces smooth mirror surfaces and allows for "plug-and-play"-type components.

So far, the MZI-PIC for backside coupling had been realized without the recess area for the stimulating optical beam and without integrating the folded micro-optical interconnect. To still prove the usability of the MZI-PIC for temperature sensing applications, the optical response to an external heat source was verified.

To be able to measure optical fiber to fiber transmission at the backside of the MZI-PIC chip and be able to apply a heat source near the sensing MZI arm on the front side, a special fiber optical setup was built at CSEM. It consists of an input and output fiber each on a three-axis micro stage, a mirror to see the opposite side of the chip, a thin electric wire on a polymer substrate as heat source and a movable binocular to directly see the backside of the MZI-PIC chip, as well as the front side in the mirror. First, the fiber-to-fiber losses of the device were optimized and measured to be around 12-18 dB. We assume, that the loss contributions were around 5-6 dB due to the grating couplers, as well as 2-6 dB due to waveguide losses. In a second step, we placed a controlled heat source using the thin electric wire driven by an alternating (0 to 2 V at 10 Hz) electrical voltage signal near the sensing arm.

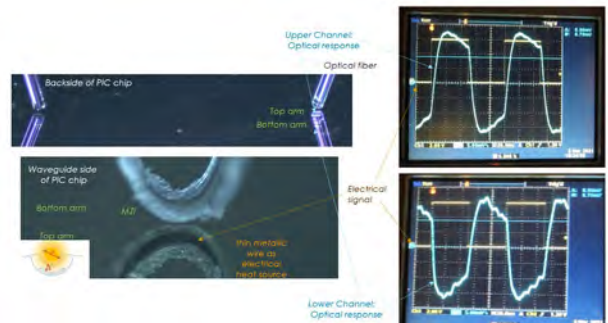


Figure 3: Optical characterization setup (fiber coupled backside, upper left; heat source induced frontside lower left) and measurement results of the optical response of the two MZI output channels in response to the metallic wire driven by an alternating voltage signal.

The detected optical curves of the two outputs did follow the electrical signal, exhibiting only some fall offs due to heat dissipation. The impressive results proved the usability of the chosen MZI-PIC technology for measuring temperature change.

The presented technologies are highly advantageous in prototyping of highly integrated and compact fiber assembled PICs. Furthermore, the implementation into high volume industrial production is straightforward, as all technologies are wafer level based. Further miniaturization, i.e., integration of all optical active components into a wristwatch type device is also feasible.

This project was a model case within the EU-project MedPhab (H2020-ICT-2019-2). The MZI-PICs have been fabricated and provided by Interuniversitair Micro-Electronica Centrum (IMEC).

# Novel Microvibration Test Facility

G. Borque Gallego, E. Klauser, Y.-J. Regamey

*Responding to the needs of more and more complex and demanding space missions, in terms of mechanical stability, CSEM designed and commissioned a novel microvibration test facility. This novel test setup allows to characterize the performances of mechanisms and actuators in terms of exported microvibrations as well as their susceptibility to external noise sources.*

The generated microvibrations by space equipment are an aspect of increasing importance in space missions, due to its impact on the satellites' performance and pointing accuracy. For this reason, an extensive characterization process is required for some of the key equipment, such as reaction wheels for spacecraft attitude control. It is then essential to be able to characterize the behavior of the equipment in early stages to consider the exported microvibrations from its design phase and eventually apply some countermeasures for its minimization. In the frame of the development of low-noise and high-precision mechanisms for space and ground applications, CSEM pursues its activities in the development of microvibration characterization and mitigation. For this purpose, and to be able to study the impact of the different designs and techniques, CSEM proceeded to the design, procurement, assembly, and validation of a novel microvibration measurement facility.

The microvibration test facility is located at the Observatory site of CSEM in Neuchâtel, in a room directly built on the bedrock of the Jura mountains, which guarantees a very stable and quiet environment. The measurement equipment, as shown in Figure 1, consists of four three-component piezoelectric sensors, preloaded between two custom-made plates, and mounted on a big seismic mass suspended over four pneumatic isolators to remove environment perturbations, over which the equipment to be characterized is fixed. Two configurations of different top-plate size have been designed to better adapt and provide characterization capabilities to payloads of different sizes.



Figure 1: CSEM microvibration characterization test bench.

The vibrations generated by the payload create a mechanical stress on the piezoelectric sensors (type 9067C and 9068C by Kistler), whose signal is conditioned by a high-sensitivity Kistler 5080A charge amplifier. The signals are then synchronously sampled at up to 20 kHz by a dSpace MicroLabBox system with 16-bit A/D converters (ADC). With such a configuration, it is possible to measure three components of both, force and torque, over a broad frequency range ( $>1$  kHz), with a very high resolution (up to 0.06 mN).

Several experiments were conducted to validate the facility. After the installation of the multi-component dynamometer and all its support equipment, an extensive characterization and validation campaign was carried out. Firstly, the RMS background noise level of 3 mN was measured. Secondly, the structure of the dynamometers was studied using both, a miniature impact hammer and a shaker, to identify its main resonance modes above which the vibration measurements would be affected by the structure, showing the first eigenmode at 2.23 kHz. The platform was then employed to characterize several objects. In the frame of the ESA sponsored project IMPROVE a stepper motor loaded with an inertia representative from photovoltaic panels was studied, allowing to develop and correlate a representative model, as shown in Figure 2.

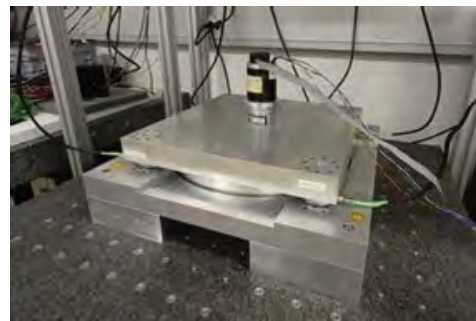


Figure 2: Stepper motor characterization.

Similarly, a magnetic bearing reaction wheel from the Swiss company Celeroton AG shown in Figure 3 was characterized, showing the potential of such system in terms of exported microvibration, and proving the high-resolution capabilities of the facility for low vibration amplitudes.



Figure 3: Magnetic bearing reaction wheel characterization, presented here with the courtesy of the Swiss company Celeroton AG.

Performed measurements showed results in line with previously performed tests, concluding thus the correct operation of the facility commissioning. Now, the facility will be made available to Swiss and European industrial partners wishing to assess the performances of their developed systems in terms of exported microvibrations.

# COOLER, a Louvered, Passive Radiator for CubeSats

P. Spanoudakis, F. Cosandier, D. Novo, P. Schwab, A. Ummel

In the frame of the COOLER project, funded by the European Space Agency (ESA), CSEM developed and manufactured a compact and in-plane opening louver with variable thermo-optical properties, targeting CubeSat applications.

Louvers are thermal control elements placed over external radiators to tune heat rejection from typically a factor 1 when fully closed to factor 5 when fully opened. The mechanism COOLER (CCompact and in-plane Opening LouverER with variable thermo-optical properties) is a device of a total area of 1 dm<sup>2</sup> used to adjust the power dissipation of a radiator to a varying heat source designed to reject heat in the range 0.1 W to 10 W. When the heat source is on, it heats up the mechanism, triggering its opening thus increasing the radiator dissipating capability. When the heat source is off (or when it is cool enough), the device cools down triggering its closure and thus insulating the radiator.

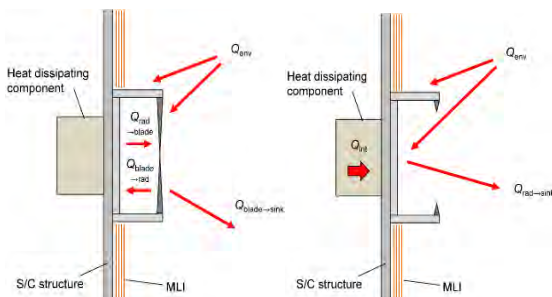


Figure 1 Simplified schematic illustration of the principal radiative heat exchanges, device closed (left), device open (right).

## Main radiator specifications

The critical requirements for the radiator are:

- Targeted for CubeSats and compact instruments
- Compact radiator design 100 × 100 × 30 mm
- Heat rejection capability >85% when fully open
- Heat rejection range 0.1 W to 10 W / device of 1 dm<sup>2</sup>
- Single actuator with activation range -50°C to +90°C
- Friction free

A trade-off study was performed evaluating eight different louver concepts before a final candidate was selected for detailed analysis and prototype testing based on a set of pre-defined criteria. The selected design called Flexible Grids is based on a stack of grids that are moved linearly one after the other to occult the surface. The guiding of these grids is performed through a flexible hinge parallelogram arrangement which provides the most compact configuration.

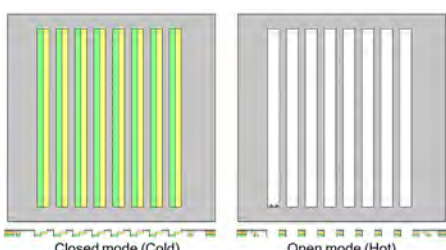


Figure 2: Flex grid in closed and open position.



Figure 3: COOLER CAD engineering model rendered image.

The actuation principle uses a normal bias spring to maintain the grids in the closed position against an end-stop. When the heat from the baseplate reaches a predefined value, the SMA (Shape Memory Alloy) actuator heats up and is activated. When the SMA is hot, the force of the bias spring is smaller than the one of the hot SMA, thus the mechanism opens. When the SMA is cold, the force of the bias spring is larger than the SMA thus maintaining the mechanism closed.

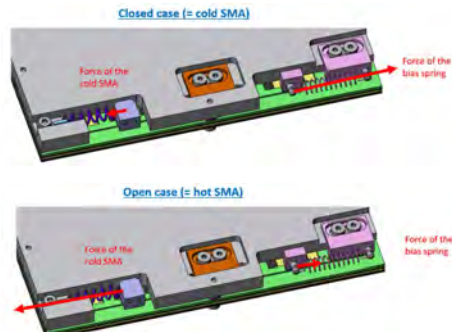


Figure 4: Passive actuation with SMA.

A space qualified SolarWhite thermal coating from ENBIO (IR) has been applied to the baseplate with a thermal emittance value  $\epsilon$  of 0.91 and thermal absorptance  $\alpha$  of 0.25.

The Finite Element Model Analysis (FEM) has shown that the mechanism can survive the environmental loads using a simple launch locking device with stress levels at acceptable values. Extensive thermal analysis was performed for four operating conditions in open/ closed positions in hot (20°C) and cold (5K) environments.

The thermal analysis results, presented in Table 1, correspond to the test conditions planned as part of the test campaign. The objective is to correlate the simulations models with the test results. In the open configuration, the current design has a power dissipation to deep space (5K) when the radiator is at 90°C of 3.2 W.

Table 1: Effective emissivity of mechanism with no coating on grids.

Load Case	Config.	Applied Heat (W)	Ambient Temp. (°C)	Thermal Plate Temp. (°C)	Effective Emissivity
LC 1.1	Open	10	20	227.1	0.319
LC 2.1	Closed	0.1	20	33	0.128

The Engineering Model was assembled, and the final test campaign will start with thermal vacuum performance, thermal balance random vibration, and thermal vacuum cycling tests to validate the proof of concept mechanism.

# ISOL—Development of a High-Performance Microvibration Isolation System

P. Spanoudakis, F. Cosandier, P. Schwab, L. Salamin

A novel hexapod platform capable of providing high microvibration attenuation performance both at low and high frequency has been designed, developed and tested in the frame of the European Space Agency project ISOL.

Hexapod platforms are a type of parallel manipulator that have been studied and developed extensively in the last 50 years due to the several advantages they present especially for applications requiring high load carrying capacity and precise positioning. A novel hexapod platform was designed, capable of providing high microvibration attenuation performance both at low and high frequency, while maintaining a system architecture that is relatively simple (e.g., no control algorithm and only flexure-based joints). A hexapod model (Figure 1) was designed and tested by Surrey Space Centre University (SSC) using a payload of reaction wheels from Surrey Satellite Technology Ltd. (SSTL) and incorporating flexure elements from CSEM integrated within each strut (Figure 2).

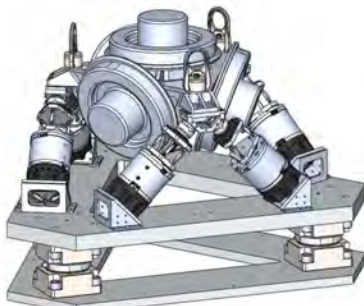


Figure 1: CAD model of prototype hexapod.

Within the lower, fixed part of the strut (hexapod leg), a series of CuBe membranes assembled in a sandwich structure permit the axial motion (2 mm max) of the mobile elements of the strut. The mobile elements consist of coils within a cylindrical arrangement of fixed magnets which provide the microvibration damping performance of the hexapod.

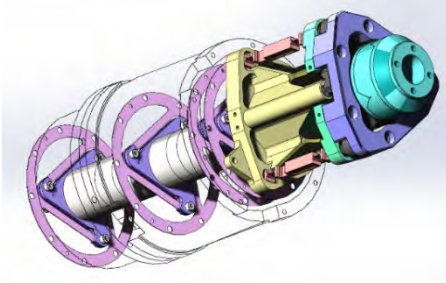


Figure 2: Flexure subassemblies within hexapod strut.

The decoupling of the strut is provided by the flex gimbal ( $R_x$ ,  $R_y$ ) and a Planar Joint (PJ) incorporating three flexlegs, each having 4 flexure hinges, that allow the mobile platform to be guided along two translations ( $x$  and  $y$ ) and one rotation ( $R_z$ ). The PJ also includes a preload spring and a locking plate to connect mechanically the output shaft to the base either through the flexure or through rigid columns. Once the axial force through the shaft is bigger than the preload force, the rigid columns are connected to the shaft, as illustrated in Figure 3. The connection is made thanks to a ball/groove type mating.

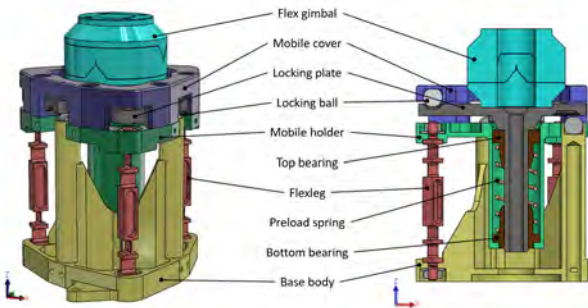


Figure 3: Flex grid in closed and open position.

To allow for the strut to be securely blocked, a 4.25 mm lateral displacement of the planar joint is required during the launch locked configuration of the hexapod. The associated maximal Von Mises stresses are 305 MPa for the Titanium flexlegs shown in Figure 4. The stress is quite homogeneously distributed in the flexures as they are all turned by 45°.

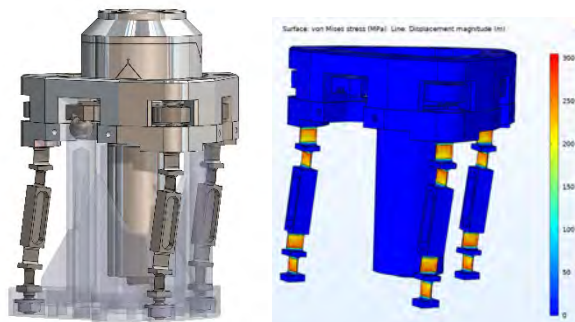


Figure 4: Planar joint model rendered image and flexure stresses.

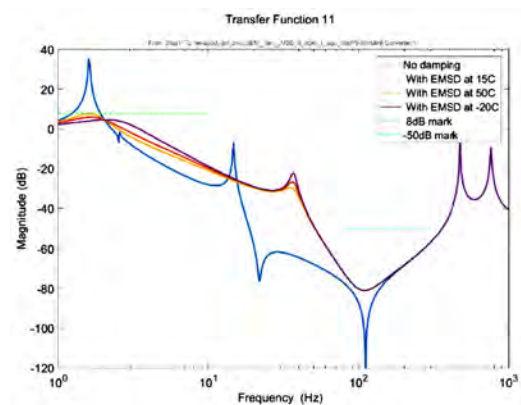


Figure 5: Example of force transfer functions, no damping blue line.

As shown in Figure 5, the transfer functions show the slope of -80 dB/dec between 30 and 100 Hz which is the operational damping range of the strut. The response then starts to go up due to the bending modes of the struts. The design optimization of the flexure stiffnesses of both the membranes and the planar joint is to increase the overall bending stiffness of the strut to values higher than 500 Hz to maintain the overall performance of the strut in the full operational range.

# LOSORA—Novel Actuator Concept for Unidirectional Displacement

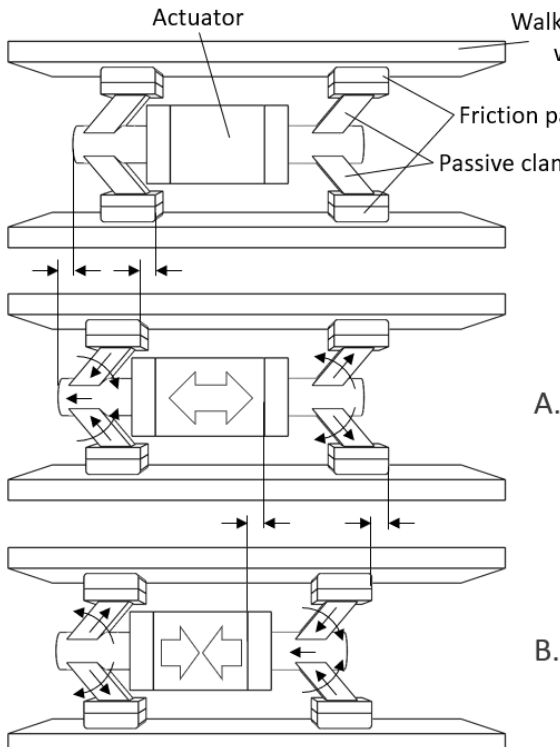
D. Grivon

A novel actuator concept for unidirectional displacement is presented. The principle of operation as well as some advantages with respect to existing solutions are illustrated. Validation of the working principle through Finite Element analysis is presented. A patent was submitted to protect the novel actuator concept. Contacts with potential industrial partners were initiated as well as a proposal to answer an ESA ITT concerning the development of a Hold Down and Release Mechanism relying on the novel actuator concept.

The new actuating principle is very simple and foresees the use of only one actuator in-between two passive clamps. The passive clamps are designed using flexible hinges so that the movement along the preferred direction of motion is facilitated with respect to the opposite direction. Alteration of extension and contraction of the actuator allows to achieve incremental unidirectional linear motion as shown in Figure 1.

Actuator extension: Friction pads on the rear clamp tend to spread increasing the contact force on walking walls and thus, the friction force, preventing the clamp to move back. Pads on the front clamp tend to approach reducing contact on external walls and thus friction force, facilitating forward motion.

Actuator contraction: Pads on the front clamp tend to spread, increasing the contact force on external walls and thus friction force, preventing the clamp to move back. Pads on rear clamp tend to approach reducing contact on external walls and thus friction force, facilitating forward motion.



- A. Extension
- B. Contraction

Figure 1: Main constitutive elements and working principle with the alternation for extension and contraction.

The main commercial advantage of the proposed solution is the reduction of the number of actuators required to implement the classical inchworm principle, thanks to the replacement of the usual clamping external piezos with the passive clamp mechanism (reduction from 3 to 1 actuator). The main outcome is the reduction of complexity in the assembly as well as in the

driving complexity (one driving electric signal instead of 3). The price to pay is the unidirectionality of the motion, but this can still represent an advantage for special function actuators (one-shot actuators as locking systems, release device, manually resettable one direction actuator). The proposed solution does not need particular surface treatments at nanoscale level, which usually require delicate manufacturing process. The most critical geometrical dimensions of the passive clamp mechanism are in the miniature, but still macroscopic domain (i.e., in the millimeter range down to the micrometer). The constitutive elements are extremely simple and do not include special geometrical features of details. This implies that traditional manufacturing techniques used to realize precision parts can be used without the need of resorting to delicate microfabrication techniques. The drive is self-locking at rest, meaning that it requires no current, and it does not generate any heat. It holds the position with maximum force. The proposed actuating principle is not limited to a particular field of application, but, depending on the different needs, it can be rather easily customized. In this respect, it is general purpose.

A validation of the working principle was performed using Finite Element analysis and COMSOL Multiphysics which confirmed the results obtained through the analytical modelling, as shown in Figure 2 below.

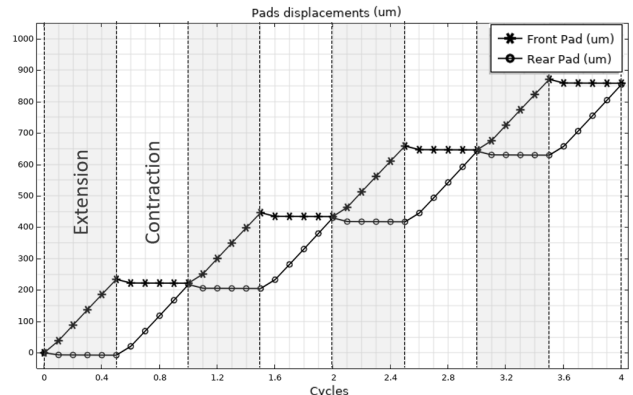


Figure 2: FE simulation of the front and rear pads displacements over a complete activation cycle.

Thanks to this further validation, a patent was submitted to the European Office on February the 21<sup>st</sup> 2021.

Some activities were initiated to assess the commercial attractiveness and the interest of possible stakeholders for this new unidirectional actuator.

# Blue-Chirped Emission in Fabry-Perot Cavity Quantum Cascade Laser at Room Temperature

S. Chin, V. Mitev, D. L. Boiko

LEVES research project is to design and validate a novel technique to produce a large and rapid frequency sweep from a commercial Fabry-Perot quantum cascade laser, enabling a cost-effective solution for numerous industrial applications of mid-infrared spectroscopy.

In the framework of the Eurostars LEVES project, two industrial and two Research & Technology Organizations developed a cost-effective trace gas analyzer by optimizing the operation parameters for standard Fabry-Perot quantum cascade lasers.

Today mid-infrared spectroscopy is one of the most fascinating topics in optics and photonics communities since it proves to have a large impact on scientific, industrial, space and medical instrumentation. Among various techniques, tunable quantum cascade lasers (QCLs) have attracted increasing attention for industrial process monitoring but also for atmospheric sensing since the fingerprint of all complex molecules are present in the mid-infrared wavelength range, which can be readily covered by the spectral range of distributed feedback (DFB) or external cavity QCLs.

To achieve cost-effective tunable operation, LEVES team has taken an advantage of an alternative approach suited for a conventional Fabry-Perot (FP) cavity QCLs. The principle to produce a wide-range frequency-swept mid-IR laser source makes use of the high sensitivity of a diagonal inter-sub band transition to the quantum confined Stark effect [1]. By carefully optimizing the injection current waveform applied to FP QCL, the lasing mode was switched from the broadband vertical transition in the active region quantum wells to the narrowband diagonal transition from the injector to the low laser level [2]. Thanks to the strong sensitivity of the diagonal transition energy to the bias field, the optical frequency of the emitted light was quasi-continuously blue-shifted during the level crossing range (Figure.1).

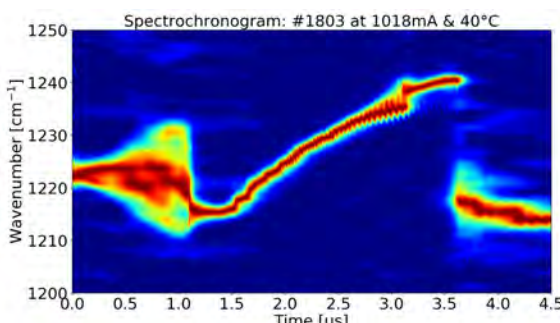


Figure 1: Spectrochronogram of a FP-QCL, driven by a current pulser with 1018 mA, 10 μs duration and 2 μs rising time at 40°C.

Instantaneous spectral properties of the emitted light were then characterized. The temporal self-scanning of the laser frequency was as broad as ~25 cm<sup>-1</sup> over a time window of 1.8 μs (Figure 2). Moreover, the standard deviation of ~0.1 cm<sup>-1</sup> over 20 repeated scans proved the high reliability of the frequency-swept laser [3].

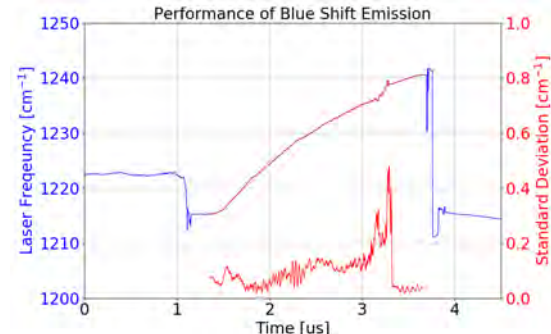


Figure 2: Characteristics of laser frequency scan and its repeatability

To validate the proof-of-concept in gas spectroscopy applications, a commercial 10 cm-long methane cell at 1 bar was placed between the laser output and a detector. The measured absorbance spectrum (Figure 3) was fitted to a model spectrum from the HITRAN database assuming the instrument response function (IRF) of 3 cm<sup>-1</sup> FWHM. The discrepancy of the retrieved gas concentration from the actual is attributed to the variation of IRF over the frequency scan. More dedicated signal processing is now being elaborated to deconvolute the effect of IRF from the signal. Yet, this first gas-cell spectroscopy result has successfully demonstrated the feasibility of LEVES approach for gas sensing applications.

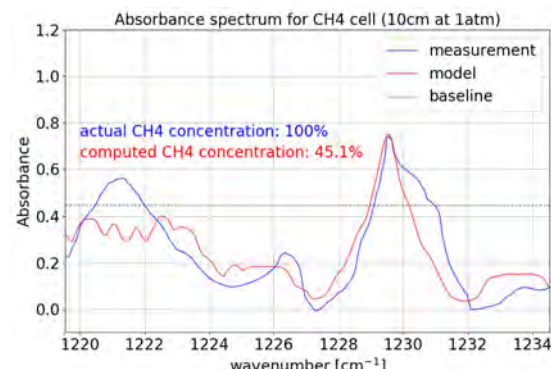


Figure 3: Measured and fitted absorbance spectra for a 10 cm-long 1-bar CH<sub>4</sub> cell, proving the feasibility of the proposed laser for gas sensing. (The baseline absorbance of 0.42 is subtracted from both curves for clarity).

The partners contributing to the project results are Alpes Lasers, Leibniz Institute for Plasma Science and Technology and neoplas control. We thank for the support from Eurostars and the State Secretariat for Education, Research & Innovation (SEFRI).

[1] A. Bismuto, R. Terazzi, M. Beck, J. Faist, "Electrically tunable, high performance quantum cascade laser", *Appl. Phys. Lett.* 96 (2010) 141105.

[2] A. V. Antonov, D. I. Kuritsyn, A. Gajic, E. E. Orlova, J. Radovanovic, V. V. Vaks, D. L. Boiko, "Switching on and off the

Risken-Nummedal-Graham-Haken instability in quantum cascade lasers", *arXiv:1711.10749* (2017).

[3] S. Chin, V. Mitev, E. Giraud, R. Maulini, S. Blaser, D. L. Boiko, "Electrically driven frequency blue-chirped emission in Fabry-perot cavity quantum cascade laser at room temperature", *Appl. Phys. Lett.* 118 (2021) 021108.

# Agile High-Power Femtosecond Laser with Programmable Burst Generation

C. Hofer, N. Torcheboeuf, S. Kundermann, C. Meier, L. Karlen, S. Lecomte

Lasers are becoming more and more widespread on industrial manufacturing floors. Of the different laser types, femtosecond lasers are particularly suited for delicate material processing where quality is essential. Recently it has been shown that burst of femtosecond pulses can increase the removal rates. Along these lines, CSEM, together with NKT Photonics Switzerland GmbH, has developed a novel laser system capable to generate programmable bursts of femtosecond pulses.

Femtosecond lasers have been developed at CSEM for applications like metrology, spectroscopy and microwave photonics since more than a decade. Over the last 5 years, high-power femtosecond lasers for industrial applications are also in CSEM's focus. Indeed, this type of lasers, like other laser types such as continuous-wave and nanosecond lasers, finds more and more industrial applications and massively expands its presence on manufacturing floors.

Femtosecond pulses, thanks to the so-called cold ablation process, are known to offer outstanding machining quality but often at the expense of processing speed. Recently it has been shown that bursts of fs pulses, instead of solitary pulses, with pulse periods in the ns range, can improve the material removal rate, hence enhancing the productivity of certain processes. This parameter adds another variable to optimize for the best process quality and efficiency. Typically, this optimization is required on a case-by-case basis and is unfortunately time consuming as well as complex to conduct.

In the framework of the Innosuisse SLAM4.0 project regrouping many industrial and academic Swiss partners, the consortium aimed to combine agile laser sources, process monitoring and artificial intelligence to ease process optimization and ensure constant high quality. As a key building-bloc, an agile femtosecond laser capable to define bursts on-the-fly, was developed among NKT Photonics Switzerland GmbH and CSEM. The laser architecture is based on interleaving pulses from a 40 MHz fs Onefive ORIGAMI oscillator to generate a 640 MHz pulse train that can be arbitrarily decimated with a fast optical modulator and hence generate the desired bursts of pulses. The number of pulses can be set from solitary pulses to bursts of 250 pulses with a burst repetition rate (BRR) from single shot to 80 MHz. To achieve such a fast-switching speed (nanosecond range), a custom-electronics based on a field-programmable gate array (FPGA) developed by CSEM was essential to drive the optical modulator. The electronics also includes a feedback loop to keep the optical modulator at the optimal point of operation. The amplification is performed using the well-known chirped pulse amplification (CPA) scheme and an aeroGAIN-BASE module from NKT Photonics, used as power amplifier stage, allowed the system to generate sub-400fs pulses with an average power of up to 50 W in a close-to-diffraction limited beam quality ( $M^2 < 1.13$ ) and at a center wavelength of 1030 nm.

The agile laser system was carefully characterized by measuring the generated pulse trains in the time domain with a photodiode and fast oscilloscope as well as the pulse duration using an autocorrelator. The oscilloscope measurements shown in Figure 1(top), illustrate the generation from solitary pulses to bursts with 20 and 50 pulses (intraburst pulse repetition rate is 640 MHz). In Figure 1 (middle), a typical autocorrelation trace of bursts is shown. Finally in Figure 1 (bottom), a beam profile of the system output demonstrates the excellent beam quality.

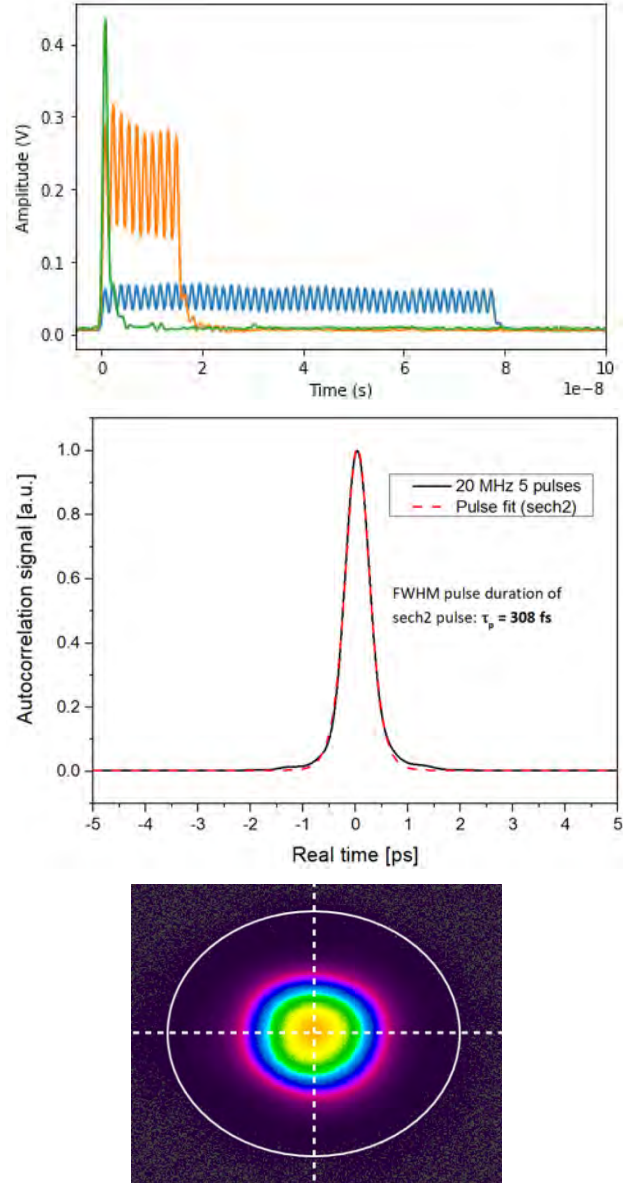


Figure 1: (top) Time traces of single pulse (green), 20 pulses per burst (orange) and 50 pulses per burst (blue). Intraburst pulse repetition rate is 640 MHz. (middle) Autocorrelation trace retrieving a pulse duration of 308 fs assuming sech<sub>2</sub> pulses and with a BRR of 20 MHz, 5 pulses per burst and with 50 W average output power. (bottom) Beam profile at 50 W average power.

CSEM would like to warmly thank Dr. Maxim Gaponenko and Dr. Gabriel Spühler from NKT Photonics Switzerland GmbH for the collaboration in the laser system development and Prof. Dr. B. Neuenschwander and his team at the Berner Fachhochschule in Burgdorf for testing the laser in micro-machining conditions. This work has been conducted with support from Innosuisse in the frame of the Impulse program under the project SLAM4.0, contract 35418.1 IP-ENG.

# Versatile Flash LiDAR Integrated in Drones

C. Pache, D. Nguyen, J.-C. Roulet

Capable of acquiring 3D images of a scene in a single snapshot, flash imaging Light Detection And Ranging (LiDAR) is considered as a key enabling technology for applications such as autonomous navigation (e.g., airborne, space), mapping (e.g., geology, underwater) and objects detection. Relying on space developments, a miniaturized flash LiDAR was designed, manufactured, and validated for drone 3D imaging. The system shall enable the mapping of shallow water coastal areas, the monitoring of underwater infrastructures and the detection of objects beneath the water surface in real-time.

Over the past years, CSEM has led the development of flash imaging LiDAR technology with the support from the European Space Agency, for autonomous landing on celestial objects and on-orbit automatized operations. A flash imaging LiDAR generates depth maps (i.e., 3D images) of a target in a single snapshot with advantages over a scanning architecture: better integration (i.e., miniaturization), longer lifetime (i.e., no mechanical fatigue), no compromise on angular resolution, measurement rate or platform stability (i.e., limited motion blur).

## Underwater imaging

Today's commercial LiDAR's developments for terrestrial applications are based on infrared light for eye safety and invisibility reasons, whereas our technology relies on a laser at a wavelength of 532 nm (green) to align to the Time-of-Flight (TOF) detector's highest sensitivity. When it comes to underwater imaging, this limitation translates into a clear advantage thanks to a gain of 1000 in transmission in comparison to LiDARs available on the market (see Figure 1).

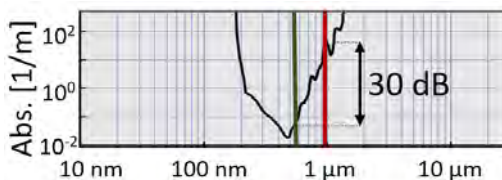


Figure 1: Water spectral absorption.

Combining this advantage with our LiDAR's inherent time-gating feature, the system can detect multiple echoes in turbid water, paving the way towards underwater imaging such as bathymetry (i.e., 3D mapping), objects detection, or infrastructure monitoring.

## Miniaturization

Illustrated in Figure 2, the designed LiDAR weighs 6.8 kg, holds in a volume of  $20 \times 17 \times 19$  cm and consumes 60 W in operation.



Figure 2: Developed flash LiDAR. CAD (left) and prototype assembly (right).

Different optical elements can be automatically positioned in the laser beam, to modify the illumination pattern and Field-of-View (FOV). Similarly, a 3-axes motorized lens allows adapting the receiver FOV in a range from 4 to 20°. These features confer increased versatility to adapt to environmental light conditions, obscurant presence, platform velocity, and target reflectivity.

The system's core consists in a state-of-the-art embedded processing unit (Xilinx Zynq Ultrascale+) that allows controlling

the data acquisition, the actuators positioning and communication. Data is acquired by 4 TOF detectors of  $64 \times 64$  pixels each, positioned side-by-side in the focal plane array. Based on Single Photon Avalanche Diodes (SPADs), each pixel of the detector precisely time stamps detection events thanks to an individual counter and a time-to-digital converter. The processing unit also acts as a master for the fiber amplifier laser that emits nanosecond pulses with high energy (10  $\mu$ J). Due to the inherent noise of SPADs, several measurements are acquired to build a depth map with sufficient quality. Each measurement is synchronized onto a single laser pulse. By summing measurements, a histogram of photon counts with respect to the distance is built for each pixel. A depth map is then computed by identifying the peak position in the histogram. An intensity image is also obtained by computing the peak energy.

## Demonstration

Prior a demonstration in dynamic conditions on-board a drone from Maritime Robotics (Norway) – occurring at the time of writing this article – we verified the system's performances in real conditions from a bridge over the Areuse river. Results are shown in Figure 3, where rocks and tree trunk are clearly visible at 2-3 meters below the water with the riverbed at a 6-meter depth.

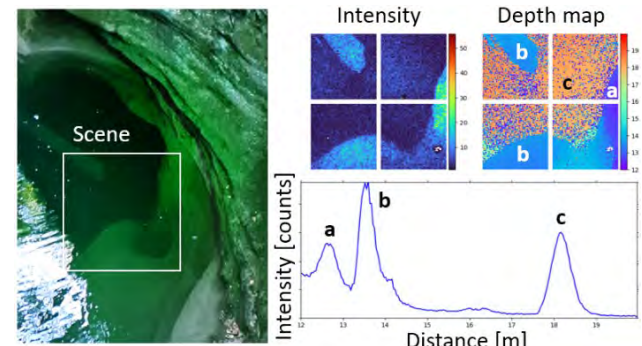


Figure 3: Static demonstration over the Areuse river.

Miniature, the developed LiDAR can be seamlessly integrated onto surface (USV), aerial (UAV), and underwater (ROV and AUV) unmanned vehicles.

## Towards embedded processing

This architecture with large detectors generates a dramatic amount of data to be processed and stored locally in real-time. The challenge of data acquisition was tackled by designing a dedicated data flow with direct transfer to a solid-state drive. The selected processing unit enables embedded data processing and compression, for which algorithms are currently being conceived.

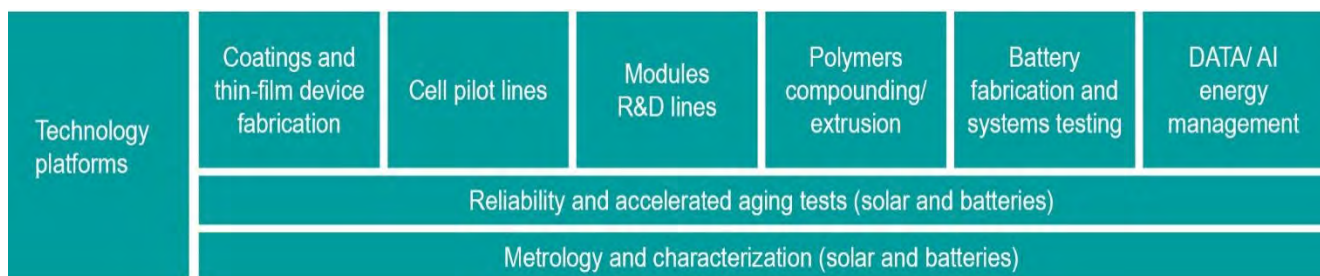
We thank InnoSuisse (Eureka-Eurostars program) for its financial support, Maritime Robotics for their excellent collaboration and the Fondazione Bruno Kessler (Italy) who developed the detector with CSEM and continue to provide information and guidance.



# SUSTAINABLE ENERGY

Christophe Ballif

In most scenarios for the decarbonization of the energy system, solar, wind, hydro, and biomass provide the bulk of the primary energy, completed to a lesser extent by nuclear and the capture of residual CO<sub>2</sub> emissions. Energy management, flexibility, and storage play a central role, the latter with time spans from a few days (hydro or batteries) to several months (e.g., hydro, biomass, or power-to-gas).<sup>[1]</sup> In this context, it makes more sense than ever to contribute to developing solutions that help save, produce, and manage energy in a sustainable way. Thanks to its rich network of industries, start-ups, and research entities, Switzerland has long been providing high-level Deep Tech and digital solutions for the cleantech market. Moreover, with its dense electrical grid and general electricity infrastructure (including pumped hydro) Switzerland can play a leading role in demonstrating the field application of novel solutions and in implementing them effectively.



*Technology platforms used for the priority axis Sustainable Energy @ CSEM. Infrastructures include extensive facilities for testing the reliability of PV modules (in partnership with SUPSI), electrochemical storage, and BMS developments, as well as digital platforms for the Digital Energy and Energy Storage Focus Areas.*

## Long-term objectives

The Focus Areas **PV and Solar Buildings** has as its first target the development of more powerful, reliable, sustainable PV solar cells and modules, with the long-term goals of crystalline silicon modules with over 25 percent efficiency and tandem modules with over 30 percent, including by combining silicon with perovskites. The substitution of critical or expensive elements such as Ag for metallization is also addressed. Second, the Area targets the development of cost-effective solutions for the increased market penetration of PV as a building material. In particular, our platforms can be used to design and produce proprietary materials and glazings for the increased reliability and versatility of solar building elements, including all kinds of optical effects.

In terms of highlights, CSEM succeeded in the up-scaling of the perovskite-on-silicon tandem technology by demonstrating a 4 cm<sup>2</sup> large, screen-printed, 27.6 percent efficient device using a perovskite top cell on a silicon heterojunction bottom cell, with a number of industry-compatible processes. CSEM, in

## Sustainable Energy (SE) at CSEM

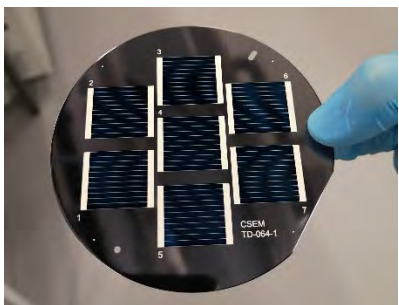
The SE research priority includes the Focus Areas **PV and Solar Buildings**, **Energy Harvesting**, **Digital Energy**, and **Energy Storage**. These activities have recently been reinforced by increased efforts related to the digitalization of energy systems and storage aspects, which will increase in significance over the coming decades. Operationally, the SE priority is based on unique technology platforms, illustrated in Figure 1, with over 2,500 m<sup>2</sup> of high-tech facilities. Researchers collaborate closely with the EPFL PV-lab in Neuchâtel, and the two share certain infrastructures. Synergies with CSEM's established activities in the fields of system design, low-power electronics, coatings, surfaces, and printing technology provide an additional, unparalleled knowledge base for all multidisciplinary projects. Synergies are reinforced with competences developed in the CSEM data program.

collaboration with Meyer Burger, released a world-record 24.7 percent efficient single-cell laminate featuring a "tunnel-IBC" solar cell with SWCT® interconnection. Finally, in 2021 the Swiss company 3S+ installed 800 m<sup>2</sup> of terracotta PV modules on the old post building in Zurich, using colored sheets from Solaxess, a technology pioneered and developed by CSEM.

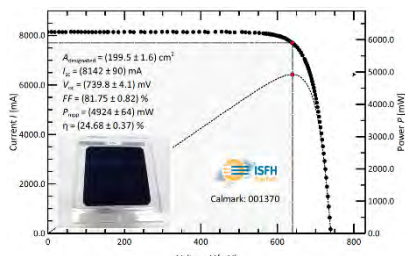
The **Energy Harvesting** Focus Area deals with customized PV elements, from nanowatts to several tens of watts, with the goal of providing customized solutions for the growing IoT market as well as for mobility applications. The latter includes the growing use of PV solutions in, for example, cars, planes, boats, logistic containers, drones, and spacecraft, with a focus on lightweight, ultra-reliable solutions. The challenges here lie in fulfilling extreme specifications with respect to a range of constraints, including mechanical, thermal, UV, and fire. Finally, across these topics we work to ensure that all related materials (e.g., the use of specialty in-house polymers for packaging) and processing steps (dedicated manufacturing solutions) are controlled to ensure perfect product reliability, and to provide a pathway to larger volume industrial uptake.

[1] Alternative scenarios based uniquely on nuclear or direct carbon capture and sequestration seem difficult for two major reasons: the huge amount of new nuclear power plants that would be needed (~10,000 by 2050) and the high costs of all carbon sequestration projects capturing at the exhausts of fossil power plants. Hence it is expected that nuclear will be a support to the transition, with no

massive increase but a useful extension, in Switzerland, of power plants' lifetime. Carbon sequestration should take place mostly through better soil management and reforestation. Residual CO<sub>2</sub> emissions, such as those of cement plants, should be captured directly.



CSEM's 27.6 % efficient perovskite/silicon tandem solar cell.



CSEM and Meyer Burger's world-record tunnel-interdigitated back-contact (IBC) laminate.



CSEM's BIPV solutions: 800 m<sup>2</sup> of terracotta modules installed in Zurich (3S; Solaxess).

As highlights, CSEM developed and fabricated a further generation of lightweight PV modules using a special coating. The modules were assembled on the wings of the plane Solarstratos, and exceeded the challenging targets set for efficiency, reliability, and light weight. Our capacity to produce energy harvesters, such as the solar dial of the new Tissot

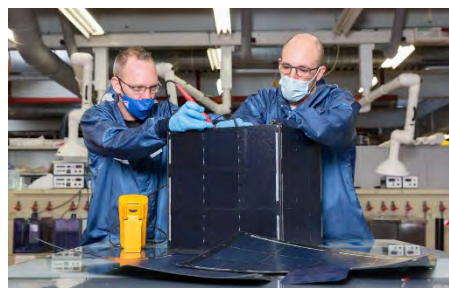
T-Touch Connect Solar, has been further consolidated, allowing for faster design and prototyping.<sup>[2]</sup> New CSEM lightweight, robust PV panels are powering the scientific equipment of CNES on board stratospheric balloons being used to study weather phenomena at high altitudes.<sup>[3]</sup>



Solarstratos, incorporating a new generation of lightweight PV panels.



Tissot T-Touch Connect Solar, incorporating PV cells designed at CSEM.



Assembly of lightweight PV panels for stratospheric applications.

The SE research priority's third Focus Area, **Digital Energy**, develops data-driven software solutions to interconnect energy vectors, to control increasingly distributed and variable energy resources and loads, and to contribute to the more efficient operation of energy assets. The targeted outcomes include solutions for the autonomous provision of flexibility by buildings or districts, for large-scale forecasting of distributed energy sources (solar, wind, hydro), as well as AI-based solutions for the predictive maintenance of energy- or environment-related assets. Our unique value proposition includes, for instance, the development of graph-based algorithms that should allow unbeatable forecasting performance, including of PV or wind production.

As recent highlights, CSEM released—as an open-source project—its Energym™ Python library, a tool for training and benchmarking data-driven building controllers. It includes several validated building models. CSEM's algorithms have also been validated for system identification, for aggregating flexible resources to provide grid management services, and for optimal inverter control. A self-hosted website implements CSEM's graph machine learning algorithms and displays live, interactive maps of current and forecast PV production as well as historical forecasts for 600 nodes in the Netherlands.



Training and benchmarking of data-driven building controllers.



Live, interactive map of current and forecast PV production.



Operational solution for the data-driven maintenance of wind turbines.

<sup>[2]</sup> CSEM, "Tissot x CSEM Collaboration" (July 2021; video), <https://www.youtube.com/watch?v=JROvjMJI1v0>.

<sup>[3]</sup> CSEM, "Balloons Will Travel Around the World to Study Weather Phenomena" (February 2021), <https://www.csem.ch/page.aspx?pid=159509>.

The last Focus Area relates to **Energy Storage**, which will play an increasingly important role in tomorrow's energy system. Based on physical battery models and advanced data treatment of electro-impedance spectroscopy data, we target the delivery of a new generation of advanced battery management systems (BMSs), allowing extended lifetime and facilitating the recycling of various types of batteries. Applications range from land to air mobility, spanning home storage to large industrial systems. Finally, we are developing software that enables the coupling and system operation of various forms of energy storage (electrochemical; power-to-gas) in conjunction with local energy use (heat pumps; district) and production (PV; wind; vehicle-to-grid (V2G)).

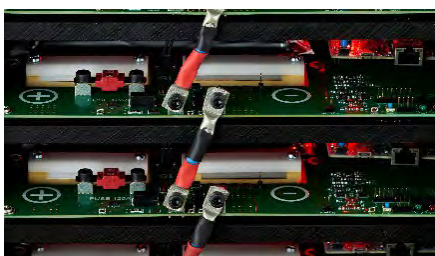
Recent highlights include the realization of the first BMS system integrating local online EIS capability and an advanced single-

cell switching concept. The approach was tested successfully with a fully functional demonstration, jointly with a proof-of-concept validation of SoC balancing. By varying the battery cell test procedure, it was shown that battery testing time for used battery cells could be reduced from hours to minutes, thus allowing the efficient sorting of battery cells for second-life applications. An online tool for the evaluation of battery aging for NMC, LFP, and LTO cell chemistries was developed, in view of evaluating battery aging for V2G applications.

A trademark was deposited for optimum storage management software NRGMAESTRO™, and has now been licensed to initial customers. On the technical side, the investigation of different solver improvement options was concluded, showing the potential to reduce the solve time by a factor of ten.



*Characterization of high-energy-density automotive pouch cells.*



*First implementation of a cell-based monitoring and activation system.*



*Second-life cells evaluated within the BAT4SEL project.*

# PeroCUBE—Development of Ubiquitous Perovskite-based Energy Harvesters and Light Emitters

A. Walter, B. A. Kamino, A. Paracchino, S.-J. Moon, S. Nicolay, Q. Jeangros

The EU H2020-funded project PeroCUBE (High-Performance Large Area Organic Perovskite devices for lighting, energy and Pervasive Communication) aims at taking advantage of the recent developments in the field of perovskite photovoltaics (PV) and light-emitting diodes (LED) to create new opportunities for the lighting, energy and telecom industries in Europe. Led by CSEM, a 14-partners strong consortium is aiming at demonstrating the first light fidelity (LiFi) communication system using an emitter and a detector made with the same family of semiconductors, i.e., metal halide perovskites.

CSEM is among the leading institutes in Europe trying to unleash the full potential of perovskite (PK) photovoltaics. Recently a record-breaking efficiency on a large area Si/PK tandem solar cell was demonstrated, using industry-relevant metallization techniques [1]. CSEM has also developed an extensive know-how on the processing of large-area single-junction perovskite minimodule devices [2], in the framework of various EU, Swiss and industrial projects. Moreover, research is on its way at CSEM to address the challenges of encapsulation and operational stability of the PK devices, bringing the technology closer to industrial viability. Drawing on this emerging maturity and the more recent results on the use of PK as a light-emitting material [3], PeroCUBE aims at exploring applications of the PK technology outside of the conventional field of PV, notably for indoor lighting, portable electronics and ultimately communication through LiFi.

In this framework, CSEM specifically develops large-area single-junction PK PV as energy harvesters for consumer electronics. The foreseen applications within the project are powerful solar lamp, and receivers for LiFi communication. We rely on blade coating as a deposition technique for the upscaling of the PK layer. This allows the deposition of uniform and continuous active layers on substrates ranging from  $5 \times 5 \text{ cm}^2$  to  $10 \times 10 \text{ cm}^2$ , with further upscaling possible.

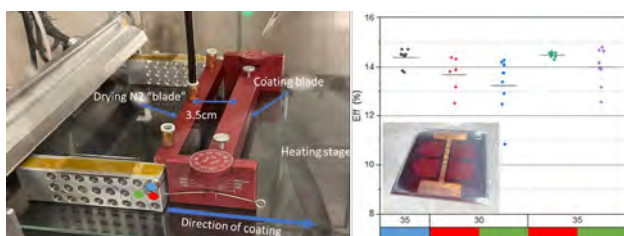


Figure 1: (left) Blade-coating setup. The colored dots depict three different possible positions of the drying blade, varying its height above the substrate and distance from the blade. (right) Efficiency of  $1 \text{ cm}^2$  cells on  $5 \times 5 \text{ cm}^2$  substrates. The colors bars correspond to the position of the drying blade. The coater heating stage was set to  $30^\circ\text{C}$  or  $35^\circ\text{C}$ .

Figure 1 presents the blade coating setup. The crystallization onset of the PK film is controlled by the evaporation triggered by the  $\text{N}_2$  drying blade and the temperature of the heating stage. We show that an optimum can be reached by controlling the  $\text{N}_2$  flow,

[1] B. A. Kamino, B. Paviet-Salomon, S.-J. Moon, N. Badel, J. Levrat, G. Christmann, A. Walter, A. Faes, L. Ding, J. J. Diaz Leon, A. Paracchino, M. Despeisse, C. Ballif, S. Nicolay, "Low Temperature Screen-Printed Metallization for the Scale-Up of Two-Terminal Perovskite-Silicon Tandems", ACS Appl. Energy Mat., 2 (2019), 3815-3821.

[2] A. Walter, S.-J. Moon, B. Kamino, S. Nicolay, "Development of record single junction minimodule devices by laser patterning", CSEM Scientific and Technical Report (2017), 84.

resulting in better uniformity of the films and ultimately higher efficiency

In parallel, CSEM will develop LEDs based on PK materials. We are notably exploring CsPb-halides systems. By varying the halide species, green ( $\text{CsPbBr}_3$ ), blue ( $\text{CsPbBr}_2\text{Cl}$ ) or red ( $\text{CsPbBr}_2\text{I}$ ) LEDs can be produced. Such inorganic PeLEDs should be more temperature-stable than their organic counterparts. Adding a molar excess of  $\text{LiX}$  ( $\text{X} = \text{Br}, \text{Cl}$  or  $\text{I}$  respectively) to the precursor solution should also strongly enhance the photoluminescence quantum yield by passivating halide vacancies in the core material [4]. Figure 2 shows three small pixels emitting in the red, green and blue parts of the spectrum depending on their respective halide composition and the additive concentration and formulation.

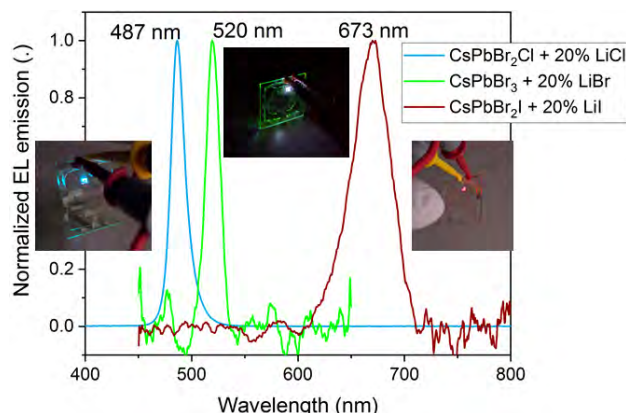


Figure 2: RGB LEDs based on CsPb-halides, passivated with Li-halides. The spectrum shows emission peaks in the desired wavelength range for the respective colors.

PeroCUBE is a collaboration between CSEM, Alpes Lasers (CH), Optiva Media (ES), Aura Light (IT), Vodafone Innovus, University of Patras, Eulambia, Noesis (GR), CNRS (FR), TU Wien (AT), Fraunhofer FEP (DE), TNO (NL), VTT (FI), and University of Oxford (GB), placed under the coordination of CSEM. The PeroCUBE project has received funding from the European Union's Horizon 2020 research and innovation program under Grant Agreement No. 861985.

[3] Q. V. Le, H. W. Jang, S. Y. Kim, "Recent Advances toward High-Efficiency Halide Perovskite Light-Emitting Diodes: Review and Perspective", Small Methods, 2 (2018), 1700419.

[4] T. Wu, J. Li, Y. Zou, H. Xu, K. Wen, S. Wan, S. Bai, T. Song, J. A. McLeod, S. Duham, F. Gao, B. Sun, "High-Performance Perovskite Light-Emitting Diode with Enhanced Operational Stability Using Lithium Halide Passivation", Angew. Chem. Int. Ed., 59 (2020), 4099.

# Progress Towards High-Efficiency Silicon/Perovskite Tandems

B. Kamino, A. Walter, F. Sahli, A. Paracchino, M. Dussouillez, S.-J. Moon, L. Lauber, C. Ballif, S. Nicolay, Q. Jeangros

The addition of a perovskite solar cell on the front side of a commercial silicon solar cell should extend the efficiency curve of silicon beyond its efficiency limit and lower the leveled cost of electricity. CSEM aims to accelerate the development of silicon/perovskite tandem solar cells and modules through the development of materials, processes, and metrology concepts, with an overall goal of producing efficient and reliable processes and products that could be transferred to industrial partners.

Crystalline silicon solar cells, the technology dominating the photovoltaic (PV) market, are approaching their practical power conversion efficiency limit of 27% with highest experimental values reaching 26.7%. Innovative approaches are now needed as improving cell efficiencies further is the best leverage to lower the leveled cost of solar electricity and accelerate the deployment of PV. This constant quest for higher efficiencies stems from the cost distribution of a PV system: balance of system expanses outweighs solar cell costs. Today, the most promising route towards cell efficiencies >30% and low electricity prices involves stacking a second solar cell on the front side of a commercial silicon device to form a tandem cell. Such a cell concept improves the use of the solar spectrum and is already validated with III-V materials. A relatively young yet highly efficient class of solar cells based on a metal halide perovskite thin film have appeared as the ideal alternative to the costly III-V materials. In addition to excellent optoelectronic properties, abundant constituent elements, and high device performance at the single-junction level (25.5%), perovskite semiconductors can be processed at low temperatures using a variety of techniques ranging from thermal evaporation to wet coating techniques, ensuring their potentially simple and cheap integration onto a commercial Si cell. Consequently, intense research efforts have enabled small-scale demonstration tandems to surpass the efficiency limit of silicon after only a few years of R&D (current record of 29.5% on 1 cm<sup>2</sup>). Thanks to this potential and quick progress, silicon/perovskite tandems are predicted to enter the PV market on the horizon of 5-10 years and industrialization efforts are ongoing.

Through several Swiss National Science Foundation, Innosuisse, European and industrial projects, CSEM is aiming to bring silicon/perovskite tandem solar cells to the industrial level. More specifically, CSEM is focusing on upscaling, reliability, and general industrialization aspects of the technology. Recent results obtained include the demonstration of 27.6%-efficient tandems with an active area of 4 cm<sup>2</sup> (Figure 1), which were co-processed on a 4-inch Si wafer with a smooth front surface (and a textured rear side). Key to these advances was the development of a low-temperature screen-printing process to metallize the front side of tandems to ensure direct compatibility with industrial requirements (throughput, compatibility with large Si wafer dimensions). For comparison, most R&D tandems demonstrated to date have featured a thermally evaporated silver grid to remain within the limited thermal budget of the perovskite material. This metallization scheme is however ill-suited for industry as it introduces resistive losses when upscaling device dimensions and is inefficient in its use of Ag.

Using the same low-temperature screen-printing metallization approach, tandem devices were also produced on 4-inch Si wafers textured on both sides. The pyramidal texture produced on both sides of the Si wafer by chemical etching reduces reflection losses, promotes light trapping, and is hence a key optical management component of Si single-junction devices.

This micron-sized texture however complicates the deposition of the micrometer-thin perovskite top cell. Standard spin-coating routes yield layers with pinholes unless the size of the Si pyramids is drastically reduced to the sub-micrometer level. An hybrid route combining thermal evaporation and a spin-coating step was selected here to conformally coat the Si pyramids irrespective of their size. Tandem solar cells produced with this approach on Si wafers textured on both sides reached a maximum performance of 26% on 4 cm<sup>2</sup>.

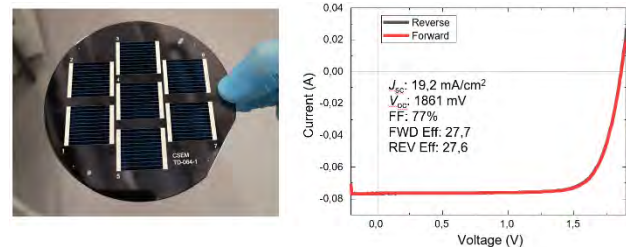


Figure 1: (left) Picture of 4-cm<sup>2</sup> tandems co-processed on a 4-inch Si wafer textured on its rear and flat on its front side; (right) current-voltage properties of a tandem cell reaching an efficiency of 27.6%.

In view of upscaling the device dimensions towards industry standards, a blade-coating process was developed to replace the spin-coating step to produce homogenous perovskite coatings on industry-representative M2 Si wafers. First tandems produced with this route featured an active area of 100 cm<sup>2</sup> and reached an efficiency of 22% (Figure 2), a first step towards the demonstration of full-area devices of industrial dimensions. The reliability aspects of the technology are also closely monitored. For that purpose, cells are encapsulated and subjected to various standard stability testing protocols. While progress is still needed to improve stability of the top cell, tandem devices typically pass damp heat tests (1000 hours at 85 % of relative humidity, 85°C with less than 10% <sub>rel</sub> of efficiency loss). Ongoing efforts are now focusing on light soaking stability, especially at elevated temperatures.



Figure 2: (left) 100 cm<sup>2</sup>-perovskite top cell processed on an M2 Si wafer; (right) tandem cell after encapsulation.

This work was financed in part by the SNF projects POWER (20B2-1\_176552), PAPET (200021\_197006), EPISODE (CRSII5\_171000), European Union's Horizon 2020 program, through an Innovation Action under the grant agreement No. 861985 (PEROCUBE) and 763977 (PERTPV).

# Building Blocks for PERx Solar Cells Upgrade

J. J. Diaz Leon, C. Alleb  , A. Descoeuilles, A. Ingenito, P. Wyss, L. Lauber, C. Ballif, S. Nicolay, B. Paviet-Salomon

The introduction of passivating contacts in silicon solar cells enables an efficiency increase by eliminating charge recombination at the metal/absorber interface. High-temperature passivating contacts are compatible with dopant activation and diffusion processes (typically at  $T > 800^\circ\text{C}$ ), hence enabling their integration with current PERx solar cells. In this work, we highlight some of the efforts undergoing at CSEM to develop passivating contacts that are easy-to-integrate in current industrial solar cell processing and allow for an efficiency increase at a competitive cost.

Passivated emitter and rear contact (PERC) solar cells are the current workhorse of the solar cell industry. These rely on a p-type Si wafer absorber with an n-type emitter on the front side and local Al contacts on the rear side.

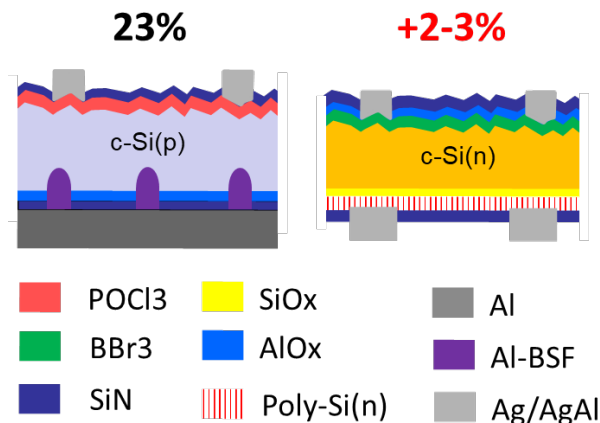


Figure 1. Current PERC (left) and PERT (right) solar cell architecture upgraded with n-type polySi on the rear side.

While the localization of the rear contacts allows for increased surface passivation and overall cell voltage, there is a trade-off between passivation and carrier extraction. Furthermore, if an n-type Si absorber in combination with a p-type emitter is used, it is possible to increase the overall voltage of the device due to the better passivation achievable on B emitters and the higher lifetime achievable in P-doped wafers. Instead of contact localization, a full area n-type passivating contact (PC) can be applied on the rear side. PolySi PCs, rediscovered in 2017<sup>[1]</sup>, rely on the combination of an interfacial oxide and doped polysilicon. PCs need to provide high passivation, efficient carrier extraction and have to be compatible with standard solar cell processing – namely dielectric deposition and firing for metallization and hydrogenation. An increase of the solar cell efficiency of 2-3% with the introduction of PCs in n-type absorbers with respect to PERC has already been achieved (Figure 1)<sup>[2]</sup>.

At CSEM, we have been working on n-type passivating contacts by sputtering. Initially demonstrated for p-type passivating contacts by ANU<sup>[3]</sup>, sputtering has been proven in the microelectronics industry, allows for single-sided deposition, and can process up to 8000 wafers per hour at low cost.

In order to industrialize sputtered polySi, it is paramount to use DC sputtering, since RF sputtering is not feasible in large scale. Figure 2 demonstrates that similar passivation ( $i\text{Voc} > 730 \text{ mV}$ ) and carrier extraction results can be achieved via RF and DC

sputtering ( $\rho_{\text{pc}} \sim 50 \text{ m}\Omega\cdot\text{cm}^2$ ), without any degradation of the passivation when using a DC sputtering process.

Doping of PCs can be done in-situ or ex-situ. In Figure 3, we show ex-situ doping using two different doping sources. While both ex-situ doping sources showed high passivation ( $i\text{Voc} > 730 \text{ mV}$ ), it was found that the "ex-situ2" process provided lower  $\rho_{\text{pc}}$  down to  $16 \text{ m}\Omega\cdot\text{cm}^2$ . With this contact resistivity and for a metallization fraction ~10%, negligible series resistance is expected in solar cell devices.

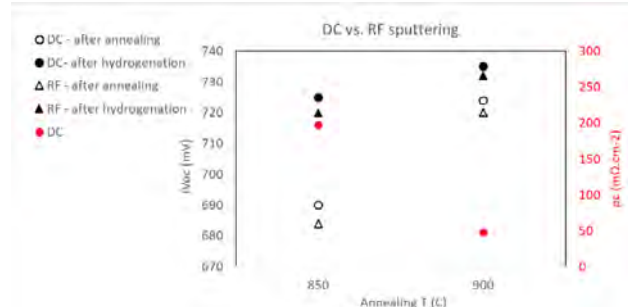


Figure 2.  $i\text{Voc}$  after annealing and after hydrogenation and  $\rho_{\text{pc}}$  after firing-through metallization of sputtered polysi using either polySi layers deposited by DC or RF sputtering at  $850^\circ\text{C}$  and  $900^\circ\text{C}$ .

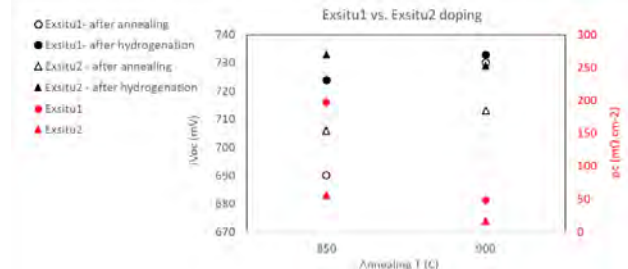


Figure 3.  $i\text{Voc}$  after annealing and after hydrogenation and  $\rho_{\text{pc}}$  after firing-through metallization of sputtered polysi using two different ex-situ doping sources at  $850^\circ\text{C}$  and  $900^\circ\text{C}$ .

Integration of sputtered polySi(n) at the rear side of bifacial PERT+ solar cells (Figure 1, right) was performed to validate this approach at industrial wafer size. Metallization was done by screen printing and firing of a metal paste. Table 1 shows the certified solar cell parameters of such a cell, showcasing the potential of this technology.

$J_{\text{sc}}$ [mA/cm <sup>2</sup> ]	$V_{\text{oc}}$ [mV]	FF [%]	Eff [%]
40.64	697	80.5	22.8

<sup>[1]</sup> A. Richter, *et al.*, Solar Energy Materials and Solar cells 173, 96 (2017).

<sup>[2]</sup> D. Chen, *et al.*, Sol. Energy Mater. Sol. Cells, vol. 206, September 2019, pp. 1–8, 2020.

<sup>[3]</sup> D. Yan, *et al.*, Applied Physics Letters 113, 061603 (2018).

# Technology Platform for High-Efficiency HJT Solar Cells

A. Descoedres, C. Alleb  , N. Badel, G. Christmann, J. Geissb  hler, L.-L. Senaud, P. Wyss, J. Zhao, C. Ballif, B. Paviet-Salomon

CSEM has set up a complete platform for the production and the characterization of both-side contacted silicon heterojunction (HJT) solar cells, as well as for advanced backside contacted devices and bottom cells for silicon/perovskite tandems. Innovative and industry-relevant solutions are continuously developed for the improvement of all cell processing steps, aiming for high-conversion efficiencies at competitive costs. The technological topics covered at CSEM include wafer bulk quality improvements, wafer texturing and cleaning by wet-chemistry, PECVD depositions of ultra-thin passivating and contact layers, PVD depositions of low-cost and/or high-mobility transparent conductive oxides, advanced cell metallization and cell interconnection processes and various cell characterization techniques. Efficiencies up to 23.6% and 24.4% are demonstrated on industrial 6-inch, screen-printed, both-side contacted p-type and n-type HJT solar cells, respectively, as well as more than 25% on back-side contacted HJT cells. The platform is unique to assess new processes, new materials, and to support the development of reliable metalisation and encapsulation schemes, which strongly impact field module performance.

The silicon heterojunction technology (HJT) is one of the most relevant solutions for driving down the costs of photovoltaic electricity in the coming years. Compared to standard crystalline silicon solar cells, HJT are able to reach higher efficiencies thanks to full-area carrier-selective passivating contacts, while at the same time being fabricated with fewer fabrication steps due to a simple cell architecture. In addition, thanks to their symmetric structure, HJT solar cells can easily be integrated in bifacial modules, leading to increased energy yield in the field.

A complete, performant and flexible platform is installed at CSEM covering all aspects of production and characterization of such industrial HJT solar cells, from as-cut wafers to finished devices (Figure 1-left). This technological platform allows CSEM conducting advanced R&D projects on specific processing steps, to develop new processes, materials and cell concepts, and also to provide services and small batch production for its customers.

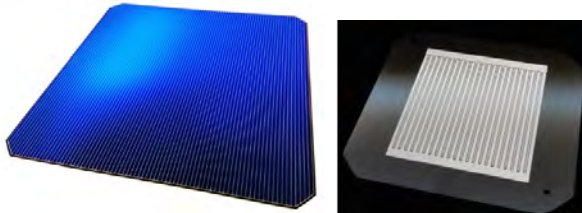


Figure 1: Pictures of a 6-inch full-area busbar-less bifacial HJT solar cell (left) and of the back side of a 25 cm<sup>2</sup> R&D IBC HJT solar cell (right) produced at CSEM.

Depending on the starting wafer bulk quality and properties, tailored high-temperature impurity gettering processes have proven to be efficient to improve final cell performance. In particular, Cz p-type c-Si material is known to be more defective than its n-type counterpart, but its lower production cost still represents an interesting advantage also for the HJT technology (usually only applied on n-type wafers). By simply adding an optimized gettering step at the very beginning of the cell fabrication process, it has been demonstrated that the performance of large-area industrial monofacial and bifacial HJT solar cells is almost at the same level on commercially available Cz p-type material than on n-type one, without any other modification of the cell fabrication process [1].

Simplification of the wafer texturing and cleaning processes is actively pursued. Specific single-side texturization processes are developed for silicon/perovskites tandem cell applications. The control of the HJT bottom cell surface morphology (textured or planar) and its uniformity is indeed of particular importance for the subsequent fabrication of the perovskite top cell. Advanced

functional ultra-thin films by PECVD are continuously investigated and optimized, since they are key to providing surface passivation and determine to a large extent the carrier transport properties within the cell. State-of-the-art surface passivation has been obtained, with for instance minority carrier lifetimes above 10 ms on both Cz n- and p-type HJT cell precursors. Performance and cost of the cell metallization part are also intensively improved, via the implementation of low-cost (indium-free) and/or high-mobility transparent conductive oxide layers and ultra-fine busbar-less metallization, applied by low-temperature silver paste screen-printing or copper electro-plating. Applying the recent developments made on the CSEM platform, 23.6% and 24.4% efficient large-area both-side contacted HJT solar cells were fabricated on p- and n-type Cz wafers, respectively, using industry-compatible processes (Figure 2), while enhancing final module reliability in combination with advanced metalisation and encapsulation schemes and materials.

Wafer Type	Cell Area [cm <sup>2</sup> ]	Cell Type	V <sub>oc</sub> , mV	J <sub>sc</sub> , mA/cm <sup>2</sup>	FF, %	Eff., %
Cz p-type	244	Bifacial	746	38.6	80.1	23.1
Cz n-type	244	Bifacial	742	38.5	82.4	23.5
Cz p-type	244	Monofacial	741	39.4	80.0	23.4
Cz n-type	244	Monofacial	740	39.5	82.1	24.0
Cz p-type	221	Monofacial	740	39.5	80.8	23.6
Cz n-type	221	Monofacial	738	39.9	83.0	24.4

Figure 2: Summary of one-sun illuminated IV cell parameters of the best large-area HJT solar cells obtained at CSEM (screen-printed busbar-less cells, in-house measurements, black chuck for bifacial cells).

Advanced interdigitated back-contacted (IBC) HJT solar cells are also being developed on this platform. In this configuration, the electrical contacts of both polarities are placed at the back side of the cell (Figure 1-right), permitting a gain in performance thanks to the complete removal of the front metallization shadowing. The "tunnel-IBC" concept developed at CSEM relies on only one patterning step using mechanical hard masking during PECVD, and on interband-tunneling carrier transport in the device [2]. Being completely photo-lithography free, this process flow permits to limit the fabrication costs of IBC HJT cells. Efficiencies above 25% have been demonstrated on 25 cm<sup>2</sup> (and over 200 cm<sup>2</sup> by industry partners) fabricated with only 10 process steps, emphasizing the relevance of the tunnel-IBC concept for future mass production of high-efficiency solar cells.

[1] A. Descoedres, et al., Prog. Photovolt.: Res. Appl. 28 (2020) 569.

[2] A. Tomasi, et al., Nature Energy 2 (2017) 17062.

# From R&D at CSEM to Meyer Burger New PV Product Launch

A. Faes, H.-Y. Li, J. Champliaud, J. E. Palou, J. Levrat, D. Petri, L. Pires, G. Nogay, L. Baume, L. Perla, G. Christmann, A. Descoedres, C. Allebé, J. Zhao, N. Badel, B. Paviet-Salomon, M. Despeisse, C. Ballif

Since 2013, CSEM PV-Center has been developing silicon heterojunction (HJT) solar cells as well as Smart Wire Connection Technology (SWCT) in collaboration with Meyer Burger. One drawback from HJT is the relative high cost of screen-printed silver metallization compared to the standard solar cells. By using SWCT, the mass of silver can be strongly reduced, down to a factor 1/5. The combination of both technologies, HJT and SWCT, enables an impressive product reliability, passing 5 times norms requirements, while reducing the silver consumption. In 2021, Meyer Burger launched a mass production of 400 MW per year of both HJT cells and SWCT modules. This is the first step, as multi-GW production plans are now announced in Europe and US by Meyer Burger. The intense research and development effort needed to bring a disruptive technology to the mass production readiness level has been possible only with the support from Innosuisse, Swiss Federal Office of Energy (SFOE) and European projects.

Silicon-heterojunction (HJT) solar cells metallization is based on low-curing temperature silver paste as the stability of amorphous -silicon nano-layer in the cell is limited to temperature below 250°C. The resistivity of the low curing temperature silver paste is about 2 to 3 times higher than standard firing-through paste. To compensate the higher resistivity, the silver mass deposited on the cell can be more than double compared to standard cells. By using multi-wire interconnection like Smart Wire Connection Technology (SWCT) the line resistance of the finger ( $R_f$ ) can be multiplied by 20 without impacting the power losses in the finger ( $P_f$ ) as the number of busbars ( $n_{BB}$ ) are changed from 5 to 18 busbars (see equation 1):

$$P_f \propto C \frac{R_f}{n_{BB}^2} \quad \text{equation (1)}$$

Using SWCT, the silver mass used for HJT cell can be lower than standard cells. CSEM has been developing the ultra-fine screen-printing process to reduce the silver paste deposit and increase cell current density within Swiss-Inno HJT SFOE project [1].

The SWCT is composed of copper wire coated with low-temperature solder alloys supported by transparent foil (see Figure 1). CSEM has been developing the technology using affordable and abundant solder alloys within SmartWire Innosuisse project, demonstrating scientific understanding of the key parameters responsible for high reliability in the field.

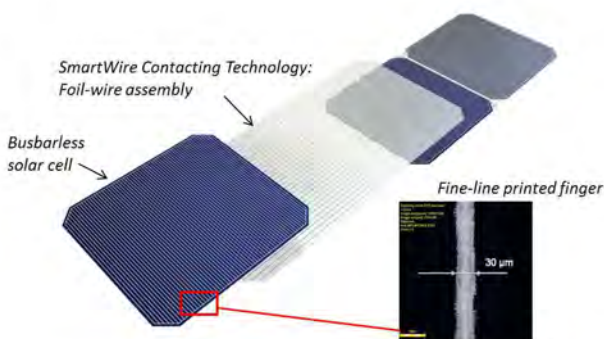


Figure 1: Smart Wire Connection Technology (SWCT) from Meyer Burger is based on 18 multi-wires interconnection supported by a transparent foil.

The development of the foil within DEFIA Innosuisse project enables to increase the performance as well as the reliability of the module. Large scale demonstration bifacial modules of 72 cells in glass/glass configuration show reliability over 1000

[1] B. Strahm, D. Lachenal, D. Bätzner, et al., The Swiss Inno-HJT project: fully integrated R&D to boost Si-HJT module performance, 29th EU PVSEC, 2014, Amsterdam, The Netherlands, p. 467.

thermo-cycles (TC) between -40°C to +85°C with no power losses, where the IEC-61215 standard requires only 200 TC with less than 5% relative power losses (see Figure 2a). For the damp-heat (DH) conditions the results are even more impressive with module reliability test at 85°C and 85% relative humidity during 14'000 h (equivalent to one-and-a-half-year test) with less than 4% relative power degradation, to be compared to 1000 h for the standard test (Figure 2b). This upscaling done in H2020 Ampere project demonstrated that the HJT-SWCT technology can pass 5 to 14 times the standard requirement.

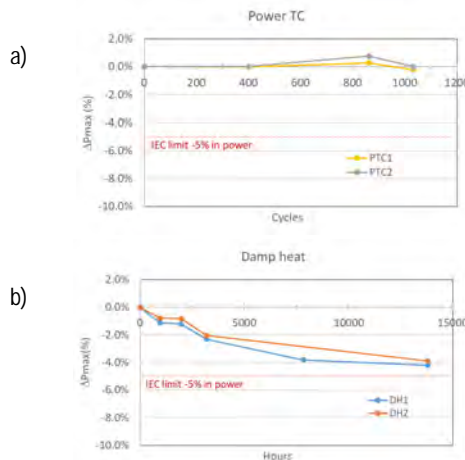


Figure 2: Relative power variation during (a) thermo-cycles (TC) and (b) damp-heat (DH) hours reliability testing for 72 cells HJT-SWCT modules in glass/glass configuration.

Also on Meyer Burger side, strong investment and development has been done with the support from SFOE at the start in 2013 (see Figure 3). In 2019, important production facility of 600 MW/y of HJT-cell and SWCT module have been commissioned to REC-Solar in Singapore. In 2021, Meyer Burger started its own production of HJT-cells and SWCT modules and announced multi-GW/y production facility in Europe and 400 MW/y in Arizona.



Figure 3: (left) Inauguration in 2013 by Doris Leuthard of the HJT cell pilot line supported by SFOE, (right) Meyer Burger SWCT module production plan of 400 MW/y capacity inaugurated in 2021 [2].

[2] A. Faes, H.-Y. Li, J. Champliaud, et al., From Innosuisse and SFOE projects to mass production of PV cells & modules, PV-Tagung, Bern, 2021.

# CSEM Coloring Technologies for Building Integration of Photovoltaics (BIPV)

L. Pires da Veiga, H. Li, J. Escarré, G. Cattaneo, U. Fuerholz, S. Pittet, T. Auderset, C. Charrière, C. Ballif, M. Despeisse

*Building Integrated Photovoltaics is dynamically penetrating the photovoltaic and construction markets. Novel solutions are designed to meet the architect's demands for the design of a building that communicates with color their capability of producing energy. In order to improve the desirability of BIPV products, CSEM R&D focuses on cost-effective, performant and aesthetics solutions that have low implementation barrier.*

Following the increasing demand for sustainable energy, the BIPV market is expected to grow from today's 3.54 billion\$ to 8.68 billion\$ by 2026. While standard PV modules are submitted to strict requirements in terms of performance and cost, the return of investment of BIPV installations is less prioritized; instead, aesthetics and customizability are key factors to be pondered during product development. Multiple technologies are therefore emerging in the field to bring design diversity to architects. All require the use of an additional colored layer or effect on the sunny side of the PV modules. As a result, this colored layer affects the modules significantly on the aspects of aesthetics, power generation, lifetime and cost. In the EU project BE-SMART, CSEM further optimized two generations for coloring of PV modules.

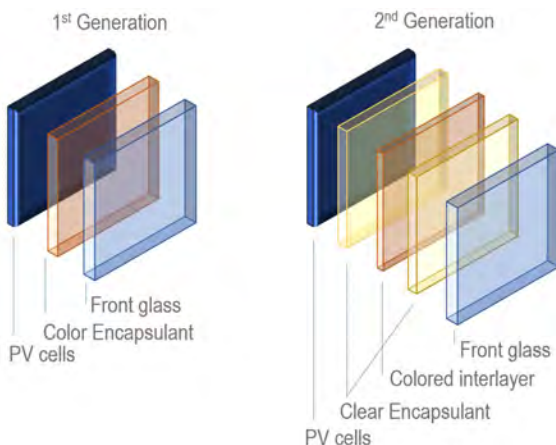


Figure 1: Comparison of different coloring techniques for PV modules.

As shown in Figure 1, the first generation involved the replacement of the clear encapsulant inside the PV module with a colored one. To reduce processing limitations, CSEM developed a second generation, consisting of a thinner colored interlayer to be combined with clear encapsulants. This generation leaves more room for process flexibility as the customer can use the same materials as in their standard PV modules to maintain reliability. Figure 2 displays an example of the color palette that CSEM has developed and transferred to Solaxess SA.



Figure 2: Solaxess single cell PV modules with CSEM's colored interlays.

The second generation has started commercialization in 2021 and has already been implemented in several sites in Europe. One example is the head office of the Zurich city emergency services, see Figure 3, of which 800 m<sup>2</sup> of roof tiles have been replaced with terracotta colored PV modules, manufactured by

3S+ company using Solaxess colored foils produced by CSEM technology.



Figure 3: BIPV rooftop in Zurich with CSEM's coloring technology.

When compared to printed glasses, CSEM's interlayer solution offers several advantages: it can easily be processed in large-scale volumes, it offers a better reliability of the color performance, the color can be more easily customized to meet the architect's demands and finally, it can be transferred to lightweight PV modules. In the frame of the EU project RE-COGNITION, CSEM is collaborating with PVLab EPFL, to whom the color foils were transferred to fabricate colored light weight modules, displayed in Figure 4.



Figure 4: Example of CSEM coloring technology developed from 1-cell module demonstration to large-area 24 cells light weight modules.

CSEM has developed a large set of module coloring techniques, materials and concepts, with varied advantages with respect to processability, integration, color rendering and final cost. The patented technologies are now being industrially deployed. Besides that, next-generation coloring technology is under development which is expected to further reduce the cost and complexity of the transformation process. In addition, the different developments performed at CSEM enabled to develop a large expertise in reliability and performance of colored PV modules for BIPV applications. CSEM is offering such expertise to various industrial partners, including advanced reliability assessment, as well as software prediction of module performance depending on targeted colors.

# Copper Metallization for Silicon Heterojunction Solar Cells

A. Lachowicz, N. Badel, J. Gay, G. Andreatta, N. Blondiaux, A. Faes, J. Diaz Leon, C. Ballif, B. Paviet-Salomon

Replacement of silver for metallization of solar cells is crucial for increasing the PV production volumes to terawatt levels, as it is required for the transition to 100% renewable energies by 2050. CSEM has developed a reliable and cost-competitive process for copper electrodeposited metallization for heterojunction cells – one of the future mainstream cell technologies – and the aim of ongoing research is to further reduce the process cost.

Photovoltaics will be the main energy source in the future, contributing almost 70% of the global demand not only for electricity, but also for mobility, buildings, and industry<sup>[1]</sup>. The required capacity of all globally installed PV will be around 70 terawatts (TW). For comparison, the PV capacity installed today has surpassed 0.7 TW and delivers 3.1% of the global electricity. This means 1% of the work is done – 99% more to go!

Although only a small amount of silver is used for one cell (~100 mg) it adds up to 2000 tons per year or 10% of the entire silver supply for today's "small" production of 150 GW. To meet the zero-carbon emissions target by 2050, the annual solar cell production must be increased at least ten-fold in the next years. This is feasible only with an extremely small silver consumption per cell (~5 mg) or with a different – more abundant – material.

CSEM has developed a reliable and cost-competitive process for copper metallization based on a PVD seed layer and patterning by inkjet printing of an organic hotmelt mask. High efficiency above 24.7% and excellent module stability have been achieved. This process has already been tested on industrial equipment and is planned for implementation in production by a solar cell manufacturer.

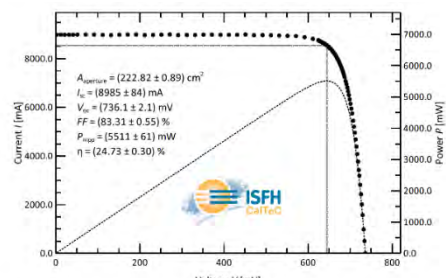


Figure 1: Certified efficiency on an industrial heterojunction cell precursor (monofacial cell with four busbars).

For further cost reduction, a short and simple process sequence is being investigated: the seed for plating is the standard screen-printed pattern, just with narrower lines and very low paste laydown. The required line conductivity is provided by the subsequently electrodeposited copper layer and even a relatively resistive copper paste can be used to form the seed-grid. A thin masking layer is then deposited on the entire wafer to prevent plating on the conductive TCO. Dielectric materials like silicon oxide or nitride (50-100 nm), aluminum oxide (5-10 nm) or a monolayer of self-assembling molecules (SAMs, 2 nm)<sup>[2]</sup> are applicable as masking layer.

The process is self-aligning: the surface of the seed-grid is rough, the masking layer here not fully tight and copper is deposited selectively only on grid positions.

[1] LUT and Energy Watch Group, Global Energy System Based on 100% Renewable Energy, 2019

[2] G. Andreatta, et al., Thin Solid Films, 2019, vol. 691 p. 137624.

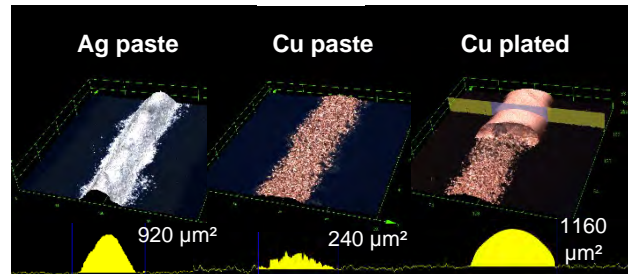


Figure 2: Confocal microscope images of printed seed-grid lines and corresponding cross section area.

The same efficiency as with standard silver paste has been reached using only a pure copper seed-grid reinforced with electrodeposited copper, i.e., silver has been fully eliminated while maintaining the cell performance.<sup>[3]</sup>

Using CSEM's proprietary contacting system, bifacial industrial size precursors are plated simultaneously on both sides enabling short process times. The system is applicable on standard wafer sizes like "M6" (edge length 166 mm), "M10" and "G12" (full square, edge 210 mm) and enables plating on cells with not connected grid segments, as it is required for half-cell modules and for high-density shingling interconnection. Additionally, contact bars in the center provide mechanical stability for such big wafers. The contacting system is already proven on wafers of 135 micrometer thickness – the future target to save silicon. A batch of 200 M2-cells from an industrial project partner has been plated without any breakage losses through contacting.



Figure 3: Industrial M6 precursor with copper electrodeposited on Ag paste seed-grid (visible at contacting points) and half-cell layout, with C18-PA SAM-mask.

This work has been partially carried out within the Ameliz project. CSEM thanks the Swiss National Science Foundation SNF and the French National Research Agency ANR for funding.

[3] A. Lachowicz, et al., Metallization and Interconnect. Workshop, 2021.

# Reliable Photovoltaic Solution for Stratospheric Applications

X. Bulliard, P. Duvoisin, H. Li, C. Charrière, S. Prabhudesai, G. Cattaneo, S. Pittet, C. Ballif, M. Despeisse

CSEM has set up a versatile platform for the manufacturing of lightweight photovoltaic (PV) modules for applications to a wide range of domains, for example stratospheric applications. The lightweight PV solutions currently equip balloons for missions in the stratosphere piloted by the CNES (Centre National d'Etudes Spatiales). The missions of a few days to several months aim at studying meteorology or climate and the developed modules provide electricity for the scientific instrumentation. In addition to lightweight and high-mechanical resistance, the PV modules have been specifically designed for functioning in the harsh stratospheric environment, under UV, ozone and temperature exposure. Intensive development on the materials composing the module, in particular on the encapsulant, was necessary to satisfy all requirements.

CSEM and CNES are collaborating on the development of novel PV solutions to power the scientific instrumentation of balloons for missions in the stratosphere. For such missions, the requirements in terms of weight, mechanical properties and reliability are important and CSEM has developed unique PV solutions based on composite materials to satisfy these criteria. The use of composite materials allows the tailoring of mechanical properties by reinforcing the strength of the module in specific area, while preserving a high toughness, for a minimum weight. In contrast to typical glass-based PV modules which exhibit a weight superior to 15 kg/m<sup>2</sup>, the products developed can show a weight below 1 kg/m<sup>2</sup>. In these developments, the structure of the modules and its constituting elements (backsheet, frontsheet and encapsulants) were redesigned. In particular, the composition of the encapsulant was formulated to withstand UV and ozone exposure in the stratosphere. The encapsulant is critical to protect the cells and maintain the whole integrity of the modules.

Two types of PV modules and solutions have been implemented for two different flight missions. In the mission Stratoile 2 (CNES), balloons are launched for typically 3 months around the equator to collect a wide range of data for a better understanding of meteorology and climate. For this mission, module with the composite-based architecture were directly fixed on the balloon basket, as shown on Figure 1a.

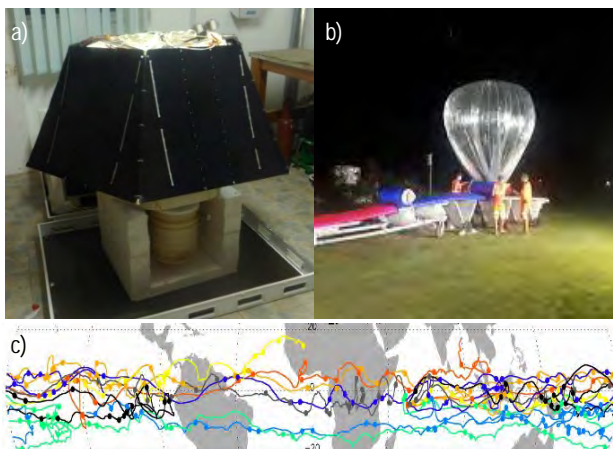


Figure 1: Pictures of the module placed on the basket of the balloon (a), the launching of the balloon (b) and the trajectory of the balloon (c) for the mission Stratoile 2 (picture courtesy of CNES; copyright A. Hertzog).

For this present case, the modules could be dimensioned according to the room available on the basket for an optimization of the performances. Custom-made module is another key point of solutions developed at CSEM. The functionality and reliability of the modules has been verified in a first validation mission of three months in 2020, and the scientific mission is now scheduled in 2021. Figure 1b shows the launching of the balloons and Figure 1c their trajectory during the validation mission.

In the project MEDOR (CNES), a larger electricity power is required, exceeding the power that could be generated by modules on the side of the basket. To circumvent this limitation, CNES and CSEM developed a solar store that hangs below the balloon. The store is folded during take-off or landing, and is deployed when the balloon reaches its cruising altitude. Figure 2 shows a picture of rear of the store during deployment. The number of elements can be tuned and adapted to the power needed for a specific mission. Non-functional elements (without solar cell) are added for mechanical purpose and to avoid shadowing on the cells by the balloon. The solar modules of 1 × 2 m (3 on the pictures) are then added and electrically connected to the rest of the store. For this use case, the rigidity of the modules was critical to avoid buckling during deployment, while the toughness should be maintained in case of impact. The right balance between these mechanical properties could be achieved by controlling the composite stacking of the module. The whole system under the balloon was tested and validated in real conditions.



Figure 2: Picture of solar store (partially shown) during deployment. The first mechanical elements are not equipped with solar cell, and the solar modules (3 on the picture) are then added to the store.

In summary, the lightweight PV modules, specifically designed for harsh stratospheric environment, have been validated in two different missions piloted by CNES. The technology finds direct applications in climate study and the knowledge gained can be used in a wide range of other applications.

# Energym, an Open-Source Library for Data-driven Building Control

P. Scharnhorst, B. Schubnel, M. Boegli, T. Gorecki, Y. Stauffer, P.-J. Alet

Smart control algorithms are a tool to reduce energy consumption and greenhouse gas (GHG) emissions in buildings. CSEM has developed the open-source Python library Energym, to test and benchmark control algorithms on a multitude of realistic building models. Using an interface similar to the popular reinforcement learning (RL) benchmarking library Gym, Energym aims at providing researchers a tool to apply RL and (learning-based) model predictive control (MPC) to buildings with standardized evaluation metrics.

With about 36% of the global final energy use [1], buildings are among the biggest energy consumers and GHG emitters worldwide. While smart control strategies promise an efficient use of e.g., heating and cooling, the majority of control strategies currently used in building control are still rather simple. They mostly fall in two categories: rule-based control, where decisions on how to run the heating and cooling equipment are done with a set of fixed rules, and PI control, a classical control strategy where parameters have to be tuned by experts for each building separately. These methods generally provide reliable performance with respect to temperature requirements, but they perform sub-optimally regarding energy consumption.

Various studies have shown the potential of more advanced control strategies like MPC, learning-based control, and RL, but a direct comparison of approaches from those categories remain mostly open.

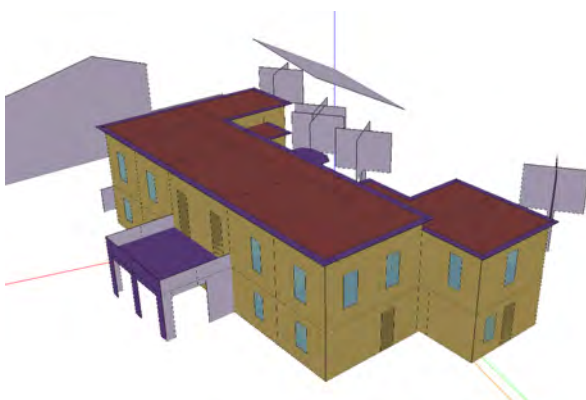


Figure 1: Envelope of the "Office" building.

Energym [2] aims at filling this gap by providing a principled way for comparing control performances. 14 simulation models are included to date, eight of which are based on the building simulation software EnergyPlus, and six based on Modelica.

The models were partly or fully calibrated. They range from single zone buildings to 27 thermal zones, include office and residential buildings, and differ in equipment and controllability. The installed equipment encompasses thermostats (Th), heat pumps (HP), batteries (Bat), air-handling units (AHU), electric vehicles (EV), and photovoltaic systems (PV). An overview of the different building classes with their installed equipment is given in Table 1.

To train controllers, the buildings can be simulated with different weather conditions over the course of a full year. Additionally, stochastic forecasts are provided to have a realistic representation of the uncertainty in weather forecasts.

Table 1: Simulation models and their equipment.

Model class	Th	HP	Bat	AHU	EV	PV
Apartments	✓	✓	✓	✗	✓	✓
Offices	✓	✗	✗	✗	✗	✓
Mixed use	✓	✗	✗	✓	✗	✗
Seminar center	✓	✓	✗	✓	✗	✓
Simple house	✗	✓	✗	✗	✗	✓
Swiss house	✗	✓	✗	✗	✗	✓

Comparability of control performances is ensured through the "evaluation mode" in Energym. When it is activated, all uncertain schedules, e.g., for the weather and forecasts, are fixed to make the simulation runs independent of stochastic variations. The time for which a simulation should be run is specified (e.g., from January to April, or for the whole year), and the final evaluation is done based on key performance indicators (KPIs).

KPIs considered in Energym measure the total power consumption, CO<sub>2</sub> emissions, or grid exchange. Custom KPIs based on the simulation outputs can also be defined.

Control strategies like MPC or RL have specific requirements on the input-output structure of the simulation models. For MPC, a scaling of the inputs and outputs to the range [0,1] can be beneficial for solving the finite-horizon optimal control problem. For RL on the other hand, a reward signal together with the standard outputs is needed for the learning. To account for this difference, simulation wrappers that perform the input-output transformations are provided, and they can be freely combined.



The library is available on Gitlab, an open-source collaborative platform and will be expanded with models contributed by the wider community.

Part of the models have been developed in the project SABINA, which has received funding from the European Union's Horizon 2020 research and innovation program under grant agreement n°731211, in collaboration with C. Fernández Bandera (UNAV), J. Salom, P. Taddeo (IREC), A. Peppas, and C. Politi (NTUA).

[1] GlobalABC, "2019 Global Status Report for Buildings and Construction: Towards a Zero-Emission, Efficient and Resilient Buildings and Construction Sector", Technical report, 2019.

[2] P. Scharnhorst, B. Schubnel, C. Fernández Bandera, J. Salom, P. Taddeo, M. Boegli, T. Gorecki, Y. Stauffer, A. Peppas, C. Politi, "Energym: A Building Model Library for Controller Benchmarking", 8, Applied Sciences 11(8), 3518 (2021) [doi:10.3390/app11083518].

# Field Demonstration of Data-driven Control for the Provision of Flexibility from Distributed Resources

R. Carrillo, Y. Stauffer, T. Gorecki, M. Boegli, P.-J. Alet

The increasing penetration of renewable energy sources (RES) and their stochastic variability create a challenge for the current power system. A solution to this challenge is to change from supply control to demand control, i.e., to adapt the demand to the generated power. This change requires an increased use of advanced control and optimization algorithms to make demand flexible through demand response technologies. CSEM has developed a software solution to control different distributed flexibility resources. The solution was deployed in a small district composed of two buildings and resulted in a 35% increase in self-consumption and 61% reduction in exported energy compared to the baseline solution.

Significant efforts have been made worldwide during the recent years to increase the penetration of RES while improving building energy efficiency. By increasing the penetration of intermittent RES, it becomes increasingly important to develop and integrate technological solutions able to absorb RES-related disruptions and sustain power grid network operation. In principle, the reliable, uninterrupted operation of energy systems relies on achieving balance between the energy consumption and generation in real time, taking into account the variability of production (i.e., weather-dependent part) and the consumption (i.e., building demand profiles, consumer behavior). Therefore, the ability to intelligently control the consumption patterns of a building and/or a district becomes increasingly important due to its potential to mitigate electricity fluctuations and reduce the available grid power demands as well as the associated costs [1].

Among available approaches for enhancing the flexibility of grid-interactive buildings, demand response (DR) is seen as promising and efficient. Through advanced DR control, buildings can become more flexible with regard to the power demand from the power grid while increasing the penetration of RES. To accommodate the growing demand for DR, CSEM developed in the framework of the European project SABINA a software solution to control distributed resources in buildings such as batteries, electric vehicles charge/discharge, and HVAC systems.

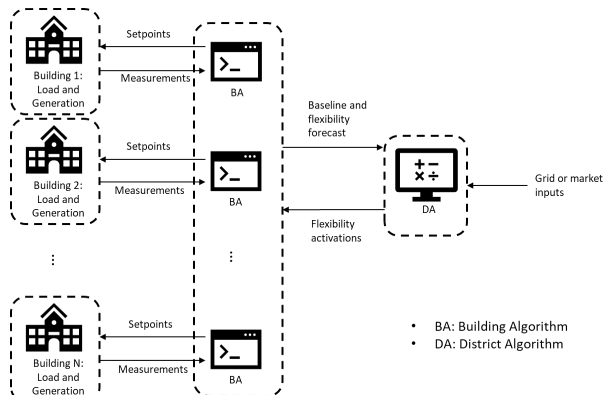


Figure 1. Multi-level control approach developed in SABINA.

The concept of the multi-level control developed in SABINA is depicted in Figure 1. The building management algorithm (BA) is the intermediate layer between the buildings and the district management algorithm (DA). The BA receives measurements of the state variables of the building (e.g., zone temperatures, power consumption of different systems, etc.). Based on this information from the building and on weather predictions on the

day ahead, the BA computes a forecast of the building's power consumption (baseline load) for the next 24 hours as well as the available flexibility (up and down) for the same period. The DA receives the baseline and flexibility forecasts from all buildings as well as the input signals from the grid operator or market. These signals can be energy prices, grid power constraints for the next 24 hours or desired power consumption for a certain period. Based on these signals and the information from the buildings, the DA computes the optimal allocation of flexibility activations among the different buildings (time and desired power of the activation) [2].

The multi-level control algorithm was deployed in a small district in the Lavrion Technological and Cultural Park at the National Technical University of Athens. The experimental campaign was performed during the summer period in Greece with different scenarios regarding photovoltaic power generation and external weather conditions. The district consists of two office buildings equipped with photovoltaic (PV) generation. In the experiments, the objective of the DA was to minimize the energy exchange between the district and the grid. Data from the building with the default control solution (rule-based control) at the same time period of the previous year was used as benchmark. The results show that the developed multi-level control algorithm decreased the exported energy to the grid by 61% avoiding power injections to the grid during peak PV production times, thus avoiding grid congestion, while the imported energy from the grid was just increased by 2%.

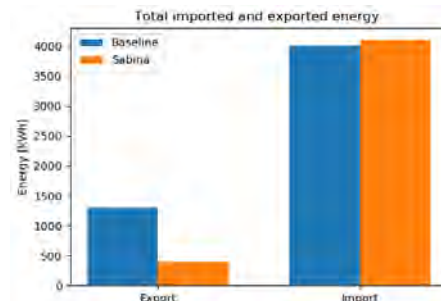


Figure 2. Normalized energy grid exchange.

Results also show that the developed solution helped the district to consume most of the generated PV energy by increasing the self-consumption by 35% compared to the baseline controller.

The SABINA project has received funding from the European Union's Horizon 2020 research and innovation program under grant agreement n°731211.

[1] IEA, "Demand Response", International Energy Agency, Paris (2020).

[2] P. Taddeo, A. Colet, R. E. Carrillo, L. Casals Canals, B. Schubnel, Y. Stauffer, I. Bellanco, C. Corchero Garcia, J. Salom, "Management and Activation of Energy Flexibility at Building and Market Level: A Residential Case Study," 5, Energies 13(5), 1188 (2020) [doi:10.3390/en13051188].

# Real-Time Forecasting of PV Production for Individual Plants at Country Scales

B. Schubnel, R. E. Carrillo, J. Simuneovic, R. Langou, P. Scharnhorst, P.-J. Alet

The fast-varying production of photovoltaic plants due to cloud motion creates a challenge for their massive integration in the electrical grid. CSEM has developed an entire analytical tool chain – live data acquisition, data processing, state-of-the-art graph machine learning, online visualization – to predict at low computing cost, high accuracy, and high resolution the power production of many individual plants at country scale and up to six hours ahead. Live forecasting results applied to data collected from the Netherlands are freely available online at <http://portal.csem.ch:9107/>.

Several approaches have been proposed to improve intra-day (up to six hours ahead) PV forecasting accuracy at the node level. Previous works use inputs from various sources, in particular ground-based cameras, satellite images, and numerical weather forecasts. But ground-based cameras are costly to install, clean and maintain, and high-resolution satellite images and numerical weather forecasts are costly to acquire. At CSEM, we have implemented a promising approach in terms of acquisition costs, computing needs and accuracy.

This approach only uses the power production data logged by the inverters of photovoltaic installations (typically at a resolution between 5 min and 15 min). Unlike pyranometers installed by meteorological service providers, the data from photovoltaic installations are affected by shading effects, orientation, tilting, and saturation. But one of their main advantages is to be scattered all over the country, and to clearly outnumber pyranometers, since there are already more than 100'000 solar installations across Switzerland [1].

We have recently developed and benchmarked several graph machine learning algorithms (group LASSO, convolutional graph LSTMs, convolutional graph transformers) using these data as sole inputs to forecast intra-day photovoltaic production for up to thousands of plants, at country scale [2,3]. These architectures can automatically capture spatio-temporal correlations between the individual plants and lead to better normalized errors than the ones using standard numerical weather forecasts with local plant models: the short-term normalized mean square error (first two hours) is almost reduced by half. We further developed spatio-temporal interpolation techniques to cope with gaps and irregular data sampling.

To showcase the capability, and in particular the scalability and low computation costs of our method, we have created an entire chain (data acquisition, preprocessing, prediction, visualization) based on openly available datasets. We use data from six hundred photovoltaic installations scattered all over the Netherlands and give live intra-day forecasts (six hours ahead, 15 minutes resolution) for each individual plant. The predictions for the 600 nodes are freely visible on CSEM's web portal.

As displayed on Figure 1, the users can see the actual and forecasted production of all registered nodes at country scale. It is also possible to check the production (Figure 2) and past and future forecasts for individual nodes. This demonstrator serves as a pilot for future industrial collaborations with meteorological service providers and energy compagnies.

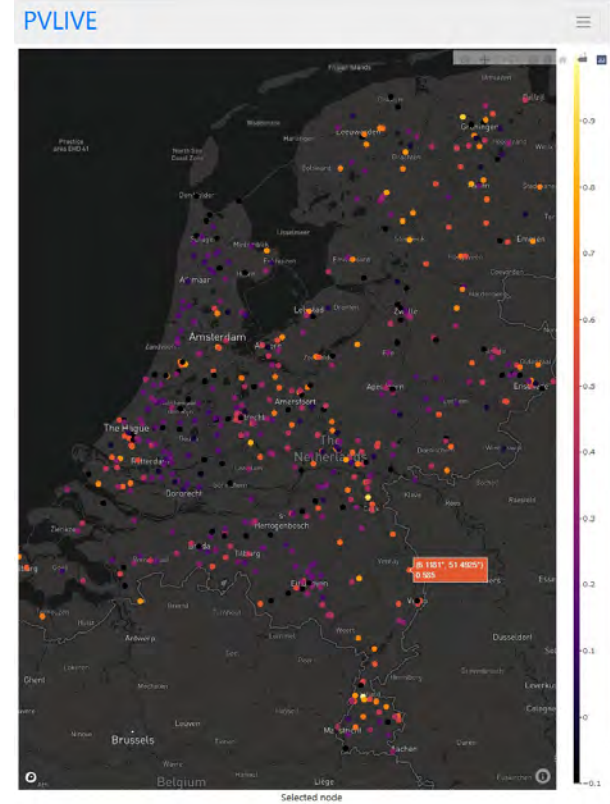


Figure 1: Map of instantaneous production levels from participating PV systems across the Netherlands.

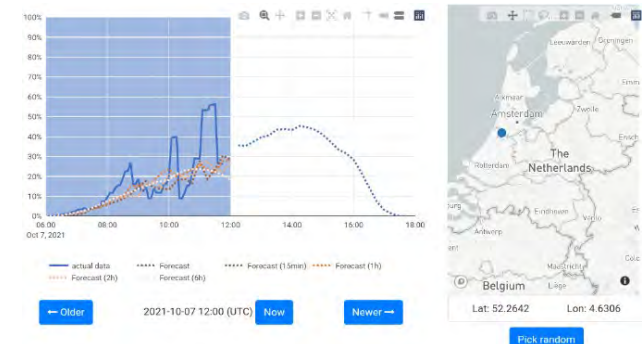


Figure 2: Past production, past and actual forecasts for an individual photovoltaic installation displayed on the web interface.

[1] Swiss Federal Office of Energy SFOE, "Electricity production plants", opendata.swiss, 29 September 2021, <https://opendata.swiss/en/dataset/elektrizitätsproduktionsanlagen>

[2] R. E. Carrillo, *et al.*, High-resolution PV forecasting from imperfect data: a graph-based solution, *Energies*, 13(21), 2020.

[3] J. Simenuovic, *et al.*, Spatio-temporal graph neural networks for multi-site PV power forecasting, 2021, submitted, <https://arxiv.org/abs/2107.13875>.

# A Control Software for Air Handling Units in Commercial Buildings

T. Gorecki, Y. Stauffer, R. E. Carillo, B. Schubnel

CSEM has developed a software solution to manage comfort and energy consumption in air handling units in buildings. It implements a predictive control approach where weather forecasts are used in combination with prediction models for the air handling unit and building to determine in real time the best strategy to heat, cool and manage air humidity in buildings. This solution was deployed in two air handling units in the CSEM headquarter building and energy savings of about 10% have been obtained together with dramatic comfort improvements in summer.



Following trends in other countries, a growing proportion of commercial buildings in Switzerland are equipped with air-based heating and cooling systems. The management of heating and cooling systems with advanced controlled techniques such as Model Predictive Control (MPC) has been widely reported to offer large saving potential without deteriorating the indoor comfort. However, adoption in industrial solutions has been slow. This can be attributed to multiple factors, first and foremost the high costs associated with designing an MPC controller for a new building<sup>[1]</sup>.

In the framework of the European project INDIGO (grant agreement no. 696098), CSEM has developed methodology and software to efficiently design MPC controllers for air handling units in building HVAC systems. This development integrates within a larger framework which optimizes the operation of district cooling networks but has the potential to be replicated to any building with an air-based heating/cooling system.

The software implements an MPC algorithm, which uses a model of the building to predict its future heating/cooling needs based on weather forecasts for a window of one day and optimizes the system supply air humidity and temperature setpoints periodically based on collected measurements. In addition, it maintains comfort inside the building by enforcing constraints on indoor temperature and relative humidity.

The main originality of the work conducted is in the model of the system. Indeed, we use a method that can efficiently rely on available historic data from a building management system, complemented by a short experimental period of about one week to test the system in regimes that are usually not explored in the regular operation of the system. The model construction is data-driven and can exploit system data, as well as simulation data

from a model, but without requiring it (availability of a simulation model is known to be a big hurdle to MPC deployment in the field). However, the model structure is inspired by physical intuition and combines two sub-models, one for the room temperature and humidity dynamics and one for the air handling unit behavior.

The software developed by CSEM includes routines to identify and prepare the building model, as well as estimation and optimization code to execute the MPC algorithm in real time.

The software has been deployed in part of the CSEM's headquarters building in Neuchatel, controlling temperature setpoints of two air handling units serving meeting rooms. On this site it was demonstrated that the MPC could generate 10% of cooling energy savings at equivalent comfort in average conditions, by successfully timing the cooling based on operating hours of the building. On the hottest days of the year, the MPC could improve comfort dramatically (tenfold based on our comfort metrics) since the default controller was not able to provide comfortable conditions during the day, only at the expense of a small (about 10%) energy consumption increase. This kind of issue is not rare in traditional rule-based controllers that need to be manually tuned in different conditions, a task often overlooked or simply impossible to perform efficiently due to the lack of appropriate tools available to the facility management staff. The MPC offers the intelligence required to reduce the need for manual tuning of the controller.

In addition, while the savings remain modest in this case, it was shown that additional control of humidity setpoints could allow savings of energy of up to 50% on a simulated building. This very promising figure still needs to be confirmed in the field.

Another advantage toward large-scale replication: our software interfaces with standard BMS protocols (bacnet) and relies on measurements and actuators that are standard and therefore do not require any hardware adaptation.

This work increases confidence in the possibility to achieve wide deployment of MPC in buildings, realizing the promise of higher efficiency thanks to advanced control. The adoption of MPC is expected to be a long process as the building industry is conservative and moves slowly. We are therefore looking for established players on the BMS or HVAC market to partner and further advance the solution developed in the frame of the INDIGO project.

<sup>[1]</sup> D. Sturzenegger, et al., "Model Predictive Climate Control of a Swiss Office Building: Implementation, Results, and Cost-Benefit Analysis", in IEEE Transactions on Control Systems Technology, vol. 24, no. 1, pp. 1-12, Jan. 2016.

# Battery Energy Storage for Optimal Renewable Power Trading

C. Brivio, P.-J. Alet, A. Hutter

CSEM has developed a battery model for Lithium Titanate cells that is suitable for energy simulation purposes to analyze battery usage for optimization of wind park operation. The project challenge has been to find a correct compromise between the model complexity – its capability to represents the non-linear electrochemical behaviors – and the computational effort required for the simulations. The model is of semi-empirical type, based on a simplification of standard electrical circuit models (ECM). The battery model developed at CSEM has been included into a wind park optimization process, which measures the added value in terms of imbalance penalty reduction and the financial return from selling the renewable power into the market. Out of the six outlined optimization strategies, two showed promising results whereby a storage owner can increase the financial return of the wind park.

The general objective of the project BESTRADE (battery energy storage for optimal renewable power trading) was to expand the knowledge about the impact of battery energy storage onto the power grid. This objective is achieved by investigating the opportunity to alleviate the financial impact of renewable energy production intermittency via the use of batteries. The specific objectives were: (i) to model the real-time behavior of a specific battery chemistry and (ii) to assess the financial value that such battery storage can bring when used in the dispatch of a wind park. For this purpose, CSEM and implementation partners Samawatt SA and Lechanché SA shared their knowledge: Leclanché as provider of LTO (lithium-titanate chemistry) cells, CSEM as producer of the battery model and SAMAWATT as the user of the model to run optimization strategies.

As regards of the first objective, CSEM faced the challenge to develop a computationally effective model to be used for long-lasting energy simulation purposes (i.e., wind park optimization analyses), without sacrificing the capability of the model itself to represent the non-linear behaviors of any battery cell. The modelling approach used for the purpose was a semi-empirical model based on a simplification of standard ECM. Specifically, a two-element ECM was chosen that includes:

- A voltage source to model the energy capabilities of the cell and to compute/update the state of charge (SoC);
- A polarization resistance to model the power capabilities and to estimate the cell overpotential in regime conditions.

Moreover, capacity fade and power fade mechanisms were also included to account for State-of-Health (SoH, i.e., capacity decrease) and State-of-Resistance (SoR, i.e., resistance increase).

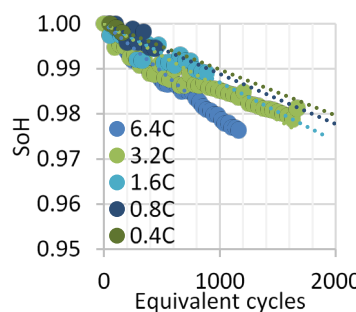


Figure 1: LTO cells under tests, and aging tests results.

The model was based on an extensive battery testing campaign carried out in two different laboratories: the energy system lab at CSEM in Neuchâtel and the Energy Storage Research Center (ESReC) in Biel (Figure 1-left).

Different testing protocols have been developed to determine the model parameters. Specifically: (i) the OCV characterization tests to derive look-up table which links the open circuit voltage with the SoC; (ii) the efficiency characterization tests to derive

the polarization resistance parameters as function of the current rate and SoC; and (iii) aging tests to determine the parameters of the SoH model (Figure 1-right) and SoR model a as function of the equivalent cycles and current rates.

The developed cell model has been scaled-up to a system level by using a per-unit approach (i.e., the power/energy ratio is preserved), implemented into Matlab script and used to run simulations. The model performance was respecting the limitation of execution time below 4s for a 24h scenario evaluation set at the beginning of the project.

As regards of the second objective, a portfolio of wind parks with a capacity of 30 MW has been used as reference scenario with an imbalance account of about 20% of the total parks capacity for a given hour. Several dispatching strategies (i.e., the battery charging/discharging signals) have been tested, from simple ones to the proprietary ones (Figure 2). The results show that simple strategies such as deviation correction, or peak/off-peak arbitrage are not profitable unless the battery storage cost drops below €150/kWh. On the contrary, more sophisticated strategies, such as stochastic optimization, proved to have a competitive advantage and could lead to a profitable outcome in the current market conditions.

The BESTRADE outcomes open room for future improvements as enhancing the imbalance price prediction model and combining it with the stochastic optimization to extract higher financial value for the wind park and battery owner.

Strat.	Storage (MWh)	Imbalance (MWh)	Imbalance P&L (€)	Day-ahead P&L (€)	Total P&L (€)	Baseline P&L (€)	Battery revenue (€)	Cycle count	Cost per cycle (€)	Battery Cost, €	Battery Profit (€)
a.	0	5,862	-81,177	1,204,749	1,123,561	1,123,561	-	-	-	-	-
a.	0.3	5,674	-79,259	1,204,749	1,125,489	1,123,561	1,928	351	11	3,685	-1,757
a.	0.5	5,571	-78,401	1,204,749	1,126,347	1,123,561	2,786	331	18	5,787	-3,001
a.	1	5,366	-76,896	1,204,749	1,127,553	1,123,561	4,292	288	35	10,081	-5,789
a.	3.5	4,693	-75,123	1,204,749	1,129,626	1,123,561	6,064	234	123	28,708	-22,643
a.	7	4,104	-77,630	1,204,749	1,127,110	1,123,561	3,549	217	245	53,101	-49,552
b.	0.3	5,932	-53,280	1,204,749	1,151,469	1,123,561	27,908	1,829	11	19,204	8,704
b.	0.5	6,082	-34,682	1,204,749	1,170,067	1,123,561	46,506	1,829	18	32,007	14,499
b.	1	6,788	-11,814	1,204,749	1,216,562	1,123,561	93,001	1,829	36	64,013	28,988
b.	3.5	13,252	244,291	1,204,749	1,449,039	1,123,561	325,478	1,829	123	224,047	101,431
b.	7	23,977	569,759	1,204,749	1,774,507	1,123,561	850,946	1,829	245	448,094	202,852
c.	0.3	5,913	-78,054	1,204,749	1,126,694	1,123,561	3,133	858	11	9,005	-5,872
c.	0.5	5,996	-75,973	1,204,749	1,128,776	1,123,561	5,215	858	18	15,009	-9,794
c.	1	6,359	-70,768	1,204,749	1,133,880	1,123,561	10,419	858	35	30,017	-19,598
d.	0.3	5,862	-81,177	1,206,178	1,125,001	1,123,561	1,440	248	11	2,608	-1,168
d.	0.5	5,862	-81,177	1,207,131	1,125,954	1,123,561	2,392	248	18	4,347	-1,954
d.	1	5,862	-81,177	1,209,513	1,128,336	1,123,561	4,774	248	35	8,693	-3,919
e.	0	5,862	-81,187	1,204,749	1,123,561	1,123,561	-	-	-	-	-
e.	0.3	6,392	-59,008	1,204,749	1,145,743	1,123,561	22,182	2,748	11	28,852	-6,670
e.	0.5	7,107	-44,217	1,204,749	1,160,531	1,123,561	36,970	2,748	18	48,087	-11,117
e.	1	9,288	-7,247	1,204,749	1,197,502	1,123,561	73,940	2,748	35	96,175	-22,234
e.	7	37,515	436,395	1,204,749	1,641,143	1,123,561	517,582	2,748	245	673,222	-155,640
f.	0.3	6,254	-71,493	1,204,749	1,133,256	1,123,561	9,695	312	11	3,277	6,417
f.	0.5	6,293	-65,031	1,204,749	1,139,718	1,123,561	16,157	312	18	5,462	10,695
f.	0.7	6,338	-58,573	1,204,749	1,146,176	1,123,561	22,614	312	25	7,647	14,967
f.	1	6,627	-48,884	1,204,749	1,155,864	1,123,561	32,303	312	38	10,924	21,379
f.	7	37,982	144,914	1,204,749	1,349,663	1,123,561	226,102	312	245	76,469	149,632

Figure 2: Wind park optimization strategies and results.

The BESTRADE project has received funding from Innosuisse under grant agreement no. 29605.1 IP-EE.

# Battery Accelerated Testing for Second-Life Li-ion Cells

P. Iurilli, C. Brivio, A. Hutter

Within the BAT4SEL<sup>[1]</sup> project, CSEM verified the validity of an accelerated testing procedure to estimate the State of Health (SoH) of second-life Li-ion cells (i.e. used Li-ion cells) with no prior knowledge of their use cases. The project objective was to give a statistical quantification of the trade-off between the SoH estimation precision and the required testing time to obtain this estimation; for this reason, a statistically representative number of samples from e-bike applications was provided to CSEM from project partner Libatton GmbH. The testing analysis was based on four selected technologies of cathode chemistries (NMC and NCA). Three types of indicators were applied (resistance-based, efficiency-based and EIS-based indicators) at different testing conditions. The results obtained were promising: testing time can be reduced up to 98% with an estimation error below 3% with respect to reference tests. Several routes of exploitations are under investigation.

Second-life applications of Li-ion cells will allow for a more sustainable battery value chain. After the first-life application, specific procedures that qualify the residual energetic value of the cell and/or module are needed. Such procedures should be fast enough not to create high additional cost for the second life repurposing entity. CSEM developed different fast testing procedures to find suitable proxies (i.e., indirect indicators) which can satisfy the two following KPIs: affordable testing time per cell and acceptable SoH estimation error (mean error and standard deviation). The whole testing campaign was based on 523 cylindrical cells (18650 format, Figure 1) of four selected technologies: LG Chem MJ1 (NMC, type A), Sony VC7 (NCA, type B), Sanyo Panasonic GA (NCA, type C), and Sony NC1 (NMC, type D).

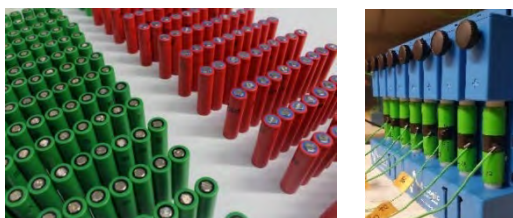


Figure 1: Used Li-ion cells (left); cells under test (right).

## Procedure and methodology

The testing methodology was based on two different sub-sets of tests: (i) diagnostic tests, where a representative sample of cells were characterized to find existing correlations between developed proxies and SoH and (ii) validation tests, where a large number of samples were tested to validate the protocols by comparison of the estimated and measured SoH values. Diagnostic and validation protocols were obtained by combining different testing phases (Figure 2):

- Phase A: resistance, efficiency and EIS measurements at random voltage (i.e., the voltage at which the cell was received)
- Phase B: full cycle for capacity/SoH measurement
- Phase C: same as Phase A, but at fixed voltage of 3.6 V

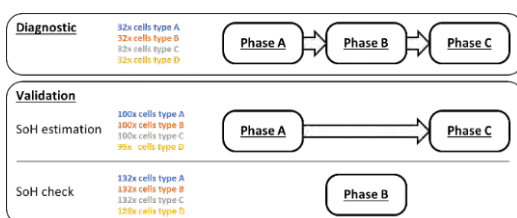


Figure 2: Combination of testing phases for diagnostic and validation.

Three main types of indicators were applied: resistance-based indicators (R-based), efficiency-based indicators (EE-based) and

EIS (impedance)-based indicators. Moreover, the correlation assessment was verified for three different testing conditions: (i) random voltage condition (i.e., testing samples at different SoC, as received); (ii) nominal voltage condition (i.e., testing samples at same SoC), and (iii) random voltage post-triage (i.e., after filtering out the cells which were outside a specific SoC interval).

## Diagnostic and validation tests results

The results of diagnostic tests showed that each proxy has its own advantage and that experiments at random SoC rarely provide a satisfactory correlation, it is hence better to discard overcharged or over-discharged cells. This was also confirmed by the validation tests where such filtering triage improved the SoH estimation of almost 20% while reducing its standard deviation. As regards the indicators, R-based indicators provided an average estimation error below 2.5%, efficiency-based indicators provided a stable estimation error around 2%, while EIS(impedance)-based indicators showed slightly higher estimation errors around 3% but lower standard deviation. The developed proxies obtained testing time of maximum 1 hour (EIS-based) down to few minutes (R-based), with a time reduction from 75% to 98% compared to standard capacity test.

## Remarks and outlook

Overall, the BAT4SEL project confirmed the validity of the accelerated testing approach developed by CSEM with the following remarks:

- A pre-triage process is a good practice before qualifying second-life cells.
- The characterization process takes 1 month per technology.
- Precision and accuracy of the testing equipment will influence the results.
- There is not the best proxy for all the different technologies. User should choose according to his/her needs regarding accuracy, robustness, available testing time, or testing machine applicability.
- Results are technology dependent, and no guarantee can be made that the investigated results will provide positive results for all technologies, adaptations might be required.

The main exploitation routes for the BAT4SEL estimation algorithm are the following: (i) to implement it into existing testing machine; (ii) to verify its applicability also at battery module level; (iii) to implement it into current or future BMSs for second-life applications. The BAT4SEL project was funded from the Swiss Federal Office of Energy under contract SI/502046-01.

[1] <https://www.aramis.admin.ch/Texte/?ProjectID=47023>

# Impact of Vehicle-to-Grid Service Provision on Batteries

S. Bhoir, C. Brivio, A. Hutter

A battery model was developed to analyze the degradation in the battery of an electric vehicle (EV) due to the provision of vehicle-to-grid (V2G) services. The model was coded in a python script so that simulations of an EV, that regularly performed V2G services, could be performed. The insights gained from these simulations assisted in the techno-economic analysis of a case study, wherein a company installs V2G chargers at its premises to profit from its employees' EVs by either providing ancillary services to the grid or by peak shaving. Three types of V2G services were simulated and the results showed that two of them had a reasonable payback period for the company, under the given conditions.

CSEM was asked to carry out a study under the frame of the InterReg RegEnergy project, where Planair S.A., Greenmotion S.A., and Groupe Renault are analyzing the integration of PVs and EVs at the Y-Parc technological park in Yverdon-les-Bains. The primary objective of the V2G study was to analyze the impact of V2G service provision on the Li-ion battery of an EV. In pursuit of this objective (i) an extensive literature review on V2G installations in Europe and the effect of V2G service provision on batteries was performed, (ii) a model to compute the amount of degradation a battery underwent, based on its usage profile, was developed, and (iii) this model was used to perform a techno-economic analysis of degradation in the battery of an EV that provided various V2G services.

The battery model developed consisted of two parts, (i) a battery dynamics model and (ii) a battery degradation model. The dynamics model includes the voltage, internal resistance, and the state of charge (SoC) change during charging and discharging phases. It was based on a simple equivalent circuit model consisting of a voltage source (which varied as a function of the SoC) and a variable resistor (which varied with the SoC and temperature). The degradation model described the calendar and cycle aging that the battery would undergo during its lifetime, thus accounting for the state of health (SoH) decrease. It was based on a semi-empirical stress factor model. The calendar aging was modelled to be dependent upon the storage SoC and temperature while cycle aging was dependent on the current rate (C-rate), temperature, average SoC and depth of discharge (DoD) during cycling. The state of resistance (SoR) increase was also modelled in a similar fashion with it being dependent on the C-rate, average SoC and DoD during cycling. The decrease in SoH and increase in SoR accounted for the capacity fade and power fade in the battery, respectively.

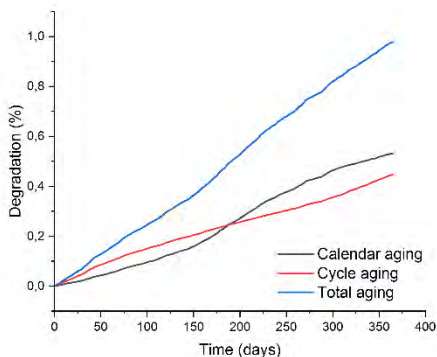


Figure 1: Illustration of the output of the degradation model.

The parameters for the model were derived using data from experiments performed on Li-ion NMC cells within the energy system lab at CSEM in Neuchâtel and the Energy Storage Research Center (ESReC) in Biel/Bienne. These experiments included Galvanostatic Intermittent Titration Technique (GITT)

tests to obtain the relation between the open circuit voltage (OCV) and SoC, and Electrochemical Impedance Spectroscopy (EIS) measurements to derive a relation between the resistance of a cell, its temperature, and SoC. The parameters for the degradation model were obtained by performing battery aging experiments at different temperatures, DoDs and C-rates.

The above model was coded in a python script, which takes the battery usage profile, number of days to be simulated, battery size, etc. as inputs and output the battery degradation over the simulated period. An example of the output is shown in Figure 1.

The model developed was used for a techno-economic analysis for a case study described as follows: A company planned to install V2G chargers at its premises so that it can use the employees' EVs to provide V2G services such as frequency containment reserve (FCR) or perform peak shaving (PS) to earn revenue or save costs, respectively. The challenge was to compute the degradation in the battery due to the V2G provision and, thereby, decide upon the amount of compensation to be given to the employees that will incentivize them to participate in this program. Finally, an evaluation of whether this was a profitable venture had to be carried out. Three scenarios were simulated wherein: (i) only FCR was provided [FCR] (ii) only PS was performed [PS] and (iii) FCR was provided simultaneously together with PS [FCR+PS]. The techno-economic analysis of the scenarios showed that considering a 12 kW charger costing CHF 1'000.-, the FCR scenario was not profitable. However, if the cost of the charger dropped to lesser than CHF 300.-, this scenario becomes more interesting. On the other side, the PS and FCR+PS scenarios are profitable after a payback period of 6 and 8 years, respectively, as shown in Figure 2.

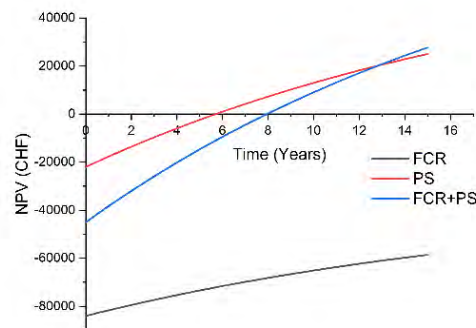


Figure 2: NPV evaluation for the 3 simulated scenarios.

CSEM and RegEnergy partners are now in discussion on how to best profit from the project results in the light of the Y-Parc V2G implementation plans. On CSEM side, next steps will be to: (i) publish the developed simulation model, and (ii) to improve it in the frame of the IEA annex 32 initiative, in which CSEM aims at developing an open-source tool to estimate the degradation impact on Li-ion batteries from different applications.

# ANNEXES

## Publications

- [1] Aderneuer, T.; Fernández, O.; Ferrini, R., "Two-photon grayscale lithography for free-form micro-optical arrays", *Optics Express*, vol. 29 (24), pp. 39511-39520, 44501
- [2] Aderneuer, T.; Fernandez, O.; Karpik, A.; Werder, J.; Marhöfer, M.; Kristiansen, P. M.; Ferrini, R., "Surface topology and functionality of freeform microlens arrays", *Optics Express*, vol. 29 (4), pp. 5033-5042, 44228
- [3] Andreatta, G. A. L.; Blondiaux, N.; Gay, J.; Unterhofer, S.; Lachowicz, A.; Faes, A., "Spray coating vs. immersion for self-assembly of gemini perfluorinated phosphonic acids on indium tin oxide", *Thin Solid Films*, vol. 732, pp. 138783, 44409
- [4] Andreeva, E.; Bhati, A. S.; Preneel, B.; Vizár, D., "1, 2, 3, Fork: Counter Mode Variants based on a Generalized Forkcipher", *IACR Transactions on Symmetric Cryptology*, vol. 2021 (3), pp. 1-35, 44440
- [5] Blaga, C.; Christmann, G.; Boccard, M.; Ballif, C.; Nicolay, S.; Kamino, B. A., "Palliating the efficiency loss due to shunting in perovskite/silicon tandem solar cells through modifying the resistive properties of the recombination junction", *Sustain. Energy Fuels*, vol. 5, pp. 2036-2045, 44197
- [6] Borque Gallego, G., "Performance and Micro-Vibrations in Magnetic Bearings for Space Actuators", Lausanne (Switzerland), EPFL, 2021
- [7] Borque Gallego, G.; Rossini, L.; Achtnich, T.; Martins Araujo, D.; Perriard, Y., "Efficiency Optimisation of Slotless Magnetic Bearing Machines", *IEEE Transactions on Industry Applications*, vol. 57 (6), pp. 6833-6843, 2021, doi:10.1109/TIA.2021.3072614
- [8] Borque Gallego, G.; Rossini, L.; Achtnich, T.; Martins Araujo, D.; Perriard, Y., "Novel Generalised Notch Filter for Harmonic Vibration Suppression in Magnetic Bearing Systems", *IEEE Transactions on Industry Applications*, vol. 57 (6), pp. 6977-6987, 2021, doi:10.1109/TIA.2021.3062587
- [9] Carrillo, R. E.; Leblanc, M.; Schubnel, B.; Langou, R.; Topfel, C.; Alet, P.-J., "High-Resolution PV Forecasting from Imperfect Data: A Graph-Based Solution", [www.mdpi.com](http://www.mdpi.com), vol. 13, pp. 5763, 44197
- [10] Cattin, J.; Petri, D.; Geissbühler, J.; Despeisse, M.; Ballif, C.; Boccard, M., "Transferability of the light-soaking benefits on silicon heterojunction cells to modules", Cornwell University, *Applied Physics*, 44378, <https://arxiv.org/abs/2107.00293v2>
- [11] Chicco, F.; Cerida Rengifo, S.; Pengg, F. X.; Le Roux, E.; Enz, C. C., "Power-Optimized Digitally Controlled Oscillator in 28-nm CMOS for Low-Power FMCW Radars", *IEEE Microwave and Wireless Components Letters*, vol. 31 (8), pp. 965 - 968, 44409
- [12] Chin, S.; Mitev, V.; Giraud, E.; Maulini, R.; Blaser, S.; Boiko, D. L., "Electrically driven frequency blue-chirped emission in Fabry-Perot cavity quantum cascade laser at room temperature", *Appl. Phys. Lett.*, vol. 118, pp. 021108, 44197
- [13] Degott, J.; Ghajarzadeh-Wurzner, A.; Hofmann, G.; Proença, M.; Bonnier, G.; Lemkaddem, A.; Lemay, M.; Christen, U.; Knebel, J. F.; Durgnat, V.; Burnier, M.; Wuerzner, G.; Schoettker, P., "Smartphone based blood pressure measurement: accuracy of the OptiBP mobile application according to the AAMI/ESH/ISO universal validation protocol", *Blood Pressure Monitoring*, 26(6), pp. 441-448, 44348, doi:10.1097/MBP.0000000000000556
- [14] Fairbrother, A.; Quest, H.; Özkalay, E.; Wälchli, P.; Friesen, G.; Ballif, C.; Virtuani, A., "Long-term performance and shade detection in building integrated photovoltaic systems", *Solar Rrl*, vol. 21005832100583, 44470, doi:10.1002/solr.202100583
- [15] Fébba, D.; Paratte, V.; Antognini, L.; Dréon, J.; Hurni, J.; Thomet, J.; Rubinger, R.; Bortoni, E.; Ballif, C.; Boccard, M., "Effects of Work Function and Electron Affinity on the Performance of Carrier-Selective Contacts in Silicon Solar Cells Using ZnSn<sub>x</sub>Ge<sub>1-x</sub>N<sub>2</sub> as a Case Study", *IEEE Journal of Photovoltaics*, vol. 11, pp. 1350-1357, 44440
- [16] Gajic, A.; Radovanovic, J.; Vukovic, N.; Milanovic, V.; Boiko, D. L., "Theoretical approach to quantum cascade micro-laser broadband multimode emission in strong magnetic fields", *Physics Letters A*, vol. 387, pp. 127007, 44197
- [17] Geissbühler, J.; Allebé, C.; Badel, N.; Wyss, P., "Advanced method for electrical characterization of carrier-selective passivating contacts using transfer-lengthmethod measurements under variable illumination", *Journal of Applied Physics*, vol. 129 (19), 19570, 44287, doi:10.1063/5.0042854
- [18] Gjiriti, E.; Reyhanitabar, R.; Vizár, D., "Power Yoga: Variable-Stretch Security of CCM for Energy-Efficient Lightweight IoT", *IACR Transactions on Symmetric Cryptology*, vol. 2021 (2), pp. 446-468, 44348
- [19] Guesnay, Q.; Sahli, F.; Ballif, C.; Jeangros, Q., "Vapor deposition of metal halide perovskite thin films: Process control strategies to shape layer properties", *APL Materials*, vol. 9, pp. 100703, 44470

- [20] Honzátko, D.; Türetken, E.; Bigdeli, S. A.; Dunbar, L. A., "Defect segmentation for multi-illumination quality control systems", *Machine Vision and Applications*, vol. 32 (6), pp. 118, 44440
- [21] Iurilli, P.; Brivio, C.; Wood, V., "On the use of electrochemical impedance spectroscopy to characterize and model the aging phenomena of lithium-ion batteries: a critical review", *Journal of Power Sources*, vol. 505, pp. 229860, 44197
- [22] Jafari, S.; Guercetti, J.; Geballa-Koukoula, A.; Tsagkaris, A. S.; Nelis, J. L. D.; -Pilar Marco, M.; Salvador, J.-P.; Gerssen, A.; Hajslova, J.; Elliott, C.; Campbell, K.; Migliorelli, D.; Burr, L.; Generelli, S.; Nielsen, M. W. F.; Sturla, S. J., "ASSURED Point-of-Need Food Safety Screening: A Critical Assessment of Portable Food Analyzers", *Foods*, vol. 10 (6), pp. 1339, 44348, doi:10.3390/foods10061399
- [23] Jokic, P.; Emery, S; Benini, L., "NN2CAM: Automated Neural Network Mapping for Multi-Precision Edge Processing on FPGA-Based Cameras", arXiv:2106.12840, June 2021.
- [24] Klumpp, M.; Hintze, M.; Immonen, M.; Ródenas-Rigla, F.; Pilati, F.; Aparicio-Martínez, F.; Çelebi, D.; Liebig, T.; Jirstrand, M.; Urbann, O.; Hedman, M.; Lipponen, J. A.; Bicciato, S.; Radan, A.-P.; Valdivieso, B.; Thronicke, W.; Gunopoulos, D.; Delgado-Gonzalo, R., "Artificial Intelligence for Hospital Health Care: Application Cases and Answers to Challenges in European Hospitals", *Healthcare*, vol. 9 (8), pp. 961, 2021-07-29, doi:10.3390/healthcare9080961
- [25] Nardin, G.; Domínguez, C.; Aguilar, Á. F.; Anglade, L.; Duchemin, M.; Schuppisser, D.; Gerlich, F.; Ackermann, M.; Coulot, L.; Cuénod, B.; Petri, D.; Niquelle, X.; Badel, N.; Lachowicz, A.; Despeisse, M.; Levrat, J.; Ballif, C.; Askins, S.; Núñez, R.; Jost, N.; Vallerotto, G., "Industrialization of hybrid Si/III-V and translucent planar micro-tracking modules", *Progress in Photovoltaics: Research and Applications*, vol. 29, pp. 819-834, 44197
- [26] Nelis, J. L. D.; Migliorelli, D.; Mühlbach, L.; Generelli, S.; Stewart, L.; Elliott, C. T.; Campbell, K., "Highly sensitive electrochemical detection of the marine toxins okadaic acid and domoic acid with carbon black modified screen printed electrodes", *Talanta*, vol. 228, 44228, doi:10.1016/j.talanta.2021.122215
- [27] Obrzud, E.; Denis, S.; Sattari, H.; Choong, G.; Kundermann, S.; Dubochet, O.; Despont, M.; Lecomte, S.; Ghadimi, A. H.; Brasch, V., "Stable and compact RF-to-optical link using lithium niobate on insulator waveguides", *APL Photonics*, vol. 6 (12), pp. 121303, 2021-12-01, doi:10.1063/5.0070103
- [28] Peters, R.; Elbers, I.; Undas, A.; Sijtsma, E.; Briffa, S.; Carnell-Morris, P.; Siupa, A.; Yoon, T.-H.; Burr, L.; Schmid, D.; Tentschert, J.; Hachenberger, Y.; Jungnickel, H.; Luch, A.; Meier, F.; Radnik, J.; Hodoroaba, V.-D.; Lynch, I.; Valsami-Jones, E., "Benchmarking the ACEnano Toolbox for Characterisation of Nanoparticle Size and Concentration by Interlaboratory Comparisons", *Molecules*, vol. (26), pp. 5315, 44348
- [29] Prosa, M.; Benvenuti, E.; Kallweit, D.; Pellacani, P.; Törker, M.; Bolognesi, M.; Lopez-Sanchez, L.; Ragona, V.; Marabelli, F.; Toffanin, S., "Organic Light-Emitting Transistors in a Smart-Integrated System for Plasmonic-Based Sensing", *Advanced Functional Materials*, 31, 2104927, 44409, doi:10.1002/adfm.202104927
- [30] Scharnhorst, P.; Schubnel, B.; Boegli, M.; Gorecki, T.; Stauffer, Y.; Fernández Bandera, C.; Salom, J.; Taddeo, P.; Peppas, A.; Politi, C., "Energym: a Building Model Library for Controller Benchmarking", *Applied Sciences*, vol. 11 (8), pp. 3518, 44197
- [31] Schindler, K. A.; Nef, T.; Baud, M. O.; Tzovara, A.; Yilmaz, G.; Tinkhauser, G.; Gerber, S. M.; Gnarra, O.; Warncke, J. D.; Schütz, N.; Knobel, S. E. J.; Schmidt, M. H.; Krack, P.; Fröhlich, F.; Sznitman, R.; Rothen, S.; Bassetti, C. L. A., "NeuroTec Sitem-Insel Bern: Closing the Last Mile in Neurology", *Clinical and Translational Neuroscience*, vol. 5 (2), pp. 13, 2021-09, doi:10.3390/ctn5020013
- [32] Sepehri, Y.; Pad, P.; Frossard, P.; Dunbar, L. A., "Privacy-Preserving Image Acquisition Using Trainable Optical Kernel", arXiv:2106.14577, June 2021.
- [33] Stauffer, Y.; Hutter, A.; Carrillo, R. E.; Saba, F.; Boegli, M.; Malengo, A., "Smart sensors network for accurate indirect heat accounting in apartment", *Journal of Building Engineering*, vol. 103534, pp., 44470, doi:10.1016/j.jobe.2021.103534
- [34] Tang, Y.; Gao, H.; Kurth, F.; Burr, L.; Petropoulos, K.; Migliorelli, D.; Guenat, O. T.; Generelli, S., "Nanocellulose aerogel inserts for quantitative lateral flow immunoassays", *Biosensors and Bioelectronics*, vol. 192, pp. 113491, 44501
- [35] Tuomiranta, A.; Alet, P.-J.; Ballif, C.; Ghedira, H., "Worldwide performance evaluation of ground surface reflectance models", *Solar Energy*, vol. 224, pp. 1063-1078, 44197
- [36] Zuncheddu, D.; Della Bella, E.; Schwab, A.; Petta, D.; Rocchitta, G.; Generelli, S.; Kurth, F.; Parrilli, A.; Verrier, S.; Rau, J. V.; Fosca, M.; Maioli, M.; Serra, P-A.; Alini, M.; Redl, H.; Grad, S.; Basoli, V., "Quality control methods in musculoskeletal tissue engineering: from imaging to biosensors", *Bone Research*, vol. 9 (46), pp. 1-26, 44470

## Proceedings

- [1] Aguet, C; *et al.*, "Feature Learning for Blood Pressure Estimation from Photoplethysmography", 2021 43rd Annual International Conference of the IEEE Engineering in Medicine & Biology Society (EMBC), 2021, pp. 463-466, doi:10.1109/EMBC46164.2021.9630665
- [2] Ahuja, A.; Badami, K.; Barbelenet, C.; Emery, S., "Comparison of Capacitive DAC Architectures for Power and Area Efficient SAR ADC Designs", 2021 IEEE International Symposium on Circuits and Systems (ISCAS), pp. 1-5, 44317, doi:10.1109/ISCAS51556.2021.9401768
- [3] Badami, K.; Pons-Sole, M.; Azarkhish, E.; Fivaz, A.; Rapin, M.; Chételat, O.; Emery, S., "Single-Battery Cooperative Sensors for Multi-Lead Long Term Ambulatory ECG Measurement", 2021 IEEE Biomedical Circuits and Systems Conference (BioCAS), 2021, pp. 1-4, 2021-10, doi:10.1109/BioCAS49922.2021.9644935
- [4] Benedito, O.; Delgado-Gonzalo, R.; Schiavoni, V., "KeVlar-Tz: A Secure Cache for Arm TrustZone: (Practical Experience Report)", DAIS'21, Valletta (Malta), pp. 109-124, 2021-06-14
- [5] Bennet, F.; Schmid, D.; Hodoroaba, V.-D.; Burr, L., "Towards a method for quantitative evaluation of nanoparticle from suspensions via microarray printing and SEM analysis", Journal of Physics: Conference Series 1953, 012002, 44197, doi:10.1088/1742-6596/1953/1/012002
- [6] Berguerand, R.; Bergamini, L.; Dallemande, P.; Franzi, E., "Integration of the ultra-low power WiseMAC with the μ111 Real Time Operating System: a performance evaluation", 17th International Conference on Wireless and Mobile Computing, Networking and Communications (WiMob), 2021, pp. 301-306, 2021-09, doi:10.1109/WiMob52687.2021.9606309
- [7] Biggio, L.; Bendinelli, T.; Neitz, A.; Lucchi, A.; Parascandolo, G., "Neural Symbolic Regression that scales", in 38th International Conference on Machine Learning (ICML) 2021, 44378, <https://arxiv.org/abs/2106.06427>
- [8] Biggio, L.; Kastanis, I., "Self-supervised pre-training on industrial time-series", 2021 8th Swiss Conference on Data Science (SDS), 2021, pp. 56-57, 44348, doi:<https://doi.org/10.1109/SDS51136.2021.00018>
- [9] Biggio, L.; Wieland, A.; Chao, M. A.; Kastanis, I.; Fink, O., "Uncertainty-Aware Prognosis via Deep Gaussian Process", IEEE Access, vol. 9, pp. 123517-123527, 2021, doi: 10.1109/ACCESS.2021.3110049.
- [10] Blondiaux, N.; Diserens, M.; Chauvy, P.-F.; Oudot, B.; Pugin, R., "Manufacturing of hierarchically structured surfaces for decorative applications", in euspen's 21st International Conference & Exhibition, 44348,<https://www.euspen.eu/knowledge-base/ICE21217.pdf>
- [11] Braun, F.; Baty, F.; Van Zaen, J.; Bonnier, G.; Renevey, P.; Theurillat, P.; Proenca, M.; Proust, Y.-M.; Boesch, M.; Schoch, O. D.; Annaheim, S.; Brutsche, M.; Ferrario, D.; Lemay, M., "Towards Unobtrusive Long-Term Monitoring of Sleep Apnea Syndrome", Biomedical Photonics Network, Zurich (Switzerland), 2021-09-12
- [12] Braun, F.; Baty, F.; Van Zaen, J.; Bonnier, G.; Renevey, P.; Theurillat, P.; Proenca, M.; Proust, Y.-M.; Boesch, M.; Schoch, O. D.; Ferrario, D.; Lemay, M.; Annaheim, S.; Brutsche, M., "Multi-Parametric Vital Sign Estimation for Monitoring of Sleep Disordered Breathing", SSP/SST - EFP Joint Annual Conference 2021, (online only), 2021-06-17
- [13] Calvo, E. M.; Renevey, P.; Lemay, M.; Bonetti, A.; Sole, M.; Cattenoz, R.; Emery, S.; Delgado-Gonzalo, R., "Ultra-low-power Physical Activity Classifier for Wearables: From Generic MCUs to ASICs", EMBC 2021, Guadalajara (Mexico), pp. 6978-6981, 2021-11-01, doi:10.1109/EMBC46164.2021.9630154
- [14] Carrillo, R. E.; Schubnel, B.; Simeunovic, J.; Langou, R.; Alet, P.-J., "Spatio-temporal machine learning methods for multi-site PV power forecasting", in IEEE Transactions on Sustainable Energy, 44317, doi:10.1109/TSTE.2021.3125200
- [15] Cerida Rengifo, S.; Chicco, F.; Le Roux, E.; Enz, C. C., "Modulation Scheme Impact on Phase Noise in FMCW Radar for Short-Range Applications", 2021 IEEE International Symposium on Circuits and Systems (ISCAS), pp. 1-4, 44317, doi:10.1109/ISCAS51556.2021.9401757
- [16] Cerida Rengifo, S.; Chicco, F.; Le Roux, E.; Enz, C. C., "An Optimized Low-Power Band-Tuning TX for Short-Range FMCW Radar in 22-nm FDSOI CMOS", IEEE 47th European Solid State Circuits Conference (ESSCIRC), 2021, pp. 467-470, doi:10.1109/ESSCIRC53450.2021.9567815.
- [17] Chicco, F.; Cerida Rengifo, S.; Le Roux, E.; Enz, C. C., "A 60 GHz QDCO with 11 GHz Seamless Tuning for Low-Power FMCW Radars in 22-nm FDSOI", IEEE 47th European Solid State Circuits Conference (ESSCIRC), 2021, pp. 291-294, 2021-09, doi:10.1109/ESSCIRC53450.2021.9567787

- [18] De Ree, M.; Vizár, D.; Mantas, G.; Bastos, J.; Kassapoglou-Faist, C.; Rodriguez, J., "A Key Management Framework to Secure IoMT-enabled Healthcare Systems", IEEE 26th International Workshop on Computer Aided Modeling and Design of Communication Links and Networks (CAMA), 2021, pp. 1-6, 2021-10, doi:10.1109/CAMA52502.2021.9617796
- [19] Faraone, A.; Sigurthorsdottir, H.; Delgado-Gonzalo, R., "Atrial Fibrillation Detection on Low-Power Wearables using Knowledge Distillation", EMBC 2021, Guadalajara (Mexico), pp. 6795-6799, 2021-11-01, doi:10.1109/EMBC46164.2021.9630957
- [20] Fernandez, O.; Aderneuer, T.; Chaves, J.; Ferrini, R., "CAD-based metrology of freeform microlens arrays, FMLAs", in Advanced Fabrication Technologies for Micro/Nano Optics and Photonics XIV, 44256, doi:10.1117/12.2579224
- [21] Ferrini, R., "A new era for free-form micro-optics manufacturing : the final frontier ...", in OSA Optical Design and Fabrication 2021 (Flat Optics, Freeform, IODC, OFT), F. Capasso, W. Chen, P. Dainese, J. Fan, J. DeGroote Nelson, F. Duerr, J. Rogers, J. Rolland, P. Clark, R. Pfisterer, H. Rehn, S. Thibault, M. Jenkins, D. Wook Kim, and N. Trela-McDonald (Eds.), OSA Technical Digest (Optical Society of America, 2021), paper JTU3B.1., 44256, doi:10.1364/FREEFORM.2021.JTU3B.1
- [22] Gaudilliere, P. L.; Sigurthorsdottir, H.; Aguet, C.; Van Zaen, J.; Lemay, M.; Delgado-Gonzalo, R., "Generative Pre-Trained Transformer for Cardiac Abnormality Detection", CinC 2021, Brno (CZ), 2021-09-13
- [23] Gnocchi, L.; Virtuani, A.; Ballif, C., "EVA for Glass/Glass Solar PV Modules: Effect of encapsulant storage conditions and process parameters", 2021 IEEE 48th Photovoltaic Specialists Conference (PVSC), 2021, pp. 2037-2042, 44348, doi:10.1109/PVSC43889.2021.9518442
- [24] Honzátko, D.; Türetken, E.; Fua, P.; Dunbar, L. A., "Leveraging Spatial and Photometric Context for Calibrated Non-Lambertian Photometric Stereo", 2021 International Conference on 3D Vision - 3DV, 44531, <https://arxiv.org/abs/2103.12106v1>
- [25] Iurilli, P.; Brivio, C.; Carrillo, R. E.; Wood, V., "DRT-based modelling framework for Li-ion cells", in 14th International Workshop on Impedance Spectroscopy, pp. 5, 44470
- [26] Jokic, P.; Azarkhish, E.; Cattenoz, R.; Türetken, E.; Benini, L.; Emery, S., "A Sub-mW Dual-Engine ML Inference System-on-Chip for Complete End-to-end Face-Analysis at the Edge", 2021 Symposium on VLSI Circuits, 2021, pp. 1-2, 44348, doi:10.23919/VLSICircuits52068.2021.9492401
- [27] Jokic, P.; Emery, S.; Benini, L., "Battery-Less Face Recognition at the Extreme Edge", 2021 19th IEEE International New Circuits and Systems Conference (NEWCAS), 2021, pp. 1-4, 44348, doi:10.1109/NEWCAS50681.2021.9462787
- [28] Jose James, R.; Spinola Durante, G.; Revol, V.; Marozau, I.; Krasnopski, K.; Fretz, M.; Mohrdiek, S., "Low temperature hermetically sealed, optically transparent miniature packages: from medical to space", 2021 IEEE 71st Electronic Components and Technology Conference (ECTC), 2021, pp. 1673-1681, 2021, doi:10.1109/ECTC32696.2021.00265
- [29] Kiener, L.; Saudan, H.; Novo, D.; Lani, S.; Bernard, G.; Miler, M.; Bilbeau, D., "Slipring rotor made by Additive Manufacturing: redesign, manufacturing and validation testing for space applications", ACTUATOR, (online only), pp. 4, 2021
- [30] Kirschmann, M. A.; Pierer, J.; Steinecker, A.; Schmid, P. A. E.; Erdmann, A., "Plenoptic Inspection System for Automatic Quality Control of MEMS and Microsystems", S. Ratcliff (Ed.): IPAS 2020, IFIP AICT 620, pp. 220–232, 2021, 2021, doi:10.1007/978-3-030-72632-4\_16
- [31] Lachowicz, A.; Andreatta, G.; Blondiaux, N.; Faes, A.; Badel, N.; Diaz Leon, J. J.; Alleb  , C.; Fontaine, C.; Haumesser, P.-H.; Jourdan, J.; Mu  oz, D.; Godard, M.; Darmon, M.; Nicolay, S.; Despeisse, M.; Ballif, C., "Project ameliz: Patterning techniques for copper electroplated metallization on heterojunction solar cells", in AIP Conference Proceedings 2367, 020010, 44197, doi:10.1063/5.0056227
- [32] Lachowicz, A.; Andreatta, G.; Blondiaux, N.; Faes, A.; Diaz Leon, J.; Christmann, G.; Alleb  , C.; Fontaine, C.; Haumesser, P.-H.; Jourdan, J.; Mu  oz, D.; Godard, M.; Darnon, M.; Nicolay, S.; Despeisse, M.; Ballif, C., "Patterning Techniques for Copper Electroplated Metallization of Silicon Heterojunction Cells", IEEE 48th Photovoltaic Specialists Conference (PVSC), 2021, pp. 1530-1533, 44348, doi:10.1109/PVSC43889.2021.9518493
- [33] Lisco, F.; Virtuani, A.; Ballif, C., "A combi-encapsulant for enhanced performance of glass-free lightweight crystalline silicon solar PV modules", 2021 IEEE 48th Photovoltaic Specialists Conference (PVSC), 2021, pp. 1965-1970, 2021-06, doi:10.1109/PVSC43889.2021.9518430
- [34] Moroney, N.; Del Bino, L.; Woodley, M. T. M.; Zhang, S.; Hill, L.; Wittwer, V. J.; Sudmeyer, T.; Wildi, T.; Oppo, G.-L.; Vanner, M.; Brasch, V.; Herr, T.; Del'Haye, P., "Spontaneous polarization symmetry breaking of light in a microresonator", Conference on Lasers and Electro-Optics Europe & European Quantum Electronics Conference (CLEO/Europe-EQEC), 2021, pp. 1-1, 2021, doi:10.1109/CLEO/Europe-EQEC52157.2021.9541879

- [35] Obrzud, E.; Sattari, H.; Voumard, T.; Choong, G.; Denis, S.; Leo, J.; Wildi, T.; Dubochet, O.; Despont, M.; Lecomte, S.; Herr, T.; Ghadimi, A.; Brasch, V., "Stability of Lithium Niobate Integrated Photonics in Nonlinear and Metrology Applications", CLEO: Science and Innovations, San Jose, California (USA), pp. JW1A.167, 2021-05-09, doi:10.1364/CLEO\_AT.2021.JW1A.167
- [36] Obrzud, E.; Sattari, H.; Voumard, T.; Choong, G.; Denis, S.; Leo, J.; Wildi, T.; Dubochet, O.; Lecomte, S.; Herr, T.; Ghadimi, A.; Brasch, V., "Stability of Lithium Niobate Integrated Photonics in Nonlinear and Metrology Applications", EFTF-IFCS 2021, (online only), 2021-12-07
- [37] Pache, C.; Meier, C.; Droz, S.; Nguyen, D.; Roulet, J.-C.; Pollini, A.; Houge, T.; Droz, F., "Miniature Flash LiDAR for Bathymetry: An Experimental Proof-of-Concept", International Geoscience and Remote Sensing Symposium (IGARSS), Brussels (BE), 2021-07
- [38] Puaud, A.; Ozanne, A.-S.; Senaud, L.-L.; Muñoz, D.; Roux, C., "Microcrystalline Silicon Tunnel Junction for Monolithic Tandem Solar Cells Using Silicon Heterojunction Technology", IEEE Journal of Photovoltaics, vol. 11, no. 1, pp. 58-64, 2021-01, doi:10.1109/JPHOTOV.2020.3038600
- [39] Rexhaj, E.; Proença, M.; Ambuehl, J.; Bonnier, G.; Lemay, M., "Evaluation of a cuffless watch-like sensor for 24-hour ambulatory blood pressure monitoring", European Heart Journal, Volume 42, Issue Supplement 1, ehab724.2348, 44409, doi:10.1093/eurheartj/ehab724.2348
- [40] Simeunovic, J.; Schubnel, B.; Alet, P.-J.; Carrillo, R. E., "Spatio-temporal graph neural networks for multi-site PV power forecasting", in IEEE Transactions on Sustainable Energy, 44501, doi:10.1109/TSTE.2021.3125200
- [41] Spanoudakis, P.; Kiener, L.; Cosandier, F.; Schwab, P.; Grivon, D.; Psoni, G.; Rellakis, D.; Bencheikh, N., "Large Angle Flexure Pivot Development and Test Campaign Results", European Space Mechanisms and Tribology Symposium, (online only), pp. 7, 2021-09-20
- [42] Spanoudakis, P.; Novo, D.; Cosandier, F.; Schwab, P.; Ummel, A.; Psoni, G.; Rellakis, D.; Struijs, R.; Fouché, F.; de Faoite, D., "COOLER, a louvered, passive radiator for Cubesats", European Space Mechanisms and Tribology Symposium, (online only), pp. 8, 2021-09-20
- [43] Torcheboeuf, N.; Mitev, V.; Balet, L.; Renevey, P.; Krakowski, M.; Resneau, P.; Larre, A.; Legoe, J.-P.; Robert, Y.; Vinet, E.; Garcia, M.; Parillaud, O.; Gerard, B.; Boiko, D. L., "Ultra-short pulse non-classical light emitters utilizing multiple wide quantum wells", 2021 Conference on Lasers and Electro-Optics Europe & European Quantum Electronics Conference (CLEO/Europe-EQEC), 2021, pp. 1-1, 44348, doi:10.1109/CLEO/Europe-EQEC52157.2021.9592609
- [44] Ukil, A.; Marin, L.; Jara, A. J.; Farserotu, J., "Human-Centric Analytics and Systems Impacting Quality of Life", in Proceedings of the 30th ACM International Conference on Information & Knowledge Management, CIKM '21, p. 4884, 44501, doi:10.1145/3459637.3482033
- [45] Valencia, F.; Polian, I.; Regazzoni, F., "Extending Circuit Design Flow for Early Assessment of Fault Attack Vulnerabilities", 24th Euromicro Conference on Digital System Design (DSD), 2021, pp. 385-388, doi:10.1109/DSD53832.2021.00065.
- [46] Vuille-dit-Bille, E.; Zubkovs, V.; Chai-Gao, H.; Boghossian, A. A.; Cattaneo, S., "Functional hydrogels for immobilization of single-walled carbon nanotube-based glucose sensors", Swiss NanoConvention 2021, Conference Abstracts, online, 2021-06
- [47] Zubkovs, V.; Vuille-dit-Bille, E.; Chai-Gao, H.; Markocic, M.; Cattaneo, S., "Hydrogel-immobilized single-walled carbon nanotube-based optical sensors for cell culture monitoring", NanoBioTech-Montreux Conference 2021, Conference Abstract, Montreux (CH), 2021-11

## Conferences and Workshops

T. Aderneuer, "Advanced Metrology of Free-Form Micro-optical Elements", Polymer Replication on Nanoscale (PRN 2021), May 2021

G. Andreatta, A. Lachowicz, J. Gay, N. Blondiaux, A. Faes, X. Lefèvre, L. Pires da Veiga, B. Kamino, A. Paracchino, "Surface and interfacial engineering of energy systems by phosphonate self-assembled monolayers", EMRS Fall Meeting 2021, online, 23 September 2021

G. Andreatta, N. Blondiaux, J. Gay, A. Lachowicz, A. Faes, C. Allebé, "Patterns for solar cells metallization using phosphonic acid self-assembled monolayers", ICASS 2021: 4th International Conference on Applied Surface Science, online, 30 June 2021

G. Basset, "Optical or Digital Security Features?", EPIC Online Webinar, Fake Drugs, Forensic Sciences and Anticounterfeiting, January 2021

- S. Bhoir, C. Brivio, E. Namor, A. Hutter, "Experimental comparison of fast-charging protocols for NMC and NCA Li-ion batteries", IEEE Vehicle Power and Propulsion Conference, October 2021
- S. Boder-Pasche, T. Valentin, F. Navaee, D. Migliozi, S. Heub, S. Graf, J. Goldowsky, S. Paoletti, V. Revol, G. Weder, "Automated and Standardized Solutions for Organoid Technology", Biointerfaces International Zurich 2021, Zurich (CH), 18-19 August 2021
- F. Crivelli, "Connected Machines", Vernissage Technology Outlook 2021 SATW, CSEM Neuchâtel / online (CH), 8 June 2021
- R. Ferrini, "A new era for free-form micro-optics manufacturing: the final frontier ...", OptecBB & Photonics Israel - Automotive & Photonics, February 2021
- R. Ferrini, "A new era for free-form micro-optics manufacturing: the final frontier ...", Photonics+, February 2021
- R. Ferrini, "A new era for free-form micro-optics manufacturing: the final frontier ...", EPIC Online Technology Meeting on Next Steps Fast Growing Freeform Optics Applications, March 2021
- R. Ferrini, "A new era for free-form micro-optics manufacturing: The final frontier ...", IVAM HighTech Summit - Optics & Photonics, August 2021
- R. Ferrini, "A new era for free-form micro-optics manufacturing: the final frontier ...", Nano & Industrie 2021: Anwendungen in der Photonik, November 2021
- R. Ferrini, "A new era for free-form micro-optics manufacturing: the final frontier ...", 20th International Conference on Nanoimprint and Nanoprint Technologies (NNT), November 2021
- R. Ferrini, "PHABULOU\$ A new era for free-form micro-optics manufacturing: the final frontier ... ", Advances in design, fabrication and applications of free-form micro-optics, June 2021
- M. Höchemer, "Spot the difference – Anomaly Detection with One-Shot-Learning", SDS2021 - 8th Swiss Conference on Data Science, Luzern (CH), 9 June 2021
- I. Kastanis, "Deep Learning for quality inspection of injection molding parts", 6th European Conference on Artificial Intelligence in Industry and Finance, online (CH), 9 September 2021
- L. Kiener, H. Saudan, F. Cosandier, G. Perruchoud, A. Ummel, V. Pejchal, S. Lani, "Add flexibility to your Systems with Compliant Mechanisms built by Additive Manufacturing", ECSSMET European Conference on Spacecraft Structures, Materials and Environmental Testing, online, 24 March2021
- F. Kurth, "Innovative Sensor Solutions for Diagnostics and Health Monitoring at Point of Care", COMPAMED, Düsseldorf (DE), 15 November 2021
- F. Loizeau, "Augmented CMOS – how to add new functions to a mature technology?", mAm 2021, Villars (CH), 04-05 October 2021
- I. Panaretou, S. Hadjitheophanous, C. Kassapoglou-Faist, P. Dallemagne, S. Louloudi, D. Karadimas, C. Panagiotou, C. Kostopoulos, K. Michail, A. Kounoudes, "OffshoreMuster: An Integrated Real Time Localisation, Mustering and Evacuation Management System For Offshore Oil & Gas Health And Safety Operations", ADIPEC 2021 Technical Conference, Abu Dhabi (UA), 15-18 November 2021
- S. Paoletti, "Organ-on-a-chip; challenges, applications an opportunity for lab scientists in various industries", Future Lab Live, digital (CH), 2 June 2021
- A. Paracchino, A. Morana, A. Meyer, L. Weninger, P.-F. Rüedi, S. Girard, "Toward combined visible, infrared and X-ray imaging", RADOPT'2021, Saint-Etienne (FR), 15-18 November 2021
- A. Pauchard, "Mon point de vue sur le ML en tant que CEO", Basel Area: Mise en œuvre du machine learning en entreprise: l'affaire du management, Online (CH), 1 June 2021
- A.-P. Radan, R. Delgado-Gonzalo, G. Bonnier, K. M. Strahm, Y. Gürgan, S. Schneider, M. Lemay, D. Surbek, "Electronic fetal monitoring system (ELAINE): Novel technique for non-invasive assessment of the fetal electrocardiogram", SGGG 2021, St. Gallen (Switzerland), 2021-06-23
- M. Russi, "Deep Learning im Einsatz für die Maschine", Aurovis TechMeet, Alpnach (CH), 7 October 2021
- M. Russi, "Deep Learning im Einsatz für die Maschine", Aurovis TechMeet, Alpnach 19 November 2021
- D. Schmid, "Trinkwasserüberwachung", csemviva!, Landquart (Sw), 15 September 2021
- D. Schmid, "Digitale Technologien - Chance und Herausforderung für die Wirtschaft", W3+ Medical Technologies, Dornbirn (AT), 22 September 2021
- P. A. E. Schmid, "3D Vision and Machine Learning", CSEM Next - Renata, Itingen (CH), 25 August 2021
- P. A. E. Schmid, "AI für die Industrie – Von Qualitätskontrolle bis Predictive Maintenance", technOvation, Luzern (CH), 7 September 2021
- P. A. E. Schmid, "AI und Machine Learning – Der Anwender im Zentrum", ifz Product & System, online (CH), 15 June 2021
- P. A. E. Schmid, "Artificial Intelligence mit Praxisbeispielen", Young Swiss Engineers, Alpnach (CH), 27 October 2021
- P. A. E. Schmid, "Condition Based Maintenance with Deep Learning", Smart Maintenance Innovation Projects Flash Talks, online (CH), 18 March 2021
- P. A. E. Schmid, "Connected Machines – Neue und unerwartete Erkenntnisse", SATW: Vernissage des Technology Outlooks 2021, Zurich (CH), 8 June 2021

P. A. E. Schmid, "Data – AI – Machine Learning: Efficient Ways for a Successful Industrial Implementation", IVAM High-Tech Summit, online (DE), 26 August 2021

P. A. E. Schmid, "Data Analytics for Industry", TechOutlook 2021: Nachhaltigkeit & Digitalisierung der gebauten Umwelt, Internet (CH), 25 March 2021

P. A. E. Schmid, "Deep Learning and Fingerprinting for Swiss rail network", Basel Area: AI for SME 2. WS Education, online (CH), 21 June 2021

P. A. E. Schmid, "Deep Learning for Inline Quality Control and Condition Based Maintenance", 2021 PDA Robotics and Automation Conference, online, 20 April 2021

P. A. E. Schmid, "Deep Learning für die Industrie - Qualitätskontrolle, Prozessoptimierung und Predictive Maintenance", W3+ Enabling Technologies, Dornbirn (AT), 23 September 2021

P. A. E. Schmid, "Deep Learning für die Industrie – von Qualitätskontrolle bis Predictive Maintenance", Swiss Mechatronics Talk, online (CH), 2 November 2021

P. A. E. Schmid, "Deepfake für die Industrie", Swiss Innovation Forum (SIF), Basel (CH), 18 November 2021

P. A. E. Schmid, "From one machine to worldwide fleet – strategies for predictive maintenance", SDS2021 - 8th Swiss Conference on Data Science, Luzern (CH), 9 June 2021

P. A. E. Schmid, "Introduction au ML", Basel Area: Mise en œuvre du machine learning en entreprise: l'affaire du management (FR), online (CH), 1 June 2021

P. A. E. Schmid, "Keynote: Deep Learning for Industrial Quality Inspection", E+H Global Production Week, Internet (CH), 28 April 2021

P. A. E. Schmid, "Keynote: Industry 4.0 & Machine Learning", Bühler Group AI Community, Internet (CH), 29 April 2021

P. A. E. Schmid, "KI als Treiber für eine sichere Industrie", Digital Economic Forum 2021, Zurich (CH), 9 September 2021

P. A. E. Schmid, "Predictive Maintenance - Use Case", Kickoff AI for SME - Basel Area, online, 20 April 2021

P. A. E. Schmid, "Vertiefung neuester Technologien für die produzierende Industrie", Swissmem Industriesektor Assembly and Factory Automation, Alpnach (CH), 22 June 2021

A. Steinecker, "Technologietransfer am CSEM – Bedeutung der regionalen Verankerung", regiosuisse-Wissenschaftsforum 2021, Andermatt, 13-14 September 2021

F. Zanella, "Microlenses for imagers at CSEM SA", EPIC Online Technology Meeting with Special focus on CMOS Imagers Applications (in cooperation with EMVA), 8 February 2021

## Research Projects

Agroscope	LEAFYE – Development of a hand reader for automatic identification of plant pests
Botnar Research Center for Child Health (BRC)	COVENTE – Improve ventilation safety by means of intra-tracheal pressure monitoring – a short-term and a long-term solution
Botnar Research Center for Child Health (BRC)	DAVINCI – Development and validation of a laminar flow test to detect COVID-19 immunity in saliva
Bridge	EMIL – Emotion in the loop, a step towards a comprehensive closed-loop deep brain stimulation in Parkinson's disease
Bridge	MAXIBRIDGE – Development of a microresonator-based optical frequency comb source
Bridge	POWER – High-performance tandem solar cells with improved stability and cost-competitive manufacturing
Bridge	VIPS – Ultra-low power visual perception system
Eurostars	3DBrainScreen – An in vitro 3D brain-on-a-chip model for advanced drug discovery and neurotoxicological assays
Eurostars	AIRSWIM – Airborne instrument (LiDAR) for reliable shallow water imaging
Eurostars	COLIDE – Coherent LiDAR demonstration based on a novel swept laser engine in the beyond 2 µm wavelength range
Eurostars	DIAMANT – Direct sensor integration by additive manufacturing technology
Eurostars	EXRIL – Frequency stabilized laser with compact low-cost fiber ferrule based optical reference

Eurostars	FEMTOXIDE – High-power femtosecond laser system based on ytterbium doped sesquioxide crystals
Eurostars	IAP-CMM – Development and clinically test of a novel multimodal sensor system (hardware and algorithms) to continuously monitor in a noninvasive and straightforward way the intra-abdominal pressure (IAP) of intensive care patients (ICPs)
Eurostars	LEVES – Mid-infrared system utilizing level-crossing chirp-spectroscopy in quantum cascade lasers
Eurostars	LONGLIGHT – Long lifetime 1.5 um modelocked lasers via improved gain glasses
Eurostars	MINIHR – A wrist worn weareable device for women for stress detection and management
Eurostars	PREVALE – Preventing anastomotic leakage by developing an anastomotic perfusion measurement device (APM)
Eurostars	SCREENBEAT – Screening and monitoring of cardiac arrhythmias and sleep apnea
Eurostars	SMARTBEAT – ECG system for HRV lifestyle assessment
Forschungsfonds Aargau	SMARTSEED-PRESTUDY – Vision concept for a smart seeding system
Hans-Eggenberger-Stiftung	MAXIHE – Objective: rack-mounted microresonator-based optical frequency comb for massively-parallel optical computing
Interreg	BATHY 3D – Autonomous boat equipped with a LiDAR for precision 3D bathymetry
Interreg	BECOM – Système de dépôt de multicouches minces et homogènes sur PCB et bio-capteurs
Interreg	INNOSMAD – Maggiore collaborazione trasfrontaliera tra imprese e altri attori dello sviluppo
Interreg	METEOR – Revêtements fonctionnels hautes performances pour composants horlogers, diagnostics et pour l'instrumentation médicale
Interreg	NEODIAM – Développement de nouveaux outils de dépôt de diamant
Interreg	SBRA – Smart bra for diagnosing breast cancer
Interreg	V2G STUDY – Vehicle2Grid battery aging study in the frame of RegEnergy project led by Planair
ITER	ITERBOLO – Bolometers prototyping for ITER
SNI – Nanoargovia	DISP-BAT – Development of flow dispersion batteries
SNI – Nanoargovia	PEPS – Printed electrochemical protein sensor
SNI – Nanoargovia	PLASPEC – PhD on plasmonic enhanced photoelectro chemistry
SNI – Nanoargovia	UltraNanoGRACO – Customized, nanostructured grating compressors for high repetition rate ultrafast lasers
SNSF	AMELIZ – Advanced metallization strategies for heterojunction solar cells
SNSF	ASTROTWIN – Dual-comb system for FP calibration used in exoplanet search
SNSF	BIOREACT – Advanced in vitro organ degeneration models for musculo-skeletal research
SNSF	BLUVES – BLue to UV extreme precision astronomical spectroscopy
SNSF	ENHEART – Exploring full content of optical signals to enhance cardiac arrhythmia screening
SNSF	PAPET – Protective, passivating & selective transport layers in perovskite/c-Si tandem solar cells
SNSF	PERSI – Advanced functional perovskites for tandem solar cells
SNSF	SALTO – Nitrides semiconductors desposited at low temperatures for photovoltaic
SNSF	SHAMAN – Shadow mask localization of thin films for back-contacted crystalline silicon solar cells & energy harvesters

SNSF / Ambizione	PUZZLE – Bridging gaps in the neuroimaging puzzle: advanced techniques for comprehensive mapping of brain anatomy and multi-scale network activity
SNSF / BRIDGE	AOP-PLUGNPLAY – Implementation of adverse outcome pathway in a “plug & play” microfluidics system. Liver fibrosis as a proof of principle
SNSF / BRIDGE Discovery	FEMTOCHIP – Efficient optical frequency comb generation based on photonic integrated resonators and temporally structured pump light
SNSF / BRIDGE Discovery	FloCHIP-X – An automated end-to-end microfluidic system for chromatin immunoprecipitation followed by next generation sequencing
SNSF / BRIDGE Discovery	GREENSPACK – Green smart packaging
SNSF / BRIDGE Discovery	LINIOS – Gas spectrometer based on lithium niobate on insulator photonics integrated circuit
SNSF / BRIDGE Discovery	OPOSSUM – Ultra-sensitive photonics accelerometers for next generation seismic sensor networks
SNSF / BRIDGE Discovery	SMARTROBOT – Towards intelligent sensor-enhanced robotic neurosurgery
SNSF / BRIDGE Proof of Concept	Photonic-based microcomb system for the next-generation data centers
SNSF / Sinergia	EPISODE – Engineering of advanced hybrid perovskite for integration with silicon photovoltaic optoelectronic devices
SNSF / SPARK	RT-ET – Real-time quality monitoring of engineered tissue for regenerative medicine
Swiss Federal Office of Energy (SFOE)	BAT4SEL – Battery accelerated testing for second life
Swiss Federal Office of Energy (SFOE)	DELAPS – Développement de contacts passivants par sputtering
Swiss Federal Office of Energy (SFOE)	HALBION – Half bifacial back-contacted silicon heterojunction solar cells
Swiss Federal Office of Energy (SFOE)	IEA-TASK13 – Performance, operation & reliability of photovoltaic systems
Swiss Federal Office of Energy (SFOE)	IPRECISE – Development of passivating contacts by PVD
Swiss Federal Office of Energy (SFOE)	OPEN-SESAME – Modelling of energy storages for simulation/optimization of energy systems – open source energy storage models
Swiss Federal Office of Energy (SFOE)	OPERA – Utilisation optimale de l'énergie renouvelable pour les immeubles collectifs en rénovation
Swiss Federal Office of Energy (SFOE)	PAPERWALL – Test and demonstration of new solution for colored PV modules
Swiss Federal Office of Energy (SFOE)	SIRIUS – Development of next generation IBC-HJT modules for mass production
Swiss Federal Office of Energy (SFOE)	SOLARBODY-OFEN – Design, development, and demonstrate a new architecture of photovoltaic modules for the automotive and its production process, seeking to anticipate the evolutionary trend of the need of photovoltaic solar panels on the electric vehicles.
Swiss Federal Office of Energy (SFOE)	SPET – Flexible Hochleistungskomponenten für die Elektrifizierung von zukünftigen aeronautischen Antriebssystemen basierend auf photoelektrischer Energieerzeugung
Swiss Federal Office of Transport (FOT)	E-HTP – Etude du potentiel de l'hydrogène dans les transports publics

## Innosuisse – Swiss Innovation Agency

55392.1 INNO-ENG	3D-EXTR_SCAN	Pre-study to evaluate technical options for a "3D-extremities-scanner" and the feasibility of combined approaches using tags and data modelling
50041.1 INNO-ENG	4KSIMS	SIM-4KMEMS
47005.1 IP-ICT	ADAPTIVESTORM	An ultra-energy-efficient AI chip for next-gen ICT applications
52948.1 IP-EE	ADASTRA	A different approach for silicon-based tandem solar cells using perovskite on back-contacted devices with three-terminal wiring to go beyond 30% power conversion efficiency
48036.1 IP-ICT	ADRIOS_LIDAR	Real-time autonomous navigation system for on-orbit servicing
56367.1 IP-ICP	AIRO-PRINT	Adaptive system for automatic identification and marking of complex parts
57735.1 INNO-ICT	AIRQUALITYDATA-STUDY	Data analytics for room cleaning detection and classification
49735.1 IP-LS	AIRVIMO	Collection system for airborne viruses
33572.1 IP-ENG	AMC	Process optimization for additive membrane care
51090.1 IP-ENG	ASPIRE	Next generation SiC power electronics for e-mobility
55307.1 IP-EE	ATLAS	Agrivoltaics based on translucent modules and low-cost architectures
37863.1 IP-ENG	BETWEEN	Button with wireless connection for smart crown
53986.1 INNO-LS	BPA-STUDY	Analysis of manufacturing process, identification of critical automation steps and development of automation concepts.
26704.2 PFLS-LS	CERAMIC-TOOTH	Development of a manufacturing solution and surface topography for dental ceramic implant applications, using a novel two-piece implant design
43533.1 IP-ENG	CERANO	Metal oxide thin film deposition is used as a novel sealing process of porous anodized aluminum to increase the durability and corrosion resistance of aluminum components.
35221.1 IP-LS	CEREBRO	ASIC-enabled depth electrodes for neural recording and ablation
44317.1 IP-EE	CHAMELEON	Advanced technologies, innovative metrology and automated manufacturing for the production in Switzerland of new generation Photovoltaic modules
56437.1 INNO-EE	CLAC	Computationally light data-driven alternative to cloud-motion forecasting for PV applications
50440.1 INNO-ENG	COGI	Compact Gimbal made by additive manufacturing
51635.1 INNO-LS	COMBAG	Étude boucle connectée 2ème génération
42657.1 IP.ICT	COSIMA	Cooperative sensors for electrographic imaging
38614.1 IP-EE	DAGR	Disruptive innovation in solar energy technologies for building (human) integrated photovoltaic
37705.1 IP-ENG	DALIE	Dry auto-localizing integrated electrodes
41190.1 IP-ICT	DEEPPROFILE	SmartProfile
35855.1 IP-LS	DENOVOCAST	Automated skin tissue formation device
56201.1 INNO-EE	DICHRO	Dichroic mirror optimization

57765.1 IP-EE	DIGERATI	Dynamic graph machine learning for high-resolution forecasting
38522.1 IP-LS	DIGITAL-SALIVA	Digital saliva health monitoring device for dental disease prevention with printed biosensors
32348.1 IP-EE	DIPPS	Development of integrated production processes for perovskite/silicon high efficiency photovoltaic
46776.1 IP-ICT	DRIVERCHECK2	Intelligent vision system for driver monitoring coupled with steering command control system for improved road safety
36538.1 IP-LS	DURALOCK	Non-autologous dura substitute with self-sticking properties, a feasibility study
58209.1 INNO-EE	EASI-FC	Estimateurs pour accélérer l'adoption de solutions numériques dans le froid commercial
51474.1 IP-ICT	E-BRAIN	Smart robust wireless control and management of heavy machines
25365.1 PFNM-NM	EMIRS2	Development of new infrared light sources for gas detection application.
34950J IP-ENG	ERGO	Ultra-low power image sensor for IoT applications
40657.1 IP-ENG	ESORTER	Vollautomatisches Sortieren von Sendungen bis 30kg stellt nach wie vor eine grosse Herausforderung dar.
43210.1 IP-ICT	FETA	Flexible low-power embedded time series signal accelerator
56608.1 INNO-ENG	FLEXOMEGAGRIP	Feasibility study of mounting a rowing performance sensor at the end of an oar at a rowing boat
41844.1 IP-ICT	GEMTELLIGENCE	Development of software for automated gemstone analysis
41472.1 IP-EE	GIFT	Greenhouse infrared filter technology
25799.2 PFIW-IW	GMD	Predictive maintenance for mill drive power train systems
25839.2 PFLS-LS	GRAINVIEW	Flow speed measurement and morphological analysis of food grains
49466.1 INNO-ENG	HEALTH MONITORING TOILET CONCEPT	A stand-alone urine biomarker measurement module that can be connected as an addon to urine-diverting toilets.
31841.1 IP-ENG	HEART	High-precision additively manufactured Ti-based active medical device component
55358.1 IP-ENG	HERACLES	Development of a wearable patch for athletes, that analyzes biomarkers in during workouts.
43410.1 IP-ENG	HIHOLO	High-quality volume diffraction gratings for digital holography microscopy for enhanced resolution, acceptance angle, and field of view
27655.1 PFNM-NM	HI-NIL	Waveguide-based combiners for augmented reality processed by high refractive index nanoimprint lithography
28715.1 IP-LS	HOPE	Hypertension detection through optical blood pressure monitoring in pregnancy by an electronic wearable (HOPE)
49997.1 INNO-ENG	HRFS	High resolution force sensor
33074.1 IP-LS	IDENT	In-mouth pH monitoring
41363.1 IP-LS	IMPLANT	Development of innovative customer-tailored composite multilayers in orthopedic- and trauma surgery
28652.1 IP-ENG	IMPULSE-3DPRINT	Digital printing on 3 dimensional freeform objects

35752.1 IP-ENG	IMPULSE-CLOSEDLOOP	Closed loop manufacturing
35562.1 IP-LS	INFINIPRINT	Multi-material microfluidic printhead for "on-the-fly" formulation for advanced bioprinting
27291.2 PFLS-LS	IN-SITU	Intelligent process control for 3D-bioprinting technology
51173.1 INNO-ENG	LABSKIN STUDY	Design and process flow concept to realize a wearable sport patch for the analysis of sweat.
56816.1 IP-LS	LARVAESORTER	Development of a novel device capable of handling zebrafish larvae for high throughput
32970.1 IP-ENG	LEADME	Drug screening technology platform based on micro-LED and high-resolution MEA
43059.1 IP-ENG	LIFELUB	Development and implementiion of a new lubrication technology
35819.1 IP-ENG	LIFI-NED	Light-field optical combiner for augmented reality
35299.1 IP-ENG	LIGHTSAFE	Light-guiding security features
57210.1 INNO-LS	LIRI	Lieberty infection risk index
51734.1 INNO-LS	LOPLUS	Machine learning powered light obscuration technology for improved robustness and particle classification
35163.1 IP-ICT	LUBRISAFE	Axino.IoT.LubriSafe, an online quality and safety control system for metal working industry
50031.1 IP-ENG	LUPINE	High-resolution position sensor
27513.1 PFNM-NM	MEMCELL	MEMS cells for miniature atomic clocks
39848.1 IP-LS	MICROHISTO	High-throughput histology on microtissues
55022.1 IP-ICT	NAVIVIB	High-resolution space grade position navigation and timing GPS/GALILEO spaceborne receiver
55896.1 INNO-ENG	NEODI	Industrialisation of boron-doped diamond electrode allowing sterilization of tape water for hand washing
52886.1 IP-LS	NEON	Neonate monitoring – Add SpO2, BP and oHRM features to OxyPRem NIRS medical system
55424.1 IP-LS	NEOS	The NeurOphthalmoscope – Early diagnosis of brain diseases
56034.1 IP-LS	NIOXIS	Nitric oxide optical sensors for inflammation monitoring
41157.1 IP-ICT	OPTIBP-ML	Optical blood pressure management smartphone app: OptiBP Market Launch
58793.1 INNO-ENG	ORIL	Escapement with free impulse
35477.1 IP-LS	PETE	Preeclampsia test at the point of care
44861.1 INNO-ENG	PIKEPERCH STUDY	Quality control of pikeperch juveniles with digital imaging
28063.1 PFNM-NM	PRECISENSE	Development of a generic, high-performance, low-cost, absolute position sensor prototype
44145.1 IP-ICT	PROXIMITY	Capture system concept validation for in-orbit debris removal demonstration
44098.1 IP-EE	PULSE	Polychromatic universal LED light source and IV extraction for novel solar cell architectures
45216.1 IP-EE	PVBLIND	Smart modular photovoltaic blind

44587.1 IP-ENG	PYRAMID	High-aspect ratio 3D pyramidal probes on CMOS MEA's for in vitro tissue model study
42194.1 INNO-EE	RAPIDE	Reactive power management in district energy systems
40504.1 IP-ENG	REDULAS	Development of advanced femtosecond laser based ultra-precision manufacturing system for smart micro- LED display
53491.1 INNO-LS	RT-LAMP	Point of care – Saliva covid rapid testing
50339.1 IP-ENG	SAPHIR	Integrated energy harvesting
54167.1 INNO-LS	SENSOSKIN	Non-invasive and continuous monitoring transdermal sensing patch
35418.1 IP-ENG	SLAM4-0	Smart laser manufacturing for precision Industry 4.0
57886.1 IP-ICT	SMARTLADLEGATE	Additive, real-time monitoring system to increase safety and efficiency for steel casting
30759.1 IP-EE	SMART-LIGHT	Safe and smart control of blind and lighting
31392.1 IP-EE	SMART-MAT	Advanced materials and design for cost-effective, high-performance and high-reliability SmartWire connection technology
43816.1 IP-ENG	SMARTSPRING	Intelligent spring that reduces machine downtime, prevents failures and helps to design the optimum spring
35056.1 IP-ENG	SOMBRERO	Automatic evaluation of thermoanalytical curves
49680.1 INNO-ENG	SOW	Solar-powered watch range extender
53012.1 IP-ICT	SPG-ROBOT	Development of a tool to automate floor processing tasks
39219.1 IP-ENG	SPP-SENS	Sail profile performance sensor
16694.2 PFIW-IW	STABILITY	Dynamische Lageregelung für Hydraulikmodule demonstriert an einem Stelzentraktor im Rebberg
34545.1 IP-ENG	STERLING	Improve the production processes of RF components by developing new silver-plating methods
55059.1 IP-ENG	SUMIT	Development of a mobile health (mHealth) wellness/lifestyle device and app for the homebased monitoring of biomarkers in urine directly from the toilet.
50561.1 IP-LS	TESTMATE	A rapid self-test for sexually transmitted diseases that provides results in minutes, supported by digital health
53829.1 INNO-LS	TSUNAMI	External ventricle catheter – Ultrasound guidance and monitoring
43052.1 IP-ENG	TURBOPREDICTIONS	Steigerung der Effizienz, der Verfügbarkeit und der Lebensdauer von Turbokompressoren aufgrund einer erweiterten Datenerhebung und - Analytik
56068.1 INNO-LS	URINE-BAG-SENSORS	Technical concept for the development of a next generation urine biomarker measurement module
51080.1 INNO-LS	VISIMONEON	Vital signs monitoring of neonates
46999.1 IP-ICT	VIVALDI	Quality control and high-accuracy tracking system for steel mills

## European Commission Projects

H2020 – CS2-CFP10 2019-01	3DGUIDE	Feasibility demonstration of 3D printing for a new efficient production method of mm-wave waveGUIDE antenna
H2020 – NMBP 2016	ACENANO	Analytical and characterisation excellence in nanomaterial risk assessment: A tiered approach
H2020 – Clean Sky	AMPWISE	Autonomous wireless current sensor for aircraft power lines
H2020-ECSEL-2019-2-RIA	ANDANTE	Ai for new devices and technologies at the edge
H2020 – ECSEL 2018-1-IA	APPLAUSE	Advanced packaging for photonics, optics and electronics for low-cost manufacturing in Europe
H2020 – Clean Sky 2	AUDACITY	Compact powerful and reliable piezoelectrlc actuator for landing gear systems
H2020 – LC-SC3-RES-6 2018	BE-SMART	Innovative building envelope for sustainable, modular, aesthetic, reliable and efficient construction
H2020 – FETOPEN	CFLOW	Coherent ultra-fast long wave infrared communications
H2020 – ECSEL-2019-1-IA	CHARM	Challenging environments tolerant smart systems for IoT and AI
H2020 – ICT 2015	DETOP	Dexterous transradial osseointegrated prosthesis with neural control and sensory feedback
H2020 – LC-SC3-EE-2019	DOMOS	Operating system for smart services in buildings
H2020 – NMBP-23-2020	EMAPS-Cardio	ElectroMechanoActive polymer-based scaffolds for heart-on-chip
H2020 – ECSEL-2020-1-IA	Energy ECS	Smart and secure energy solutions for future mobility.
H2020-FETPROACT-2020-2	EXPERIENCE	The "Extended-Personal Reality": augmented recording and transmission of virtual senses through artificial-intelligence
H2020 – ICT 2016	FED4SAE	Federated CPS Digital Innovation Hubs for the Smart Anything Everywhere Initiative
H2020 – MSCA-ITN 2016	FOODSMARTPHONE	Smartphone analyzers for on-site testing of food quality and safety
H2020 – SPACE 2018	HEATPACK	New generation of high thermal efficiency components packages for space
H2020 – SC1-2019-Single-Stage-RTD	HEDIMED	Human exposomic determinants of immune mediated diseases
H2020 – MSCA-ITN-2019	HIDDEN	Hunting invisibles: dark sectors, dark matter, and neutrinos
H2020 – LC-SC3-RES-15 2019	HIGHLITE	High-performance low-cost modules with excellent environmental profiles for a competitive EU PV manufacturing industry
H2020 – LC-SC3-RES-15 2019	HIPERION	Hybrid photovoltaics for efficiency record using integrated optical technology
H2020 –CS2-CFP07-2017-02	HIPNOSIS	Hardware implementation of pilot-non-intrusive cognitive states identification system
H2020 – EEB 2017	HYBUILD	Innovative compact hybrid electrical/thermal storage systems for low energy buildings
H2020-FETFLAG-2018-2020	MACQSIMAL	Miniature hot atomic vapor cells-based quantum devices for sensing and metrology applications
H2020 – NMBP-FOF-2018	MANUELA	Additiive manufacturing using metal pilot line

H2020 – NMBP 2017	MANUSQUARE	Manufacturing ecosystem of qualified resources exchange
H2020 – ICT-2019-2	MEDPHAB	Photonics solutions at pilot scale for accelerated medical device development
H2020 – ICT 2015	MIRPHAB	Mid-infrared photonics devices fabrication for chemical sensing and spectroscopic applications
H2020 – ICT 2017	MOLOKO	Multiplex photonic sensor for plasmonic-based detection of contaminants in milk
H2020 – ECSEL 2019-1-IA	MOORE4MEDICAL	Accelerate innovation in emerging medical devices with open technology platforms.
H2020 – BG-2020-1	NAUTILOS	New approach to underwater technologies for innovative, low-cost ocean observation
H2020 – LC-SC3	NEON	Next-generation integrated energy services for citizen energy communities
H2020 – SFS 2018	NUTRISHIELD	Fact-based personalized nutrition for the young
H2020 – EIC-FTI-2018-2020	OFFSHOREMUSTER	An integrated emergency response decision support system for enhancing workers' safety in offshore oil & gas operations
H2020 – NMBP-FOF 2018	OLEDSOLAR	Innovative manufacturing processes and in-line monitoring techniques for the OLED and thin film and organic photovoltaic industries (CIGS and OPV)
H2020 – SC1-2019 Single-Stage-RTD	ORGANTRANS	Controlled organoids transplantation as enabler for regenerative medicine translation
H2020 – CS2-CFP07-2017-02	PEGGASUS	Pilot eye gaze and gesture tracking for avionics systems using unobtrusive solutions
H2020 – NMBP-TR-IND-2019	PEROCUBE	High-performance large area organic perovskite devices for lighting, energy and pervasive communications
H2020 – LCE 2017	PERTPV	Perovskite thin-film photovoltaics
H2020 – ICT-2019-2	PHABULOUS	Pilot-line providing highly advanced & robust manufacturing technology for optical free-form micro-structures
H2020 – FETFLAG 2018	PHOG	Sub-poissonian photon gun by coherent diffusive photonics
H2020 – DT-2020-1	PHOTONHUB	One-stop-shop open access to photonics innovation support for a Digital Europe
H2020 – EIC-FTI-2018-2020	PHOTONSENS	A plug-and-play photonics-based biosensing platform for salmon pathogen detection
H2020 – SPACE 2018	PULSAR	Space robotics
H2020 – FETOPEN-2018-2019-2020-4	RADIAL	Radiation source of light for picosecond laser pulse applications
H2020 – MSCA-RISE	RDC2MT	Research, demonstration, and commercialization of DC microgrid technologies
H2020 – LC-SC3-RES-4 2018	RE-COGNITION	Renewable cogeneration and storage technologies integration for energy autonomous buildings
H2020 – SEC 2016/7	ROBORDER	Autonomous swarm of heterogeneous robots for border surveillance
H2020 – ICT 2018-2	SARMENTI	Smart multisensor embedded and secure system for soil nutrient and gaseous emission monitoring

H2020 – SC1-2019 Single-Stage-RTD	SBR	Smart bone regeneration
H2020 – SPACE 2018-2020	SELECTOR	Surface mount technology (SMT) compatible electromechanical relay for compact redundancy ring
H2020 – BHC-2018-2020	SIM4BDR	Smart bone regeneration
H2020 – CS2-CFP10-2019-01	SMARTWISE	Smart miniaturized and energy autonomous regional aircraft wireless sensor
H2020 – LC-BAT-2020-3	SPARTACUS	Spatially resolved acoustic, mechanical, and ultrasonic sensing for smart batteries
H2020 – ECSEL-2020-1-IA	STORAI GE	Embedded storage elements on next MCU generation ready for AI on the edge
H2020 – SPACE-2019	SURPRISE	Super-resolved compressive instrument in the visible and medium infrared for earth observation applications
H2020 – CS2-CFP10 2019-01	SWISSMODICS	Development of a sensor with wide spectrum sensitivity for monitoring of damage and defects in composite structures
H2020 – EE 2016/7	TABEDE	Towards building ready for demand response
H2020 – ICT-37-2020	TRIAGE	Ultra-broadband infrared gas sensor for pollution detection
H2020 – INFRAIA-2020-1	VIPERLAB	Fully connected virtual and physical perovskite photovoltaics lab
H2020 – ICT 2018-2	WELMO	Wearable electronics for effective lung monitoring
H2020 – ICT 2019-2	ZEROAMP	Designing robust ultra-low-power circuits

## Space Projects

### ESA Projects

A-CSAC	NAVISP-EL1-032 – Advanced concept for chip-scale atomic clocks
ATOM	Manufacturing of the complex feature demonstrator for space application made of meta matrix composite (MMC) having the specific modulus >30 GPa·cm <sup>3</sup> /g.
BIDTS	Benchmarking of integrated digitalisation technologies for application to new space projects and future ESA missions
CCM_MTG	Development and manufacture of corner cube mechanisms for MTG satellite
CLUPI	CLUPI instrument for Exomars
COLA	Exploitation of the potential of laser sheets and fast detectors to detect and identify the trajectory of particles in the mm-cm range in-situ
COMAM	Development of a compliant mechanism based on additive manufacturing
COMO	Coronavirus remote monitoring of outpatients with heart rate, breathing rate and skin temperature
COOLER	Compact opening louver
CRUSSADER	Capture system for servicing and debris removal
ELAINE	Electronic fetal monitoring system
ELISAMET	LISA laser system performance metrology – Volume 1: Technical proposal
EUSO-B2	Elegant breadboard LIDAR for extrem universe space observation – Phase B2
EXPOSITION	Integrated flex pivot position sensor
FIFREDO	Fibered frequency doubler at 1560 nm
GERANIUM	Generative artificial intelligence for high performing inversion models

HIGHTS	Highly thermally conductive silver sintered die mounting
HOPP	Photodiode development
IMPROVE	Microvibration simulation and analysis tools
ISABELA	Development of a fine steering mirror breadboard
ISOL	Development of a high performance microvibration isolation system
LAFP	Development of a large angle flex pivot for space applications
LIDISOR2	Development of an experimental optical ranging payload for future Galileo satellites
MACAREW	Magnetic characterization of reaction wheels
MCC-X	Miniaturised motion controller customization for robotic exploration
MDP CHEF	Cost-effective hermetically sealed chip fuses
MILA4GROUND	Proof of concept for MILA ground applications
NIRS	NIR immersed grating in transmission for high resolution spectroscopy
NPI-BEARING	Miniature magnetic bearings for space actuators
OBSIDIAN	On-board system identification for uncertainty modelling & characterization
OSIP-VIB	Adaptive regulation for micro-vibration active-passive isolation systems
OSRC	Digital stabilisation electronics for lasers
PHOTAC	Etude pour une nouvelle génération d'horloge atomique
REAC	Reliability evaluation of MEMS by accumulative tests for space application
R-MTS	Development and fabrication of robust miniature timing source (R-mTS) engineering models (EMs). These R-mTS EMs are double-resonance miniature atomic clocks.
SLOTT	Straylight lidar verification tool, hardware pre-development
SMARTIES	Design, procurement and qualification testing of a Slip Ring assembly rotor based on additive manufacturing
TRICYCLE	Technology review of high-performance gyroscopes
ULTEEM	Ultra-long term EEG monitoring
WALLIE	Development new TOF detector. Follow-up MILA
WAVEGUIDE	Waveguide switches based on friction-free mechanisms

## Industrial Property

### Patent portfolio

In 2021, 7 propositions for new inventions were received internally and 8 new patent applications were filed (8 regular applications and 0 provisional application).

The patent portfolio has been further enhanced by the extension to different countries of 21 patent applications based on prior patent applications (7 cases of "filing under priority" and 12 cases of "entries into national/regional phase" and 2 cases of "filing of divisional patent application").

## Collaboration with Research Institutes and Universities

<i>University</i>	<i>Institute</i>	<i>Professor</i>	<i>Field of collaboration</i>
Adolphe Merkle Institut	Soft Matter Physics and Polymer Chemistry	U. Steiner, C. Weder	Bioinspired nanomaterials
Agroscope	Animal Production Systems and Animal Health	C. Ollagnier	Vital sign monitoring in livestock (pigs)
AIT Austrian Institute of Technology		L. Sajti	Magnetic inks

<i>University</i>	<i>Institute</i>	<i>Professor</i>	<i>Field of collaboration</i>
Alpen-Adria-Universität Klagenfurt, Austria	Digital Age Research Center	E. Andreeva	Cryptography & security
AO Research Institute Davos	Regenerative Orthopaedics	S. Grad, M. Stoddart	Biosensing
BFN, Bern University of Applied Sciences	Mikro- und Medizintechnik	G. Gruener	Joint Innosuisse with Prolistic: eSorter; Joint Innosuisse with Asyrl; BinPicking & Robotics
Cantonal Hospital St. Gallen	Lung Center	F. Baty, M. Bösch	Unobtrusive assessment of sleep apnea using a wrist-worn device
CEA-INES		Dr. Munoz	Silicon heterojunction, metallization
CHUV	Department of Anesthesia	P. Schoettker	Automated pulse oximeter waveform analysis to track changes in blood pressure during anesthesia induction: A proof-of-concept study
CHUV Lausanne	Head and Neck Surgery	S. Christian	Multispectral endoscopy for real time delineation in surger.
EMPA	Advanced Materials Processing	P. Hoffmann	Solid state lighting; Surface texturing
EMPA	Laboratory for Thin Films and Photovoltaics	F. Fu	Perovskite based tandem cells
EPF Lausanne	Advanced NEMS Laboratory	G. Villanueva	Nanofabrication of devices made out lithium niobate on insulator
EPF Lausanne	Advanced Quantum Architecture Laboratory	E. Charbon	Micro-optics
EPF Lausanne	Automatic Control Lab	C. Jones	Automatic building model identification and optimized control
EPF Lausanne	Computer Vision Laboratory	P. Fua	Reduced labelling machine learning
EPF Lausanne	Department Engineering Mechanics of Soft Interfaces	J. M. Kolinski	Smart interfaces/coatings
EPF Lausanne	EPFL-ECAL Lab	N. Henchoz	Digital experience – Meditation study in collaboration with Ming Shan (Bullet's Taoist center)
EPF Lausanne	High Energy Physics Laboratory	O. Schneider	Micro-optics
EPF Lausanne	ICLAB Integrated Circuits Laboratory	C. C. Enz	60GHz radar, approximate arithmetic, ULP radio and protocol for WiseSkin
EPF Lausanne	Laboratory of Advanced Semiconductors for Photonics and Electronics	N. Grandjean	Solid state lighting
EPF Lausanne	Laboratory of Integrated Performance in Design	M. Andersen	Human centric lighting
EPF Lausanne	Laboratory of Nanobiotechnology	A. Boghossian	Biosensors
EPF Lausanne	Laboratory of Physics of Complex Matter	L. Forro	Nanomaterials
EPF Lausanne	LAP Processor Architecture Laboratory	P. lenne	Embedded systems

<i>University</i>	<i>Institute</i>	<i>Professor</i>	<i>Field of collaboration</i>
EPF Lausanne	Laboratory of Solar Energy and Building Physics, LESO	J. L. Scartezzini	Human centric lighting
EPF Lausanne	LTS2 Signal Processing Laboratory 2	J.-P. Thiran	Multispectral imaging for water quality monitoring
EPF Lausanne	LTS4 Signal Processing Laboratory 4	P. Frossard	Privacy preserving machine learning and hierarchical computing
EPF Lausanne	Materials Science and Engineering	K. Scrivener	Minor elements
EPF Lausanne	Microengineering	D. Briand, V. Subramanian	Printed electronics
EPF Lausanne	PV-Lab	C. Ballif	High-performance solar cells and high-reliability PV modules
EPF Lausanne	School of Computer and Communication Sciences	M. Payer	Embedded security
EPF Lausanne	School of Engineering	R. Logé	Materials and alloys
EPF Lausanne	School of Engineering, Institute of Bioengineering	D. Van De Ville	Cuffless blood pressure estimation using raw photoplethysmography signal
EPF Lausanne	Signal Processing Laboratory	P. Frossard	Graph machine learning for power forecasting
EPF Lausanne	STI IEM DESL	M. Paolone	Predictive maintenance for batteries
EPF Lausanne	STI IEM SCI-STI-AS	A. Skrjervic	Wireless power transfer
EPF Lausanne	TCL Telecommunications Circuits Laboratory	A. P. Burg	Ultra-low power design, bias control
ETH Zurich	Computer Vision Laboratory	L. van Gool	Machine learning
ETH Zurich	Data Analytics Lab	T. Hofmann	Machine learning
ETH Zurich	Department of Biosystems Science and Engineering	A. Hierlemann	Organoid sorting
ETH Zurich	Department of Chemistry and Applied Biosciences	M. Kovalenko	Fluorescence lifetime imaging
ETH Zurich	Department of Health Sciences and Technology	S. Sturla	Biosensing
ETH Zurich	Department of Information Technology and Electrical Engineering	M. F. Yanik	Neuroinformatics
ETH Zurich	Energy-Efficient Circuits and IoT Systems	T. Jang	Analog-to-Digital converters
ETH Zurich	Institute for Electronics, D-ITET	V. Wood	State-of-health modeling for batteries
ETH Zurich	Integrated Systems Laboratory	L. Benini	RISC-V, neural network
ETH Zurich	Mobile Health Systems Lab	W. Karlen	Development and evaluation of a slow wave sleep modulation framework including continuous blood pressure and glucose monitoring

<b>University</b>	<b>Institute</b>	<b>Professor</b>	<b>Field of collaboration</b>
ETH Zurich	Particle Technology Laboratory	S. Abegg	Sensor
FHGR, University of Applied Sciences of the Grisons	Departement Angewandte Zukunftstechnologien, Institut für Photonics und ICT IPI	U. Hauser-Ehniger	Solid state lighting
FHGR, University of Applied Sciences of the Grisons	Kompetenzzentrum für Datenanalyse, Visualisierung und Simulation	B. Studer	Biosensing
FHNW, University of Applied Sciences and Arts Northwestern Switzerland	Institut für Nanotechnische Kunststoffanwendungen	M. Kristiansen	Micro and nano structuring
FHNW, University of Applied Sciences and Arts Northwestern Switzerland	Institute for Chemistry and Bioanalytics	D. Meinel	Biosensing
FHNW, University of Applied Sciences and Arts Northwestern Switzerland	Institute of Chemistry and Bioanalytics	L. Suter-Dick	Biosensing and 3D in-vitro models
FHNW, University of Applied Sciences and Arts Northwestern Switzerland	Institute of Product and Production Engineering	B. Resan	Lasers
Fondazione Bruno Kessler	Integrated Radiation and Image Sensors	L. Gasparini	Time-of-flight LiDAR detectors
Geneva University Hospital	Paediatric Emergency Division	M. Rida Benissa	Diagnosis based on AI on chest sounds
HE-ARC, University of Applied Sciences and Arts Western Switzerland	Engineering – Medical Devices	A. Kaempfer-Homsy	Biosensing
HSLU, Lucerne University of Applied Sciences and Arts	CC Electronics	E. Niederberger	Solid state lighting
HSLU, Lucerne University of Applied Sciences and Arts	CC Autonomous Systems and Robotics	T. Prud'homme	Vision, polarization camera; Calving detection in the barn with vision systems
Idiap Research Institute	Speech and Audio Processing	M. Magimai Doss	Detection of QRS landmark in ECG signals
Idiap Research Institute	Speech and Audio Processing	P. Motlicek	Modal a people monitoring system using multiple sensing modes (video, audio, ...)
IFREMER	Centre Méditerranée	J. Opderbecke	Bathymetric LiDAR
Imperial College of London, United Kingdom	Faculty of Engineering, Department of Electrical and Electronic Engineering	P. Mitcheson	Wireless power transfer

<b>University</b>	<b>Institute</b>	<b>Professor</b>	<b>Field of collaboration</b>
Imperial College of London, United Kingdom	Faculty of Engineering, Department of Electrical and Electronic Engineering	E. M. Yeatman	Energy harvesting for wireless sensor networks in aerospace applications; Smart materials
Institut für Kristallzüchtung, Berlin	Zentrum für Lasermaterialien	C. Kränkel	New laser crystals for high-power short pulse sources
IOB, Institute of Molecular and Clinical Ophthalmology Basel		M. Renner	Retina organoid sorting
IOR, Istituto Ortopedico Rizzoli, Bologna, Italy	2nd Orthopaedic and Traumatology Clinic	S. Zaffagnini	Clinical implantation and assessment
IPC-Oyonnax-France	Innovation Plasturgy Composites	L. Tenchine	Injection molding
National Research Council of Italy	Institute of Applied Physics (IFAC)	V. Raimondi	Compressive sensing for space applications
National Technical University of Athens	School of Mechanical Engineering	I. Paraskevas	Systems identification methods
ONERA-France	Meudon Center	M.-C. Mérienne	Pressure sensitive painting
ONERA-France	Modane-Avrieux Center	O. Guillerme, F. Paraz	Pressure sensitive painting
Politecnico Di Torino	Electronics and Telecommunications	E. Magli	Compressive sensing for space applications
Robert Bosch Hospital	Clinical of Geriatric Rehabilitation	C. Becker	Fall prediction and detection
Sant'Anna School of Advanced Studies, Pisa	Institute of Communication, Information and Perception Technologies (TeCIP)	A. Bogoni	Photonics radar
SIAF, Swiss Institute of Allergy and Asthma Research	Molecular Allergology	K. Bärenfaller	Biosensing
SUPSI, University of Applied Sciences and Arts of Southern Switzerland	IDSIA Dalle Molle Institute for Artificial Intelligence	L. M. Gambardella	Machine learning
SUPSI, University of Applied Sciences and Arts of Southern Switzerland	PV-Laboratory	M. Caccivio	Metrology
Swiss Tropical and Public Health Institute	Department of Medicine	D. Paris	Diagnostics
Università Campus Bio-Medico, Roma, Italy	Department of Orthopaedics and Trauma Surgery	V. Denaro	Clinical implantation and assessment
Université de Bourgogne, France	LE2I	J. Dubois	Remote vital signal monitoring
University Hospital Basel	Cardiology	A. Salome Vischer, T. Burkard	Accuracy of the RIVA digital blood pressure measurement app - a Pilot Study
University Hospital Basel	Department ENT Surgery	M. Caversaccio	Image-guided micro-surgery for hearing aid implantation

<b>University</b>	<b>Institute</b>	<b>Professor</b>	<b>Field of collaboration</b>
University Hospital Basel	Research Center for Clinical Neuroimmunology and Neuroscience	J. Lorscheider	Improving monitoring solutions for multiple sclerosis patients
University Hospital Bern	Department of Cardiology and Clinical Research	E. Rexhaj	Clinical study on 24h ambulatory blood pressure monitoring in 70 hypertensive patients using wrist-located optical sensors
University Hospital Bern	Department of Cardiology and Clinical Research	E. Rexhaj, S. Rimoldi	Clinical validation of a PAP sensor against non-invasive medical gold standard
University Hospital Bern	Department of Cardiovascular Surgery	D. Reineke	Clinical study on non-invasive blood pressure monitoring in 40 patients carrying a left ventricular assist device
University Hospital Bern	Department of Intensive Care Medicine	J. Schefold, D. Reinecke	Validation of the extended AVA product with the non-invasive measure of the BP in reference to the medical gold standard and with a 40-patient cohort (pregnant women)
University Hospital Bern	Lung Cancer Center	G. Kocher	Machine learning for efficient surgery
University Hospital Bern	Universitätsklinik für Frauenheilkunde	A. Radan	Introduce artificial intelligence (AI) and machine learning in cardiotocography (CTG) interpretation to improve clinical use; Wearable system for foetal ECG monitoring
University Hospital Bern	Universitätsklinik für Frauenheilkunde	D. Surbek	AI-based decision support system for delivery & Fetal monitoring by transabdominal electrocardiogram recording: the ELAINE pilot project
University Hospital Bern	Universitätsklinik für Neurologie, Leitender Arzt, Geschäftsführender Direktor Schlaf-Wach-Epilepsie-Zentrum (SWEZ)	K. Schindler	Epilepsy detection and prediction
University Hospital Bern	Universitätsklinik für Pneumologie	S. Ott	Unobtrusive assessment of sleep stages using a wrist-worn device
University of Athens, Greece	Dept. of Informatics & Telecommunications	S. Hadjiefthymiades	Internet of Things, location-based services, mobile and vehicular applications
University of Basel	Chemistry	E. Constable, C. Housecroft	Photochemistry
University of Basel	Psychiatry Hospital / Center for Chronobiology	C. Cajochen	Human centric lighting; Chronobiology
University of Bern	Quantum Optics Lab	A. Stefanov	Entangled photons for microscopy
University of Bern – ARTORG	Organs-on-Chip Technologies	O. Guenat	Biosensing

<i>University</i>	<i>Institute</i>	<i>Professor</i>	<i>Field of collaboration</i>
University of Essex, Colchester, United Kingdom	School of Computer Science and Electronic Engineering	L. Citi	Point-process and machine-learning-based neuro-muscular decoding/control algorithms
University of Geneva	Astronomy Department	F. Bouchy	NCCR PlanetS
University of Geneva	School of Economics and Management	S. Engelke	Non-contact heart rate monitoring through vision system
University of Geneva	Sensors Group at Institut für Neuroinformatik	S.-C. Liu	Neuroinformatics
University of Gothenburg, Sweden	Department of Orthopaedics	J. Wessberg	Sensory feedback
University of Neuchâtel	Complex Systems Group	V. Schiavoni	Security and data privacy in IoT systems; Usage of Trusted Execution Environments for cloud computation (IntelSGX) and IoT protocols (ARM's TrustZone)
University of Neuchâtel	Institute of Biology	E. Joseph	Technologies for heritage materials
University of Neuchâtel	Institute of Biology	P. Junier, F. Kessler	Ultrastructural investigation
University of Neuchâtel	Laboratoire Temps-Fréquence	G. Miletí	Atomic clocks
University of Neuchâtel	Institute of Biology	F. Kessler	Ultrastructural investigation
University of Pavia	Department of Chemistry	M. Pesavento	Chemical sensor
University of Sherbrooke	Neonatology	E. Fortin-Pelerin	Evaluation of PAP measurement accuracy in sheep
University of Zurich	Institute of Neuroinformatics	T. Delbrück	On-chip convolutional neural network for visual scene processing
Vienna University	Department of Physical Chemistry	P. Lieberzeit	Chemical sensor
ZHAW, Zurich University of Applied Sciences	School of Engineering, Winterthur	R. Locher	Joint Innosuisse with Mettler-Toledo: Automatic evaluation of thermoanalytical curves

## Teaching

	<i>Title of lecture</i>	<i>Context</i>	<i>Location</i>
M. Dadras	Microscopy	Microscopy and nanoscopy for ultrastructural investigation	University of Neuchâtel
M. Despont	Packaging and hybridization, the valorization of MEMS technologies	Micro- 534 advanced MEMS 2021 (D. Briand)	EPF Lausanne
L. A. Dunbar	Digital transformation	EMBA	EPF Lausanne
B. Gallinet	Photonic applications of micro and nano-structured surfaces	Erasmus Mundus Joint Master Degree Photonics for Security Reliability and Safety	Université Jean Monnet, St-Etienne
L. Kiener, F. Cosandier	Compliant mechanisms design course	Design of mechanisms	ESMAT (online)

	<i>Title of lecture</i>	<i>Context</i>	<i>Location</i>
N. Marjanovic, F. Zanella	Organic and printed electronics	Master course MICRO-505	EPF Lausanne
R. Pugin	Micro/nano-structured functional surfaces & components	Highlights in microtechnology – Summer School	EPF Lausanne
O. Sereda, P. Bowen	Powder characterisation and dispersion	CCMX course	EPF Lausanne

## Theses

### PhD Degrees Awarded in 2021

<i>Name</i>	<i>University</i>	<i>Title</i>
T. Aderneuer	University of Basel	Free-form micro-optical arrays: CAD tools, quality control, and metrology for lighting solutions
M. Auchlin	EPF Lausanne, Swiss Space Center	New reliability assessment of MEMS components under accumulative testing for space application
G. Borque Gallego	EPF Lausanne	Performance and micro-vibrations in magnetic bearings for space actuators
F. Chicco	EPF Lausanne	Low-power and wide-tuning range frequency generation for FMCW radars in advanced CMOS technologies
L. Driencourt	University of Basel	Plasmon-enhanced water splitting
T. Frei	EPF Lausanne	Radiation hard, micro-engineering solutions for thermal management in high energy physics and space applications,
Z. Halvorsen	ETH Zurich	Advanced microfluidic platforms for pathogen detection
P. Jokic	ETH Zurich	Efficient neural network acceleration for low power edge processing devices
T. C. Müller	EPF Lausanne	Adaptive body biasing in strong body factor technologies
L.-L. Senaud	EPF Lausanne	Electrical losses mitigation in silicon heterojunction solar cells
Y. Tang	University of Bern – ARTORG	Nanocellulose applications in biosensing devices

### CSEM Employees carrying out a PhD & PhD Funded by CSEM

<i>Name</i>	<i>Professor / University</i>	<i>Theme / CSEM Unit</i>	<i>Start year</i>
C. Aguet	P. Frossard / EPF Lausanne	Data-driven approaches for non-invasive cuffless blood pressure monitoring / Systems	2019
F. Ayhan	G. Villanueva / EPF Lausanne	LiNbO <sub>3</sub> waveguide microfabrication for broadband optical frequency combs for astronomical spectrometers calibration light / Systems	2020
G. Bernard	R. Logé, L. Pambagian / EPF Lausanne and ESA	Development of a production method of metal matrix composite for space applications using laser powder bed fusion / Micro & Nano Systems	2020
S. S. Bhoir	M. Paolone / EPF Lausanne	Exploitation of electrochemical impedance spectroscopy for predictive maintenance for batteries / Sustainable Energy Center	2021
L. Biggio	T. Hofmann / ETH Zurich	Machine learning based domain adaptation and interpretability for time-series / Regional Center – Alpnach	2019

Name	Professor / University	Theme / CSEM Unit	Start year
R. Blum	G. Milet / University of Neuchâtel	Long-term frequency stability improvement of a 2-photon Rubidium clock / Systems	2021
B. Bonnal	C. Dehollain / EPF Lausanne	A novel architecture of remotely powered, multiplexed, and ultra-low-power cooperative sensors for high-quality electrical impedance tomography / Systems	2019
S. Cerida Rengifo	C. Enz / EPF Lausanne	FMCW radar front-end / Integrated & Wireless Systems	2018
S. Del Giovane		New generation point of care sensing / Regional Center – Landquart	2021
M. Dussouillez	C. Ballif / EPF Lausanne	Identification and mitigation of the degradation mechanisms of perovskite solar cells / Sustainable Energy Center	2019
Y. El-Zein	K. Huguenin / University of Lausanne	Privacy-preserving data transmission and processing in digital health / Systems	2019
P. L. Gaudillière	EPF Lausanne	Embedded machine learning for the controlling of PPG-based systems / Systems	2021
D. Honzátko	P. Fua / EPF Lausanne	Defect detection using deep learning / Integrated & Wireless Systems	2018
P. Iurilli	V. Wood / ETH Zurich	State-of-health modeling for batteries / Sustainable Energy Center	2019
S. Jafari	S. Sturla / ETH Zurich	Electrochemical biosensing in food safety / Regional Center – Landquart	2017
L. Jeanningsros	J.-P. Thiran / EPF Lausanne	Classification of cardiac arrhythmia based on PPG / Systems	2020
E. Klauser	A. Karimi / EPF Lausanne	Adaptive control of a high-performance active-passive hybrid micro-vibration isolation system for sensitive payloads / Systems	2020
S. Narduzzi	S.-C. Liu / ETH Zurich	Ultra-low-power resource algorithms for neuromorphic hardware / Integrated & Wireless Systems	2020
E. Ntavelis	L. van Gool / ETH Zurich	Multimodal learning & generation: Utilizing diverse inputs to generate & manipulate images / Regional Center – Alpnach	2019
C. Sainz Martinez	M. Bach Cuadra / CHUV	MRI and EEG processing applied to human brain structure and function / Systems	2020
C. Sampaio Da Silva	A. Hierlemann / ETH Zurich	Organoid sorting / Regional Center – Alpnach	2021
P. Scharnhorst	C. Jones / EPF Lausanne	Reinforcement learning for building and grid control / Sustainable Energy Center	2019
Y. Sepehri	P. Frossard / EPF Lausanne	Smart edge for hierarchical vision systems / Integrated & Wireless Systems	2020
I. Sideris	M. Bambach / ETH Zurich	Data-driven modeling for metal additive manufacturing process optimization / Regional Center – Alpnach	2021
J. Simeunovic	P. Frossard / EPF Lausanne	Network time series forecasting for smart grid application / Sustainable Energy Center	2019
E. Vuille-dit-Bille	EPF Lausanne	Acoustic manipulation of organoids and microtissues / Micro & Nano Systems	2021

## Commissions and Committees

P.-J. Alet	European Commission, Innovation and Networks Executive Agency: expert European technology and innovation platform – photovoltaics (ETIP-PV): executive committee (member), steering committee (member), "Digital PV and grid" working group (leader) European technology and innovation platform – smart networks for the energy transition (ETIP-SNET): governing board (member) Intersolar Europe: conference committee (chairman), Intersolar Award jury (member)
F. Amez-Droz	CSEM Representative, Swiss Association of Science Journalism
G. Basset	Chairman of the conference, Product authentication & brand protection: becoming global and digital (Trustech 2021)
N. Blondiaux	Member of the council of the Academy of Engineering and Technology (AET) Member of the scientific committee of the EUSPEN 21st international conference & exhibition
S. Cattaneo	Expert for MSE Master Theses at OST Eastern Switzerland University of Applied Sciences Expert for W.A. de Vigier Foundation Innovation Coach for INOS Innovations Netzwerk Ostschweiz
F. Cosandier	International Scientific Committee, EUSPEN
P. Dallemande	Secretary and Swiss representative of Technical Committee 5 "Information Technology Applications", International Federation for Information Processing (IFIP)
R. Delgado-Gonzalo	Expert Group in Digital Health in the Swiss Alliance for Data-Intensive Services
M. Despeisse	n-PV workshop committee, EUPVSEC topic organizer, SolarPower Europe
M. Despont	Jury Member at the thesis of Thimothée Frei "Thermal management of components for high energy physics experiments and space applications" with Prof. V. Gass Member of the editorial board of Microelectronic Engineering Journal (Elsevier) Regional Program Chair of the 21st International Conference on Solid-State Sensors, Actuators and Microsystems (Transducers 2021) Vice-Chairman of the Swiss-MNT network
L. A. Dunbar	Academic co-Lead of Machine Learning Clinic in the Swiss Alliance for Data-Intensive Services Co-Chair of the Industrial Automation, Communication, Networking and Informatics Track of IEEE ICIT 2021 Members of the subcommittee FA10 on Computer Vision and Human-Machine Interaction in Industrial and Factory Automation Jury Member of the BCN Innovation Prize Jury Member of the Shapers Industry 4.0 Prize
S. Emery	Member of the Technical Committee of the IEEE SOI-3D-Subthreshold (S3S) Conference
J. R. Farserotu	Chair of ETSI Technical Committee Smart Body Area Networks (TC SmartBAN) Chair and Research Co-ordinator the Hermes Partnership Co-organizer Fourth Workshop on Knowledge-driven Analytics and Systems Impacting Human Quality of Life (KDAH-CIKM-2021) Co-convenor of a special session at URSI 2021 on ETSI SmartBAN in Medical IoT
R. Ferrini	Chair of the Swissphotonics Solid State Lighting - (SSSL) Swiss National Laboratory for Solid State Lighting Managing Director of the PHABULOU\$ Pilot Line Association Member of SciPiL (the Scientific Partnership in Lighting by Luger Research) Member of the Advisory Board of the Swiss Lighting Forum Member of the Program Committee of the FRED – Forum Romand de l'éclairage et de la domotique
S. Fricke	Chairman of M4IVD Board Member of the Organising Committee, Swiss ePrint 2021

B. Gallinet	Member of scientific committee, International Workshop on Metallic Nano-Objects (MNO 2021)
S. Generelli	Member of the organising committee Swiss Point-of-Care Symposium 2021
E. Györvary	<p>Member &amp; CSEM representative of EARTO Working Group on Emerging Technologies for Healthcare</p> <p>Member of Finnish Chamber of Commerce in Switzerland</p> <p>Member of the Board of EPOSS Association</p> <p>Member of the Board of European Organ-on-Chip Society (EUROoC)</p> <p>Member of the Core Team of Team Finland in Switzerland</p> <p>Member of the Extended Board of the Heterogeneous Technology Alliance (alliance federating the Fraunhofer (microelectronics), VTT, CEA-Tech, and CSEM) &amp; leading the Health &amp; AgriFood Platform</p> <p>Member of the Program Scientific Committee of EUROoCS 2021 event</p> <p>Member of the Scientific &amp; Organizing Committee of "Next Gen Organ-on-Chip &amp; Organoids" event</p> <p>Member of the Scientific Board of Swiss Integrative Center for Human health (SICHH), Fribourg</p> <p>Member of the Steering Board of Innovation Group Digitalization at Swiss Food Research</p>
J. Haesler	<p>CSEM representative EARTO Working Group Space Research</p> <p>CSEM representative ESA BIC Switzerland</p> <p>CSEM representative Swiss Space Office (SSO)</p> <p>CSEM representative SWISSMEM Swiss Space Industries Group (SSIG)</p> <p>CSEM representative Quantum Industry Consortium (QuIC)</p> <p>Member and CSEM representative organization committee Quantum Industry Day in Switzerland (QIDIS)</p>
H. Heinzelmann	<p>Member of the Executive Board, EARTO</p> <p>Member of the Foundation Board, Switzerland Innovation</p> <p>Member of the Steering Committee, CCMX Competence Center for Materials Science and Technology</p> <p>Member of the Strategic Advisory Board "Produktion der Zukunft", Austrian Federal Ministry of Transport, Innovation and Technology BMVIT</p> <p>Membre du Conseil d'Administration de Centredoc</p> <p>Référent externe, Université de Genève, CAS "Sustainable Development: Horizon 2030</p>
M. Höchemer	SDS 2022 Scientific Program Committee
A. Hutter	<p>Commission des énergies et de l'eau de la ville de Neuchâtel</p> <p>Federal Office of Transport (FOT), Energy Strategy for Public Transport 2050 (ESPT 2050) programme, expert</p> <p>Innosuisse expert</p> <p>Vice-President iBAT Association (<a href="http://www.ibat.swiss">www.ibat.swiss</a>)</p>
C. Joder	Member of the Advisory Board of IAT (Center of Innovation for Assistive Technologies) at Swiss Paraplegic Center, Nottwil
R. Jose James	Chairman Swiss Chapter IEEE Electronic Packaging Society
C. Julia-Schmutz	Communication Coordinator within the Heterogeneous Technology Alliance (HTA) CSEM Representative, BioAlps
H. F. Knapp	<p>Board of Directors member for cluster initiative Toolpoint for Lab Science</p> <p>Jury member for the Innovationspreis of the Industrie- &amp; Handelskammer Zentralschweiz</p> <p>Jury member for Zinno Ideenscheck</p> <p>Pre-jury member for Swiss Technology Award</p>

G. Kotrotsios	IDIAP, Member of the International Advisory Board Member of Microcity Consultancy Committee Member of the Advisory Board of the NTN Innovation Booster Photonics Member of the Board of AM-TTC (Advanced Manufacturing Technology Transfer Centers) Initiative Member of the Board of the Heterogeneous Technology Alliance (HTA) Member of the Steering Committee of the SATW Advanced Manufacturing Research Alliance Member of the Swiss Academy of Engineering Sciences SATW Micronarc, member of the Group of Experts
M. Krieger	CSEM Representative Expert Workgroup Data driven Business Models, Swiss Alliance Data intensive services CSEM Representative Greater Zurich Area (GZA) CSEM Representative Innovation Expert Group Food Packaging at Swiss Food Research CSEM Representative SEMI global semiconductor industry association CSEM Representative Smart Card Forum Switzerland (SCF) CSEM Representative Zürcher Handelskammer (ZHK) CSEM Representative, Advanced Factory Automation workgroup of Swissmem (AFA)
F. Kurth	Member of the technical program committee, International Conference on Miniaturized Systems for Chemistry and Life Sciences 2021 (mTAS 2021)
M. Lemay	Board Member, Swiss Society for Biomedical Engineering
N. Marjanovic	Member of the Organising Committee, Swiss ePrint 2021
S. Mohrdiek	Member of Photonics21 Work Group 6 – Design and Manufacturing of Components and Systems Member of Swissmem Fachgruppe Photonics Swissphotonics, Head of Swiss Photonic Packaging Laboratory (SPPL)
J.-L. Nagel	Member of the Editorial Board of the "Journal of Low Power Electronics" (JOLPE)
T. Offermans	Technical Cordinator of the PHABULOUS Pilot Line Association
S. Paoletti	Chair of the Swiss Symposium in Point of care diagnostics European Liquid Biopsy Society Member Executive Board member of biotechnet, Switzerland and co-lead of the IVD platform Member of the Bridge proposal evaluation panel
A. Pauchard	CNCI Chambre Neuchâteloise du Commerce et de l'Industrie, Neuchâtel Conseil d'administration de Silatech SA
R. Pugin	Member of the Expert Committee of the Association NTN Innovative Surfaces Member of the Omega Foundation Council Member of the Scientific Committee of the 4M Micro-Nano Manufacturing Association Member of the Scientific Committee of the World Congress on Micro and Nano Manufacturing
V. Revol	Co-Founder and deputy head of the Digital Innovation Hub LifeHub.Swiss ( <a href="http://www.lifehub.swiss">www.lifehub.swiss</a> ) Entrepreneur coach for MicroCity Start-Up Program InnoSuisse expert
D. Ruffieux	Chair of the RF and mm-Wave Circuits Track of the International Technical Program Committee of the European Solid State Circuit Conference (ESSCIRC)
E. Schaller	Member of the Executive Board of sensors.ch, Switzerland

P. A. E. Schmid	Academic co-lead expert group ML-Clinic (ML in Industrial Practice) Swiss Alliance for Data-Intensive Services CSEM Representative Swiss Mechatronics Cluster Founder and regional lead Digital Innovation Hub Robotics & Artificial Intelligence ( <a href="http://www.raisehub.swiss">www.raisehub.swiss</a> ) INOS accredited coach for RIS OST Industry 4.0 topic leader NTN Innovation Booster Databooster ( <a href="http://www.databooster.ch">www.databooster.ch</a> ) Member expert group Industry 4.0 SATW Steering committee PDA Robotics & Automation
P. Steiert	Advisory Board Member for Institute für Chemistry and Biological Chemistry at the ZHAW Advisory Council for cluster initiative Toolpoint for Lab Science Member of the Executive Board for Verein Startup Pilatus Member of the Executive Board of the PHABULOUS Pilot Line Association
A. Steinecker	CSEM Representative EPoSS and Member of Working Group Robotics CSEM Representative IVAM
M. Zinggeler	European Liquid Biopsy Society (ELBS) Member Swiss Nanoscience Institute (SNI) Member

## Prizes and Awards

June 2021	Best Demo Paper award to Petar Jokic and his co-authors for their work entitled "A Sub-mW Dual-Engine Machine Learning Inference System-on-Chip for Complete End-to-end Face-Analysis at the Edge." International Symposium on VLSI Technology and Circuits, Kyoto (Japan).
June 2021	ResMIQ Best Student Paper award presented to Petar Jokic and co-authors for their work entitled "Battery-Less Face Recognition at the Extreme Edge." IEEE International New Circuits and Systems Conference (NEWCAS), Toulon (France).
June 2021	Quantum Electronics and Optics Division (QEOD) of the European Physical Society (EPS) Thesis Prize for Applied Aspects, was presented to Dr. Maxim Karpov for his Doctoral Thesis "Dynamics and Applications of Dissipative Kerr Solitons."
July 2021	Best Paper award on electric storage published in the IEEE Transactions on Energy Conversion Journal for paper presented to C. Brivio, V. Musolino, M. Merlo and C. Ballif for their paper "A Physically-based Electrical Model for Lithium-Ion Cells".
September 2021	Best Paper award given at the 14th International Workshop on Impedance Spectroscopy to Pietro Iurilli and co-authors for their work entitled "DRT-Based Modelling Framework for Li-Ion Cells".
September 2021	Venture Kick CHF 150,000 to kick-start MATIS – Monitoring Art with Technology, Innovation, and Science – assisting art authenticators in distinguishing forgeries.
October 2021	EARTO Award 2021, 3 <sup>rd</sup> place in the category "Impact Expected" for the project denovoCast with start-up CUTISS.
October 2021	Florian Burri received the Siemens Excellence Award regional prize for his Bachelor thesis entitled "Deep-Learning Solution for a Robotic Bin-Picking Task".



**CSEM SA**  
Jaquet-Droz 1  
CH-2002 Neuchâtel

**ALPNACH**  
Untere Grundlistrasse 1  
CH-6055 Alpnach

**BERN**  
Freiburgstrasse 2  
CH-3008 Bern

**LANDQUART**  
Bahnhofstrasse 1  
CH-7302 Landquart

**MUTTENZ/BASEL**  
Mattenstrasse 22  
CH-4058 Basel

**ZURICH**  
Technoparkstrasse 1  
CH-8005 Zurich



**CONTACT**  
[www.csem.ch](http://www.csem.ch)  
[info@csem.ch](mailto:info@csem.ch)  
[jobs@csem.ch](mailto:jobs@csem.ch)